Technical Physics, Vol. 46, No. 3, 2001, pp. 273–279. Translated from Zhurnal Tekhnicheskoĭ Fiziki, Vol. 71, No. 3, 2001, pp. 1–8.
Original Russian Text Copyright © 2001 by Gladkov, Gladyshev.

THEORETICAL AND MATHEMATICAL PHYSICS

On Fluctuations in Liquids and Gases

S. O. Gladkov and I. V. Gladyshev

Moscow State Institute of Radio Engineering, Electronics, and Automation (Technical University),
pr. Vernadskogo 78, Moscow, 117454 Russia

Received December 2, 1999

Abstract—The Lagrangian formalism is used to derive a system of nonlinear inhomogeneous dissipative differential equations describing the nonlinear dynamics of interrelated fluctuations of density, $\delta\rho$, and temperature, δT, in a medium. With these equations, the unstable (with respect to initial conditions) phase trajectory describing parameter fluctuations in the ρ–T plane was obtained. By numerically solving the equations, we show that $\delta\rho$ and δT oscillate in time almost periodically, which is typical of fluctuations. © *2001 MAIK “Nauka/Interperiodica”.*

The evolution of various processes of self-organization, which occur in dissimilar materials and, moreover, are studied in unrelated (at first sight) sciences, such as biophysics, biology, geology, chemical kinetics, medicine, etc., is usually described in terms of dissipative motion equations in a suitable phase space. These equations are derived by varying some classical action function proportional to the system Lagrangian, which is invariant by the transformation group $t = Rt = -t$, $x = RX = -x$.

The solution to many problems needs a rigorous mathematical description of nonlinear system behavior. It is necessary first to estimate the time it takes for phase subsystems to come into equilibrium states. Second, we must picture the motion trajectory in the related phase space.

Our interest in such issues is not purely cognitive. Associated solutions may be of importance in various applications. The problem to be solved in this paper falls into the group of problems outlined above and could be called classical. The object of investigation is the dynamics of interrelated density and temperature fluctuations in gases and liquids. The problem is also of interest because, as far as we know, papers where the time dependence of these fluctuations was reported are lacking.

The relaxation of most systems to equilibrium can very often be described phenomenologically by the equation $dx/dt = -\gamma x$, where γ is the damping factor (the reciprocal of relaxation time). Temperature and density are no exception: similar equations for them can formally be written as $dT'/dt = -\gamma_1 T'$, $d\rho'/dt = -\gamma_2\rho'$. These equations must uniquely follow from the principle of least action according to the formal rule $dx/dt = \gamma\delta S/\delta\bar{x}$, where $\bar{x} = \{T', \rho'\}$ and $\gamma = \{\gamma_1, \gamma_2\}$. When jointly involved in the action S, the initially independent parameters T' and ρ' satisfying these equations become “interrelated” and must lead to some unstable solution. The point $T' = 0$, $\rho' = 0$ is a point of unstable equilibrium: the phase trajectory given parametrically in the form $T' = T'(t)$, $\rho' = \rho'(t)$ stays infinitely long near other points (their coordinates are calculated below) and circumscribes a complex closed figure. The absence of the asymptotically stable solution $T' = 0$, $\rho' = 0$ comes as no surprise. This means that nonlinear interrelation between the parameters T' and ρ' exists. This interrelation causes some stable trajectory to appear, and it is this trajectory that describes the genuine fluctuation phase equilibrium of any similar two-dimensional scalar system. It will be shown that, depending on initial conditions u_0 and v_0, the system is brought either into the origin $u = v = 0$ when the initial conditions are specified far from it or into points $u_0 v_0$ otherwise.

It is usually believed that temperature and density obey the well-known heat conduction and sound vibration equations. In fact, according to [1], we can write

$$\partial T'/\partial t = \chi\Delta T', \quad \partial^2\rho'/\partial t^2 - c_{st}^2\Delta\rho' = 0, \qquad (1)$$

where $T' = T - T_0$ and $\rho' = \rho - \rho_0$ are small deviations of temperature and density from some values T_0 and ρ_0.

Equations (1) become interrelated when nonlinear terms in the system Lagrangian are taken into account. The corresponding equations can be found by using the principle of least action [2]. Small parameters in the related expansion are numerical factors that will for simplicity be calculated for the case of an ideal gas.

Let us introduce two independent dimensionless functions

$$\begin{aligned} u &= \rho'/\rho_0 = (\rho - \rho_0)/\rho_0, \\ v &= T'/T_0 = (T - T_0)/T_0. \end{aligned} \qquad (2)$$

The constants T_0 and ρ_0 will be renormalized after the nonlinear equations are solved. Note that both T_0 and ρ_0 are not equilibrium parameters of the system. Equilibrium (genuine) values are determined from the condi-

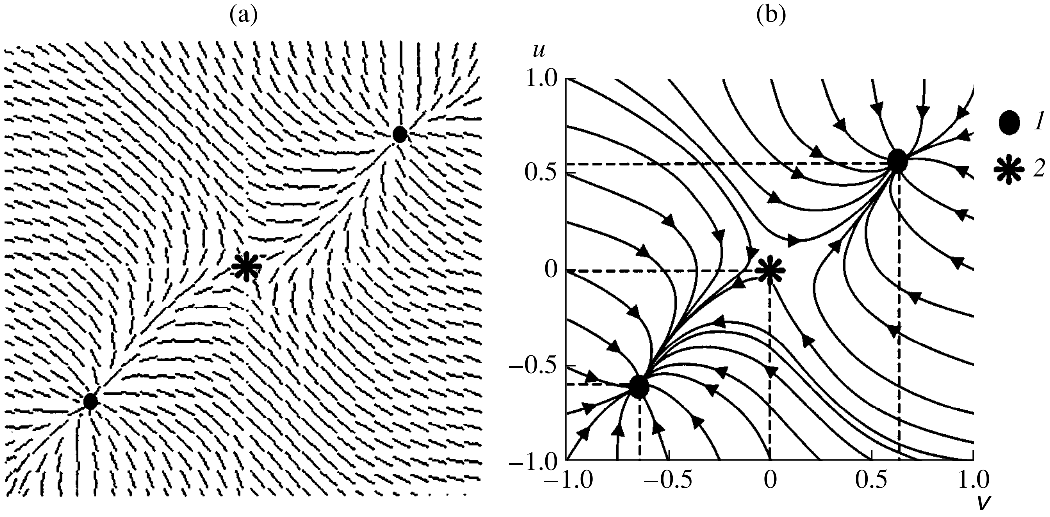

Fig. 1. Integral curves at $c_V = 3/2$ obtained by (a) the method of tangents and (b) integrating $\dot{u}(t)$ and $\dot{v}(t)$. *1*, stable node; *2*, saddle point.

tion for the asymptotic stability of a solution. Classical action function σ can generally be written in terms of independent variables u and v as follows:

$$\sigma\{u, v\} = (1/T_0)\int d\tau d^3\bar{x} L\{u, v\}, \qquad (3)$$

where $\tau = t/t_0$ is dimensionless time, t_0 is the time for the system to enter equilibrium, $d^3x = dV$ is a volume element, and the system Lagrangian L has the form

$$\begin{aligned} L\{u, v\} &= (a\rho_0^2/2c_{st}^2)[(\partial u/\partial t)^2 - c_{st}^2(\nabla u)^2] \\ &+ (bT_0^2/2c_T^2)[(\partial v/\partial t)^2 - c_T^2(\nabla v)^2] \\ &- K_1\nabla u\nabla v - K_2|u|(\nabla v)^2 - K_3|v|(\nabla u)^2 - K_4|v|\nabla u\nabla v \\ &- K_5|u|\nabla u\nabla v - K_6|v|(\nabla v)^2 - K_7|u|(\nabla u)^2 - g_1u^2/2 \\ &- g_2v^2/2 - g_3uv - g_4u^2|v| - g_5v^2|u| - g_6u^2|u| \qquad (4) \\ &- g_7v^2|v| - g_8u^2v^2 - g_9u^3v - g_{10}uv^3 - g_{11}u^4 - g_{12}v^4 \\ &+ g_{13}u^4|u| - g_{14}v^4|v| - g_{15}u^4|v| + g_{16}v^2u^2|u| \\ &+ g_{17}v^2u^2|v| - g_{18}v^4|u| + g_{19}u^6 + g_{20}v^6 - g_{21}u^5v \\ &+ g_{22}v^2u^4 - g_{23}v^3u^3 + g_{24}v^4u^2 - g_{25}v^5u. \end{aligned}$$

The Lagrangian is invariant by change of signs of fluctuations u and v because it contains their modules. The constants a, b, and g_i ($i = 1, 2, 3,\ldots, 25$) can be calculated, while the constants K_i (i = 1, 2,…, 7) have a phenomenological nature. The constant c_{st} is the longitudinal speed of sound in the medium, and c_T is the speed with which temperature fluctuations travel in the material. The dissipative motion equations are defined as

$$\partial\mathbf{A}/\partial\tau = (V/N)\delta\sigma/\delta\mathbf{A}, \qquad (5)$$

where $\mathbf{A} = (u, v)$. Similar equations were used by one of the authors in [3].

To find the constants a and b, we set $g_i = K_i = 0$. Then, we come to the heat conduction equation and the relaxation equation for density ρ. Indeed, using (3), (4), and (5), we obtain

$$\partial u/\partial t = \nu\Delta u, \quad \partial v/\partial t = \chi\Delta v, \qquad (6)$$

where ν is the kinematic viscosity and χ is the diffusivity. Hence,

$$a = t_0T_0\nu/\rho_0^2, \quad b = t_0\chi/T_0. \qquad (7)$$

The constants g_i are uniquely determined from the expansion of the Helmholtz thermodynamic potential F in powers of V' and T'. Up to the six-order terms, we have

$$\begin{aligned} F' + ST' + PV' &= -0.5(\partial P/\partial V)_TV'^2 - 0.5(C_V/T)T'^2 \\ &- (\partial P/\partial T)_VT'V' - (\partial^2P/\partial V^2)_T(V'^3/6) \\ &- (\partial^2P/\partial T^2)_V(V'T'^2/3) - (\partial^2P/\partial T\partial V)(T'V'^2/3) \\ &- \partial[(C_V/T)/\partial T](T'^3/6) - (\partial^3P/\partial V^3)_T(V'^4/24) \\ &- \partial^2[(C_V/T)/\partial^2T](T'^4/24) - (\partial^3P/\partial T^2\partial V)(T'^2V'^2/6) \\ &- (\partial^3P/\partial V^2\partial T)(T'V'^3/8) - (\partial^3P/\partial T^3)_V(T'^3V'/8) \\ &- (1/5!)\{(\partial^4P/\partial V^4)_TV'^5 + \partial^3[(C_V/T)/\partial^3T]T'^5 \qquad (8) \\ &+ 2(\partial^4P/\partial V^3\partial T)T'V'^4 + 2(\partial^4P/\partial V^2\partial T^2)T'^2V'^3 \\ &+ 2(\partial^4P/\partial V\partial T^3)T'^3V'^2 + 2(\partial^4P/\partial T^4)T'^4V'\} \end{aligned}$$

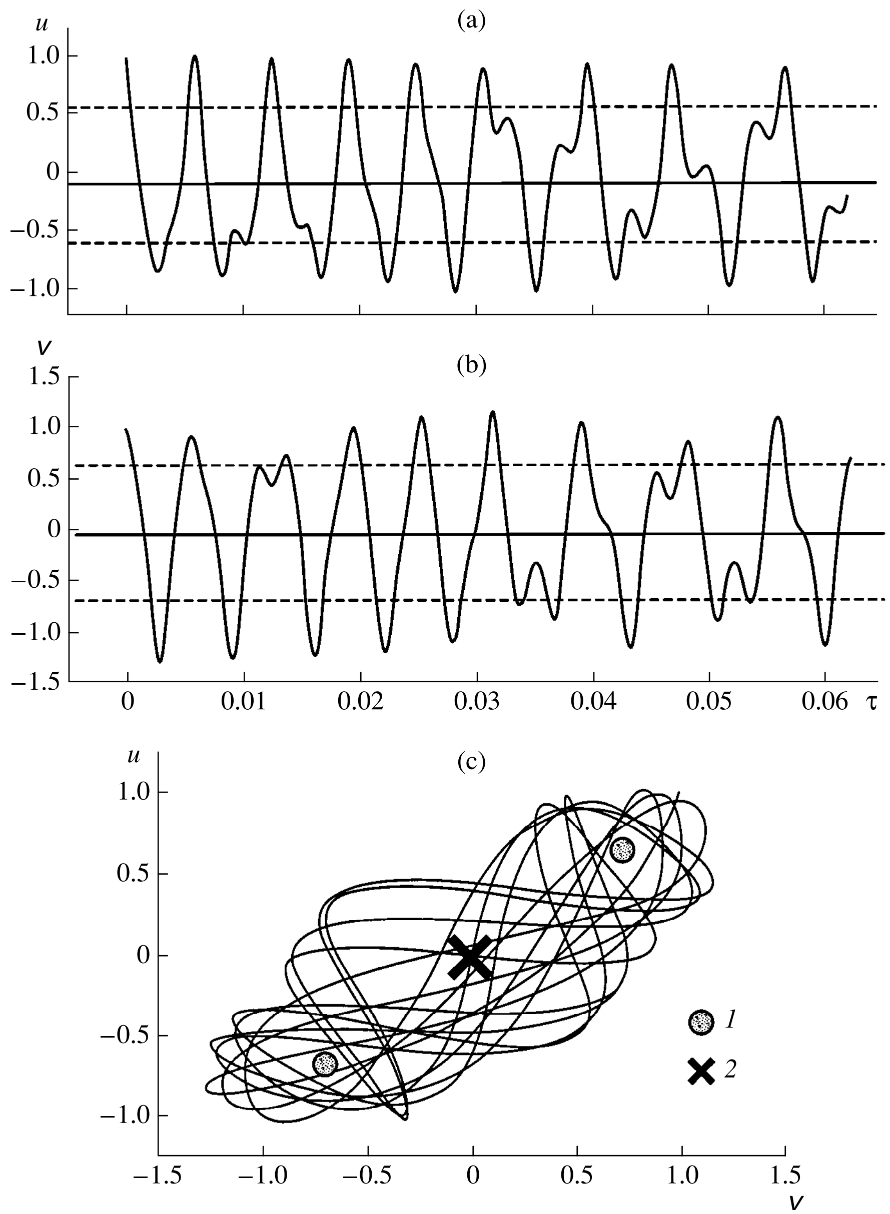

Fig. 2. Relative fluctuations (a) u and (b) V vs. dimensionless time τ. (c) Related phase trajectory for $c_V = 3/2$ and initial conditions $u(0) = V(0) = 1$. *1*, nodes; *2*, time-averaged coordinates. The time step is $\Delta t = 10^{-6}$.

$$+ (1/6!)\{-(\partial^5 P/\partial V^5)_T V'^6 - \partial^4[(C_V/T)/\partial^4 T]T'^6$$

$$-6(\partial^5 P/\partial V^4\partial T)T'V'^5 - 6(\partial^5 P/\partial V^3\partial T^2)T'^2V'^4$$

$$-6(\partial^5 P/\partial V^2\partial T^3)T'^3V'^3 - 6(\partial^5 P/\partial V\partial T^4)T'^4V'^2$$

$$-6(\partial^5 P/\partial T^5)T'^5V'\}.$$

Then, the coefficients g_i divided by the volume are

$$g_1 = -(\partial P/\partial V)_T V_0, \quad g_2 = -c_V T_0,$$

$$g_3 = -(\partial P/\partial T)_V T_0, \quad g_4 = -(\partial^2 P/\partial T^2)_V (T_0^2/3),$$

$$g_5 = -(\partial^2 P/\partial T\partial V)(V_0 T_0/3),$$

$$g_6 = -(\partial^2 P/\partial V^2)(V_0^2/6),$$

$$g_7 = -[(\partial/\partial T)(c_V/T)](T_0^3/6),$$

$$g_8 = -(\partial^3 P/\partial T^2\partial V)(V_0 T_0^2/6),$$

$$g_9 = -(\partial^3 P/\partial T^3)_V (T_0^3/8),$$

$$g_{10} = -(\partial^3 P/\partial V^2\partial T)(T_0 V_0^2/8),$$

$$g_{11} = -(\partial^3 P/\partial V^3)_T (V_0^3/24),$$

$$g_{12} = -[(\partial^2/\partial T^2)(c_V/T)](T_0^3/24),$$

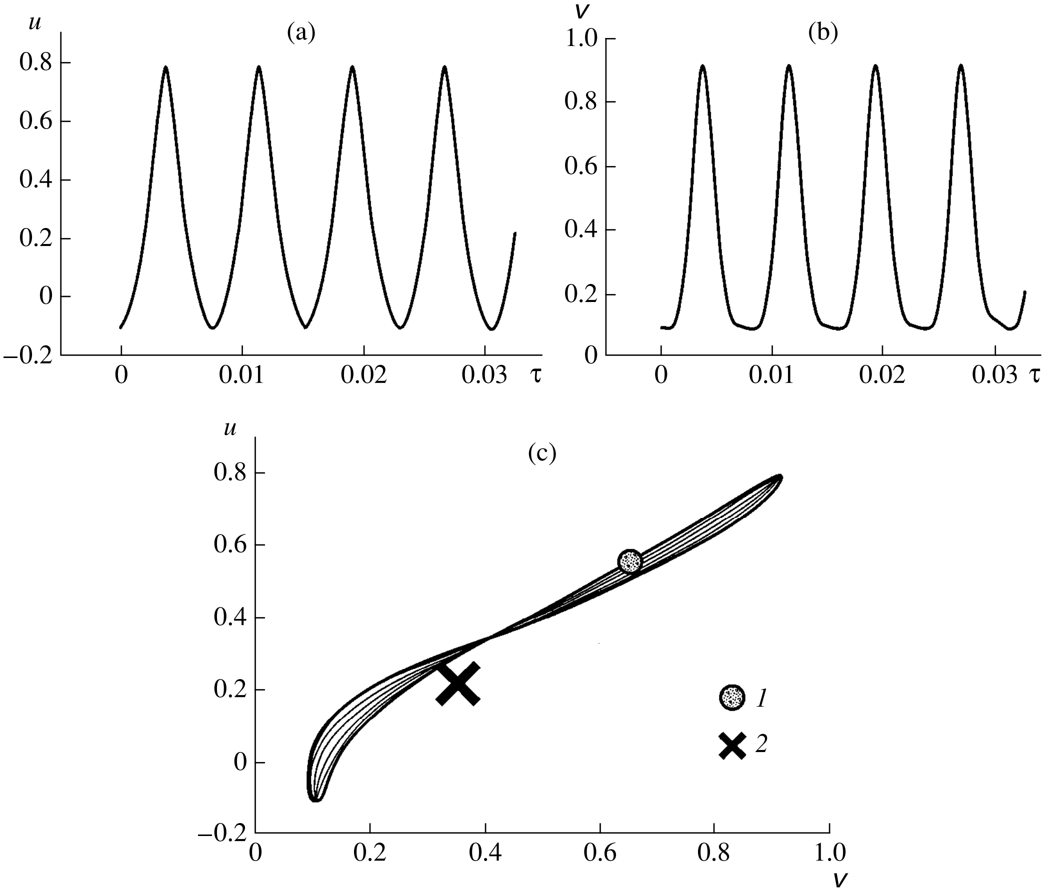

Fig. 3. Relative fluctuations (a) u and (b) v vs. dimensionless time τ. (c) Related phase trajectory at $c_V = 3/2$ and initial conditions $u(0) = -0.1$ and $v(0) = 0.1$. *1*, node; *2*, time-averaged coordinates. The time step is $\Delta t = 10^{-6}$.

$$
\begin{aligned}
g_{13} &= -(\partial^4 P/\partial V^4)(V_0^4/5!),\\
g_{14} &= -[(\partial^3/\partial T^3)(c_V/T)](T_0^4/5!),\\
g_{15} &= -2(\partial^4 P/\partial V^4 \partial T)(V_0^4 T_0/5!),\\
g_{16} &= -2(\partial^4 P/\partial V^2 \partial T^2)(T_0^2 V_0^3/5!),\\
g_{17} &= -2(\partial^4 P/\partial V \partial T^3)(T_0^3 V_0^2/5!),\\
g_{18} &= -2(\partial^4 P/\partial T^4)(T_0^4 V_0/5!),\\
g_{19} &= (\partial^5 P/\partial V^5)V_0^6/6!,\\
g_{20} &= -[(\partial^4/\partial T^4)(c_V/T)](T_0^6/6!),\\
g_{21} &= (\partial^5 P/\partial V^4 \partial T)T_0 V_0^5/5!,\\
g_{22} &= (\partial^5 P/\partial V^3 \partial T^2)T_0^2 V_0^4/5!,\\
g_{23} &= (\partial^5 P/\partial V^2 \partial T^3)T_0^3 V_0^3/5!,\\
g_{24} &= (\partial^5 P/\partial V \partial T^4)T_0^4 V_0^2/5!,\\
g_{25} &= (\partial^5 P/\partial T^5)T_0^5 V_0/6!,
\end{aligned}
\tag{9}
$$

where $c_V = C_V/V$ is the specific heat at constant volume. The transition to density fluctuations in (8) is straightforward: $V' = -M\rho'/\rho_0^2$, where M is the constant mass of the material. It is clear that such an expansion of the free energy in powers of u and v is correct only when the resulting series is convergent. The best convergence is provided at the points of asymptotically stable solutions. Indeed, if T_0 and ρ_0 are not the coordinates of an asymptotically stable point (we show below that such is the case for ideal gas), then the genuine asymptotically closed cycles around which the phase trajectories circumscribe complex figures are determined by nonlinear terms in the expansion of F in powers of u and v. Suppose that there are several nonzero solutions ($u \neq v \neq 0$) and some of them satisfy conditions $u_i \ll 1$ and $v_i \ll 1$, where $i = 0, 1, 2, \ldots, k$ (k is the number of solutions in the vicinity of zero). Then, among these solutions is the one providing phase volume contraction [div$\mathbf{v} < 0$, $\mathbf{v} = (v_x, v_y)$, where v_x and v_y are the right-hand side of (12)]. Moreover, the linearization of the right-hand side of the equations around this point

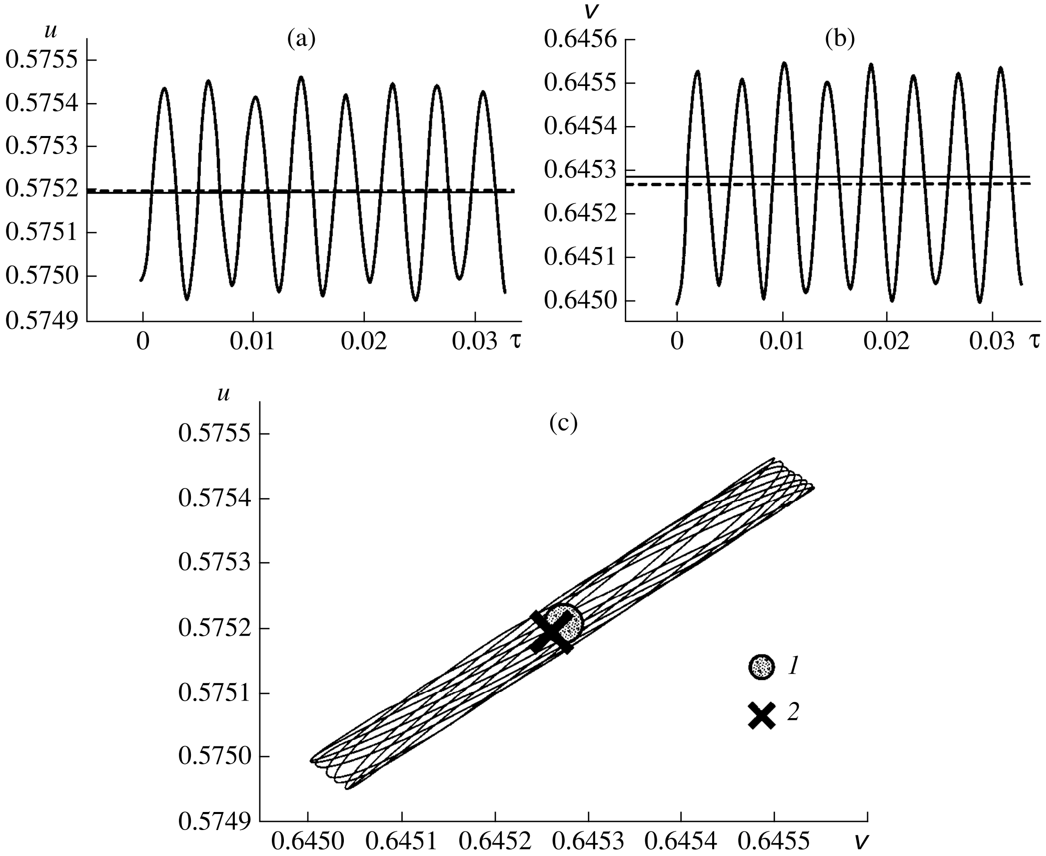

Fig. 4. Relative fluctuations (a) u and (b) v vs. dimensionless time τ. (c) Related phase trajectory at $c_V = 3/2$ and initial conditions in the immediate vicinity of the stable point $u_0 = 0.5752$ and $v_0 = 0.6453$. *1*, node; *2*, time-averaged coordinates. The time step is $\Delta t = 10^{-6}$.

results in the characteristic equation with negative eigenvalues of the matrix.

Let us consider ideal gas as an example. Setting the Boltzmann constant k_B to be equal to one, we have $PV = NT$ and from (9) get

$$\begin{gathered} g_1 = P_0, \quad g_2 = -c_V T_0, \quad g_3 = -P_0, \\ g_4 = g_8 = g_9 = 0, \quad g_5 = g_6 = -P_0/3, \\ g_7 = c_V T_0/6, \quad g_{10} = -P_0/4, \\ g_{11} = P_0/4, \quad g_{12} = -c_V T_0/12, \\ g_{13} = -NT_0/5, \quad g_{14} = c_V T_0/20, \\ g_{15} = NT_0/10, \quad g_{16} = g_{17} = g_{18} = 0, \\ g_{19} = -NT_0/6, \quad g_{20} = c_V T_0/30, \\ g_{21} = NT_0/30, \quad g_{22} = g_{23} = g_{24} = g_{25} = 0. \end{gathered} \tag{10}$$

In view of (4), (5), (8), and (10), the nonlinear dissipative equations take the form

$$\begin{aligned} \partial u/\partial\tau &= \nu t_0(\Delta u - c_{st}^{-2}\partial^2 u/\partial t^2) - k_1\Delta v \\ &+ k_2(\nabla v)^2 - 2k_3\nabla(v\nabla u) - k_4[v\Delta v + (\nabla v)^2] \\ &- k_5 u\Delta v + k_7[(\nabla u)^2 + 2u\Delta u] - u + v + v^2/3 \\ &+ u^2 + 3vu^2/4 - u^3 - u^4 - 2u^3 v/5 - u^5 - u^4 v, \\ \partial v/\partial\tau &= \chi t_0(\Delta v - c_T^{-2}\partial^2 v/\partial t^2) - k_1\Delta u \end{aligned} \tag{11}$$

Fluctuation points under initial conditions $u(0) = 0.1$ and $v(0) = 0.1$.

c_V	$\lvert u_0\rvert$	$\lvert v_0\rvert$	div **v**
3/2	0.302	0.432	–2.24
5/2	0.32	0.417	–3.54
7/2	0.352	0.394	–4.58
9/2	0.285	0.378	–5.33
11/2	0.305	0.361	–6.02
13/2	0.317	0.308	–5.27
15/2	0.331	0.344	–7.53
17/2	0.328	0.337	–8.17
21/2	0.329	0.326	–9.42
25/2	0.323	0.320	–10.74

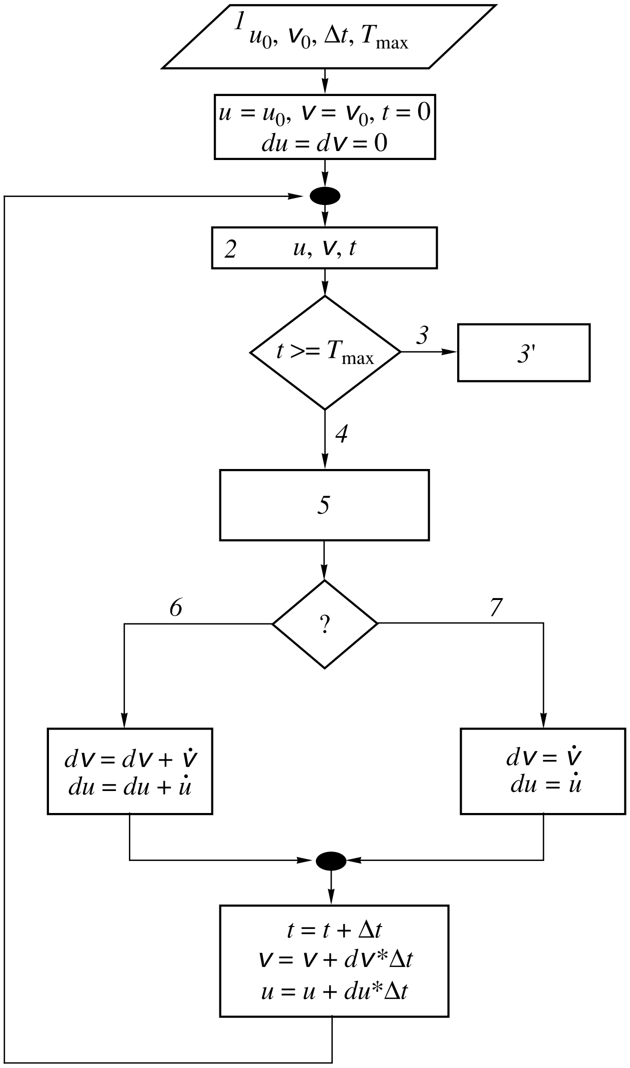

Fig. 5. Program for calculating the integral curves and phase trajectories: *1*, input; *2*, output; *3*, YES; *3'*, stop; *4*, no; *5*, calculation of $\dot{u}(u, v)$ and $\dot{v}(u, v)$; *6*, trajectories; and *7*, integral curves.

$$-k_2\nabla(u\nabla v) + k_3(\nabla u)^2 - k_4 v\Delta u$$

$$-k_5[u\Delta u + (\nabla u)^2] + k_6[(\nabla v)^2 + 2v\Delta v]$$

$$+u + c_v v + 2uv/3 - 3c_v v^2 + u^3/4 + c_v v^3/3$$

$$-c_v v^4/4 - u^4/10 + c_v v^5/5 - u^4/5,$$

where $k_i = K_i/T_0$ has a dimension of cm^2.

Consider solutions to equations (11) when the density and the temperature are uniformly distributed over volume V. If $\partial u/\partial t \gg (\nu/c_{st}^2)\partial^2 u/\partial t^2$ and $\partial v/\partial t \gg (\chi/c_T^2)\partial^2 v/\partial t^2$, we can neglect the second derivative for times $\delta t \gg \max\{\nu/c_{st}^2, \chi/c_T^2\}$ in these equations. Then, the nonlinear differential equations defined parametrically can be written as follows:

$$\begin{aligned}\partial u/\partial t &= -u + v + s_1(v^2/3 + u^2) + 3vu^2/4\\ &\quad - u^3 - s_1(u^4 + 2u^3 v/5) - u^5 - u^4 v,\\ \partial v/\partial t &= u + c_v v + s_2(2uv/3 - 3c_v v^2) + u^3/4\\ &\quad + c_v v^3/3 - s_2(c_v v^4/4 + u^4/10) + c_v v^5/5 - u^4/5,\end{aligned} \tag{12}$$

where $s_1 = |u|/u$ and $s_2 = |v|/v$ are the sign functions.

The stationary points are determined from the usual conditions $\partial u/\partial\tau = \partial v/\partial\tau = 0$, and linearized system (12) gives the characteristic equation $\lambda^2 - (c_v - 1)\lambda - c_v - 1 = 0$. It follows from this equation that the point $u^* = v^* = 0$ is not an asymptotically stable point of phase equilibrium of the linear differential equation [4] (Fig. 1). Taking into account the nonlinear terms in the expansion allows us to calculate the genuine points of fluctuation equilibrium that are defined by the following equations:

$$\begin{aligned}&-u + v + v^2/3 + u^2 + 3vu^2/4 - u^3 - u^4\\ &\quad - 2u^3 v/5 - u^5 - u^4 v = 0,\\ &u + c_v v + 2uv/3 - 3c_v v^2 + u^3/4 + c_v v^3/3\\ &\quad - c_v v^4/4 - u^4/10 + c_v v^5/5 - u^4/5 = 0.\end{aligned} \tag{13}$$

Solving these algebraic equations numerically, we arrive at three fluctuation points in the real space. The phase domain grows when the scalar $\nabla\mathbf{v} = \partial v_x/\partial u + \partial v_y/\partial v$, with v_x and v_y being the right-hand side of (12), is positive ($\nabla\mathbf{v} > 0$) and contracts when it is negative ($\nabla\mathbf{v} < 0$) [5]. The case $\nabla\mathbf{v} = 0$ refers to conservative systems and is omitted here. The coordinates of a point at which $\nabla\mathbf{v}$ is calculated depend on c_v. When, for example, $c_v = 3/2$ and the initial conditions $u(0) = 0.1$ and $v(0) = 0.1$, we have $u_0 = 0.302$, $v_0 = 0.432$, and $\nabla\mathbf{v} = -2.24$ (see the table); hence, the phase domain contracts. This is the fluctuation point, where the equilibrium gas density ρ_{eq} and the equilibrium temperature T_{eq} must be determined. We have $T_{eq} = T_0(1 + v_0)$ and $\rho_{eq} = \rho_0(1 + u_0)$, and ρ_0 and T_0 are "renormalized" with these formulas as $\rho_0 = \rho_{eq}/(1 + u_0)$ and $T_0 = T_{eq}/(1 + v_0)$.

It is not surprising that this point is unique. Under special initial conditions (Figs. 2–4) and due to the Hamiltonian symmetry, the phase trajectory is brought either into the negative domain in the plane u–v [$u(0) = v(0) = -0.1$] or into the positive one [$u(0) = v(0) = 0.1$], approaching the point (the cross in Figs. 2–4) in various ways. It is also seen that $u(t)$ and $v(t)$ oscillate (Figs. 2a–4a, 2b–4b).

For the initial conditions $u(0) = v(0) = 1$, integration yields the stationary point in the first quadrant (Fig. 1). However, the numerical calculation of the phase trajectory shows that, under these initial conditions, the system oscillates around the point 0–0 (Fig. 2). The fluctu-

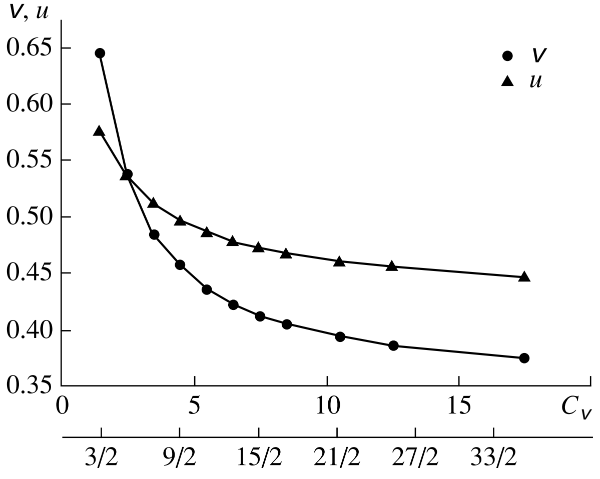

Fig. 6. Coordinates of stable points vs. specific heat c_V.

ation point lies between stationary points irrespective of initial conditions. Equations (12) were integrated using a program shown in Fig. 5.

The dependence of relative fluctuations on the specific heat is given in Fig. 6. It has to be noted that the above results for ideal gas may be generalized for real gases and liquids. They differ from ideal gas only in values of the parameters u and V, which, in turn, depend on the quantities involved in (9).

CONCLUSION

It is reasonable that, previously, the absence of basic prerequisites did not allow scientists to completely describe the evolution of fluctuations in gases and liquids. In view of the recent advances in this field [6–12], some ideas and concepts, as applied to our problem, need refinement. That is why the problem stated differs from classical fluid dynamics problems [1]. It was solved in terms of the Lagrangian formalism and classical action function, which is very convenient for considering nonlinear effects. As was expected, the numerical analysis of the equations covering nonlinear terms in the Lagrangian revealed the absence of asymptotically stable points. The values of u_0 and V_0 found by integration are the centers of closed cycles or points around which the system fluctuates. Thus, in terms of fluctuations, the genuine quasi-equilibrium point is that around which the system oscillates over its life, as illustrated in Figs. 2–4. The phase trajectory oscillates around the fluctuation points (marked by the cross in the figures with a high frequency). Therefore, the ergodic description of the parameters of such a system around these points is also valid. The qualitative picture of fluctuations does not depend on the integration step. The step was changed from 10^{-3} to 10^{-20}, resulting only in a travel of the functions $u(t)$ and $V(t)$ along the time axis τ in a bellowslike fashion. As seen from Figs. 3a and 3b, the frequency of these fluctuations equals $\omega \approx 2\pi/0.25t_0 = 8\pi/t_0$ for a step of $\Delta\tau = 10^{-6}$.

REFERENCES

1. L. D. Landau and E. M. Lifshitz, *Course of Theoretical Physics*, Vol. 6: *Fluid Mechanics* (Nauka, Moscow, 1986; Pergamon, New York, 1987).
2. L. D. Landau and E. M. Lifshitz, *Course of Theoretical Physics*, Vol. 1: *Mechanics* (Nauka, Moscow, 1973; Pergamon, New York, 1988).
3. S. O. Gladkov, Perspekt. Mater., No. 1, 16 (2000).
4. I. G. Petrovski, *Ordinary Differential Equations* (Nauka, Moscow, 1964; Prentice-Hall, Englewood Cliffs, 1966).
5. A. Yu. Loskutov and A. S. Mikhaĭlov, *Introduction to Synergetics* (Nauka, Moscow, 1990).
6. *Turbulence and Predictability in Geophysical Fluid Dynamics and Climate Dynamics: International School of Physics "Enrico Fermi," Varenna, 1983*, Ed. by M. Ghil, R. Benzi, and G. Parisi (North-Holland, Amsterdam, 1985), Course 88.
7. *Chaos in Astrophysics*, Ed. by J. R. Buchler *et al.* (Reidel, Dortrecht, 1985).
8. *Random Fluctuations and Pattern Growth: Experiments and Models*, Ed. by H. E. Stanley and N. Ostrowsky (Kluwer, Dordrecht, 1988).
9. H. G. Schuster, *Deterministic Chaos* (Physik-Verlag, Weinheim, 1984; Mir, Moscow, 1988).
10. *Fractals in Physics*, Ed. by L. Pietronero and E. Tosatti (North-Holland, Amsterdam, 1986; Mir, Moscow, 1988).
11. H. Haken, *Information and Self-Organisation: A Macroscopic Approach to Complex Systems* (Springer-Verlag, Berlin, 1988; Mir, Moscow, 1991).
12. S. O. Gladkov, *Physics of Composites: Thermodynamical and Dissipative Properties* (Nauka, Moscow, 1999).

Translated by V. Gurskiĭ

Technical Physics, Vol. 46, No. 3, 2001, pp. 280–286. Translated from Zhurnal Tekhnicheskoĭ Fiziki, Vol. 71, No. 3, 2001, pp. 9–16.
Original Russian Text Copyright © 2001 by Shiryaeva.

GASES AND LIQUIDS

Linear Wave Interaction at the Charged Fluid–Fluid Interface under Tangential Discontinuity of the Velocity Field

S. O. Shiryaeva
Demidov State University, Sovetskaya ul. 14, Yaroslavl, 150000 Russia
e-mail: shir@uniyar.ac.ru

Received February 25, 2000

Abstract—Capillary wave flow in a two-layer fluid with the upper layer moving parallel to the charged interface at a constant velocity is treated within a linear mathematical model. Interaction between waves excited on the free surface of the upper layer and at the interface results not only in classical Kelvin–Helmholtz instability (at low velocities of the upper layer) but also in oscillatory instability of the interface. The instability increment depends on the fluid density ratio, translational velocity, and charge density at the interface. *© 2001 MAIK “Nauka/Interperiodica”.*

INTRODUCTION

Kelvin–Helmholtz instability of the charged interface between two ideal immiscible fluids of different densities, either occupying the semi-infinite space or with the upper fluid flowing at a constant velocity U parallel to the interface, is of great applied interest in geophysics, technical physics, and chemical engineering [1–8]. It has been studied in detail both experimentally and theoretically. Nevertheless, certain features of this instability still remain unclear. The case in point is a nonideal situation when the upper fluid has a finite thickness. In practice, this situation is associated with wind-induced excitation of waves on the water surface. Based on Kelvin–Helmholtz instability, the theoretical model of this phenomenon substantially overestimates the critical wind velocity at which the waves start building up. Miles’s calculations [1] in the framework of the boundary layer concept with allowance for air and water viscosity yield a significantly better estimate of the critical wind velocity. According to Miles’s theory, the cause of wave excitation is the shear flow of air in the boundary layer with a velocity depending on the vertical coordinate, while air motion outside the boundary layer does not affect this process. The thickness of the boundary layer is known [9] to be small and proportional to the square root of the kinematic air viscosity. In this regard, it is natural to raise the question as to how the critical conditions for Kelvin–Helmholtz instability [i.e., the instability of the interface between two ideal (nonviscous) fluids] change when the upper fluid has a finite thickness.

(1) Turn to the simplest model, in which the fluids are considered incompressible. Let h and ρ_1 be the thickness and density of the upper dielectric fluid and let the lower perfectly conducting fluid with the density ρ_2 occupy the semi-infinite space $z < 0$. The lower fluid is subjected to the gravitational field $\mathbf{g}$ ($\mathbf{g} \parallel -\mathbf{n}_z$, where $\mathbf{n}_z$ is the unit vector of the Cartesian $0Z$ axis, which is orthogonal to the interface, and the $X0Y$ plane coincides with the unperturbed interface). Assume that the interface unperturbed by capillary flow carries a uniformly distributed electric charge of density σ.

To study the stability of capillary waves in this system, we solve the problem for the harmonic potentials ψ_1 and ψ_2 of the flow velocity field for the upper and lower fluids, respectively, in the Cartesian coordinate system:

$$\Delta\psi_j = 0, \quad j = 1, 2 \tag{1}$$

with the boundary conditions

$$z = h\colon \frac{\partial\psi_1}{\partial z} \approx U\frac{\partial\zeta}{\partial x} + \frac{\partial\zeta}{\partial t}, \tag{2}$$

$$\rho_1\frac{\partial\psi_1}{\partial t} + \rho_1 g\zeta + \frac{1}{2}\rho_1[(\nabla\psi_1)^2 - U^2] - \alpha_1\frac{\partial^2\zeta}{\partial x^2} = 0, \tag{3}$$

$$z = 0\colon \frac{\partial\psi_1}{\partial z} \approx U\frac{\partial\xi}{\partial x} + \frac{\partial\xi}{\partial t}, \tag{4}$$

$$\frac{\partial\psi_2}{\partial z} \approx \frac{\partial\xi}{\partial t}, \tag{5}$$

$$\begin{aligned}\rho_1\left\{\frac{\partial\psi_1}{\partial t} + g\xi + \frac{1}{2}[(\nabla\psi_1)^2 - U^2]\right\}\\ = \rho_2\left[\frac{\partial\psi_2}{\partial t} + g\xi\right] - P_\sigma - \alpha_2\frac{\partial^2\xi}{\partial x^2}.\end{aligned} \tag{6}$$

Here, Δ is Laplacian; $\zeta(x, t)$ is a perturbation of the free surface of the upper layer; $\xi(x, t)$ is a perturbation of the interface due to capillary wave flow; $\mathbf{U}$ is the constant velocity of the upper fluid relative to the lower one, its

1063-7842/01/4603-0280$21.00 © 2001 MAIK “Nauka/Interperiodica”

direction defining the orientation of the $0X$ axis; α_1 and α_2 are the surface tension coefficients of the free surface and the interface, respectively; $P_\sigma = 4\pi\zeta^{-1}\sigma_2 k\zeta$ is the electrostatic pressure exerted on the interface when the uniform electrostatic charge distribution is disturbed by the capillary flow of the fluid [10]; and ξ is the permittivity of the upper fluid.

The velocity field potential for the directed flow of the upper fluid has the form xU. Therefore, the total velocity field potential for the upper fluid can be written as the superposition

$$\psi_1(\mathbf{r}, t) = xU + \psi_1^0(\mathbf{r}, t),$$

where $\psi_1^0(\mathbf{r}, t)$ describes capillary wave flow in the upper fluid.

Capillary flow is produced by thermal molecule motion and is characterized by extremely low amplitudes $\zeta_0 \sim (kT/\alpha_1)^{1/2}$ and $\xi_0 \sim (kT/\alpha_2)^{1/2}$, where k is the Boltzmann constant and T is absolute temperature.

(2) Let us derive a differential equation that describes the time evolution of the amplitudes of capillary wave modes on the free surface of the upper fluid and at the interface. The waves arise as a result of the electrostatic field pressure and the tangential discontinuity of the velocity field at the interface. We should take into account that the velocity field potential in the lower fluid must vanish as the distance between the interface and an observation point tends to infinity. According to [7, 9], this means that $\psi_2(\mathbf{r}, t) \sim \exp(kz)$. We also assume that, in the upper layer, the velocity field potential depends on the Z coordinate as

$$\psi_1^0(\mathbf{r}, t) \sim (A_1(t)\exp(kz) + A_2(t)\exp(-kz)). \tag{7}$$

Formula (7), combined with the boundary conditions, yields

$$z = 0\colon \frac{\partial\psi_1}{\partial z} = \frac{\partial\psi_1^0}{\partial z} = kG(A_1, A_2)\psi_1^0; \qquad \frac{\partial\psi_2}{\partial z} = k\psi_2; \tag{8}$$

$$z = h\colon \frac{\partial\psi_1}{\partial z} = \frac{\partial\psi_1^0}{\partial z} = kH(A_1, A_2, kh)\psi_1^0;$$

$$G(A_1, A_2) = \frac{A_1 - A_2}{A_1 + A_2};$$

$$H(A_1, A_2, kh) = \frac{A_1\exp(kh) - A_2\exp(-kh)}{A_1\exp(kh) + A_2\exp(-kh)}; \tag{9}$$

$$G = \frac{H - \tanh(kh)}{1 - H\tanh(kh)}.$$

It is easy to see that, when $\tanh(kh) > H$ or $1 > H\tanh(kh)$, the signs of the coefficients G and H are opposite. One can consider that the coefficients G and H are time-independent if A_1 and A_2 have identical time dependences.

Assume that the perturbations of the free surface of the upper fluid, $\zeta(x, t)$, and the interface, $\xi(x, t)$, associated with capillary wave flow are periodic:

$$\zeta \sim \exp(-ikx), \quad \xi \sim \exp(-ikx). \tag{10}$$

Then, substituting expressions (8)–(10) into boundary conditions (2), (4), and (5), we find

$$z = h\colon \psi_1^0(\mathbf{r}, t) = \frac{1}{kH}\left(U\frac{\partial\zeta}{\partial x} + \frac{\partial\zeta}{\partial t}\right) = \frac{1}{kH}\left(-ikU\zeta + \frac{\partial\zeta}{\partial t}\right); \tag{11}$$

$$\psi_1(\mathbf{r}, t) = xU + \frac{1}{kH}\left(-ikU\zeta + \frac{\partial\zeta}{\partial t}\right);$$

$$z = 0\colon \psi_1^0(\mathbf{r}, t) = \frac{1}{kG}\left(U\frac{\partial\xi}{\partial x} + \frac{\partial\xi}{\partial t}\right) = \frac{1}{kG}\left(-ikU\xi + \frac{\partial\xi}{\partial t}\right); \tag{12}$$

$$\psi_1(\mathbf{r}, t) = xU + \frac{1}{kG}\left(-ikU\xi + \frac{\partial\xi}{\partial t}\right);$$

$$\psi_2(\mathbf{r}, t) = \frac{1}{k}\frac{\partial\xi}{\partial t}, \tag{13}$$

where i is the imaginary unit.

Note that

$$\nabla\psi_1 = \mathbf{U} + \nabla\psi_1^0, \qquad (\nabla\psi_1)^2 \approx U^2 + 2\mathbf{U}\nabla\psi_1^0 \equiv U^2 + 2U\frac{\partial}{\partial x}\psi_1^0. \tag{14}$$

We substitute expressions (10)–(14) into dynamic boundary conditions (3) and (6) and use a linear approximation in ζ and ξ to obtain the desired differential equations. They describe the time evolution of the amplitudes of the capillary waves on the free surface of the upper fluid layer and at the interface:

$$\frac{\partial^2\zeta}{\partial t^2} - 2ikU\frac{\partial\zeta}{\partial t} + (H\omega_0^2 - k^2U^2)\zeta = 0, \tag{15}$$

$$\omega_0^2 \equiv gk + \alpha_1\rho_1^{-1}k^3,$$

$$\frac{\partial^2\xi}{\partial t^2} - 2ik\rho U\frac{\partial\xi}{\partial t} + (\rho G\omega_*^2 + \rho k^2U^2)\xi = 0, \qquad \omega_*^2 \equiv \rho_1^{-1}[gk(\rho_2 - \rho_1) + \alpha_2k^3 - 4\pi\varepsilon^{-1}\sigma^2k^2], \tag{16}$$

$$\rho \equiv \rho_1/(G\rho_2 - \rho_1).$$

Expressions (15) and (16) are ordinary differential equations with constant coefficients; their solutions can be written as

$$\zeta = \zeta_0 \mathrm{Re}[\exp\{it[kU \pm (Hkg + H\alpha_1\rho_1^{-1}k^3)^{1/2}]\}], \quad (17)$$

$$\xi = \xi_0 \mathrm{Re}[\exp\{it[-k\rho U \pm (G\rho(\omega_*^2 + \rho\rho_2\rho_1^{-1}k^2U^2))^{1/2}]\}], \quad (18)$$

where ζ_0 and ξ_0 are the initial amplitudes of the capillary waves and Re[f] is the real part of the function f.

(3) The physical meaning of these solutions is defined by the signs of radicands in the exponents, which, in turn, depend on the signs of the coefficients $G = G(A_1, A_2)$ and $H = H(A_1, A_2, kh)$ in (8) and (9).

In particular, when $H > 0$, it follows from formula (17) that the free surface of the upper fluid executes wave motion whatever values are taken by the physical parameters of the fluid, the wave frequency being given by the bracketed expression in the exponent in (17). In accordance with the Doppler effect, the frequency is a linear function of the directed flow velocity in the upper medium as a whole. The free surface of the upper fluid may become unstable only when $H < 0$ presumably because of its interaction with the motion of the interface. However, the linear approximation does not reveal this instability.

According to (18), the spectrum of capillary flows at the interface is more complicated. If the thickness of the upper fluid is large, $G < 0$ (the parameter ρ is also negative) and we come to the situation [7] when conditions for interface instability are specified by the superposition of Kelvin–Helmholtz and Tonks–Frenkel instabilities. Solution (18) is periodic when the physical parameters are such that the radicand in (18) is positive, i.e., when the surface charge density σ at the interface and the velocity U of the upper fluid as a whole are low. As σ and U increase, the radicand changes sign and the imaginary unit can be removed from the root sign. In this case, the positive value of the radical determines the instability increment of that branch of the solution describing interface waves with the frequency $k\rho U$. The negative value of the radical determines the damping decrement of the other branch of wave motions with the same frequency $k\rho U$.

As the thickness of the upper fluid decreases, the coefficient $G(A_1, A_2)$ grows, becoming positive at a certain value of h. If G is within $[0, \rho_1/\rho_2]$, the parameter ρ remains negative and the imaginary unit can again be removed from the radical in (18). In this case, the unstable wave motion of the interface becomes stable. When $G > \rho_1/\rho_2$, the interface may become unstable only at a sufficiently high surface charge density σ, because, in this case, the flow of the upper fluid as a whole parallel to the interface exerts a stabilizing effect on it.

It should be noted that the situation where the denominator in the expression for ρ approaches zero is similar to the familiar dead-sea effect [11]. In this case, the amplitude of waves at the interface significantly grow.

Thus, when the thickness h of the upper fluid in a two-layer system of immiscible fluids is finite, wave motion excited at the interface is unstable in several ranges of the parameters σ (surface charge density) and U (velocity of the upper fluid as a whole).

Consider particular asymptotic situations.

(4) When the upper fluid is very thick ($kh > 6$), waves excited at the interface and on the free surface do not interact. The depth of penetration of wave motion excited on the free surface is known to be on the order of the wavelength: $h \sim \lambda \equiv 2\pi/k$ [11]. Therefore, it can be expected in the above two-layer system that waves on the free surface and at the interface will interact only when $kh < 6$ (as corroborated below by calculations based on the appropriate dispersion relation). For $kh > 6$, it is easy to check that $H \approx 1$; therefore, the free surface supports waves described by solution (17) at $H \approx 1$. In this case, it can be assumed that interface waves are similar to those originating when the upper layer is bounded from above by a planar rigid surface for which the condition

$$z = h: \frac{\partial\psi_1}{\partial z} = 0, \quad (19)$$

following from (2) at $\zeta \equiv 0$, is met.

Then, the fluid velocity potential in the upper layer, $\psi_1^0(\mathbf{r}, t)$, depends on the z coordinate as $\sim\cosh(k(h - z))$ and the coefficient G can be written as

$$G \equiv -\tanh kh.$$

Now, the time dependence of the wave amplitude at the interface takes the form

$$\xi = \xi_0 \mathrm{Re}\left[\exp\left\{it\left[\frac{\rho_1 kU}{\rho_2 \tanh kh + \rho_1} = \left(\frac{\rho_1 \tanh kh}{\rho_2 \tanh kh + \rho_1}\left(\omega_*^2 - \frac{\rho_2 k^2 U^2}{\rho_2 \tanh kh + \rho_1}\right)\right)^{1/2}\right]\right\}\right],$$

and the critical condition for interface instability is given by

$$gk(\rho_2 - \rho_1) + \alpha_2 k^3 - 4\pi\varepsilon^{-1}\sigma^2 k^2 - \frac{\rho_1\rho_2 k^2 U^2}{\rho_2 \tanh kh + \rho_1} = 0.$$

This relationship shows that, in accordance with the general physical concepts of Kelvin–Helmholtz instability, the critical velocity U, at which the instability arises, increases as the thickness of the upper fluid decreases [while remaining large enough for condition (19) to be valid].

(5) In the other limiting case, $kh \ll 6$, wave interaction is strong and the system behaves in quite a different manner. Consider the situation when the upper fluid is so thin that the velocity field of capillary flow in it is nearly independent of its thickness h. In this case, the absolute values of the coefficients G and H can be assumed to be almost equal. In the framework of our model, which is linear with respect to small perturbations ζ and ξ, wave interaction may be only of the resonance nature, i.e., may take place only when the frequencies and wave numbers of interacting waves are equal. Assume that the interface is unstable and vibrates, according to (18), with a frequency $k\rho U$ and an amplitude increasing at a rate depending on the radical in the exponent.

Let the capillary flow in the upper fluid be a continuous wave process (i.e., $H > 0$) and let the interface be unstable in terms of the superposition of Kelvin–Helmholtz and Tonks–Frenkel instabilities [7] (i.e., $G < 0$). Clearly, when the signs of H and G are opposite, interaction between waves excited on the free surface of a very thin layer and at the interface is the strongest because the waves are in antiphase. Impose the condition that frequencies (17) and (18) of wave motions be equal:

$$kU \pm (Hkg + H\alpha_1\rho_1^{-1}k^3)^{1/2} = -kU\frac{\rho_1}{G\rho_2 - \rho_1}. \qquad (20)$$

According to our assumption, $G \approx H$; therefore, (20) yields the quadratic algebraic equation for the unknown constant H:

$$H^2 - HL + R = 0,$$
$$L \equiv kU^2(g + \alpha_1\rho_1^{-1}k^2)^{-1} - 2\rho_1\rho_2^{-1}, \quad R \equiv (\rho_1\rho_2^{-1})^2. \qquad (21)$$

For the sake of simplicity, consider the situation when $L > R$. Then, both roots of the equation are positive and can be written as

$$H_1 \approx L - RL^{-1}, \quad H_2 \approx RL^{-1}. \qquad (22)$$

At $G \approx -H$, according to (18), the instability increments corresponding to different roots H_j are approximately proportional to $H_j^{1/2}$ and the roots H_1 and H_2 are of different orders of magnitude. Therefore, these motions can easily be distinguished.

When R and L are arbitrary, Eq. (21) can have roots of opposite signs, as well as complex conjugate roots. Complex values of H_j correspond to strong interaction between the waves on the free surface and at the interface, the former being involved in the unstable motion of the latter.

The above analysis is qualitative and relies on a series of assumptions and simplifications. Therefore, it is reasonable to substantiate it by numerically studying the evolution of capillary flow (for various values of the physical parameters of the system) with an appropriate dispersion relation.

(6) We will find a solution to problem (1)–(6) in the form

$$\psi_1 = (A_1\exp(kz) + A_2\exp(-kz))\cos(kx - \omega t) + Ux,$$
$$\psi_2 = B\exp(kz)\cos(kx - \omega t),$$
$$\zeta = C\sin(kx - \omega t), \quad \xi = D\sin(kx - \omega t).$$

By substituting these expressions into boundary conditions (2)–(6) and setting the determinant composed of coefficients A_1, A_2, B, C, and D preceding the unknown amplitudes equal to zero, one easily obtains the dispersion relation for the problem [12]. In terms of dimensionless variables, in which $\rho_2 = \alpha_2 = g = 1$ (and, therefore, the capillary constant for the lower fluid taken as the characteristic spatial scale is also equal to unity), the desired dispersion relation has the form

$$\begin{gathered}
[1 + \rho\tanh(kh)]\omega^4 - 2Uk[2\rho\tanh(kh) + 1]\omega^3 \\
+ \Big[\rho\tanh(kh)\Big[6(Uk)^2 - \frac{k}{\rho}\Big(1 + \frac{\alpha k^2}{\rho}\Big)\Big] \\
+ k[1 + k^2 + \alpha k^2 - Wk] - (Uk)^2\Big]\omega^2 \\
- 2k^2U[2\rho kU^2\tanh(kh) - (1 + k^2 + \alpha k^2 - Wk)]\omega \qquad (23) \\
- k^2\Big[\rho\tanh(kh)\Big[1 + \frac{\alpha k^2}{\rho} + U^4k^2 \\
+ \Big(\frac{\alpha k^2}{\rho} + 1\Big)(1 - k^2 + Wk)\Big] + U^2k[1 + k^2 - Wk - \rho]\Big] = 0, \\
W \equiv 4\pi\sigma^2\varepsilon^{-1}, \quad \rho \equiv \rho_1, \quad \alpha \equiv \alpha_1.
\end{gathered}$$

(7) Plots of the real and imaginary parts of the complex frequency against the dimensionless velocity U (Figs. 1–4) show numerical results on the effect of the upper layer thickness on the evolution of the instability. The results were obtained from (23). In these figures, the real part of the complex frequency defines the wave frequency of the fluid, while the imaginary part is responsible for the instability increment (for $\mathrm{Im}\,\omega > 0$) or the damping decrement (for $\mathrm{Im}\,\omega < 0$).

In Fig. 1 (at $h = 5$), branches *1*–*3* of the dispersion relation describe capillary flows at the interface; branches *4* and *5*, those excited on the free upper surface. The latter branches are parallel straight lines making some angle (in accordance with the Doppler effect) with the abscissa (U) axis. Clearly, branch *4* describes a wave traveling in the direction $\mathbf{U}$, while branch *5* corresponds to a similar wave traveling in the opposite direction.

Figure 1 shows that, as we noted above, when the dimensionless thickness of the upper fluid is sufficiently large, waves excited on the free upper surface and at the interface do not interact and the evolution of Kelvin–Helmholtz instability (characterized by branch *3*)

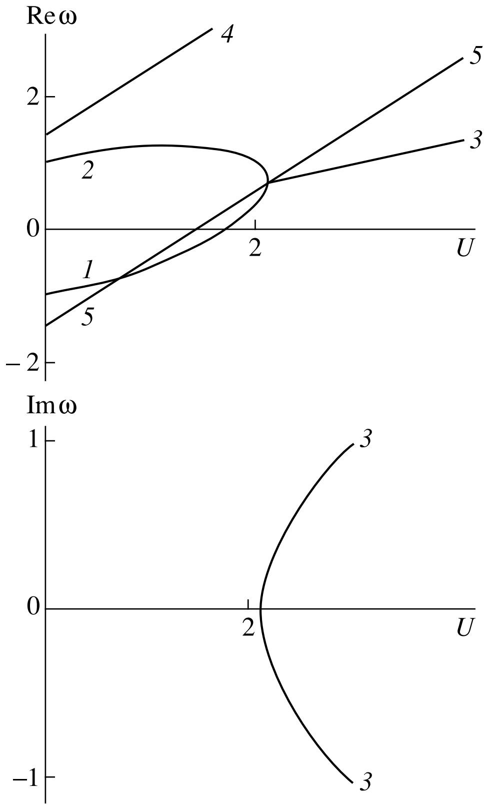

Fig. 1. Real and imaginary parts of the dimensionless complex frequency vs. dimensionless velocity of the directed motion of the upper fluid at $k = 1$, $\alpha = 0.5$, $\rho = 0.5$, $W = 0$, and $h = 5$.

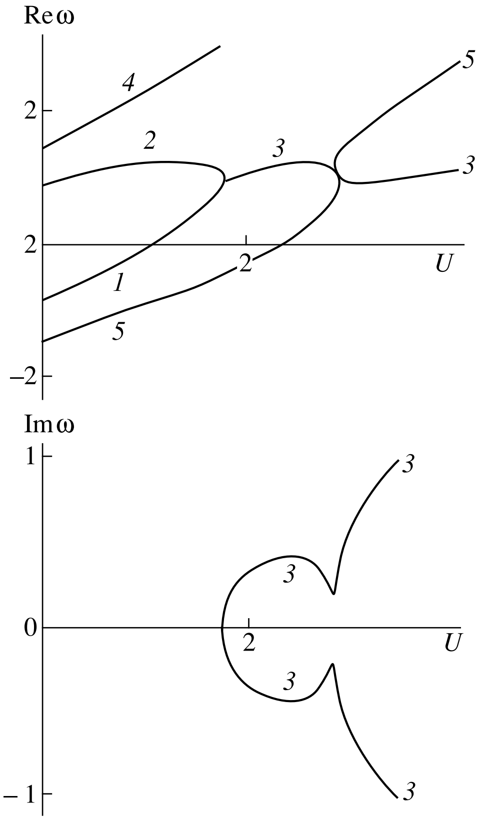

Fig. 2. Same as in Fig. 1 at $h = 1$.

is the same as in the classical case of the infinite thickness of the upper fluid ($h \longrightarrow \infty$). At a certain velocity of the upper medium, $U = U_*$, branches *1* and *2* merge, forming two wave motions *3*. The amplitude of one of them exponentially decreases in time with a decrement defined by the negative part of the imaginary component of branch *3*, while the amplitude of the other exponentially increases with an increment defined by the positive part of the imaginary component of branch *3*.

When the dimensionless thickness of the upper fluid decreases to $h \approx 1$ or below (Figs. 2–4), branches *1–3* start interacting with branches *4* and *5*. This gives rise to new composite motions *6–10* and distorts branches *1*, *2*, and *4*. Branches *4*, *6*, *7*, and *9* describe continuous wave motions, while branches *8* and *10* cover both exponentially convergent vibrations (for which $\mathrm{Im}\,\omega < 0$) and exponentially divergent (unstable) vibrations (for which $\mathrm{Im}\,\omega > 0$). Unstable motion *10* corresponds to classical Kelvin–Helmholtz instability. Its critical velocity U_* increases with decreasing thickness of the upper fluid (Figs. 1–4). Unstable motion *8* results from the interaction between capillary motions excited on the free upper surface and at the interface. As follows from Figs. 3 and 4, when the dimensionless thickness h of the upper fluid decreases, the region of unstable motion *8*, unlike that of unstable motion *10*, shifts towards lower velocities U_* of the upper fluid and its increment decreases.

Figure 5 plots the real and imaginary parts of the complex frequency calculated at $U = 1$ and $h = 0.0001$ from dispersion relation (23) against the parameter W. This parameter characterizes the stability of the charged surface of a fluid with respect to its self-charge (i.e., the possibility for Tonks–Frenkel instability). The branches are numbered as in the previous figures. Branch *10* describes aperiodic Tonks–Frenkel instability (caused by the high surface charge density at the interface), imposed on oscillatory Kelvin–Helmholtz instability (cased by the discontinuity in the velocity field at the interface). Calculations show that motion *8* caused by interaction of waves excited on different surfaces (by the same mechanism as in Figs. 2 and 3) stands out when the dimensionless thickness of the upper fluid layer is about several hundredths.

Figures 4 and 5 show that, as the upper fluid becomes thinner, the velocity critical for interface instability caused by interaction between waves of different origin decreases. The presence of unneutralized charge at the interface enhances this effect.

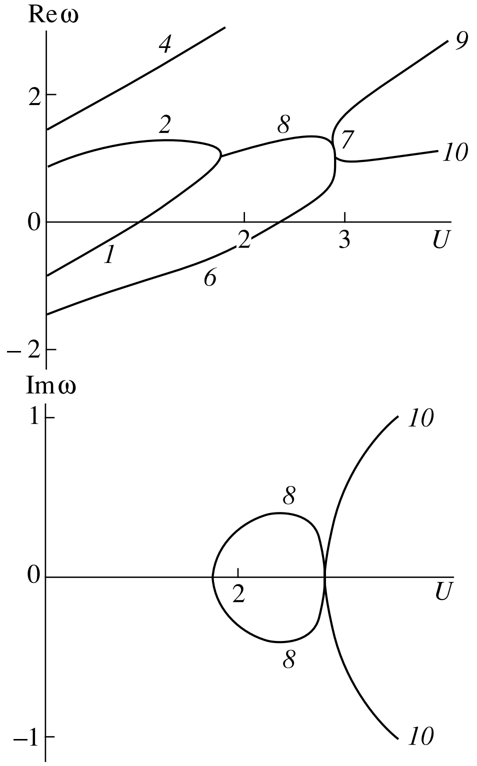

Fig. 3. Same as in Fig. 1 at $h = 0.9$.

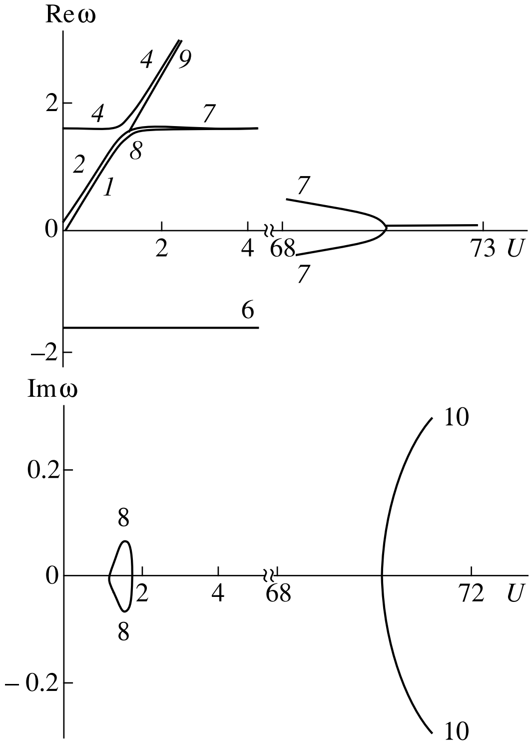

Fig. 4. Same as in Fig. 1 at $h = 0.001$.

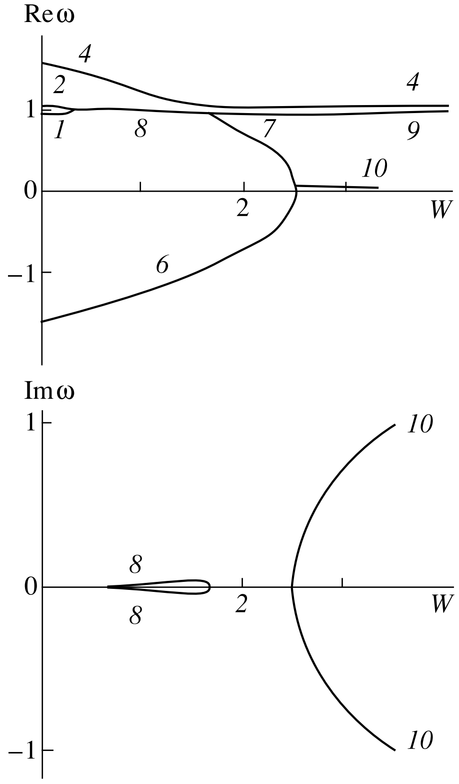

Fig. 5. Real and imaginary parts of the dimensionless complex frequency vs. dimensionless parameter W at $k = 1$, $\rho = 0.5$, $\alpha = 0.5$, $h = 0.0001$, and $U = 1$.

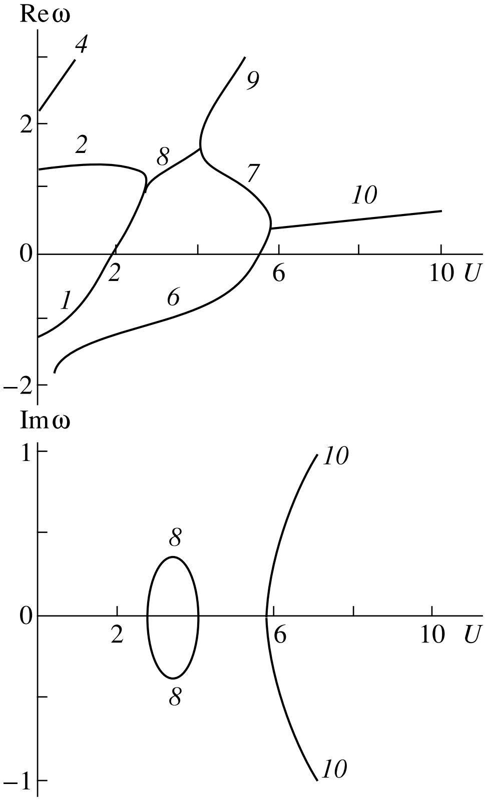

Fig. 6. Real and imaginary parts of the dimensionless complex frequency vs. dimensionless velocity of the directed motion of the upper fluid at $k = 1$, $\alpha = 0.5$, $h = 0.9$, $W = 0$, and $\rho = 0.1$.

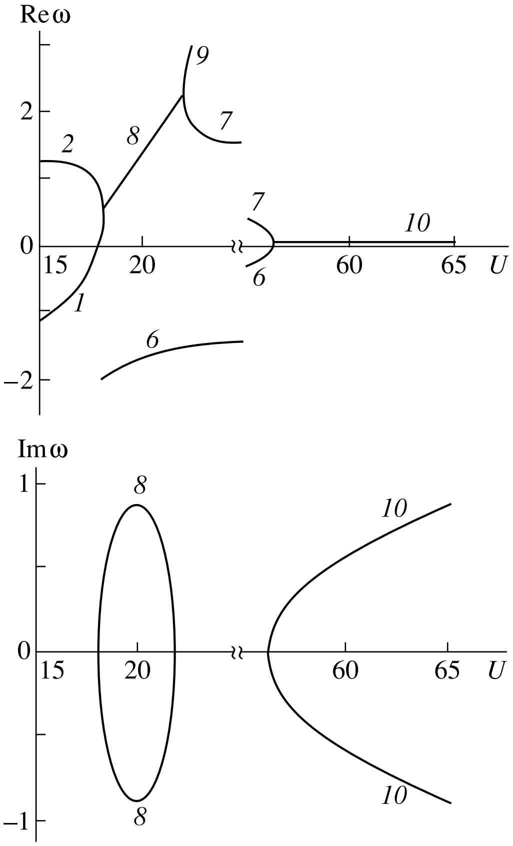

Fig. 7. Same as in Fig. 6 at ρ = 0.001.

Figures 6 and 7 plot the real and imaginary parts of the complex frequency calculated at a constant thickness of the upper fluid against the dimensionless velocity *U* for different dimensionless densities of the upper fluid. The branches are numbered as in Figs. 3 and 4, their physical meaning also being the same (in Fig. 7, branch *4* lies outside the domain shown). As the density ρ of the upper medium decreases, the ranges of the dimensionless velocity *U* where the instability is described by branches *8* or *10* move toward greater values of *U* and the distance between the branches increases. Interestingly, the increment of the instability due to wave interaction (branch *8*) significantly grows, approaching that for branch *10*.

Calculations illustrated in Figs. 3 and 6 imply that a decrease in the density of the upper medium increases its thickness at which motion *8*, due to wave interaction, is initiated.

CONCLUSION

When the thickness of the upper fluid is less than the capillary constant of the lower fluid, capillary flows on the upper surface free and at the interface interact, resulting in an additional, earlier unknown, oscillatory instability. Critical conditions for this instability relax with decreasing layer thickness, with a simultaneous drop in the instability increment. The presence of unneutralized electric charge at the interface enhances this effect.

The comparison of the numerical analysis of dispersion relation (23) (Sections 6 and 7) with the qualitative analysis (Sections 2–5) shows that, in terms of mathematical physics, and in the linear approximation used, interaction between different branches of capillary wave motion can be visualized through boundary conditions.

REFERENCES

1. J. W. Miles, Appl. Mech. Rev. **15**, 685 (1962).
2. P. H. Le Blond and L. A. Mysak, *Waves in the Ocean* (Elsevier, Amsterdam, 1978; Mir, Moscow, 1981).
3. R. D. Sydora, J. S. Wagner, J. S. Lee, *et al.*, Phys. Fluids **26**, 2986 (1983).
4. A. D. Sneyd, J. Fluid Mech. **156**, 223 (1985).
5. Yu. A. Stepanyants and A. L. Fabrikant, Usp. Fiz. Nauk **159** (1), 83 (1989) [Sov. Phys. Usp. **32**, 783 (1989)].
6. V. M. Kuznetsov and P. M. Lushnikov, Zh. Éksp. Teor. Fiz. **108**, 614 (1995) [JETP **81**, 332 (1995)].
7. O. A. Grigor'ev and S. O. Shiryaeva, Zh. Tekh. Fiz. **66** (2), 23 (1996) [Tech. Phys. **41**, 124 (1996)].
8. A. I. Grigor'ev, V. A. Koromyslov, and S. O. Shiryaeva, Zh. Tekh. Fiz. **69** (5), 7 (1999) [Tech. Phys. **44**, 486 (1999)].
9. L. D. Landau and E. M. Lifshitz, *Course of Theoretical Physics*, Vol. 6: *Fluid Mechanics* (Nauka, Moscow, 1986; Pergamon, New York, 1987).
10. L. D. Landau and E. M. Lifshitz, *Course of Theoretical Physics*, Vol. 8: *Electrodynamics of Continuous Media* (Nauka, Moscow, 1982; Pergamon, New York, 1984).
11. L. N. Sretenskiĭ, *The Theory of Wave Motion in Fluids* (Nauka, Moscow, 1977).
12. V. G. Levich, *Physicochemical Hydrodynamics* (Fizmatgiz, Moscow, 1959).

Translated by A. Khzmalyan

Technical Physics, Vol. 46, No. 3, 2001, pp. 287–291. Translated from Zhurnal Tekhnicheskoĭ Fiziki, Vol. 71, No. 3, 2001, pp. 17–21.
Original Russian Text Copyright © 2001 by Baryshnikov, Basargin, Chistyakova.

An Experimental and Theoretical Study of Shock-Wave Propagation through Reactive Gases under Conditions Causing a Transformation of the Flow Structure

A. S. Baryshnikov, I. V. Basargin, and M. V. Chistyakova

Ioffe Physicotechnical Institute, Russian Academy of Sciences, St. Petersburg, 194021 Russia

Received July 6, 2000; in final form, July 28, 2000

Abstract—Experimental observations of the transformation of the structure of shock waves entering the discharge gap of either a transverse or decaying glow discharge are presented. It is found that the total impulse of the shock wave pressure remains constant. A variation in the speed of sound, that is, the shock wave velocity, at which total dispersion of the wave occurs is found to be nonmonotonous across the discharge gap. The times over which the wave structure keeps changing after switching off the discharge have been more accurately determined. On the basis of the obtained experimental data and earlier results, a conclusion on the mechanism of this effect has been drawn. This mechanism is related to the dispersion of disturbances making up the wave structure in a relaxing medium (such as the glow discharge plasma). On the basis of a theory of this kind of dispersion, using the experimental data, and comparing energetic and temporal characteristics of the internal states of the plasma under study and the mode of sound disturbances (which according to the experiment, are responsible for the effect), we have succeeded in determining the $O_2(a^1\Delta_g)$ state whose relaxation brings about this effect. *© 2001 MAIK “Nauka/Interperiodica”.*

The instability of a shock wave and the flow of an exothermically reacting gas in the wake of the wave front (combustion and dissociation) is well known [1]. At present, there is interest in studies of the instability of a shock-wave flow accompanied with endothermic reactions (dissociation and ionization). Some examples are the instability of a bow shock wave and the induced flow in polyatomic dissociating gases [2] or the instability of the shock-wave structure in a glow discharge plasma [3]. This interest is mainly caused by the possibility of reducing the drag on a body by eliminating the energy expended to increase the entropy of the shock wave. It is known that the higher the shock-wave strength, the greater this drag reduction.

Similar phenomena are observed in shock waves propagating through chemically reactive polyatomic gases [2], in ionizing shock waves [4], and in shock waves in a glow discharge plasma [3, 5, 6].

It is found that both in polyatomic gases and in the plasma, the instability is due to internal physicochemical processes. For example, the maximum in the energy spectrum of turbulent disturbances in polyatomic gases coincides with the chemical transformation energy [7]. In plasmas of the glow and decaying discharges in air, this effect also cannot be explained by the electrodynamics theory alone. Results reported in [8] show that even after the discharge has been turned off, the pressure distribution behind the shock wave remains to a considerable degree different from the classical distribution for about 100 s. In a plasma of approximately the same parameters [9], the deionization time is 10^{-5} s and the time of gas cooling is ~10^{-4} s, while the deexcitation time of the vibrational states is on the order of 10^{-2} s. Thus, the common feature of all the effects considered is the fact that they are related to the physicochemical processes occurring in gases. However, their mechanisms are different. For example, the mechanism in polyatomic gases, although not thoroughly understood, has been discussed in numerous publications, which unfortunately are not well known to the general reader. This mechanism is related to the baroclinicity of the flows of chemically reactive gases, regardless of whether the energy is released or absorbed in the reactions [10]. In this case the eddy mode of the disturbances is stronger, and although the pressure perturbation is not great, it is still large enough in comparison with the pressure in front of the shock wave so as to cause a disturbance of the shock-wave front. Calculations of the amplitude and the evolution time of a disturbance at the shock-wave front for the model of a vortex possessing an energy corresponding to that of the chemical transformations [11] are in good agreement with the experimental data. Subsequent investigations of the instability of a plane-parallel flow of a chemically reactive gas in the shock layer in front of the body indicate that the flow becomes unstable with respect to high-frequency disturbances even if the transversal velocity profile has no inflection point [12], that is, not only at the flow separation point but also in front of the body in the shock layer.

So far, in a glow discharge, the transformation of the shock-wave structure has no unambiguous theoretical

Table 1. The characteristic transformation times of the flow structure

Shock wave velocity, km/s	F''_1		F''_2	
	1–10 ms	10–100 ms	1–10 ms	10–100 ms
1.85	1.0	13 70	3.6	13
1.44	2.3 4.0	–	3.6	18 22
1.17	–	18	–	13
0.99	5.1	–	3.0	32 13 78

Note: The 1st harmonic F_1 features a single hump and the 2nd harmonic F_2 features two humps.

explanation. There are some hypotheses concerning the nature of its mechanism. Historically, the first to appear was the hypothesis of the ion-sound dispersion of the shock wave [13]. However, apart from experimental data demonstrating that the effect does not depend on the presence of a charged component in the gas [8], there are simple estimates made on the basis of well-known formulas of the speed of ion sound (the Mach number in the experiment is close to unity) showing that it is five times as high as the speed of sound in plasma and twice as high at the center of the discharge. Such a drastic increase of the precursor velocity is not observed in these regions, and at the center the increase in wave velocity is negligible [8].

The emergence of an ion-sound soliton due to modulation instability is also doubtful because the maximum soliton size (wavelength), as can be demonstrated, is $l = r_D(\rho_0/\Delta\rho)^{1/2} \approx 0.3$ mm, where ρ_0 is the plasma density in front of the shock wave, $\Delta\rho$ is the density jump over the shock wave, and r_D is the Debye radius. This value of the disturbance wavelength is smaller than that observed in the experiment by an order of magnitude. At larger values, the density cavity, if it exists, must collapse [14].

Ultimately, there exists a hypothesis explaining the flow transformation as caused by the energy radiated by the plasma. Radiation is characterized by dispersion, and its absorption factor depends on the wavelength. The process of energy transfer by radiation can also be described using nonlinerar Korteveg–de-Vreas–Burgers equations [15]. The solution of these equations, similar to the case of ion-sound waves, gives oscillations of the density and other characteristics of the flow behind the shock wave, the oscillation amplitude of small disturbances being equal to two-thirds of the wave-front amplitude. Such a behavior is not observed in experiments; more importantly, the radiation (for example, at the wavelength of excited atomic oxygen, ≈1000 Å) has an absorption factor of $k_p \approx 10^{-5}$ cm, and for this reason practically no energy absorption occurs in front of the shock wave at a distance equal to the characteristic wavelength of the initial wave (30 mm). Another model [16] describes a mechanism of fast (though not considerable) cooling of the plasma behind the shock wave due to radiation from pseudo-metastable states of atomic oxygen. It should be noted that in a number of experiments, a radiation burst in the region of unstable flow behind the shock wave was observed [17]. In [18], a kinetic mechanism was proposed which includes a number of fairly slow secondary processes (lasting about 10–100 s in the regime needed for the effect to exist). Calculations show that this kind of mechanism can provide a local pressure increase behind the shock wave of approximately 20% [16]. In the experiment, however, a much higher pressure is observed.

Thus, the mechanism of this effect has yet to be ascertained. To understand its nature, two series of experiments were carried out. One of them is a continuation of the study [8] of the time after switching off the discharge supply, during which the effect persists. The structure transformation times are derived from analysis of the Fourier series expansion of the signal. These transformation times can be compared with characteristic times of the processes involved and a process responsible for the identified instability. According to experimental results, there should be just one such process because the signal on–off time ratios are approximately unity [15]. This also means that the dominant harmonics in the Fourier expansion series of the signal are the first, the second, and perhaps two more harmonics. In the experiment, variation of the amplitudes of the harmonic with time was determined. It was easy to determine the approximate time in which the amplitudes of the two strongest harmonics dropped by an order of magnitude, 10^{-2} s. A more accurate value, as well as other likely transformation times, can be determined as the time when the second time derivative of the dependence becomes zero, i.e., the moment when a new relationship tends to take over from the previous one. This situation can be compared to the change of acceleration sign of a body moving under the action of a system of forces while the body velocity still has not changed its direction. We have succeeded, without worsening the data accuracy, in finding all times when the second derivative becomes zero. The results in various time scales are presented in Table 1.

It is seen that as the shock-wave velocity decreases, the structure transformation time (1st harmonic) slightly increases, while for the second harmonic it does not depend on velocity. A velocity of 1.17 km/s should be noted. When the shock wave enters the test area at this velocity, the signal shape structure does not change during the first 10 ms. In Table 1, it is seen that the second harmonic of the signal undergoes changes in time intervals from 3.0 to 3.6 ms and from 13 to 20 ms. The structure transformation times for the first harmonic also change from 1 ms to 5.1 ms. This confirms the conclusion concerning the physicochemical nature of the effect discussed since the characteristic times turned out to be on the order of 10^{-2} s.

In the second series of experiments, time-independent energy (dynamic) characteristics of the effect were measured. In these experiments, the minimum velocity of the shock wave at which the effect still took place was measured at the entrance. At this velocity the primary wave (or the precursor) vanishes, and the wave does not split in two. The wave velocity also becomes equal to the propagation velocity of small mode disturbances giving rise to the precursor. The results are presented in the figure. The occurrence of dips should be noted in the monotonous variation of the measured speed of sound in the plasma across the discharge gap. This is one more confirmation that the speed of sound measured in the experiment depends on the concentration of some excited components which, as the estimations show, also varies nonmonotonously across the gap, being determined by the physicochemical processes dominating in different layers of the discharge. It is also seen that in plasma the speed of sound is intermediate between the values for hot gases and ion-sound disturbances. Hence, it cannot be related to either of these two modes of disturbance.

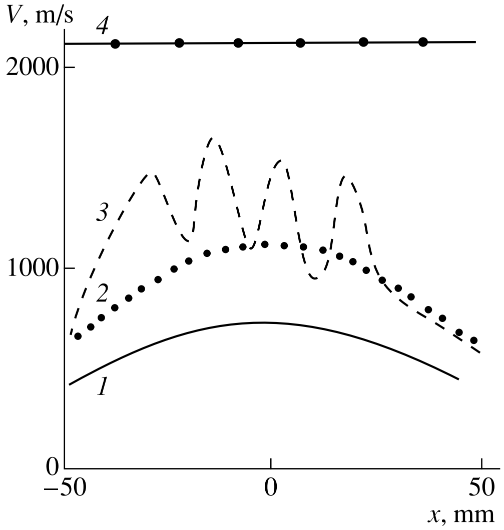

(*1*) Profile of the speed of sound in a heated gas across the discharge gap; (*2*) Profile of the speed of sound in plasma calculated in [19]; (*3*) Profile of the speed of sound in plasma measured experimentally; (*4*) Profile of the speed of ion sound calculated using the measured electron temperature.

To elucidate the nature of the additional mode, account should be taken of one more experimental observation, which appears to be fundamental not only for determining the impact of the effect on the drag on bodies moving through the plasma but also for getting insight into the nature of the mechanism. It was not a problem to calculate the integral pressure impulse in the course of computer processing of the experimental results. It turned out that, at the time of transformation of the signal shape structure, the wave pressure impulse is equal to that in air at the same wave velocity. This means that the effect does not change the total pressure impulse but only transforms the pressure distribution behind the wave or the wave dispersion. Besides, the high-frequency waves lead the low-frequency waves. The former generate the precursor shock wave, and the latter cause a relatively smooth pressure change over the second wave. Apart from the spreading of the secondary wave, the fact that formation of the precursor with a rather steep front is observed is unusual.

Investigations of such a dispersion caused by relaxation in gases were carried out both theoretically [20, 21] and experimentally [22]. A dispersion equation for the high-frequency sound-wave component [20] has the form

$$\Theta^2 u_{\xi\xi} - u = -m\Theta v_{\xi\xi}/2 - m\Theta^2 v_{\xi\xi\xi}/2, \tag{1}$$

where $u = v_t + vv_\xi\beta$; the subscripts denote differentiation with respect to the index; γ is the adiabatic exponent of the gas (the ratio of specific heats); $\Theta = \tau/T$ is the ratio of the internal process relaxation time τ to the period T of sound disturbances; v is the sound wave velocity (or, in a compressible medium, the reciprocal of density); $\xi = (x - c_0t)/c_0T$ is the wave variable (x being the distance and t the time); c_0 is the speed of the low-frequency sound component (no dispersion); $\beta = (\gamma + 1)/2$; $m = (c_\infty^2 - c_0^2)/c_0^2 = (\partial P/\partial\eta)_\rho$ is the so-called degree of dispersion (P being the pressure, ρ the gas density, and η the relaxation parameter); and c_∞ is the speed of the high-frequency sound component.

After simple calculations and Laplace transformation (the Laplace parameter p is substituted for $\partial/\partial t$), we get

$$\begin{aligned} p(\Theta^2 v_{\xi\xi} - v) = {} & vv_\xi + m\Theta v_{\xi\xi}/(2\beta^2) - 3\Theta^2 v_{\xi\xi}v_\xi \\ & - \Theta^2 v_{\xi\xi\xi}v - m\Theta^2 v_{\xi\xi\xi}/(2\beta^3). \end{aligned} \tag{2}$$

It is easy to see that when expression $(Q^2v_{\xi\xi} - v)$ becomes zero, a situation analogous to resonance arises in which the Laplace parameter tends to infinity. It is easy to see that the term $(Q^2v_{\xi\xi} - v)$ can be zero only for a certain relation between the wave frequency $f = 1/T$ and the wave number $k = 1/\lambda$, where λ is the wavelength of the disturbance normalized for the standard wavelength c_0T. In fact, this relation defines the phase velocity $v_f = c_0\tau f$ of the buildup of disturbances. Having experimentally determined the propagation velocity of small disturbances, one can determine the frequency of the growing disturbances. The above, as can be seen, is the thermodynamic condition for the buildup of period-

Table 2. Comparison between various relaxation processes

Parameters	Electron relaxation	Vibrational relaxation	Experiment
Relaxation time τ, s	10^{-5}	10^{-3}	0.36×10^{-2} 1.3×10^{-2}
Frequency of disturbances, kHz	10^4	100	28 7.7
Attenuation factor [24], dB/m	$>10^4$	2	0.1 2.1×10^{-2}
Attenuation distance, m	$<10^{-3}$	10	87 1000

ical disturbances when they are in phase with the internal process [23].

Another resonance condition is also usually considered, which follows from the physically justified requirement for a limit on the buildup of disturbances. If this condition is not met, the waves of the resonance frequency will not exist (in other words, their amplitude will be infinite). This additional condition is derived by equating the right-hand side of equation (2) to zero. The right-hand side simplifies near the resonance, and the additional condition is in fact a constraint on the radiation pressure of the sound signal, that is, on its kinetic energy

$$E_k = [2m(\gamma - 1)]/[3(\gamma + 1)^2]\Theta. \qquad (3)$$

Inasmuch as use is made of nondimensional quantities, the energy should be of an order of unity. Calculating the coefficient of Θ with the use of parameters typical for plasma ($\gamma = 1.3$ and $m = 0.1$), we find the critical value $\Theta = 10^2$ at which the resonance condition (3) is met.

A comparison of attenuations of sound waves for various internal processes is given in Table 2. The wave frequency is determined from the critical resonance condition ($f = 10^2/\tau$).

It can be seen that the electron relaxation might cause a resonance only for hyperfrequency waves, which are effectively attenuated over a distance of less than 1 mm. Thus, the electron relaxation cannot be the dominant mechanism of the effect under study. The characteristic times found in the experiment (the last column in Table 2) correspond to the vibrational relaxation or to the secondary processes in the plasma involving a number of complicated and complex ions, which are specific for a low-temperature plasma.

Using a measured wave-velocity value at which the effect vanishes (that is, the propagation velocity of weak disturbances of the mode responsible for the effect), one can determine the wave energy of this mode. On the other hand, this energy must correspond to the energy of the mode of the internal processes responsible for the emergence of the effect. Calculated per one molecule, this energy is on the average 3.7×10^{-20} J or, in spectroscopic units, 1880 cm^{-1} (which is 0.23 eV). This value is closer to the energy of vibrational quanta in molecules rather than to the energy of electron levels. At the same time, the bonding energy in complex ions NO^+–N_2 and O_2^+–H_2 (0.2 eV) in a plasma is also close to that value. However, it should be taken into account that the concentration of excited molecules in the plasma in the regimes under study is approximately an order of magnitude less than the concentration of all particles [25]; therefore, one should look for excitation levels of an order of 2–3 eV, for example, metastable excitation levels of oxygen [26]: 0.98 eV for $O_2(a^1\Delta_g)$ and 1.63 eV for $O_2(b^1\Sigma_g^+)$. Other metastable levels of air have the following energy levels: 4.7 eV for $NO(b^4\Pi)$ and 6.17 eV for $N_2(A^3\Sigma_u^+)$. Note that according to calculations in [25], it is the numerical concentration of $O_2(a^1\Delta_g)$ which is an order of magnitude less than the concentration of the neutral particles, while the concentration of $O_2(b^1\Sigma_g^+)$ is two orders less. The concentration of other metastable states is also 2–3 orders less. From this, it follows that when analyzing the effect mechanism it is necessary to pay attention to the state $O_2(a^1\Delta_g)$. Not only is the concentration of this state high (due to low excitation energy), but it also has a very long radiation lifetime of 2.7×10^3 s [26]. Besides, from calculations in [25] it follows that the thermal excitation time (and the deexcitation time as well) in approximately the same regimes of glow discharge reaches a few milliseconds; i.e., it is in agreement with the duration of the first substantial structure transformation after switching off the discharge. Thus, the experimental investigations carried out have allowed us to ascertain that the mechanism of the effect is the dispersion of the high-frequency component of sound disturbances. Apparently, the dispersion occurs due to physicochemical relaxation of the $O_2(a^1\Delta_g)$ excited state of oxygen in the plasma.

REFERENCES

1. Ya. B. Zel'dovich, G. I. Barenblatt, V. B. Librovich, and G. I. Makhviladze, *Mathematical Theory of Combustion and Explosion* (Nauka, Moscow, 1980).
2. A. S. Baryshnikov, A. P. Bedin, V. G. Maslennikov, and G. I. Mishin, Pis'ma Zh. Tekh. Fiz. **5**, 281 (1979) [Sov. Tech. Phys. Lett. **5**, 113 (1979)].
3. I. V. Basargin and G. I. Mishin, Pis'ma Zh. Tekh. Fiz. **15** (8), 55 (1989) [Sov. Tech. Phys. Lett. **15**, 311 (1989)].
4. G. K. Tumakaev, V. G. Maslennikov, and B. V. Serova, Pis'ma Zh. Tekh. Fiz. **6**, 354 (1980) [Sov. Tech. Phys. Lett. **6**, 152 (1980)].
5. I. V. Basargin and G. I. Mishin, Pis'ma Zh. Tekh. Fiz. **11**, 209 (1985) [Sov. Tech. Phys. Lett. **11**, 85 (1985)].

6. V. A. Gorshkov, A. I. Klimov, G. I. Mishin, *et al.*, Zh. Tekh. Fiz. **57**, 1893 (1987) [Sov. Phys. Tech. Phys. **32**, 1138 (1987)].
7. A. S. Baryshnikov, A. P. Bedin, V. G. Derevyanko, and F. F. Rumyantsev, Preprint No. 816, FTI (Ioffe Physicotechnical Institute, Academy of Sciences of USSR, Leningrad, 1983).
8. A. S. Baryshnikov, I. V. Basargin, E. V. Dubinina, and D. A. Fedotov, Pis'ma Zh. Tekh. Fiz. **23** (4), 18 (1997) [Tech. Phys. Lett. **23**, 259 (1997)].
9. A. S. Zarin, A. A. Kuzovnikov, and V. M. Shibkov, *Freely Localizated Microwave Discharge in Air* (Neft' i Gaz, Moscow, 1996).
10. A. S. Baryshnikov, N. Yu. Vasil'ev, and A. B. Safonov, Fiz. Goreniya Vzryva, No. 1, 101 (1987).
11. A. S. Baryshnikov and N. Yu. Vasil'ev, Chislennye Metody Mekh. Sploshnoĭ Sredy **17** (5), 3 (1986).
12. A. S. Baryshnikov, Pis'ma Zh. Tekh. Fiz. **22** (16), 53 (1996) [Tech. Phys. Lett. **22**, 667 (1996)].
13. I. V. Basargin and G. I. Mishin, Preprint No. 880, FTI AN SSSR (Ioffe Physicotechnical Institute, Academy of Sciences of USSR, Leningrad, 1984).
14. L. A. Artsimovich and R. Z. Sagdeev, *Plasma Physics for Physicists* (Atomizdat, Moscow, 1979).
15. G. M. Zaslavskiĭ and R. Z. Sagdeev, *Introduction to the Nonlinear Physics* (Nauka, Moscow, 1988).
16. A. S. Baryshnikov, in *Proceedings of the 17th International Symposium on Rarefied Gas Dynamics, Aachen, 1990*, Ed. by A. E. Beylich (VCH, New York, 1991), p. 263.
17. A. Sufian and A. P. Ryazin, Vestn. Mosk. Univ., Ser. 3: Fiz., Astron. **25** (1), 94 (1984).
18. A. S. Baryshnikov, Pis'ma Zh. Tekh. Fiz. **23** (22), 53 (1997) [Tech. Phys. Lett. **23**, 881 (1997)].
19. A. P. Bedin, Pis'ma Zh. Tekh. Fiz. **23** (16), 88 (1997) [Tech. Phys. Lett. **23**, 654 (1997)].
20. V. E. Nakoryakov and A. A. Borisov, Fiz. Goreniya Vzryva **12**, 414 (1976).
21. Yu. A. Pishchal'nikov, O. A. Sapozhnikov, and V. A. Khokhlova, Akust. Zh. **42**, 412 (1996) [Acoust. Phys. **42**, 362 (1996)].
22. V. G. Andreev, R. O. Cleveland, Yu. A. Pishchal'nikov, *et al.*, Akust. Zh. **45**, 13 (1999) [Acoust. Phys. **45**, 8 (1999)].
23. K. I. Artamonov, *Thermohydroacoustic Stability* (Atomizdat, Moscow, 1991).
24. *Physical Quantities. Handbook*, Ed. by I. S. Grigor'ev and E. Z. Melikhov (Énergoizdat, Moscow, 1991).
25. Yu. S. Akishev, A. A. Deryugin, V. B. Karal'nik, *et al.*, Fiz. Plazmy **20**, 585 (1994) [Plasma Phys. Rep. **20**, 525 (1994)].
26. A. A. Radtsig and B. M. Smirnov, *Reference Data on Atoms, Molecules, and Ions* (Atomizdat, Moscow, 1980; Springer-Verlag, Berlin, 1985).

Translated by N. Mende

Technical Physics, Vol. 46, No. 3, 2001, pp. 292–298. Translated from Zhurnal Tekhnicheskoĭ Fiziki, Vol. 71, No. 3, 2001, pp. 22–28.
Original Russian Text Copyright © 2001 by Kagadeĭ, Kozyrev, Osipov, Proskurovskiĭ.

GAS DISCHARGES, PLASMA

Current–Voltage Characteristics of a Reflex Discharge with a Hollow Cathode and Self-Heating Electrode

V. A. Kagadeĭ*, A. V. Kozyrev, I. V. Osipov***, and D. I. Proskurovskiĭ****
** Research Institute of Semiconductor Apparatus, Tomsk, 634050 Russia*
*** High Current Electronics Institute, Siberian Division, Russian Academy of Sciences, Akademicheskiĭ, pr. 4, Tomsk, 634055 Russia*
**** Tomsk State University of Control Systems and Radio Electronics, Tomsk, 634050 Russia*
e-mail: vak@lve.hcei.tsc.ru

Received October 8, 1999

Abstract—Results are presented from experimental studies of the current–voltage characteristics of a reflex discharge with a self-heating electrode used in a source of atomic hydrogen. The processes occurring in a discharge cell and governing the main features of the characteristics obtained are investigated theoretically. An explanation of the general features of the discharge is proposed. It is shown that an abrupt decrease in the discharge voltage with increasing hydrogen flow rate is associated with penetration of the plasma into the hollow cathode and the ignition of a hollow cathode discharge. It is demonstrated that, as the discharge current increases, the glow discharge gradually transforms into an arc discharge with a heated cathode. *© 2001 MAIK “Nauka/Interperiodica”.*

INTRODUCTION

Glow and arc gas discharges are widely used to produce low-temperature plasmas and charged-particle beams. In connection with the development of micro- and nanoelectronics technology, interest arose in using these types of discharges to produce intense flows of neutral atoms and radicals [1, 2]. The simple design of the discharge cell and stable operation in the continuous mode make dc glow discharges in crossed $\mathbf{E} \times \mathbf{H}$ fields (such as magnetron or Penning discharges) attractive from the point of view of producing neutral flows. However, because of the rather high voltage required for a glow discharge and the fact that the glow discharge can transform into a cathode-spot discharge as the current increases, the glow discharge cell is a source of contamination of a processed semiconductor structure by the products of cathode erosion. Arc discharges with heated cathodes are free of these disadvantages; however, the use of a directly heated cathode makes the design of such a system too complicated. It is possible to combine the advantages of these types of discharges if a heat-insulated self-heating electrode (SHE) heated to temperatures at which thermoelectronic emission comes into play is introduced into a glow discharge cell [3, 4].

In [5], the production of atomic hydrogen flows using a low-voltage reflex discharge with a hollow cathode and an SHE was suggested. Preliminary studies [6, 7] have shown that this type of discharge makes it possible to create an atomic hydrogen source that has some advantages over other types of discharges and can find wide application in microelectronics technology. In this case, the discharge current is governed by mechanisms typical of both the glow discharge and the arc discharge with a heated cathode. However, the contribution of each of these mechanisms to the discharge current is still poorly understood.

In this paper, the current–voltage (*I*–*V*) characteristics of a low-voltage reflex discharge with a hollow cathode and an SHE are studied in detail. The features of the discharge are explained on the basis of a theoretical analysis of the processes occurring in the discharge cell. The results of the analysis form a basis for analyzing the general features of the generation of atomic hydrogen flows and for optimizing the source design.

DESIGN OF THE DISCHARGE CELL AND THE EXPERIMENTAL TECHNIQUE

An axisymmetric discharge cell (Fig. 1) was used to produce the combination of a reflex hollow-cathode discharge and a magnetron discharge. A hollow cathode *1*, cylindrical anode *2*, and reflector cathode *3* were immersed in the magnetic field of a permanent magnet *4* and formed the cell of the reflex hollow-cathode discharge. On the other side, a heat-insulated rod SHE *5*, which was electrically connected to the hollow cathode *1* and the anode *2*, formed the cylindrical magnetron cell.

The SHE *5*, made of a tungsten rod $2r_0 = 2$ mm in diameter, extended 5–8 mm into the anode cavity. The cathodes were made of magnetic steel. The hollow-cathode diameter $2r_1$ was 4 mm, and the cavity length was 35 mm. The anode, made of nonmagnetic stainless steel, had an inner diameter $2r_a = 1$ cm and height $h = 1$ cm. The electrodes *1*–*3* were forced cooled with water. The samarium–cobalt magnet *4* produced a magnetic field of $B \sim 0.08$ T.

The working gas (especially pure hydrogen) was injected into the cell through a hole at the end of the hollow cathode *1*. The gas flow rate varied within the range from 2.5 to 52 sccm, and the pressure in the working chamber was 10^{-3}–10^{-1} Pa. The particle flow, consisting of a mixture of atomic and molecular hydrogen, flowed out of the discharge cell through a hole *6* in the reflector cathode *3*. The small aperture of the hole *6* allowed us to produce a pressure drop between the cell and the working chamber and substantially limited the possibility of sputtered and charged particles flowing out of the cell (magnetic field lines *7* are shown in the figure).

A continuous gas discharge was ignited in the cell when the power from a stabilized dc power source was applied. Before measuring the *I*–*V* characteristics of the discharge, the discharge cell was conditioned by igniting a discharge with a current of $I = 2$ A lasting 10 min. Each point in the *I*–*V* characteristic was measured after a steady-state discharge had been established. The time during which the steady state was established reached several seconds. This time was determined by the thermal inertia of the SHE.

EXPERIMENTAL RESULTS

Figure 2 shows the *I*–*V* characteristics obtained for different gas flow rates. Curves *1* and *2* correspond to a hollow cathode without an SHE. In fact, these curves coincide with the well-known *I*–*V* characteristics of a Penning cell with a cold hollow cathode [8]. At discharge currents of $I < 0.1$ A, an ordinary reflex (Penning) discharge with an increasing *I*–*V* characteristic is excited. Since, under these conditions, the electric field and charged particles do not penetrate into the hollow cathode, it does not affect the discharge. At discharge currents of $I \cong 0.2$–0.3 A, the plasma density increases and the cathode-sheath thickness decreases, so that the plasma starts to penetrate into the cavity. As a result, a region appears in the *I*–*V* characteristic in which the discharge voltage somewhat decreases as the current increases (which is known as the hollow-cathode effect). However, at even slightly higher currents, the voltage begins to increase with the current again, but at a significantly lower rate than for the Penning discharge with flat cathodes. This voltage increase is required to create favorable conditions for electron emission not only near the entrance to the cavity, but also deep in the cavity [8].

The introduction of SHE *5* into cavity *1* changes the situation radically. On one hand, at low currents, the hollow-cathode effect is now difficult to observe, because electrode *5*, which is at the cathode potential, occupies the central part of the cavity. On the other hand, the introduction of an SHE results in the excitation of a magnetron discharge and the appearance of an additional source of electrons injected into the gas, which leads to its ionization. At low discharge currents, electron emission is completely determined by γ-processes; as a result, the increase in the current is accompanied by an increase in the discharge voltage (region *I* in Fig. 2). However, a further increase in the current leads to heating of the SHE by the ions bombarding the cathode (which is confirmed by visual observations) and to an appreciable thermoelectron emission. Under these conditions, a high voltage is not needed to sustain the discharge. As the current increases, the discharge voltage decreases (region *II*), because the discharge is sustained by electron emission from the SHE.

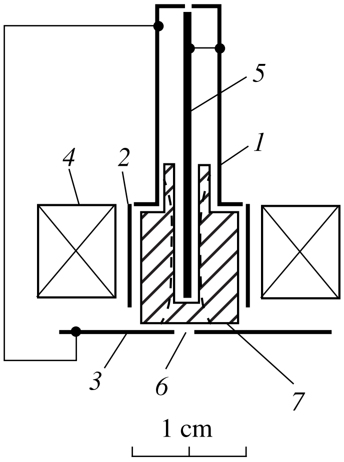

Fig. 1. Electrode system of the discharge cell of the atomic hydrogen source.

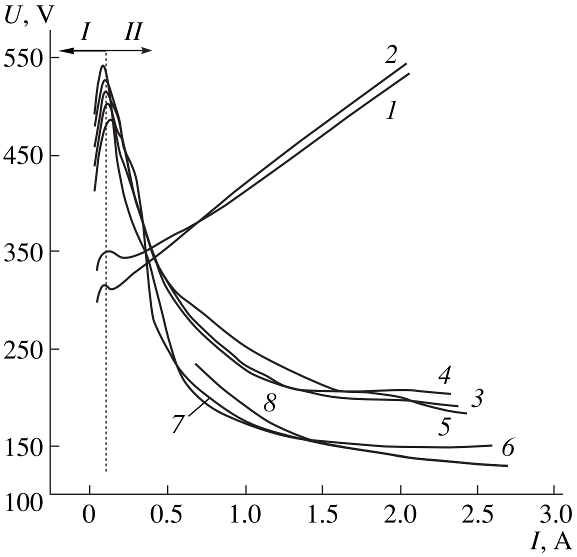

Fig. 2. *I*–*V* characteristics of the reflex hollow-cathode discharge without SHE (*1*, *2*) and with an SHE (*3*–*8*) for different gas flow rates Q: (*1*) 10.8, (*2*) 17.5, (*3*) 2.7, (*4*) 3, (*5*) 4.2, (*6*) 6.2, (*7*) 18.6, and (*8*) 51.3 sccm.

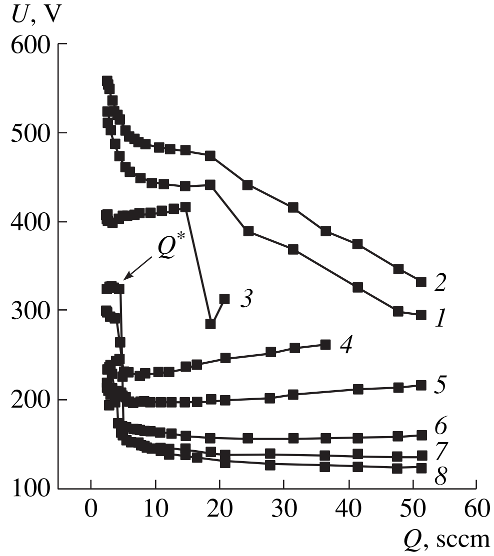

Fig. 3. Discharge voltage as a function of the hydrogen flow rate for the reflex discharge with a hollow cathode and an SHE for various discharge currents: (*1*) 0.045, (*2*) 0.1, (*3*) 0.3, (*4*) 0.45, (*5*) 0.6, (*6*) 1, (*7*) 1.5, and (*8*) 2.2 A.

Competition between secondary electron–ion emission and thermoelectron emission leads to the appearance of a maximum in the *I–V* characteristic. Its position is determined by the current at which thermoelectron emission from the SHE comes into play. As the gas flow rate increases, the position of the maximum monotonically shifts toward higher currents and lower voltages. A more detailed analysis revealed the following peculiarity in the behavior of the power $P_{\max}$ defined as the product of the discharge current and the voltage at the maximum of the *I–V* characteristic. For gas flow rates of 2.7–4.2 sccm, the value of $P_{\max}$ is almost constant and is about 50 W. For Q = 6.2–31.5 sccm, we have $P_{\max} \cong 65$ W. In absolute value, these data agree well with the results obtained in [3], where, for a 4-mm-diameter rod SHE, $P_{\max} \cong 180$ W and, for a 1-mm-diameter SHE, it is equal to 21 W. The value of $P_{\max}$ measured in our experiments is several times lower than the power that was required in [4, 7] for thermoelectron emission from the self-heating heat-insulated hollow cathode to come into play (~200–250 W). This shows that heating a rod SHE with a magnetron discharge is more efficient than heating a hollow self-heating cathode with a reflex hollow-cathode discharge.

It is interesting that, at the dropping branch of the *I–V* characteristic, the set of curves is divided into two groups. The curves corresponding to relatively low values of the gas flow rate (Q ~ 2.7–4.2 sccm) fall into the first group, whereas the second group consists of the curves corresponding to high values of the gas flow rate (Q ~ 6.2– 51.6 sccm). The first group of *I–V* characteristics is characterized by higher discharge voltages than the second group.

More detailed data can be obtained from analyzing the dependences of the discharge voltage U on the gas flow rate in Fig. 3. These curves were measured independently in different experiments. It is seen that, in all the curves, there exists a typical inflection point Q^* where the curves are kinked. At low currents (0.045–0.1 A), as the gas flow rate increases, the slope of the curves changes abruptly at the point Q^*. At higher currents (0.3–2.2 A), the discharge voltage abruptly drops at this point and then varies only slightly, even when the gas flow rate varies by one order of magnitude. As the discharge current increases, the inflection point Q^* shifts toward lower discharge voltages. Visual observations of the emission hole show that, as the gas flow rate increases, the discharge emission sharply decreases at the point $Q = Q^*$.

The sharp decrease in the discharge voltage and emission intensity at the point Q^* may be explained by the change in the discharge shape. We suggest that, at low gas flow rates ($Q < Q^*$), only a magnetron discharge occurs in the discharge cell, which results in both the efficient heating of the part of electrode *5* that is located inside the anode cavity and intense emission from the discharge. At $Q \geq Q^*$, the plasma penetrates into the hollow cathode, thus initiating a reflex hollow-cathode discharge, which occurs simultaneously with a magnetron discharge. In this case, the discharge voltage drops abruptly and the temperature (emission intensity) of the SHE decreases because of an increase in both the plasma volume and the cathode area capable of thermoelectron emission.

Oscillograms of the discharge current show that, at low gas flow rates ($Q < Q^*$), when the magnetron discharge takes place, the discharge current oscillates at a frequency of ~100 kHz; the amplitude of these oscillations increases as the gas flow rate decreases. Apparently, when the gas flow rate and the hydrogen pressure in the discharge cell are both low, the diffusion mechanism cannot ensure the transport of magnetized electrons from the cathode to the anode. This results in the onset of current instabilities, whose amplitude increases as the role of diffusion transport decreases. At $Q > Q^*$, the discharge with a hollow cathode occurs and, at the same time, the current oscillations disappear. The disappearance of the oscillations indicates that, when the hollow cathode comes into play, the electron transport mechanism changes substantially and more favorable conditions are created for the current to flow through the discharge region.

Observations of the erosion of the electrodes and SHE *5* show that erosion occurs primarily at the rod SHE on the side facing the reflector cathode *3* (visible erosion of the electrodes was detected after a 50-h continuous discharge). The SHE, which is initially cylindrical, becomes conical, with the vertex facing the reflector cathode. This indicates that the plasma density along the axis of the discharge cell reaches its maximum near the end of the SHE. The erosion area seen on the surface of the reflector cathode consists of two characteristic regions: the central region of maximum erosion with the same diameter as the SHE and the annular region of lesser erosion with the same diameter as the hollow cathode. At the other area of the reflector-cathode surface, erosion traces are almost invisible. The presence of regions with different degrees of erosion indicates that, along the radius of the discharge cell, there are regions with comparable diameters where the plasma densities are different.

THEORETICAL MODEL OF THE DISCHARGE

To better understand the nature of the discharge under study, we use a simplified model allowing us to calculate the basic plasma parameters and the *I*–*V* characteristics of the discharge. The following basic simplifications are assumed:

(a) We consider the discharge conditions under which the voltage drop across the cathode sheath is almost equal to the total discharge voltage. The interelectrode volume is mainly filled with a quasineutral plasma (the discharge column) separated from the electrodes by narrow sheaths whose sizes are assumed to be negligible.

(b) We assume that a flow of fast electrons is formed in the cathode sheath, the electron energy being approximately equal to the discharge voltage. This electron flow transports the energy from the power supply into the plasma and ionizes the gas.

(c) We completely neglect gas ionization by relatively slow electrons of the plasma column. The role of the plasma electrons in this model reduces merely to carrying a part of the electron current through the gap across the magnetic field.

(d) Since the discharge ions are not magnetized, we assume that the ion current, which is equal to the saturation current (Bohm current), is uniformly distributed over the entire cathode surface.

(e) The SHE is assumed to be heat-insulated; i.e., energy is lost through radiation only.

(f) We assume that the role of the discharge excited in the hollow cathode reduces to the generation of additional fast electrons that flow from the cavity toward the axial region of the main discharge.

The calculation of the *I*–*V* characteristics includes several steps: calculation of the fast-electron density distribution along the discharge gap; calculation of the ion, fast-electron, and plasma-electron current distributions in the discharge column; calculation of the secondary γ-electron current and the thermoelectronic emission current from the rod cathode; formulation of the conditions for the current to be self-sustaining; and determination of the *I*–*V* characteristics of the discharge from these conditions.

The fast-electron distribution n_f in the column is calculated from the continuity equation using the τ-approximation for the loss of such electrons. The fast electrons come into the plasma both from the flat end surfaces of the hollow and reflector cathodes and from the central rod; they are lost in the plasma volume in the characteristic time τ_i. Hence, the continuity equation for the flow of fast electrons j_f in cylindrical coordinates takes the form

$$r^{-1}d(rj_f)/dr = (2j_{f\perp}/h) - n_f/\tau_i, \tag{1}$$

where h is the height of the discharge cell and the first term on the right-hand side describes electron production through emission from the flat end surfaces of the cathode $j_{f\perp}$.

A similar discharge model was considered in [9], where it was shown that the electron flow across the magnetic field may be attributed to diffusion and can be approximated by

$$j_f = -D_f(dn_f/dr), \quad D_f = \langle r_{Le}^2 \nu_f \rangle, \tag{2}$$

where r_{Le} is the electron Larmor radius and ν_f is the scattering rate characterizing the momentum loss of fast electrons (this rate is higher than the gas-molecule ionization rate $\nu_i = (E_0/\varepsilon_i)/\tau_i$, where $E_0 = eU_c$ is the initial electron energy, ε_i is the average energy for the formation of an electron–ion pair, and U_c is the cathode potential drop).

For the sake of simplicity, as in [9], we assume that the fast-electron diffusion coefficient across the magnetic field (of induction B) is constant and equal to a certain average value

$$D_f \cong (m\nu_f/3eB^2)U_c. \tag{3}$$

It is seen that this coefficient is proportional to the cathode potential drop and the collision frequency (the working gas pressure).

Substituting expression (2) into Eq. (1) and solving the latter with boundary condition (2) for the given value of the fast-electron flux density from the central rod, we obtain

$$n_f/n_w = 1 + (h/2l_D)(j_{f0}/j_{f\perp})K_0(\rho)/K_1(\rho_0), \tag{4}$$

where j_{f0} is the fast-electron flux density at the axis-side column boundary ($r = r_0$), K_0 and K_1 are the modified Bessel functions, and

$$n_w = 2\tau_i j_{f\perp}/h, \quad l_D^2 = D_f\tau_i, \quad \rho = r/l_D. \tag{5}$$

The density n_w is produced by the fast γ-electrons arriving from the flat end surfaces of the cathode. The second term on the right-hand side of (4) is due to diffusion of magnetized fast thermoemission electrons in the radial direction. Their penetration depth and, consequently, the extension of the gas-ionization region is characterized by the quantity

$$l_D = [(m\nu_f/3eB^2)U_c(E_0/\varepsilon_i)/\nu_i]^{1/2} = [m(\nu_f/\nu_i)/3\varepsilon_i]^{1/2}(U_c/B). \quad (6)$$

The ratio between the scattering and ionization rates for fast electrons, ν_f/ν_i, may be assumed to be approximately constant; below, we will assume that this ratio is equal to 2. The diffusion length l_D depends linearly on the initial electron energy and is inversely proportional to the magnetic induction. In our model, the length of the region where the gas is ionized by thermoemission electrons does not depend explicitly on the gas-particle density (pressure), because both the diffusion coefficient of fast electrons across magnetic field lines and the lifetime of fast electrons are inversely proportional to the gas-particle density.

Now, we write the time-independent continuity equation for the plasma (slow) electron flux density j_s, assuming that they are produced only by ionization of the gas by fast electrons:

$$r^{-1}d(rj_s)/dr = \nu_i n_f = (eU_c/\varepsilon_i)n_f/\tau_i. \quad (7)$$

Integrating (7) for the current produced by the plasma electrons, we obtain

$$I_s(\rho) = (\mu+1)\{I_{f\perp}(\rho^2-\rho_0^2)/(\rho_a^2-\rho_0^2) + I_{f0}[1-\rho K_1(\rho)/\rho_0 K_1(\rho_0)]\}, \quad (8)$$

where $\mu = (eU_c/\varepsilon_i) > 1$ is the electron-multiplication coefficient, $\rho_0 = r_0/l_D$, $\rho_a = r_a/l_D$, and r_a is the anode radius. Here, we introduce the current of the plasma electrons $I_s = 2\pi hrej_s$; the current of the fast electrons coming into the column from the flat end surfaces of the cathode, $I_{f\perp} = 2\pi l_D^2(\rho_a^2 - \rho_0^2)ej_{f\perp}$; and the current of the fast thermoemission electrons arriving at the plasma column from the rod SHE, $I_{f0} = 2\pi hr_0 ej_{f0}$.

Taking into account expressions (2) and (4), the expression for the fast-electron current can be written in the form

$$I_f(\rho) = I_{f0}\rho K_1(\rho)/\rho_0 K_1(\rho_0). \quad (9)$$

Note that the electrons arriving at the plasma from the flat end surfaces of the cathode do not contribute to the fast-electron current, because they produce a uniform electron density in the column and thus the diffusion current (2) is absent.

Now, we add together the two currents (8) and (9) to obtain the electric current at the anode produced in the discharge column by electron multiplication under the action of the fast electrons emitted from the cathode,

$$I_a = (\mu+1)I_{f\perp} + \mu I_{f0}[1-\rho_a K_1(\rho_a)/\rho_0 K_1(\rho_0)] + I_{f0}. \quad (10)$$

Current (10) must be equal to the total current at the cathode:

$$I_c = [I_{em} + I_{i0}(1+\gamma)](1-\delta), \quad (11)$$

where I_{em} is the thermoemission current from the rod, I_{i0} is the total ion current at the cathode, and the dimensionless factor $0 \le \delta < 1$ determines the fraction of the total current that flows through the hollow cathode; in the absence of a discharge in the hollow cathode, we set $\delta = 0$.

We equate (11) to (10) and take into account that the ion-current distribution is uniform over the entire cathode surface. Then, in view of the equations $I_{f\perp} = \gamma I_{i0}S_w/(S_w + S_0)$ and $I_{f0} = I_{em} + \gamma I_{i0}S_0/(S_w + S_0)$, with a simple manipulation, we obtain

$$(\mu G + \delta)(I_{em}/I_{i0}) + \mu\gamma[(S_w + GS_0)/(S_w + S_0)] + \delta(1+\gamma) = 1, \quad (12)$$

where $G = 1 - \rho_a K_1(\rho_a)/\rho_0 K_1(\rho_0) < 1$ is the dimensionless factor accounting for the geometry of the discharge, $S_w = 2\pi(r_a^2 - r_0^2)$ is the area of the flat end surfaces of the cathode, and $S_0 = 2\pi r_0 h$ is the surface area of the SHE.

Equation (12), which may be called the self-sustained discharge condition, contains two unknown quantities: the thermoemission and ion currents at the cathode (note that the term in square brackets in the second summand varies within a rather narrow range from 0.8 to 1). For low thermoemission currents in the absence of a discharge in the hollow cathode, the self-sustained discharge condition takes the simplest form, $\mu\gamma \cong 1$.

The second equation relating the thermoemission and ion currents is derived from the heat balance for the SHE and the expression for the thermoemission current. The heat balance gives the expression for the rod temperature T_c:

$$S_0\varepsilon_T\sigma T_c^4 = U_c I_{i0}S_0/(S_0 + S_w), \quad (13)$$

where σ is the Stefan–Boltzmann constant and $\varepsilon_T \cong 0.5$ is the radiant emissivity of tungsten.

If the cathode temperature is known, we can determine the value of the thermoemission electron current

$$I_{em} = S_0 A_0 T_c^2 \exp(-\varphi_w/kT_c), \quad (14)$$

where $\varphi_w = 4.54$ eV is the electronic work function and $A_0 \cong 70$ A/cm^2 K^2 is a factor calculated from the reference data for tungsten [10].

If the geometrical parameters, the coefficients for elementary processes ε_i and γ, the cathode voltage drop (the discharge voltage) U_c, and the fraction δ of the total current that flows through the hollow cathode are known, then Eqs. (12)–(14) allow us to calculate three unknown quantities: the ion and thermoemission currents and the rod temperature. Then, using (11), we can determine the total discharge current and calculate the *I–V* characteristics of the discharge.

An example of the results of such calculations is presented in Fig. 4. In the calculations, we used actual geometrical dimensions of a cell and assumed that ε_i = 40 eV and $\gamma = 0.08$. These values are in accordance with the data cited in the literature.

The calculated *I–V* characteristics at high currents are similar to the experimental ones. As the current increases, the discharge voltage decreases. If a discharge is ignited in the hollow cathode, then the discharge voltage drops abruptly; this drop is more pronounced at low discharge currents. Furthermore, the greater the fraction of the current flowing through the hollow cathode (i.e., the higher the factor δ), the greater the drop in the discharge voltage. It is worth noting that the latter result is not trivial and is explained by the fact that the discharge in the hollow cathode increases the number of fast electrons in the central region of the discharge cell.

The results of calculating the SHE temperature (Fig. 4) show that, as the fraction of the current flowing through the hollow cathode increases, the SHE temperature decreases. This is because the thermoelectron-emission area increases due to heating of the part of the SHE located inside the hollow cathode. We note that the actual maximum temperature of the SHE must be somewhat higher than the calculated one. The reason is that, in the model used, the ion current is assumed to be uniformly distributed over the entire cathode surface, whereas, taking into account the erosion pattern of the SHE, the maximum ion-current density occurs at the SHE end facing the reflector cathode.

DISCUSSION OF RESULTS

On the whole, the general features of the discharge observed in the experiment can be explained by the model described above.

Thus, in the experiment, we can distinguish two discharge regimes as shown in Fig. 3. The first regime is observed at low gas flow rates ($Q < Q^*$) and is characterized by an enhanced discharge voltage. The second regime corresponds to higher gas flow rates ($Q > Q^*$) and is characterized by a low voltage. Furthermore, at discharge currents $I \leq 0.1$A, the transition from the first to the second regime is accompanied by a gradual decrease in the discharge voltage, whereas at $I \geq 0.3$ A, the transition to the low-voltage regime occurs abruptly when the gas pressure exceeds a certain threshold value.

This behavior of the *I–V* characteristics can be related to the change in the depth to which the plasma penetrates into the hollow cathode. At relatively low discharge currents, the sheath thickness near the hollow-cathode aperture is so large that the plasma cannot penetrate deep into the cavity. The sheath thickness d_c can be easily estimated from the "three-halves power law"

$$d_c^2 \cong (4\varepsilon_0/9)(2q/M_i)^{1/2} U_c^{3/2}/j_{i0}, \qquad (15)$$

where ε_0 is the permittivity of a vacuum and j_{i0} is the ion-current density at the cathode.

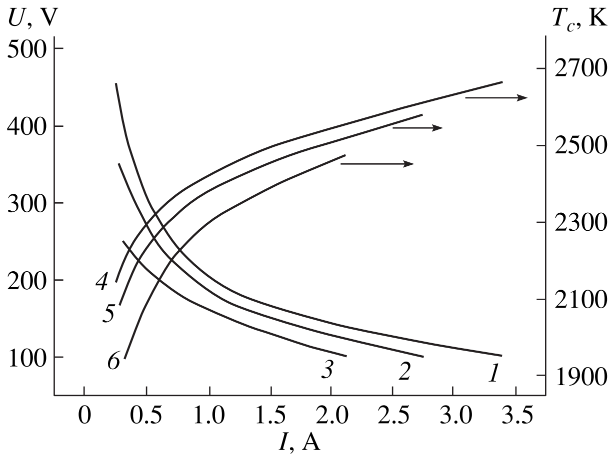

Fig. 4. Calculated *I–V* characteristics of the reflex discharge with a hollow cathode and an SHE (*1–3*) and dependences of the temperature of the SHE on the discharge current (*4–6*) for different values of δ: (*1, 4*) 0, (*2, 5*) 0.25, and (*3, 6*) 0.5.

When the ion-current density at the cathode j_{i0} is at a level of 0.1 A/cm^2 and the voltage across the sheath U_c is about 400 V, we obtain an estimate of 0.6 mm for the thickness d_c of the cathode sheath. Taking into account that the sheath exists not only near the hollow cathode, but also near the SHE, we find that the double thickness of the cathode sheath near the cavity aperture is ~1.2 mm. This thickness is nearly equal to the size of the entrance slit of the cavity ($r_1 - r_0$ = 1 mm). It should also be taken into account that the total thickness of the cathode sheath can be larger than the value prescribed by (15), because, near the sheath, there is an adjacent "presheath" in which the gas is additionally ionized [11].

It is important that estimate (15) is independent of the gas pressure and depends only on the discharge current and the voltage across the cathode sheath. This means that, at low currents, the situation cannot change radically when the gas pressure in the cell increases. This is clearly seen in Fig. 3: even a substantial increase in the gas flow rate (i.e., the increase in the gas pressure in the discharge cell) results merely in a slow decrease in the discharge voltage, which may be related, e.g., to a light flexing of the plasma boundary inward the cavity.

As the discharge current increases ($I \geq 0.3$ A), the cathode-sheath thickness decreases, which, under certain conditions, can allow the plasma to penetrate into the cavity. The penetration of the plasma, the heating of

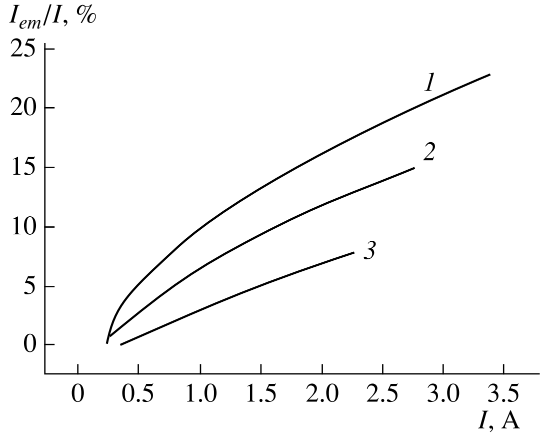

Fig. 5. Fraction of the thermoelectron emission current in the total discharge current vs. the discharge current for δ = (*1*) 0, (*2*) 0.25, and (*3*) 0.5.

the part of the SHE that is located inside the cavity, and the oscillations of fast electrons inside the hollow cathode result in a sharp increase in the efficiency of the ionization inside the cavity and a decrease in the cathode drop, which in turn leads to a decrease in the cathode-sheath thickness. As a result of these processes, the plasma rapidly fills the cathode cavity and the discharge changes abruptly from one stable mode to another.

Let us examine the condition under which the discharge in a hollow cathode can be ignited. Experimental data show that the discharge is ignited when the gas flow rate reaches a certain limiting value Q^*. From general considerations, it is clear that the discharge in the cavity cannot occur if the pressure is less than a certain critical value. The critical gas density below which the plasma cannot be sustained in a long narrow cavity can be found from the condition that a fast electron ionize at least one gas molecule. Taking into account that, for an electron with an energy of ~200–300 eV, the ionization cross section is $s_i \cong 10^{-16}$ cm^2 (15) and the depth of the cathode cavity from which an electron moving along a curved magnetic line can arrive at the anode cavity is estimated as $L \cong 1.5$ cm, we obtain that the value of the critical density is about $n_c \cong 7 \times 10^{15}$ cm^{-3}. This corresponds to a gas flow rate of $Q \sim 8.3$ sccm. At nearly the same gas flow rate Q^*, we observe an abrupt decrease in the discharge voltage (Fig. 3).

The depth L to which the plasma penetrates into the cavity can be used to estimate the value of δ (the fraction of the current flowing through the cavity). This fraction must be approximately equal to the ratio of the area of the inner cavity surface to the total cathode area. The estimate yields a value of $\delta \cong 1/[1 + (S_0 + S_w)/2\pi L(r_1 + r_0)] \cong 0.5$; i.e., nearly one-half of the discharge current can flow through the hollow cathode.

At currents of $I \geq 0.3$ A, the discharge voltage is almost independent of the pressure. This result was obtained in both the experiment and the discharge modeling. The reason is that the electrons are strongly magnetized so that, independently of the gas density, they cause approximately the same number of ionization events before arriving at the anode. In addition, an increase in the fraction of the thermoemission current can also lead to a weaker dependence of the I–V characteristic on the gas pressure.

Figure 5 shows the calculated fraction of the thermoelectron-emission current for different values of the discharge current. It is evident that this fraction increases with current, attaining 23% for $I = 3.3$ A. Taking into account that the temperature is not uniformly distributed along the SHE, we must admit that this value can be even higher. Thus, as the discharge current increases, the glow discharge gradually transforms into an arc discharge with a heated cathode.

REFERENCES

1. A. Sherman, J. Vac. Sci. Technol. B **8**, 656 (1990).
2. S. Gourrier, P. Friedel, P. Dimitriou, and J. B. Theeten, Thin Solid Films **84**, 379 (1981).
3. A. P. Semenov and M. V. Mokhosoev, Zh. Tekh. Fiz. **54**, 2276 (1984) [Sov. Phys. Tech. Phys. **29**, 1337 (1984)].
4. V. A. Gruzdev and O. E. Troyan, Available from VINITI No. 5041-1388.
5. V. A. Kagadeĭ, D. I. Proskurovskiĭ, and O. E. Troyan, RF Patent No. 2 088 056.
6. V. A. Kagadeĭ and D. I. Proskurovskiĭ, J. Vac. Sci. Technol. A **16**, 2556 (1998).
7. V. A. Kagadeĭ, D. I. Proskurovskiĭ, and L. M. Romas’, Élektron. Prom–st., Nos. 1–2, 34 (1998).
8. Yu. E. Kreĭndel’, *Plasma Sources of Electrons* (Atomizdat, Moscow, 1977).
9. S. P. Nikulin, Zh. Tekh. Fiz. **68** (7), 56 (1998) [Tech. Phys. **43**, 795 (1998)].
10. *A Reference Book for Physical Quantities*, Ed. by I. S. Grigor’ev and E. Z. Meĭlikhov (Énergoatomizdat, Moscow, 1991).
11. Yu. P. Raizer, *Gas Discharge Physics* (Nauka, Moscow, 1987; Springer-Verlag, Berlin, 1991).

Translated by N. Larionova

Technical Physics, Vol. 46, No. 3, 2001, pp. 299–306. Translated from Zhurnal Tekhnicheskoĭ Fiziki, Vol. 71, No. 3, 2001, pp. 29–36.
Original Russian Text Copyright © 2001 by Kudryavtsev, Kuranov, Mishakov, Tkachenko, Skoblo, Chaĭka.

GAS DISCHARGES, PLASMA

Peculiarities of Plasma Decay in the Afterglow of a Low-Pressure Pulsed Discharge in Oxygen

A. A. Kudryavtsev, A. L. Kuranov, V. G. Mishakov, T. L. Tkachenko,
I. N. Skoblo, and M. O. Chaĭka
St. Petersburg State University, St. Petersburg, 198904 Russia
e-mail: akud@ak2138.spb.edu

Received February 24, 2000

Abstract—Weakly ionized plasma of a pulsed-discharge afterglow in oxygen at low pressures (0.05–0.15 torr) is investigated using probe diagnostics. The plasma conductivity is measured by supplying an additional probing current pulse at a certain instant during the afterglow. The spectral line intensities are also measured to additionally monitor the densities of charged particles. The measurements of the time behavior of the electron density in an oxygen afterglow plasma confirm the previous conclusion that the electrons escape due to enhanced diffusion, which results in the formation of an ion–ion plasma. The possibility of realizing the opposite ultimate case—the detachment decay regime with an increase in the electron density to the density of positive ions in the first stage and the transition to the electron–ion plasma in the second stage—is demonstrated. *© 2001 MAIK "Nauka/Interperiodica".*

In recent years, investigations of the spatial and temporal characteristics of a pulsed plasma of electronegative gases has attracted increasing interest. This is mainly related to the experimentally revealed possibility of substantially improving the operation of different devices by using a pulsed power supply. As examples, we can mention ion sources [1], plasma etching reactors [2], and other modern plasma technology devices [3]. The parameters of different plasma components can be rather easily controlled by varying the duration of the active phase, the on-duty ratio, supplied power, and other characteristics of a repetitive discharge. In these studies, rather unexpected effects and phenomena were revealed. For example, it was repeatedly reported that, in the initial stage of decay, the density of negative ions N_n can increase, while the densities of positive ions N_p and electrons N_e monotonically decrease [1–4]. This inference was based on the sharp increase in the flux of negative ions onto the wall recorded in mass spectrometry measurements or the growth of the probe current due to laser photodetachment, whose rate is proportional to the density ratio N_n/N_e. In the literature, these effects are associated with a relative increase in the rate of formation of negative ions with respect to the rate of their collisional loss in the bulk of the discharge afterglow, in contrast to the discharge active phase, when these rates are equal to each other.

This point of view was criticized in [5], in which an alternative explanation based on the specific character of diffusion loss of charged particles in a plasma of electronegative gases [7] was proposed. As was shown earlier [6, 7], even in the simplest case when plasmochemical processes can be neglected (i.e., when diffusive decay of a simple electropositive plasma is described by an exponential law), the process of plasma decay in electronegative gases can be divided into two stages. When $N_n/N_e < b_e/b_n$ (where b is the corresponding mobility), the number of electrons and positive ions in the plasma decreases, while the negative ions are trapped in the plasma bulk by the self-consistent radial field and the wall potential drop. In the second stage (when $N_n/N_e > b_e/b_n$), the decay is governed by ion–ion ambipolar diffusion, whereas the electrons are almost absent. A drastic change in the regime of plasma decay, which is consistent with such a decay scenario, was observed even in [8] for a low initial electronegativity $\alpha_0 = N_n/N_e \ll 1$. It was found in [9] that the transition to an ion–ion plasma proceeded with sharpening; i.e., almost all the electrons escape from the plasma bulk in a finite time t_0, which is mainly determined by the value of α_0. As was shown in [9], for a high electronegativity ($\alpha_0 > 1$), the escape of electrons is accompanied by a relatively small change in the densities of positive and negative ions. Since this interesting phenomenon is apparently fairly general and universal in character, it is worthy of further investigations.

In this work, we continue the investigations of an oxygen afterglow plasma [9]. In addition to probe measurements, the plasma conductivity was measured by supplying an additional probing current pulse at a certain instant during the afterglow. Spectral lines intensities were also measured to additionally monitor the densities of charged particles. The experiments were carried out in the oxygen discharge afterglow, between discharge current pulses with an amplitude of i = 6–600 mA. The duration of the active phase was 50 μs,

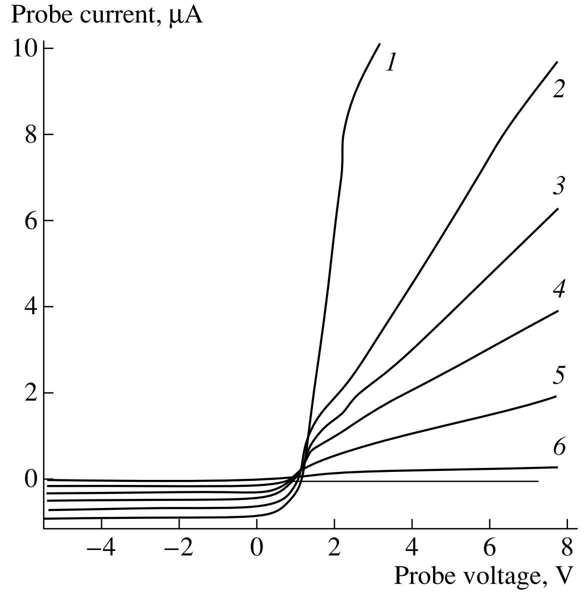

Fig. 1. Probe *I–V* characteristics in an oxygen afterglow for $p = 0.07$ torr, $i = 6$ mA, and different time delays: (*1*) 25, (*2*) 125, (*3*) 225, (*4*) 325, (*5*) 525, and (*6*) 625 μs.

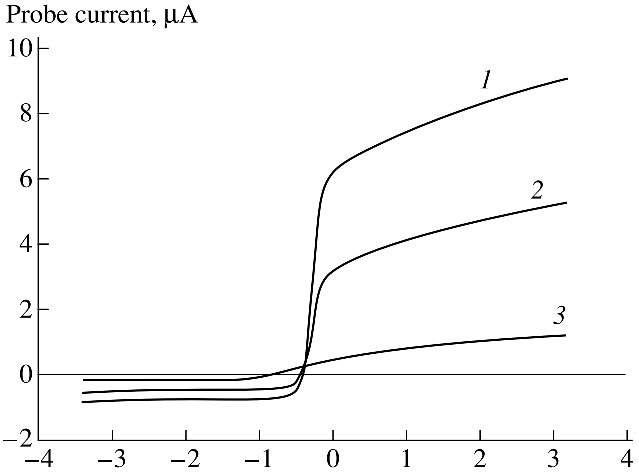

Fig. 2. Probe *I–V* characteristics during a neon afterglow for $p = 0.07$ torr, $i = 6$ mA, and different time delays: (*1*) 225, (*2*) 425, and (*3*) 845 μs.

and the pulse repetition period was 4 ms. The oxygen pressure was varied in the range $p = 0.04$–0.15 torr. A glass tube of radius $R = 1.7$ cm with cold nickel electrodes and sealed movable electrical probes was used.

The measurement scheme allowed us to record the probe current–voltage (*I–V*) characteristics with a time resolution of 5–10 μs. The shape and time behavior of the measured *I–V* characteristics are similar to those obtained earlier in [9] (Fig. 1). It is seen that, in the initial stage of plasma decay, the probe characteristics are ordinary in shape; i.e., the saturation currents of negative particles are higher than the saturation currents of positive particles, $i_{es} + i_{ns} \gg i_{ps}$. This is explained by the fact that the electron saturation current is relatively large ($i_{es} \gg i_{ns}$), even for $N_e < N_n$, due to the low electron mass ($m \ll M$) and, correspondingly, due to the higher electron velocity. Then, by the instant t_0 (for the conditions of Fig. 1, $t_0 \approx 600$ μs), the current of negative particles decreases substantially and, at $t > t_0$, the value of $i_{es} + i_{ns}$ becomes comparable to i_{ps}. In the second stage ($t > t_0$), the probe characteristics are almost symmetric, which was naturally interpreted in [9] as the formation of an ion–ion (electronless) plasma. In other words, in this stage, the plasma should mainly consist of positive and negative ions and a vanishingly small number of electrons. We note that such unusual behavior of N_e in the afterglow cannot be observed in a simple plasma (without negative ions), because, in such a plasma, the equality $N_e = N_p$ is always satisfied and, hence, $i_{es} \gg i_{ps}$. Test measurements in a neon afterglow showed that, as was expected, $i_{es}/i_{ps} \gg 1$ at any instant during the afterglow (Fig. 2), although the absolute values of the saturation currents decrease during plasma decay. Since the saturation currents are proportional to the densities of the corresponding plasma components, their time dependences measured for the fixed probe potential allow us to describe the time behavior of the densities of positive and negative particles. Using the probe *I–V* characteristics in Fig. 1, we determined the time dependences of the saturation currents of negative particles $i_{es} + i_{ns}$ (Fig. 3) and positive particles i_{ps} (Fig. 4) at a probe potential of ±3 eV, respectively. It is seen that, in the first stage of decay, the current of negative particles, which is determined by the electrons, drops drastically at $t_0 \approx 600$ μs and becomes close to the ion current. This indicates that the decay of the electron component proceeds in a typical regime with a strong positive feedback, i.e., the regime with sharpening [10]. In this case, the current of positive ions i_{ps} shows no peculiarities and decays nearly by an exponential law with the time constant $\tau \approx 350$ μs (Fig. 4). This value agrees well with the ambipolar diffusion time of positive ions [11]

$$t_p = R^2/(2D_p(2.4)^2). \tag{1}$$

For $p = 0.07$ torr and a diffusion constant of positive ions $D_p = 0.07$ cm^2/s, we obtain $t_p \approx 400$ μs from Eq. (1). Later on, at $t > t_0$, the currents of positive and negative particles are similar in magnitude (hence, $N_n \approx N_p$) and decay at the same rate.

In the initial stage of decay, the recorded ratio of $i_{es} + i_{ns}$ to i_{ps} is 10–50, which corresponds to the experimental limit for monitoring the change in the ratio of the probe electron current to the ion current. Unfortunately, the theoretical limit $\sqrt{M/m}$ is very rarely attained in experiments even for a simple plasma of electrons and positive ions [12]. It was reported recently [13, 14] that, under similar experimental conditions, the recorded ion saturation currents may be up to 10 times higher than the current calculated using the orbital motion limit (OML) theory. This may be caused by rather different reasons, depending (among other factors) on the temperatures and densities of the electrons and ions and on other parameters determining the experimental values of the saturation currents.

Thus, when measuring the probe currents, we can monitor the dynamics of the decrease in the ratio of the electron density to the ion density by a factor of no more than several tens. Further changes in the electron density are masked by the current of negative ions. To independently test such unusual behavior of the electron density (in comparison with the behavior of the ion densities), one can use other methods, in particular, measurements of the plasma conductivity. As is known, the plasma current in an external field E is determined by the densities and mobilities of charged particles:

$$i_d = e\pi R^2(\bar{N}_e b_e + \bar{N}_p b_p + \bar{N}_n b_n)E, \tag{2}$$

where $\bar{N}_j$ is the averaged density of the jth charged component ($j = e$, n, or p) over the cross section of a tube of radius R.

For the Bessel profile, we have $\bar{N}_j = 0.43N_j(0)$. Since $b_e \gg b_p$, b_n, the current flowing through the discharged tube is almost equal to the electron current, while $N_n/N_e < b_e/b_n$. For known i_d, E, and b_e, the value of N_e can be easily determined using Eq. (1). For example, the experimental dependences $b_e(E/p)$ for oxygen are given in [15]. An analysis of these data shows that $b_e \approx 1000$–$1200\ \text{cm}^2/(\text{V s})$ and varies only slightly in the range of $E/p = (0.03$–$0.3)$ V/(cm torr) under investigation. Since $b_p = 2.2\ \text{cm}^2/(\text{V s})$ and $b_n = 3.2\ \text{cm}^2/(\text{V s})$ [11], the experimental time dependence i_d/E should be proportional to $N_e(t)$ up to $(N_p + N_n)/N_e \lesssim 200$.

To measure the plasma conductivity at a certain instant during the afterglow, an additional voltage pulse producing a longitudinal electric field was applied to the tube electrodes [16]. The pulse current was determined from the voltage drop across a known resistance, and the field was determined from the voltage between two probes. As is known, the probing pulse parameters should satisfy the following requirements [16, 17]: (i) in order to produce a non-self-sustained discharge in a decaying plasma and thus to obtain a fixed electric field E in the plasma column, the pulsed voltage applied to the electrodes must be higher than the electrode voltage drops; (ii) to prevent the electron density from changing appreciably due to ionization and diffusion toward the wall, the pulse duration should not be too long and the pulsed electric field should not be too strong. In our experiments, we used probing pulses with durations of 10–30 μs and amplitudes of 100–600 V. The results of i_d/E measurements at different times under the same conditions ($p = 0.07$ torr and $i = 6$ mA) are also presented in Fig. 3. For simplicity, the curves are normalized to the saturation probe current at $t = 200$ μs. It is seen that the time dependences $N_e(t)$ determined in different ways are qualitatively similar in shape and that the rate at which the electron density decays increases with time. For comparison, the results of the corresponding measurements for the same discharge current and two pressure values ($p = 0.07$ and 0.15 torr) are presented in Fig. 5. It is seen that the dependences are qualitatively similar. The only difference is that the characteristic time during which the electrons escape from the plasma increases about two times. Naturally, this effect is associated with a decrease in the diffusion coefficient, which is proportional to the gas pressure p [see Eq. (1)]. We note one more interesting fact. As is seen from Figs. 3 and 5, the measured time dependences of i_d/E change only slightly in the initial stage of the afterglow and even

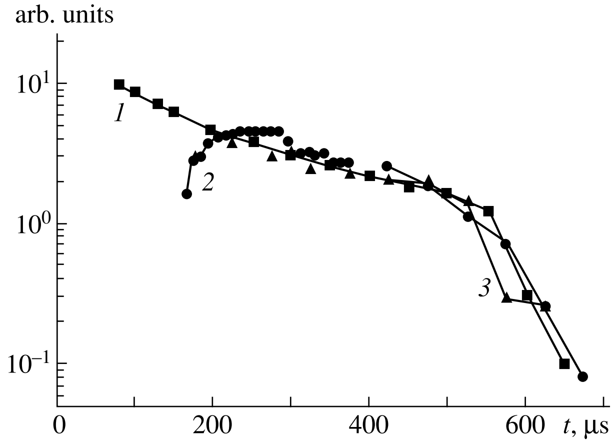

Fig. 3. Time behavior of the electron characteristics for $p = 0.07$ torr and $i = 6$ mA: (*1*) saturation currents of negative particles $i_{es} + i_{ns}$ at a probe voltage of +3 V according to data from Fig. 1, (*2*) measured values of i_d/E, and (*3*) measured values of I_λ during the heating pulse.

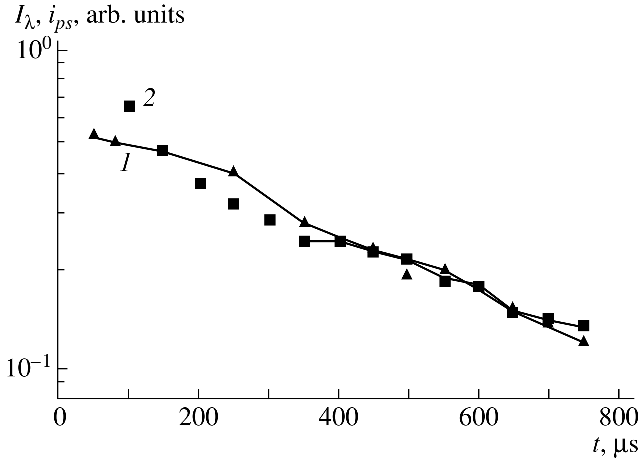

Fig. 4. Time behavior of the ion characteristics for $p = 0.07$ torr and $i = 6$ mA: (*1*) saturation currents of positive ions i_{ps} at a probe voltage of –3 V according to data from Fig. 1 and (*2*) intensity I_λ.

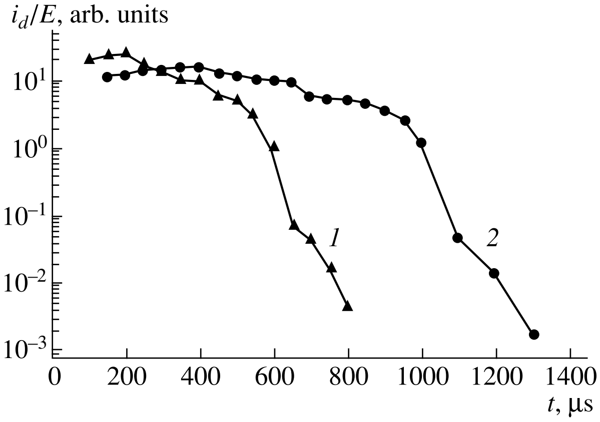

Fig. 5. Measured time dependence of i_d/E for $i = 6$ mA at $p =$ (*1*) 0.07 and (*2*) 0.15 torr.

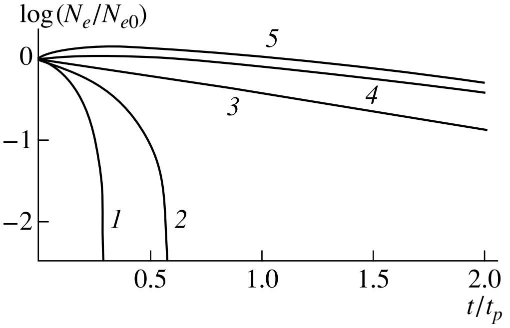

Fig. 6. Dependences $\log(N_e(t)/N_e(0))$ calculated using Eq. (15) for $N_n(0)/N_n(0) = 3$ and different values of $\nu_d t_p$: (*1*) 0, (*2*) 0.5, (*3*) 1, (*4*) 1.5, and (*5*) 2.

tend to increase. This fact is evidence of a possible increase in $N_e(t)$, which has not been observed previously in probe measurements.

A simple independent method for monitoring the ion densities in a decaying plasma is to measure the intensities of spectral lines. For this purpose, the line emission of atomic oxygen at $\lambda = 777$ nm is suitable. The intensity of this line in the afterglow is determined by ion–ion recombination [18] and, hence, is proportional to the product of the ion densities $N_p(t)N_n(t)$. The time dependences of the intensity I_λ measured for the same gas pressure and a current of 200 mA are shown in Fig. 4. For convenience, they are normalized to the ion current at $t = 150$ μs (curve *2*). It is seen that the curves descend exponentially with time, like the probe current of the positive ions i_{ps} (curve *1*). On the one hand, this indicates that the given radiating level is populated due to ion–ion recombination; on the other hand, this makes it possible to independently control the behavior of ions in the afterglow. An exception is a short time interval after the discharge is switched off. During this time interval, the intensity I_λ decreases more rapidly because the electron temperature is still high and the radiating level is more efficiently populated due to electron excitation. The populating rate depends exponentially on T_e; hence, the corresponding part of the I_λ decay curve is related to the rapid initial decrease in the electron temperature. Since this part of the curve does not account for the change in the ion density, it should be excluded from consideration.

The recorded emission of the same spectral lines may also be used to monitor the behavior of $N_e(t)$ in the afterglow. For this purpose, we measured I_λ during a heating pulse with an amplitude such that the population of excited levels was determined by electron-impact excitation. Then, for a fixed field E and, hence, fixed electron temperature T_e, the measured intensities should be proportional to the electron density N_e at every instant during the afterglow. Since the excitation constants depend exponentially on T_e, the measurements should be carried out for the same value of the field E. The relative intensities I_λ normalized for convenience to the electron current at $t = 200$ μs are also shown in Fig. 3. The intensities were measured during a heating pulse of approximately the same amplitude. It is seen that this dependence corresponds well to the change in $N_e(t)$ determined by other methods.

Hence, the measurements of the electron and ion densities carried out by different methods agree well with each other and corroborate the previously observed specific features of the diffusive decay of a plasma of electronegative gases [9]. These features are associated, first of all, with a rather untypical time dependence of the electron density in the afterglow.

The simplest model of the decay of an electronegative gas plasma was presented in [5, 9]. This model allows one to understand the main features of the decay. During the low-pressure afterglow, when the bulk plasmochemical processes can be neglected in comparison with diffusion, we have

$$dN_p/dt = -N_p/t_p \tag{3}$$

and, thus, the positive ion density decays by the exponential law

$$N_p(t) = N_{p0}\exp(-t/t_p). \tag{4}$$

In Eqs. (3) and (4), in the first stage, we can use expression (1) for the characteristic time of ambipolar diffusion of positive ions t_p. A more general expression for the coefficient of ambipolar diffusion of positive ions D_{ap} was derived in [11] under the assumption that the electrons and negative ions in the discharge volume obey the Boltzmann distribution. Neglecting b_p and b_n in comparison with b_e, we obtain from [11]

$$D_{ap} = D_p\frac{1 + K + 2K\alpha}{1 + K\alpha}. \tag{5}$$

Here, $K = T_e/T$ is the ratio of the electron temperatures to the temperature of heavy particles.

It is seen from Eq. (5) that, in the presence of negative ions and for $\alpha > 1$, we have $D_{ap} = 2D_p$ according to expression (1). In the first stage of decay, when T_e is even slightly higher than T [7], i.e., for

$$K - I > 2N_p b_p/(N_e b_e), \tag{6}$$

the N_n flow is directed from the wall into the discharge volume. Negative ions are trapped in the plasma bulk by the ambipolar electric field, and their flux onto the wall is zero. In this case, only the spatial distribution of negative ions changes, while the averaged density of negative ions remains unchanged [7]. Then, it follows from Eq. (4) that the electron density

$$N_e(t) = N_{p0}\exp(-t/t_p) - N_{n0} \tag{7}$$

decreases rapidly in a time of

$$t_0 = t_p \ln(N_{p0}/N_{n0}) \tag{8}$$

and, at $t > t_0$, only positive and negative ions actually remain in the plasma, so that $N_p \sim N_n > N_e$. In this case, the ambipolar potential changes sharply and the negative ions are no longer confined in the plasma. Therefore, the beginning of the second stage is accompanied by a sharp increase in the current of negative ions to the wall [7]. When the electron density N_e decreases so much that the inequality $N_e b_e < N_p b_p + N_n b_n$ is satisfied, the electrons almost instantly (in the regime of free diffusion) escape onto the wall and only positive and negative ions remain in the plasma: $N_p = N_n$. Therefore, in the second stage ($t > t_a$), the plasma decay is governed by ion–ion ambipolar diffusion:

$$N_p = N_n = N_p(t_0)\exp(-t/t_i), \tag{9}$$

where t_i is the characteristic time of ion–ion ambipolar diffusion.

The intensification of N_e decay with time is related to the fact that, in the first stage of decay, the negative ions are trapped in the plasma bulk and their flux onto the wall is zero. Therefore, the equality of fluxes of positive and negative particles onto the wall is caused by the electrons and positive ions; i.e., the relation

$$N_p/t_p \approx N_e/t_e \tag{10}$$

is satisfied.

Since $N_p = N_n + N_e > N_e$, condition (10) requires that the inequality $t_p > t_e$ be satisfied. The lower N_e in comparison with N_n, the faster the electrons escape onto the wall; i.e., the process intensifies continuously. As was mentioned in [9], for high initial electronegativity (i.e., when $\alpha_0 > 1$ and $t_e \ll t_p$), the escape of almost all the electrons from the plasma is accompanied by only a small change in the ion density.

The above model of diffusion decay describes the main features of the observed behavior of the charged particle densities in the afterglow. The density of positive ions decreases exponentially according to Eq. (4), while the electrons, according to Figs. 1–5, escape from the plasma in a time t_0 given by Eq. (8). The model fails only to describe the growth in i_d/E (and, hence, in $N_e(t)$) in the initial stage. Apparently, this growth cannot only be attributed to diffusion processes. On the other hand, as is seen in Fig. 3, the electron current to the probe decreases monotonically, which most likely indicates that the electron density changes in the same way. Thus, it seems expedient to begin by analyzing the possible reasons for increasing N_e in the low-pressure discharge afterglow in electronegative gases before searching for the explanation of the above discrepancy between the experimental data.

Above, when analyzing the decay of a low-pressure, weakly ionized plasma at times $t \lesssim t_0 \lesssim t_p$, we neglected the bulk plasmochemical reactions involving charged particles. Below, we consider their possible influence in detail. Ionization processes have a high energy threshold, and the corresponding constant of these processes k decreases sharply during the afterglow due to rapid electron cooling. Thus, these reactions can be neglected during the afterglow. For the same reason, we can also neglect dissociative attachment (k_a) from the ground state,

$$O_2 + e \longrightarrow O^- + O, \tag{11}$$

which, according to, e.g., [11, 19], determines the production of negative ions in the active phase of a discharge.

Dissociative attachment via highly excited molecule states near the dissociation boundary,

$$O_2^{**} + e \longrightarrow O^- + O, \tag{12}$$

has also recently been discussed in the literature. The importance of this process for the production of negative hydrogen ions in high-current pulsed discharges has already been mentioned in [20]; currently, this process is attractive for interpreting the experimental data on low-pressure, highly ionized oxygen plasma [18, 21]. The constant k_a^{**} of nonthreshold reaction (12) depends weakly on T_e and, hence, changes only slightly after the discharge is switched off. When analyzing the experimental data, it was concluded in [21] that k_a^{**} can even increase sharply as T_e decreases. Our opinion of the conclusions made in [18, 21] was presented in [22]. Here, we only note that the attachment processes, which should lead to a decrease in N_e, do not explicitly manifest themselves in the dependences we observed. Therefore, further on, we will not consider these processes when analyzing the possible reasons for the growth of N_e.

For typical values of the constants of dissociative and ion–ion recombination $k_r \approx 10^{-7}$ cm^3/s [11] and for the densities $N_p \le 10^{10}$ cm^{-3}, the characteristic recombination time is relatively large: $t_r \gg t_p \simeq t_0$; i.e., recombination ion losses can also be neglected at times $t \lesssim t_0$.

Let us consider the detachment processes which lead to an increase in N_e and, accordingly, to a decrease in N_n. These reactions proceed via collisions with atomic oxygen,

$$O^- + O \longrightarrow O_2 + e, \tag{13}$$

and metastable oxygen molecules,

$$O^- + O_2^* \longrightarrow O_2 + O + e. \tag{14}$$

Here, the rate constants are $k_{d1} = 1.9 \times 10^{-10}$ cm^3/s and $k_{d2} = 3 \times 10^{-10}$ cm^3/s, respectively [11]. The densities of the corresponding long-lived states N and N_2^* may change rather slowly with time, while the detachment constants do not depend on T_e. Therefore, the efficiency of processes (13) and (14) may change slightly when passing from the active phase of a discharge to the afterglow. The results of numerical investigations show that the relative concentrations of oxygen atoms and metastable oxygen molecules (N and N_2^*, respectively) in a discharge can attain several percent of the gas density (see, e.g., [11, 19, 23]); i.e., they are fairly high. Correspondingly, under these conditions, the characteristic detachment time can be from tens to hundreds of microseconds, which is comparable with t_0. Therefore, electron detachment influences, first of all, the electron balance during the decay of a weakly ionized plasma. In the above model, assuming for simplicity that the detachment rate is constant, we obtain

$$N_e(t) = N_{p0}\exp(-t/t_p) - N_{n0}\exp(-\nu_d t) \tag{15}$$

instead of Eq. (7).

It is seen that two radically different limiting regimes can be realized. For $\nu_d t_p < 1$ (the sharpening regime), when the production of electrons due to detachment is less efficient than their diffusion loss, the electron density decreases with time. This case is similar to the one considered above, where we neglected all the bulk processes and took into account the diffusion processes only. Hence, the physical reason for a rapid decrease in the electron density with the subsequent formation of an ion–ion plasma is the same for both cases. The only difference is that, because of the additional production of electrons due to detachment, the characteristic detachment time t_{0d} is somewhat longer than t_0 given by Eq. (8):

$$t_{0d} = t_0/(1 - \nu_d t_p). \tag{16}$$

Nevertheless, the electron density decays with an increasing rate and, in a characteristic time t_{0d}, a transition to an ion–ion (electronless) plasma occurs.

In the opposite case ($\nu_d t_p > 1$), detachment plays an important role. This regime should be realized at higher gas pressures, because $\nu_d t_p \sim p^2$. Here, in contrast, the density $N_e(t)$ should first grow monotonically, asymptotically approaching $N_p(t)$ in a characteristic time

$$t_m = (t_p/(1 - \nu_d t_p))\ln(N_{p0}/(\nu_d t_p N_{n0})). \tag{17}$$

Then, in the second stage, when the density of negative ions is relatively low, ordinary electron–ion ambipolar diffusion dominates. This regime can be called the detachment regime. In this case, $N_e(t)$ varies in the opposite manner compared to the purely diffusive decay of an electronegative plasma considered above. The condition $\nu_d t_p = 1$ is, in essence, a bifurcation point which separates the regime of the sharpening of electron escape from the plasma bulk and the regime in which the electron density grows due to detachment up to the density of positive ions. Figure 6 shows the model dependences $N_e(t)$ calculated from Eq. (15) for different values of $\nu_d t_p$. It is seen that, as the parameter $\nu_d t_p$ varies, decay with sharpening ($\nu_d t_p < 1$) passes to the detachment regime ($\nu_d t_p > 1$).

Since detachment can strongly affect the character of the decay of a low-pressure, weakly ionized plasma of electronegative gases, it is desirable to know beforehand whether this phenomenon will take place in a real situation. The simplest way to find out is to analyze the relationship among the fluxes of charged particles in the active phase of a discharge. In a steady-state discharge, the balance of negative ions is governed by attachment and detachment,

$$\nu_a N_{e0} = \nu_d N_{n0}, \tag{18}$$

while the balance of positive ions is governed by ionization and diffusion toward the wall,

$$\nu_i N_{e0} = N_{p0}/t_p. \tag{19}$$

Hence, for $\nu_a > \nu_i$, we have $\nu_d N_{n0} > N_{p0}/t_p$. Then, in the initial stage of decay, when the constants k_a and k_i decrease rapidly, while k_d remains constant, we obtain $\nu_d N_n - N_e/t_e > 0$; i.e., the local growth of $N_e(t)$ should occur. In the opposite case, after switching off the discharge, we will have $dN_e/dt < 0$ and, as was mentioned above, detachment can only slightly decelerate the decrease in the electron density during decay.

Thus, the realization of one or another of the possible decay scenarios depends mainly on the relationship between attachment and ionization (or, correspondingly, ion diffusion) in the active phase of a discharge. The problem of charged particle diffusion in the positive column of a discharge in an electronegative gas was discussed in detail in [24]. According to the classification suggested in [24], the realization of the above regimes is determined by the dimensionless attachment factor α ($\alpha = k_a t_{an}$, where $t_{an} = R^2 T_i/(D_n T_e (2.4)^2)$ is the ambipolar life time of negative ions). For $\alpha > 1$, attachment is more important than ionization, whereas in the opposite case, the ionization rate is close to the usual Schottky regime ($\nu_i t_p \approx 1$) [24]. In practice, a transition from $\alpha < 1$ to $\alpha > 1$ should occur as the gas pressure

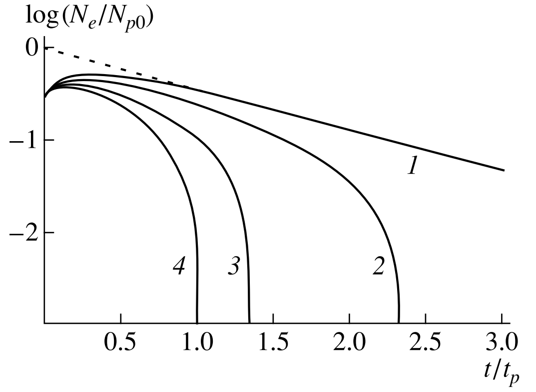

Fig. 7. Solutions to the model problem of decay described by Eqs. (3) and (20) for $N_n(0)/N_p(0) = 0.3$ with an exponentially decreasing detachment rate given by Eq. (21) for different values of $\nu_{d0}t_p = 4\nu^*t_p$: (*1*) 0, (*2*) 2, (*3*) 4, and (*4*) 6. The dashed curve shows the dependence $\log(N_p(t)/N_p(0))$ calculated using Eq. (4).

increases. For tubes of radius $R \sim 1$ cm, this corresponds to a pressure of $p \sim 0.1$–1 torr.

Hence, the realization of one of the two limiting regimes discussed above depends, first of all, on the parameter $\nu_d t_p$. In a real situation, the detachment rate $\nu_d = k_{d1}N + k_{d2}N_2^*$ may decrease with time due to the decrease in the densities of oxygen atoms and metastable oxygen molecules. Therefore, in practice, as t_p varies only slightly, both the above limiting regimes may be observed. In the initial stage of decay, when $\nu_d t_p > 1$, the detachment regime of decay is realized and the electron density increases. Then, as ν_d decreases, diffusion becomes dominating and the decay is completed with a rapid escape of electrons from the plasma bulk. To illustrate this, Fig. 7 shows the solution to the model set of equations consisting of Eq. (3) and the equation

$$dN_e/dt = \nu_d N_n - N_p/t_p, \tag{20}$$

with the detachment rate ν_d decreasing with time by the exponential law

$$\nu_d = \nu_{d0}\exp(-\nu^* t). \tag{21}$$

It is seen that, in this case, the electron density may vary nonmonotonically during the plasma decay. Therefore, the decrease in i_e/E observed in the initial stage of the afterglow (Figs. 3, 5), which reflects the behavior of $N_e(t)$, is, in principal, possible. A monotonic decrease in the probe electron current, which seems to contradict this fact, may be associated with a more rapid decrease in T_e just after switching off the discharge, which masks a weak growth in N_e. Estimates based on the data of [19, 23] show that an intermediate relationship between the attachment and ionization rates is most likely realized in the active phase of a discharge. Taking into account the above and based on the experimental results presented, we cannot definitely assert that the detachment regime of decay discussed above can be realized. Undoubtedly, this interesting phenomenon deserves further detailed experimental investigation.

Thus, in this work the plasma conductivity has been measured using probe diagnostics and by applying a probing current pulse at a certain instant during the afterglow. Spectral line intensities are also measured in order to additionally monitor the charged particle densities. The measurements of the time behavior of the electron density in an oxygen plasma during the afterglow confirm our previous conclusion that the diffusive escape of electrons from the plasma bulk proceeds with an increasing rate and an ion–ion plasma is formed. The possibility of realizing the opposite limiting case, i.e., the detachment regime of decay with the growth of the electron density up to the density of positive ions in the first stage and with a transition to an electron–ion plasma in the second stage, is also shown.

ACKNOWLEDGMENTS

We thank L.D. Tsendin for fruitful discussions. This work was supported by the Russian Foundation for Basic Research (project no. 98-02-17778) and the Ministry of Education of the Russian Federation (grant no. 97-0-5.3-33).

REFERENCES

1. M. V. Hopkins, M. Bakal, and W. G. Graham, J. Appl. Phys. **70**, 2009 (1991).
2. S. Samukawa and H. E. Ohtake, J. Vac. Sci. Technol. A **14**, 3049 (1996).
3. M. A. Lieberman and S. Ashida, Plasma Sources Sci. Technol. **5**, 145 (1996).
4. D. Hayashi and K. Kadota, J. Appl. Phys. **83**, 697 (1998).
5. A. A. Kudryavtsev, Pis'ma Zh. Tekh. Fiz. **22** (17), 11 (1996) [Tech. Phys. Lett. **22**, 693 (1996)].
6. L. D. Tsendin, Zh. Tekh. Fiz. **55** (12), 2318 (1985) [Sov. Phys. Tech. Phys. **30**, 1377 (1985)].
7. A. V. Rozhanskiĭ and L. D. Tsendin, *Collisional Transport in a Partially Ionized Plasma* (Énergoatomizdat, Moscow, 1988).
8. D. Smith, A. G. Dean, and N. G. Adams, J. Phys. D **7**, 1944 (1974).
9. S. A. Gutsev, A. A. Kudryavtsev, and V. A. Romanenko, Zh. Tekh. Fiz. **65** (11), 77 (1995) [Tech. Phys. **40**, 1131 (1995)].
10. *Sharpening Modes. Evolution of Idea. Series Cybernetics*, Ed. by I. M. Makarov (Nauka, Moscow, 1999).
11. H. S. W. Massey, *Negative Ions* (Cambridge Univ. Press, Cambridge, 1976; Mir, Moscow, 1979).
12. V. I. Demidov, N. B. Kolokolov, and A. A. Kudryavtsev, *Probe Methods for Studying Low Temperature Plasmas* (Énergoatomizdat, Moscow, 1996).
13. I. D. Sudit and R. C. Woods, J. Appl. Phys. **76**, 4488 (1994).

14. R. Johnsen, E. V. Shun’ko, and T. Gougousi, Phys. Rev. E **50**, 3994 (1994).
15. E. W. McDaniel, *Collision Phenomena in Ionized Gases* (Wiley, New York, 1964; Mir, Moscow, 1967).
16. G. N. Gerasimov, R. I. Lyagushchenko, and G. P. Startsev, Opt. Spektrosk. **30**, 606 (1971).
17. V. A. Ivanov and Yu. É. Skoblo, Zh. Tekh. Fiz. **51**, 1386 (1981) [Sov. Phys. Tech. Phys. **26**, 796 (1981)].
18. T. Ishikawa, D. Hayashi, K. Sasaki, and K. Kadota, Appl. Phys. Lett. **72**, 2391 (1998).
19. G. Gousset, C. M. Ferreira, M. Pinheiro, *et al.*, J. Phys. D **24**, 290 (1991).
20. V. V. Kuchinskiĭ, V. G. Mishakov, A. S. Tibilov, and A. M. Shukhtin, Opt. Spektrosk. **34**, 1043 (1975).
21. D. Hayashi and K. Kadota, Jpn. J. Appl. Phys. **38**, 225 (1999).
22. A. A. Kudryavtsev and L. D. Tsendin, Pis’ma Zh. Tekh. Fiz. **26** (13), 93 (2000) [Tech. Phys. Lett. **26**, 582 (2000)].
23. V. V. Ivanov, K. S. Klopovskiy, D. V. Lopaev, *et al.*, IEEE Trans. Plasma Sci. **27**, 1279 (1999).
24. L. D. Tsendin, Zh. Tekh. Fiz. **59** (1), 21 (1989) [Sov. Phys. Tech. Phys. **34**, 11 (1989)].

Translated by M. Astrov

Technical Physics, Vol. 46, No. 3, 2001, pp. 307–310. Translated from Zhurnal Tekhnicheskoĭ Fiziki, Vol. 71, No. 3, 2001, pp. 37–40.
Original Russian Text Copyright © 2001 by Poletika, Egorova, Kulikova, Zuev.

SOLIDS

Supersonic Testing of Mechanical Property Uniformity in Hot-rolled Steel

I. M. Poletika, N. M. Egorova, O. A. Kulikova, and L. B. Zuev
Institute of Strength Physics and Materials Science, Siberian Division, Russian Academy of Sciences,
Akademicheskiĭ pr. 2/1, Tomsk, 634021 Russia

Received November 19, 1999; in final form, April 24, 2000

Abstract—Physicomechanical properties of 09G2S hot-rolled steel plates (velocity of ultrasound, hardness, and impact toughness) were found to be nonuniform because of different rates of strain and recrystallization over a plate. The lower the rolling-stop temperature, the higher the nonuniformity. Correlations between these properties are deduced, and the use of velocity of ultrasound as a parameter characterizing mechanical properties is justified. *© 2001 MAIK “Nauka/Interperiodica”.*

INTRODUCTION

The velocity of ultrasound (designated here as V_R) in metals is known to depend on their structure and properties [1–3]. That is why V_R can be used as an information parameter in nondestructive inspection of steel and alloys, for example, at the stage of acceptance control [4–6]. Specifically, it seems appropriate to apply this method to rolled steel. In this case, structure and property uniformity over a plate is often difficult to provide because of its large dimensions, which is sometimes intolerable. Therefore, rolled steel manufacturers and consumers must have express and precision facilities for incoming and outgoing control, respectively. The proper selection of a reliable information parameter and accurate conversion of its value to a desired property for nondestructively testing strength properties of steels become especially topical for application-specific material. In this work, we check the potential of ultrasound velocity as such an information parameter.

EXPERIMENT

Specimens were prepared from 09G2S (0.09% C, 1.32% Mn, 0.64% Si, 0.02% P, 0.027% S, 0.02% Cr, 0.02% Ni, and 0.05% Cu) hot-rolled steel. Their structure and mechanical properties were varied by changing the rolling-stop temperature in a plate mill in a wide range (in the industry, this temperature is actually varied in narrow limits during rolling). The specimens were cut from 10-mm-thick plates and measured $800 \times 150 \times 10$ mm. The rolling-stop temperature T_{ft} was set equal to 830, 880, and 950°C. The impact toughness K_V was determined on *V*-notched specimens according to State Standard 9454-78 at a temperature of –25°C, which falls into the temperature interval of ductile–brittle transition for this steel. For this purpose, a total of 50 specimens were cut from the same plate (the rolling direction was aligned with the long axis). On each of them, the Vickers hardness *HV* and the velocity of ultrasound V_R were measured (30 points per specimen), and the microstructure was examined. The values of V_R were determined with an ISP-12 device [3]. It exploits autocirculation of ultrasound pulses and generates trains of surface acoustic (Rayleigh) waves with a carrier frequency $\nu = 1$ MHz. These waves penetrate into the metal to a depth $\lambda = V_R/\nu \approx 2.5$ mm [1]. This autocirculation device measures the V_R with an accuracy of 0.003–0.005%, as follows from multiple measurements of this parameter [3]. Such a high value is due to the reliable contact between piezoelectric transducers and specimens, which is provided by using a special contact-improving liquid and magnetic clamps. In our case, sufficient measurement statistic also improves the accuracy.

We tried to refine the earlier correlation between impact toughness and hardness, as determined from V_R values [4–6]. Results obtained will form the basis for a nondestructive acoustic technique for determining impact toughness, one of the most important strength properties.

RESULTS AND DISCUSSION

The study of V_R values and mechanical properties of the plates rolled at different T_{ft} showed that, at $T_{\text{ft}} =$ 830°C, the plate steel is inhomogeneous. The hardness, impact toughness, and V_R vary in wide limits within a single plate, namely, $1880 \le HV \le 2160$ MPa, $0.4 \le K_V \le 3.3$ MJ/m^2, and $2877 \le V_R \le 2886$ m/s. Throughout the entire hardness range and in a wide range of impact toughness, a linear correlation between V_R and *HV* and also between V_R and K_V is observed (Figs. 1, 2).

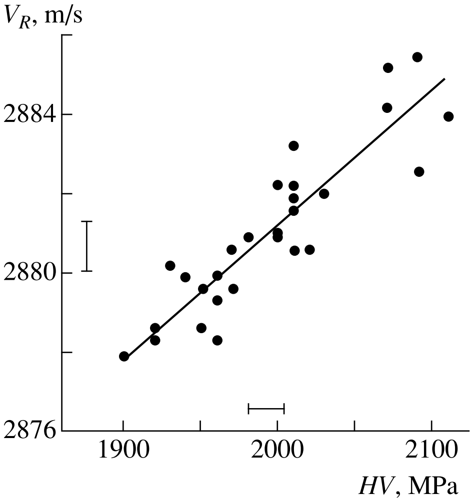

Fig. 1. Correlation between the velocity of ultrasound in 09G2S steel and its hardness at T_{ft} = 830°C.

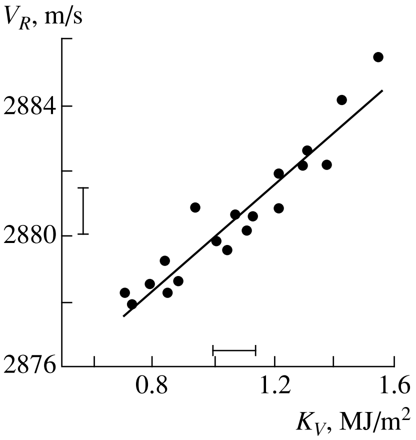

Fig. 2. Correlation between the velocity of ultrasound and impact toughness.

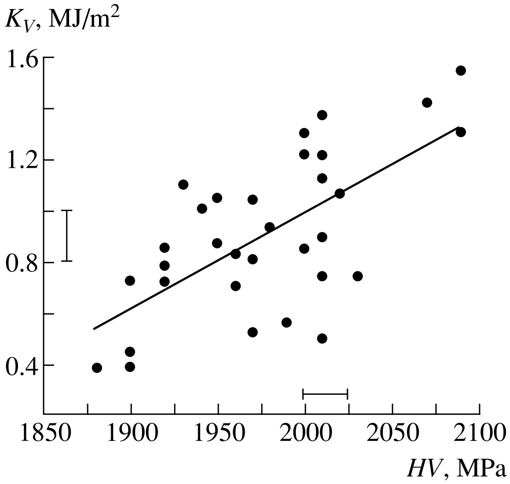

Fig. 3. Correlation between the impact toughness and hardness of 09G2S steel.

Associated correlation relationships obtained by the least-squares method [7] have the form

$$V_R = 3.4 \times 10^{-2} HV + 2813, \qquad (1)$$
$$V_R = 8.0 K_V + 2871. \qquad (2)$$

The coefficients of correlation are relatively high: χ_1 = 0.90 for (1) and χ_2 = 0.94 for (2). The values of K_V and HV are also linearly correlated (Fig. 3):

$$K_V = 3.8 \times 10^{-3} HV - 6.6 \qquad (3)$$

with a coefficient of correlation χ_3 = 0.66.

It is natural to assume that a variation of these parameters over the plate is related to structure modification. To reveal the reasons for V_R, HV, and K_V nonuniformity at T_{ft} = 830°C, we studied the steel structure near the fracture surface. It turned out that the impact toughness and hardness were high at the initial stages of recrystallization (Fig. 4a). It should be noted that, at T_{ft} = 830°C, deformation becomes complete already in the ferritic–pearlitic range. In this case, micrographs show coarse ferrite grains stretched in the direction of rolling and bounded by pearlite grains rolled into stitches. Recrystallization develops in regions adjacent to grain boundaries. Initial ferrite grains split up and become finer (Fig. 4a). In the regions of high K_V and high toughness, the mean pearlite grain size determined with the secant method was ~5 μm (sometimes ≈2.5 μm). Low values of K_V and toughness are observed in regions with the more developed recrystallized structure (Fig. 4b). Here, the stitch arrangement is absent. The mean size of a ferrite grain is ~8 μm.

The structural difference between various regions is due to the fact that the plastic strains in the metal are distributed nonuniformly. Mutually compensating hardening and softening processes (such as recovery, polygonization, and recrystallization) also proceed nonuniformly at low rolling temperatures. According to [8], for any initial strain, there exists a threshold rolling temperature starting from which strain hardening is removed, giving rise to the growth of new recrystallized grains.

To estimate the material nonuniformity, we measured V_R and HV over the plate with a step equal to the size of the supersonic probe (~30 mm) of the ISP-12 device. It was found that regions with high and low V_R and HV alternate in 120–160 mm intervals when the V_R is measured in the rolling direction. In the transverse direction, the effect is weaker: the V_R value varies only slightly relative to the mean value.

An increase in T_{ft} favors both dynamic and static recrystallization of the strained steel; as a result, the nearly equiaxial grain structure forms (Fig. 4c). The structure becomes still more equilibrium when strain hardening is removed during solid-phase recrystallization on cooling. This all reduces the structural nonuniformity. A spread in V_R, HV, and K_V over the plate

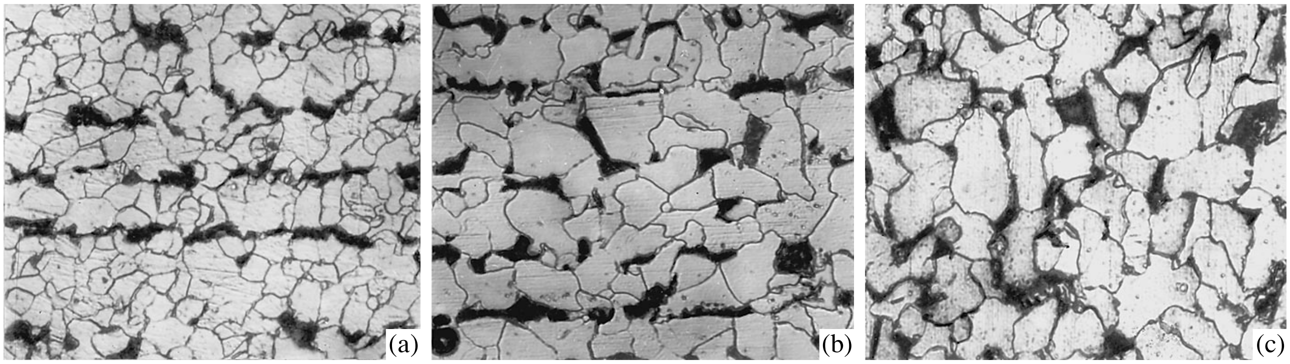

Fig. 4. Microstructure of 09G2S steel. (a) High-K_V area (×800) and (b) low-K_V area (×500) at T_{ft} = 830°C; (c) T_{ft} = 950°C (×500).

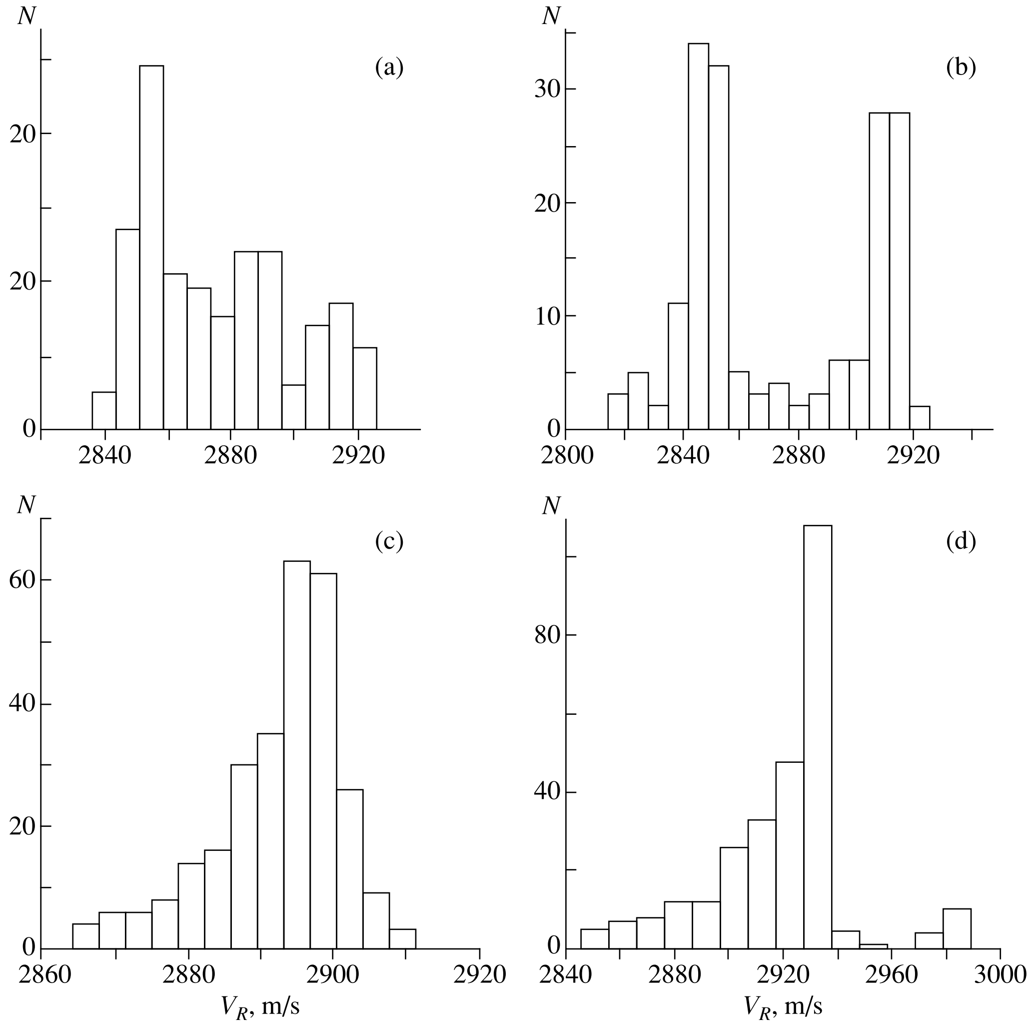

Fig. 5. V_R distribution in steel plates along the rolling direction for T_{ft} = (a) 830°C, (b) 880°C, and (c) 950°C; (d) in the direction transverse to that of rolling at T_{ft} = 830°C.

decreases, and the correlations fail. At T_{ft} = 950°C, the parameters vary in the narrower intervals: $2879 \le V_R \le 2883$ m/s, $1920 \le HV \le 1990$ MPa, and $0.2 \le K_V \le 0.5$ MJ/m^2.

The behavior of K_V and HV at T_{ft} = 830°C is consistent with theoretical and experimental literature data concerning dependences of mechanical properties on the grain size [8]. Effects underlying a change in the velocity of ultrasound may be anisotropy of strained steel properties (in particular, elastic moduli), deformation of ferrite and pearlite grains during rolling, nonuniform distribution of impurities, and unequal density in various areas of the metal.

Of great interest is the distribution of V_R values in the specimens studied. Figure 5 shows these values for steel plates with different T_{ft}'s. As T_{ft} grows, the distribution first becomes bimodal and then unimodal, indicating that the properties become more uniform. Also noteworthy is the simpler V_R distribution in the direction transverse to that of rolling (Fig. 5d), suggesting that the variation of the properties in this direction is less. The steep fall at large V_R's means that this parameter approaches its maximum possible value, which is characteristic of the defect-free material.

CONCLUSION

Qualitatively, linear correlation relationships (1)–(3) can be explained by the fact that all three parameters are dependent on the elastic properties of the metal. In fact [1], $V_R \sim (G/\rho)^{1/2}$, where G is the shear modulus and ρ is the density. At the same time, the shear modulus is related to strain hardening characteristics of metals and alloys [8–11]. An accurate quantitative relationship between the parameters studied has not yet established.

Note that, basically, the impact toughness can nondestructively be estimated using correlation relationship (3), which relates it to the hardness. However, because of the small coefficient of correlation in this case ($\chi_3 = 0.66$), such an estimate appears to be unreliable and is less accurate than that obtained by the acoustic method from (2).

REFERENCES

1. J. Krautkrämer and H. Krautkrämer, *Werkstoffprüfung mit Ultraschall* (Springer-Verlag, Berlin, 1986; Metallurgiya, Moscow, 1991).
2. L. L. Rokhlin, *Acoustical Properties of Light Alloys* (Nauka, Moscow, 1974).
3. V. V. Murav'ev, L. B. Zuev, and K. L. Komarov, *Speed of Sound and Structure of Steels and Alloys* (Nauka, Novosibirsk, 1996).
4. I. M. Poletika, N. M. Pakhilova, L. B. Zuev, and O. A. Kulikova, Fiz. Khim. Obrab. Mater., No. 3, 118 (1997).
5. I. M. Poletika, D. R. Loskutov, N. M. Pakhilova, *et al.*, Stal', No. 3, 63 (1998).
6. L. B. Zuev, I. M. Poletika, B. S. Semukhin, *et al.*, Metalloberflache **53** (9), 324 (1999).
7. A. K. Mitropol'skiĭ, *Technique of Statistical Calculations* (GIFML, Moscow, 1961).
8. M. L. Bernshteĭn, *Structure of Deformed Metals* (Metallurgiya, Moscow, 1977).
9. T. Tokuoka and Yu. Iwashimizu, Int. J. Solids Struct. **4**, 383 (1968).
10. S. Z. Bokshteĭn, *Diffusion and Structure of Metals* (Metallurgiya, Moscow, 1973; Oxonain Press, New Delhi, 1985).
11. *Treatise on Materials Science and Technology*, Vol. 25: *Embrittlement of Engineering Alloys*, Ed. by C. L. Briant and S. K. Banerji (Academic, New York, 1983; Metallurgiya, Moscow, 1988).

Translated by V. Isaakyan

Technical Physics, Vol. 46, No. 3, 2001, pp. 311–315. Translated from Zhurnal Tekhnicheskoĭ Fiziki, Vol. 71, No. 3, 2001, pp. 41–45.
Original Russian Text Copyright © 2001 by Ambrok, Kalashnikov, Kukushkin.

Influence of Selective Heating on the Kinetics of the Late Stage of First-Order Phase Transitions

A. G. Ambrok, E. V. Kalashnikov, S. A. Kukushkin
Institute of Mechanical Engineering, Russian Academy of Sciences, St. Petersburg, 199178 Russia
e-mail: ambrok@ipme.ru, kev@ipme.ru, ksa@math.ipme.ru

Received June 8, 2000

Abstract—The effect of radiation on the kinetics of the late stage of first-order phase transitions (Ostvald ripening) was studied. In particular, features of the growth kinetics of nuclei were revealed in relation to their size and time of exposure to radiation. Possible approaches to controlling the nucleus growth kinetics were shown.

INTRODUCTION

By now, theoretical approaches to the study of first-order phase transition kinetics are fairly well developed. A comprehensive analysis was carried out in [1, 2]. It is known that the overall process of a first-order phase transition can be broken down into the following stages: nucleation; the growth of separate nuclei; and coalescence into the late stage, that is, Ostvald ripening, at which the growth of larger nuclei proceeds through dissolution of the smaller ones. At the stage of Ostvald ripening, the structure of the new phase is formed, which is why it is best to control the growth process at this stage. The control of structure and composition is mainly achieved by choosing the temperature regime and by varying the power of the component sources [3]. The needs of modern technologies demand both selective actions on the separate components and the creation of a particular spatial distribution of the components. Such growth conditions can be obtained by using the local or selective action of external fields.

Selectivity can be realized in conditions of condensation and film growth from the gas phase, as well as in conditions of the decomposition of a supersaturated uniform solid solution under the influence of radiation. In this case, the absorption coefficients of the newly formed phase differ significantly from the coefficients of the initial one.

The present study is concerned with a particular case, namely, with the effect of selective heating (radiation) on the kinetics of the late stage of first-order phase transitions (Ostvald ripening). The distinctive feature of Ostvald ripening is that the system is a statistical ensemble of growing nuclei of the new phase, which interact with each other and the environment through the thermal and diffusion fields. Selective heating in this case results in the possibility of affecting nucleus growth kinetics by heating of the discrete particles of the ensemble.

The behavior of an individual particle under different thermal conditions has been studied fairly extensively [4–8]. Formally, the description of such behavior can be divided into two groups of problems. The first group considers heating (cooling) of an individual particle without movement of the surface confining it. The second group involves problems which take into account interface movement, but within the limits of the semi-infinite model.

In terms of the ensemble, it is necessary to take into account the interconsistent particle behavior, where some particles can grow via dissolution of the others. This problem was solved in [9] by consideration of the particle in some general thermal field. However, the problem of the behavior of the growing particle ensemble under the action of an external selective heat source has not yet been solved. The subject of this study is the evolution of the ensemble of growing particles of the new phase under the action of an external selective heat source.

STATEMENT OF THE PROBLEM AND MAIN EQUATIONS

Consider an ensemble of new phase nuclei incorporated into a transparent film (matrix). The nuclei of the new phase can be either single-component or can consist of different chemical components or compounds. Both heat and mass transfer control the growth process of the nuclei. Therefore, in the general case it is necessary to solve the heat and diffusion problems simultaneously. However, in accordance with [3], the process of Ostvald ripening can be separated into “heat” and “concentration” ripening. In this study, we will restrict our consideration to heat ripening. This approximation is justified by the existence of the large difference in the transfer coefficients, namely, between the thermal diffusivity and diffusion coefficients (several orders of magnitude).

Let radiation with wavelength λ be incident on the surface of the system. Assume that $\lambda > 10^{-4}$ cm is considerably larger than the size of the nuclei; therefore, we ignore the Rayleigh scattering and the dependence of the optical properties (reflection and absorption coefficients) on the wavelength.

According to [8] the main equations which describe the kinetics of Ostvald ripening of the new phase nuclei have the following form:

$$\frac{\partial f(R,t)}{\partial t} + \frac{\partial}{\partial R}\left[f(R,t)\frac{dR}{dt}\right] = 0, \tag{1}$$

$$Q_0 = Q(t) + \frac{4\pi}{3}\frac{L}{\omega}\int_0^\infty f(R,t)R^3 dR, \tag{2}$$

where $f(R, t)$ is the distribution function of nuclei over their sizes R, t is time, L is the latent heat of the phase transition, ω is the volume occupied by an atom in the nucleus, Q_0 is the difference between the quantities of heat at T_K and T at the start of Ostvald ripening, $Q(t)$ is the difference between the quantities of heat at T_K and T at the instant t, T_K is the equilibrium temperature of melting, and T is the current temperature.

In order to solve the system of equations (1) and (2), it is necessary to know the growth rate of the new phase core (dR/dt). This value can be obtained by solving the Stephan problem [4, 5],

$$\frac{k_1}{r^2}\left[\frac{\partial}{\partial r}\left(r^2\frac{\partial T_1}{\partial r}\right)\right] + F = \frac{\partial T_1}{\partial t}, \tag{3a}$$

$$\frac{k_2}{r^2}\left[\frac{\partial}{\partial r}\left(r^2\frac{\partial T_2}{\partial r}\right)\right] = \frac{\partial T_2}{\partial t}, \tag{3b}$$

where Eqs. (3a) and (3b) describe the temperature distribution in the nucleus and in the matrix, respectively.

Equations (4) and (5) are the boundary conditions which must be fulfilled at the nucleus boundary:

$$-K_1\frac{\partial T_1}{\partial r} + K_2\frac{\partial T_2}{\partial r} = \frac{L}{\omega}\frac{dR}{dt}, \tag{4}$$

$$T_1|_{r=R} = T_2|_{r=R} = T_R, \tag{5}$$

where k_i is the thermal diffusivity coefficient; F is the density of the incoming radiation; T_i is temperature; K_i is the heat conductivity coefficient; the lower indices 1, 2 in Eqs. (3)–(5) and below refer the value to the particle and environment, respectively; and T_R is the temperature at the nucleus boundary.

Solving the Stephan problem presents considerable difficulties related to the need to account for the movement of the boundary of the new phase nucleus. Within the limits of the set problem, the external source affects the growing nuclei, which incorporates further difficulties. Nevertheless, it can be simplified by taking into account the finite time of action of the radiation on the nucleus in comparison with the characteristic times of establishing the temperature in the particle and in its environment.

HEAT PROBLEM FOR A SINGLE PARTICLE

The heat problem of nucleus growth can be divided into asymptotic cases, which enable one to obtain reasonable analytic expressions for the velocities of the interface movement and to group them with the equations of the nuclei growth kinetics. For the subsequent analysis we will carry out asymptotic estimations of the heat problem for the new phase nucleus. These estimations are based on separation of the characteristic times τ_j, which would be correlated with the duration of the external heating pulse τ_i. The first of these times, τ_1, is related to the linear size (R) of the particles and, particularly, to the time of establishment of the steady-state temperature in the whole particle:

$$\tau_1 = R^2/4k. \tag{6}$$

The second characteristic time τ_2 is determined by the same relationship but is related to the time in which the steady-state temperature is established around a selected particle in the matrix. Here, k_i is the thermal diffusivity coefficient, $j = 1$ for the particle, and $j = 2$ for the matrix. The nuclear size R at the late stage is varied from 10^{-7} to 10^{-4} cm. For metallic incorporation, $k \sim 0.3$ cm^2/s and for a nonconducting medium, $k \sim 3 \times 10^{-3}$ cm^2/s. Since at the late stage of growth, supercooling Δ is small, $\Delta/\Delta_0 \ll 1$, the quasi-equilibrium heat conductivity equation can be used (Δ_0 is the supercooling at the start of OR). The small ratio τ_2/τ_f (where τ_f is the characteristic time of phase transformation, $\tau_f \sim L\rho R^2/K\Delta$, L is the heat of phase transformation, ρ is the density, and K is the heat conductivity coefficient) allows use of the condition of quasi-equilibrium at the particle surface [3]. For the particular value of the pulse duration $\tau_i = 10^{-9}$ s, the boundary value of the particle radius is $R_B = 3.5 \times 10^{-6}$ cm. As an example, the characteristic times τ_1 and τ_2 and corresponding particle radii R are presented in the table.

R, cm	τ_1, s	τ_2, s	τ_f, s
1×10^{-7}	8×10^{-15}	8×10^{-13}	5×10^{-9}
5×10^{-5}	2×10^{-9}	2×10^{-7}	1×10^{-3}

Based on these estimations, three variants (A, B, C) of the relationship between the pulse duration τ_i and characteristic time τ_j can be separated out. In accordance with these variants, we will obtain different boundary conditions for the temperature of the particles, which will enable us to obtain the velocity of the interface movement for each of these variants.

(A) The pulse duration τ_i is far less than the characteristic time τ_2 (see table, second line). In this case, we can ignore the particle heat exchange with the matrix. This results in a spatially uniform temperature distribution in the particle, and from the system of equations (3), only the equation for the particle remains, which assumes the form

$$\rho C\frac{dT}{dt} = (1-\varepsilon)IS_n, \tag{7}$$

where ε is the reflection coefficient; C is the heat capacity; I is the radiation intensity; and S_n is the absorption cross-section area, which is equal to $S_n = \pi R^2$.

Then the expression for the particle temperature has the form

$$T_n = T_m + \frac{\beta_1}{R}, \quad \beta_1 = \frac{3}{4}\frac{I(1-\varepsilon)\tau_I}{C_V}, \tag{8}$$

where C_V is the heat capacity per unit volume and R is the radius of the particle.

(B) The pulse duration τ_i exceeds the characteristic time τ_2 (see table, first line). The time in which the particle temperature enters the steady-state regime thus appears to be far less than the duration of the pulse action. In this case, Eqs. (3), with regard to the boundary conditions (4), transform to the balance equation

$$\rho C\frac{dT}{dt} = (1-\varepsilon)IS_n + KS_\sigma\frac{dT_m}{dr}, \tag{9}$$

where S_σ is the area of the entire particle surface.

The value dT_m/dr can be obtained by solving the steady-state heat-conduction equation

$$\left.\frac{dT_m}{dr}\right|_{r=R} = -\frac{T_n - T_m}{R}.$$

Thus, the particle temperature can be expressed in the form

$$T_n = T_m + \beta_2 R, \quad \beta_2 = \frac{I(1-\varepsilon)}{4K}. \tag{10}$$

(C) Unlike the first two variants, in which the external energy is absorbed by the particle surface, in this variant, absorption by the entire particle volume occurs. This is possible if the skin-layer thickness is comparable with the size of the particle (this variant refers to the first line of the table). Then the heat balance equations for the particular particle temperature assume the following form:

$$\rho C\frac{dT}{dt} = \alpha IV_n + KS_\sigma\frac{dT_m}{dr}, \tag{11}$$

and the particle temperature takes the form

$$T_n = T_m + \beta_3 R^2, \quad \beta_3 = \frac{aI(1-\varepsilon)}{3K}, \tag{12}$$

where $a = 10^{16}$ cm^{-1} is the absorption coefficient.

In order to study the evolution of the ensemble of new phase nuclei, it is necessary to determine the growth rate of a separate nucleus in accordance with Eqs. (1) and (2).

GROWTH RATE OF THE NEW PHASE NUCLEUS

Equations (8), (10), and (12) enable the velocity of the interface movement to be obtained for each of the listed cases using Eq. (4). Let us present the expressions for the dispersed particle growth rate without regard for the action of the radiation. We ignore the boundary kinetics, and hence, the limiting process is the heat conductivity.

The equilibrium temperature near the surface of a new phase nucleus of radius R is determined by relationship [3], which is evident from the Gibbs–Thomson equation

$$T_R = T_K - \frac{\alpha}{R}, \quad \alpha = \frac{2\sigma T_K\omega}{L}, \tag{13}$$

where T_R is the temperature at the interface, T_K is the temperature of the phase transition, ω is the volume per particle, σ is the interphase energy, and the supercooling will be determined as $\Delta = T_K - T$ (T is the current temperature).

The equation for the growth rate and the equation for the critical radius determined by the condition $dR/dt = 0$ will have the form

$$\frac{dR}{dt} = \frac{K\omega}{LR}\left(\Delta - \frac{\alpha}{R}\right), \quad R_K = \frac{\alpha}{\Delta}, \tag{14}$$

where R_K is the critical radius of the nucleus of the new phase: if $R < R_K$, then the nucleus melts; if $R > R_K$, it grows.

Now consider the effect of radiation. The boundary conditions (temperature at the grain boundary), growth rate, and critical radius for different variants are determined as

variant A

$$\begin{gathered} T_{r=R} = T_K - \frac{\alpha}{R} + \frac{\beta_1}{R}, \\ \frac{dR}{dt} = \frac{K\omega}{LR}\left(\Delta - \frac{\alpha - \beta_1}{R}\right), \quad R_{K1} = \frac{\alpha - \beta_1}{\Delta}; \end{gathered} \tag{15}$$

variant B

$$\begin{gathered} T_{r=R} = T_K - \frac{\alpha}{R} + \beta_2 R, \quad \frac{dR}{dt} = \frac{K\omega}{LR}\left(\Delta - \frac{\alpha - \beta_2 R^2}{R}\right), \\ R_{K2} = \left(\sqrt{\frac{\Delta^2}{4\beta} + \frac{\alpha}{\beta}} - \frac{\Delta}{2\beta}\right); \end{gathered} \tag{16}$$

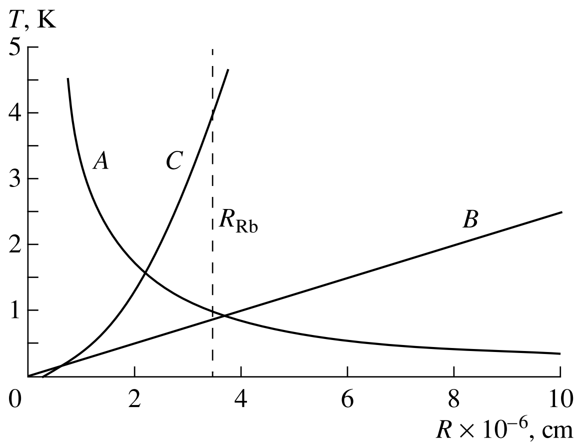

The dependence of the temperature of the nucleus on its radius. R_B—the boundary radius value, *A*–*C*—different variants.

variant *C*

$$T_{r=R} = T_K - \frac{\alpha}{R} + \beta_3 R^2,$$

$$\frac{dR}{dt} = \frac{K\omega}{LR}\left(\Delta - \frac{\alpha - \beta_3 R^3}{R}\right), \quad R_{K3} = \nu + u,$$

$$\nu = \sqrt[3]{\frac{\alpha}{2\beta_3} + \frac{\sqrt{3}}{18\beta_3}\sqrt{\frac{4\Delta^3 + 27\alpha^2\beta_3}{\beta_3}}}; \tag{17}$$

$$u = \sqrt[3]{\frac{\alpha}{2\beta_3} - \frac{\sqrt{3}}{18\beta_3}\sqrt{\frac{4\Delta^3 + 27\alpha^2\beta_3}{\beta_3}}}.$$

Relationships (15)–(17) show the different character of the dependencies of the critical radius R_{K1} on supercooling, of the temperature $T_{r=R}$ at the nucleus boundary on the radius, and of the nucleus growth rate on supercooling and radius. Thus, in variant *A*, $T_R \sim R^{-1}$ and $R_K \sim \Delta^{-1}$ as for the case of the absence of the external heat source (13), (14), respectively. In variants *B* and *C*, these dependences are very different.

Determining the nucleus growth rate we turn to consideration of the ensemble kinetics under the action of radiation.

ENSEMBLE OF DISPERSED PARTICLES

In order to describe the evolution of the ensemble of dispersed particles in accordance with [10], it is necessary to change to the normalized "canonical" coordinates both in the equation for the growth rate and in Eqs. (1) and (2). Then the expression for the growth rate without radiation transforms into the following equations:

$$\frac{dU^3}{d\tau} = \gamma(U-1) - U^3,$$

where

$$\gamma = \frac{Bdt}{x^2dx}, \quad B = \frac{K\alpha\omega}{R_{K0}^3 L}, \quad U = \frac{R}{R_K}, \tag{18}$$

$$\tau = \ln x^3, \quad x = \frac{R_K}{R_{K0}},$$

where R_{K0} is the critical radius at the beginning of Ostvald ripening.

Considering the radiation in the normalized coordinates for variant *A*, the expression for the growth rate has the same form as without radiation. However, the values of critical radius R_{K1} and γ_1 will differ from the analogous values in Eqs. (13) and (17):

$$\gamma_1 = \frac{B_1dt}{x^2dx}, \quad B_1 = \frac{K\alpha\omega}{R_{K10}^3 L}\left(1 - \frac{\beta_1}{\alpha}\right). \tag{19}$$

The general form of the distribution function in the zeroth hydrodynamic approximation for nuclei with $R > R_B$ remains intact. However, the formation rate of the distribution function will depend on the intensity, since the value γ_1 determines the formation rate of the general distribution function.

For variants *B* and *C*, the situation will be very different. As can be seen from the expression for the critical radius (16), (17), it is directly proportional to the supercooling. As Δ tends to zero the critical radius will decrease faster than Δ and approach a certain limiting value $(\alpha/\beta)^{1/2}$, on the condition that $\beta > \alpha R_{K2} \longrightarrow 0$. As a result, we find that, on the release of supercooling, the critical radius decreases and the entire ensemble of particles dissolves. For the third variant, the situation is only intensified.

Thus, as the radiation is absorbed in the first variant *A*, in which the pulse duration is far less than the characteristic time (τ_2) for the matrix, the critical radius shifts to lower values and the nuclear growth rate decreases. Along with this, as the condition $\alpha > \beta_1$ is fulfilled, Ostvald ripening occurs. In variants *B* and *C*, the Ostvald ripening process does not occur.

These results are in accordance with qualitative physical reasoning. Indeed, in variant *A*, the small particles will dissolve much faster and the process of Ostvald ripening is possible, although it will proceed with some slowing. For variants *B* and *C*, the particles with the larger radius will be considerably more strongly heated and correspondingly dissolve faster (curves *B* and *C* in figure).

DISCUSSION

In this paper, the effect of an external selective heat source on the process of Ostvald ripening of the new phase nucleus ensemble is considered. The assignment of the characteristic times determined by the physical properties of the substances and their correlation with the duration of the external action allows different variants of heating of discrete particles to be revealed. Such an assignment of different variants at once reveals the kinetics of nucleus growth (their growth rate) and the evolution of the particle ensemble on selective heating in the heat-ripening approximation. An essential feature is the pulsed character of the action of radiation on the new phase formation. Continuous action of radiation results in the slowdown of the growth process of the nuclei and in subsequent total homogenization of the system.

On the basis of optical and thermal properties of the nuclei and medium it is necessary to choose certain values of the pulse intensity and duration. In the figure, the dependences of the particle temperature on its radius are presented. For the corresponding choice of these values for the nuclei with $R > R_B$, the Ostvald ripening process will proceed and the particles with $R < R_B$ will dissolve and supply material for the "large" nuclei. R_B is determined from relationship (7). Thus, in a system in the Ostvald ripening process a distinctive size selection can be achieved.

An important feature of the analysis is the identification of the peculiarities of ensemble evolution under the action of external pulsed selective heating. The change in evolution is expressed in an explicit dependence on the incoming radiation intensity of the value γ (19) that appears in Eq. (18) for the growth rate in normalized coordinates. Such action reduces to the direct dependence of the rate of the distribution function variation [10] on the intensity of action.

The performed analysis and the obtained relationships and estimations are the starting base for future study of multicomponent systems. Naturally, the expressions for the influence of radiation remain valid for diffusion Ostvald ripening as well and assume great importance in multicomponent systems. This approach allows the growth kinetics of one or another component to be affected selectively in complex chemical systems in accordance with their optical and thermal properties.

ACKNOWLEDGMENTS

This study was partly supported by the Russian Foundation for Basic Research (grant nos. 98-03-32791, 99–03–32768), by the Russian Federal Center "Integration" (grant no. A0151), and by the NATO program "Science for Peace" (Stp 973252).

REFERENCES

1. S. A. Kukushkin and A. V. Osipov, Khim. Fiz. **15** (9), 5 (1996).
2. S. A. Kukushkin and A. V. Osipov, Usp. Fiz. Nauk **168**, 1083 (1998) [Phys. Usp. **41**, 983 (1998)].
3. S. A. Kukushkin and V. V. Slezov, *Disperse Systems on Solid Surfaces* (Nauka, St. Petersburg, 1996).
4. H. S. Carslaw and J. C. Jaeger, *Conduction of Heat in Solids* (Clarendon, Oxford, 1959; Nauka, Moscow, 1964).
5. A. V. Lykov, *Theory of Heat Conduction* (Vysshaya Shkola, Moscow, 1967).
6. B. Ya. Lyubov, *Theory of Crystallization in Large Volumes* (Nauka, Moscow, 1975).
7. R. W. Hopper and D. R. Uhlmann, J. Appl. Phys. **41**, 4023 (1970).
8. Yu. Kaganovskii and M. Rosenbluh, Appl. Phys. Lett. **69**, 3297 (1996).
9. S. A. Kukushkin, Fiz. Tverd. Tela (Leningrad) **27**, 2987 (1985) [Sov. Phys. Solid State **27**, 1794 (1985)].
10. I. M. Lifshits and V. V. Slezov, Zh. Éksp. Teor. Fiz. **35**, 479 (1958) [Sov. Phys. JETP **8**, 331 (1958)].

Translated by M. Lebedev

Technical Physics, Vol. 46, No. 3, 2001, pp. 316–321. Translated from Zhurnal Tekhnicheskoĭ Fiziki, Vol. 71, No. 3, 2001, pp. 46–51.
Original Russian Text Copyright © 2001 by Levin, Bormontov, Volkov, Ostroukhov, Tatarintsev.

OPTICS, QUANTUM ELECTRONICS

Charge Distribution in a MIS Insulator from Spectral Characteristics of Photoemission Current

M. N. Levin, E. N. Bormontov, O. V. Volkov, S. S. Ostroukhov, and A. V. Tatarintsev
Voronezh State University, Universitetskaya pl. 1, Voronezh, 394693 Russia
e-mail: levin@lev.vsu.ru

Received June 7, 1999; in final form, March 21, 2000

Abstract—The field dependence of photoemission currents in a MIS structure was derived for the case when the space charge is randomly distributed over the insulating layer. It was found analytically that the position of the top of the potential barrier for electrons photoinjected from the gate into the insulator is defined by the derivative of this barrier with respect to the external field strength. A method for correctly determining the space charge profile in a MIS insulator is suggested. The profile is derived from a family of spectral characteristics taken at different gate voltages. The method is especially suitable for profiling the negative charge in MIS insulators. © *2001 MAIK "Nauka/Interperiodica".*

INTRODUCTION

It has long been known that photoemission current (PEC) induced by UV radiation in MIS structures is highly sensitive to the charge localized in the insulator. This opens unique possibilities for studying the space distribution of this charge [1, 2]. However, they have not been fully exploited thus far, so that the development of reliable photoemission methods for space charge profiling in MIS insulators remains topical.

The method for space charge profiling in the insulator of a MIS structure using the field dependences of PET was first suggested by Powell and Berglund [3]. In this method, the charge distribution is studied at the emitting boundary and the area of the insulator is taken such that a change in the potential barrier for carriers emitted by the action of an external field can be detected. The basic disadvantage of the method, which calls into question its reliability, is that the effect of the charge being studied on the scattering of photoemitted electrons by the counter field of the barrier is ignored. It is carrier scattering that defines the dependence of PEC on the barrier position [4]. The use of a phenomenological parameter previously found for an electrically neutral insulator is inappropriate, and the determination of this parameter for an insulator with an unknown (desired) charge distribution from field dependences of PEC is impossible.

If the density of the positive charge is high, its field shifts the potential barrier of photoemitted electrons so close to the emitter that carrier scattering by the counter field can be neglected for any gate voltage. In this case, the field dependence of PEC is defined by the field dependence of the potential barrier, and the charge distribution parameters can be found for specific cases provided that a functional form of the distribution is specified. In [5], the field dependence of PEC in a MIS structure was analyzed in the case when the insulator regions adjacent to the semiconductor and the gate are uniformly charged. A method for determining the thickness of the charged layers and the charge density from the current–voltage characteristic of PEC was suggested.

Unlike field dependences of PEC, its spectral characteristics, i.e., PEC vs. UV photon energy curves recorded at a fixed external field, can discriminate between the effects the barrier height and the barrier peak position have on PEC. Techniques for the correct determination of the barrier height at the semiconductor–insulator interface from spectral characteristics of PEC have been elaborated. They exclude the influence of UV radiation interference in thin-film MIS structures on the intensity absorbed in the emitter [6, 7].

In this paper, we describe a procedure for finding the space distribution of the density of charge randomly occupying the MIS insulator. The desired distribution is obtained from field dependences of the barrier height that, in turn, are derived from PEC spectral curves recorded at different gate voltages.

THEORY

The essence of our procedure is as follows. The potential barrier height for photoemitted carriers is the sum of the image force potential, the potential of an external field, and that of the charge under study. The distributions of the first two across the insulator are known. The barrier height vs. field relationship can be derived from a family of PEC spectral curves. Therefore, if the field dependence of the barrier peak position is determined, one can find the coordinate dependence of the barrier height and hence, the distribution of the inner field potential across the insulator. From the inner field potential distribution thus obtained, the desired charge distribution in the insulator can be found.

The barrier height $\Delta\Phi$ and the coordinate of its peak x_0 directly enter into the well-known phenomenological expression for PEC spectral dependence [1, 2]:

$$I(h\nu) = A(h\nu - \Delta\Phi)^p \exp\left(-\frac{x_0}{l}\right), \tag{1}$$

where $h\nu$ is the UV photon energy. The parameters A, p, and l, appearing in Eq. (1) depend, respectively, on the absorbed radiation intensity in the emitter, mechanisms of carrier optical excitation in the emitter, and mechanisms of emitted carrier scattering in the counter field of the barrier.

The electrostatic field of the charge in the insulator is found by solving Poisson's equation

$$\frac{\partial^2\varphi(x)}{\partial^2 x} = -a\rho(x) \tag{2}$$

with the boundary conditions $\varphi(0) = 0$, $\varphi(d) = V_g$. Here, $\rho(x)$ and $\varphi(x)$ are the distributions of the charge and the potential across the insulator, respectively; $a \equiv q/(\varepsilon_0\varepsilon_{0x})$; ε_0 is the permittivity; ε_{0x} is the low-frequency relative permittivity of the insulator; d is the insulator thickness; V_g is the gate voltage; and q is the charge of an electron. The potential φ is reckoned from the conduction band bottom of the electrically neutral insulator for the unbiased gate. The distance x is measured from the emitting boundary.

The distributions of the space charge field and potential in the insulator that are found from Eq. (2) with the given boundary conditions and with image forces from the emitter side taken into account are given by

$$\begin{aligned} E(x) = {} & \frac{b}{2x^2} - \frac{V}{d} - a\int_0^d \rho(x)dx \\ & + \frac{a}{d}\int_0^d x\rho(x)dx + a\int_0^x \rho(x)dx, \end{aligned} \tag{3}$$

$$\begin{aligned} \varphi(x) = {} & \frac{b}{2x} + \frac{V}{d}x + ax\int_0^d \rho(x)dx - \frac{a}{d}x\int_0^d x\rho(x)dx \\ & + a\int_0^x x\rho(x)dx - ax\int_0^x \rho(x)dx, \end{aligned} \tag{4}$$

where $b \equiv q/(8\pi\varepsilon_0\varepsilon_i)$, ε_i is the optical permittivity of the insulator, $V = V_g - \varphi_s$ is the voltage drop across the insulator, and φ_s is the surface potential of the semiconductor.

Equations (3) and (4) allow the determination of the barrier height for emitted electrons in the presence of the space charge in the insulator:

$$\Delta\Phi = \Phi_0 - \frac{b}{x_0} - a\int_0^{x_0} x\rho(x)dx, \tag{5}$$

where Φ_0 is the barrier height in the electrically neutral insulator for the unbiased gate.

The condition that the field is zero at the potential extremum, $E(x_0) = 0$, yields the equation that relates the external field strength in the insulator $E_{ex} = -(V/d)$ to the coordinate x_0 of the barrier peak:

$$E_{ex} = \frac{b}{2x_0^2} + a\int_0^{x_0} \rho(x)dx - \frac{a}{d}\int_0^d (d-x)\rho(x)dx. \tag{6}$$

From Eqs. (5) and (6), the derivative of the $\Delta\Phi$ with respect to x_0 and the derivative of x_0 with respect to E_{ex} can be represented as

$$\frac{\partial(\Delta\Phi)}{\partial x_0} = x_0(bx_0^{-3} - a\rho(x_0)), \tag{7a}$$

$$\frac{\partial x_0}{\partial E} = (bx_0^{-3} - a\rho(x_0))^{-1}. \tag{7b}$$

From these relationships, one can derive the field dependence of the barrier extremum coordinate,

$$x_0 = \frac{\partial(\Delta\Phi)}{\partial E_{ex}} \tag{8}$$

and find the space charge density distribution within the area where a change in the barrier peak position is detected:

$$\rho(x_0) = \frac{1}{a}\left(bx_0^{-3} - \left(\frac{\partial x_0}{\partial E_{ex}}\right)^{-1}\right). \tag{9}$$

Thus, the space charge density distribution across a MIS insulator can be determined from a family of spectral curves for steady-state PEC that are taken at different E_{ex}. From experimental PEC spectral curves, one constructs the $\Delta\Phi(E_{ex})$ curve, then differentiates this function with respect to E_{ex} to obtain the extremum coordinate x_0 vs. E_{ex} dependence, and finally, using the $x_0(E_{ex})$ relationship, calculates the distribution $\rho(x)$ with Eq. (9).

The charge density profile $\rho(x)$ can be found in the interval from $x_0^{\min}$ to $x_0^{\max}$. The former coordinate corresponds to the maximal external field strength $E_{ex}^{\max}$; that is, the lower limit of the ($x_0^{\min}$, $x_0^{\max}$) interval is dictated by the electric strength of the insulating film. The upper limit $x_0^{\max}$ is specified by the minimal field

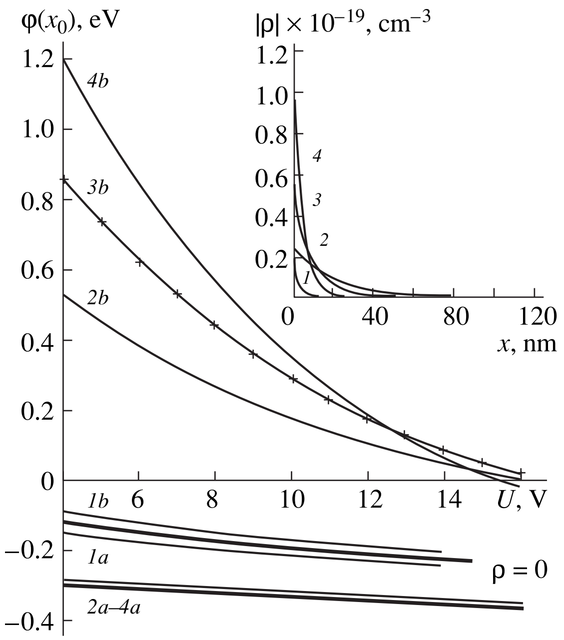

Fig. 1. Field dependences of the potential barrier height $\varphi(x_0) = \Phi_0 - \Delta\Phi$ for photoemitted electrons. The insulator is charged *1a*–*4a* positively and *1b*–*4b* negatively. In the insert, $\rho(x) = \rho_0\exp(-kx/d)$ with $|\rho_0|$ and k are, respectively, (*1*) 1×10^{18} and 2, (*2*) 2×10^{18} and 5, (*3*) 5×10^{18} and 10, and (*4*) 1×10^{19} cm^{-3} and 20.

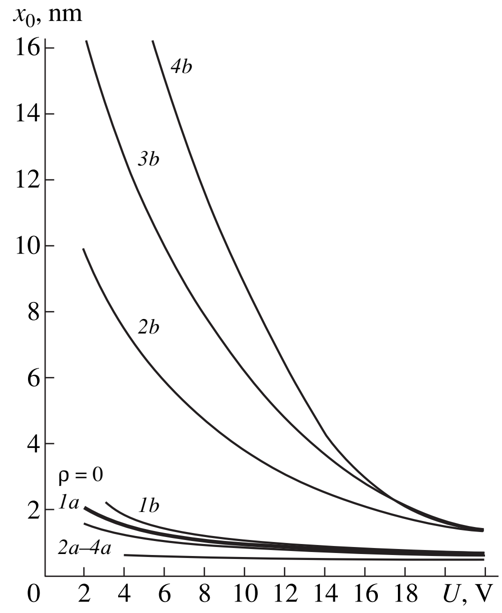

Fig. 2. Field dependences of the barrier peak position x_0. *1a*–*4a* and *1b*–*4b* are the same as in Fig. 1.

strength at which the steady-state PEC can be measured.

In this method of studying the space charge distribution, preliminary determination of the phenomenological parameter l, which accounts for carrier scattering up to the barrier peak, is unnecessary. Moreover, a family of PEC spectral curves taken at various values of E_{ex} can be used for determining the free path l of photoinjected carriers in an insulator with randomly distributed localized charge. Indeed, from Eq. (1), we have

$$l = -x_0(p\ln(A^{-1/p}\tan(\alpha)))^{-1}, \qquad (10)$$

where α is the slope of the PEC spectral characteristic in the $\sqrt[p]{I} - h\nu$ coordinates. The parameter A is found from the slope of the spectral characteristic at the maximal external field strength [in this case, $\exp(-x_0/l) \approx 1$; and the coordinate $x_0(E_{ex})$, from Eq. (8).

The potentialities of the method were estimated by numerically calculating field dependences of the height and peak position of the barrier for different charge distributions (Fig. 1) in the insulator of a MIS structure. Corresponding field dependences of the height of the barrier and the coordinate of its extremum are represented in Fig. 2. The results indicate that the method is especially efficient if the insulator is negatively charged. The potential profiles (Fig. 3) imply that the barrier is highly sensitive to the presence of a negative charge and varies only slightly when the charge is positive. A negative charge considerably extends the insulator area where the charge distribution can be determined, while a positive charge shifts the barrier toward the emitting boundary and almost fixes its position.

EXPERIMENT

Experiments were carried out on Au–SiO$_2$–Si MOS structures with semitransparent electrodes. The silicon dioxide layer with a thickness $d \approx 110$ nm was grown on silicon n-wafers (a dopant concentration of 2×10^{15} cm^{-3}) by oxidation in dry oxygen at 1050°C. After oxidation, some wafers were annealed in hydrogen at 400°C for 20 min to produce electron traps in the oxide. Gold electrodes (radius $r \approx 0.2$ cm, thickness $h \leq 70$ nm) were applied on the cold substrate by mask evaporation in a vacuum. Once the oxide on the back side of the wafer had been removed by chemical etching, an ohmic contact (indium–gallium eutectic) was formed. The effective charge Q_{0t} in the insulator and the spectral interface state density D_{it} at the Si/SiO$_2$ interface that were determined from the high-frequency capacitance–voltage (C–V) characteristics were found to be 1.3×10^{11} cm^{-2} and 1.8×10^{11} eV^{-1} cm^{-2} for hydrogen-annealed MOS structures and 2.7×10^{11} cm^{-2} and 3.4×10^{11} eV^{-1} cm^{-2} for unannealed structures.

Hydrogen-annealed structures were exposed to intense UV radiation (exposure time to 1 h). A DRSh-1000 mercury lamp was used as a radiation source. The structures were irradiated at a gate voltage of $U_g = 30$ V. At the early stage of irradiation, the UV intensity generated a PEC on the order of 10^{-8} A. The radiation-induced variation of the effective charge in the insulator

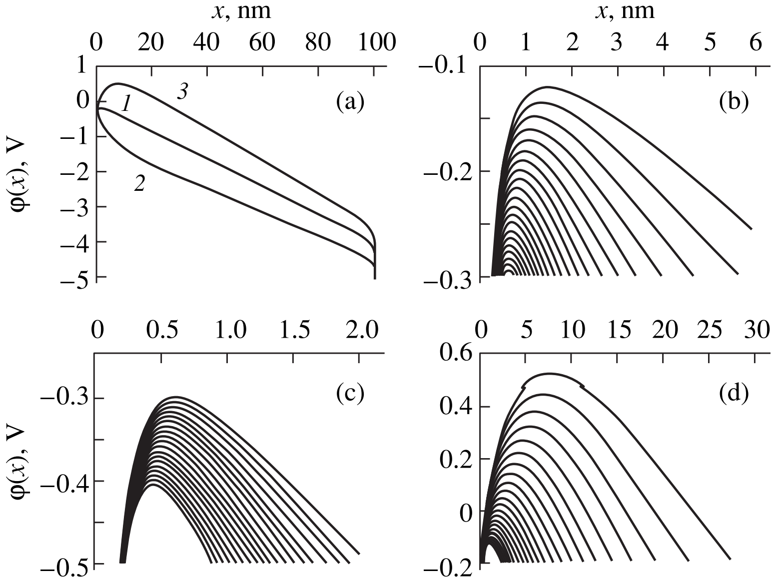

Fig. 3. Potential distribution $\varphi(x)$ across the MIS insulator. (a) $\varphi(x)$ calculated for (*1*) $\rho(x) = 0$, (*2*) $\rho(x) = 10^{19}\exp(-20x/d)$, and (*3*) $\rho(x) = -10^{19}\exp(-20x/d)$ at $U = 4$ V. (b)–(d) The position of the barrier height at $U = 4 + 0.5n$ V ($n = 0, 1, 2, \ldots$) for charge distributions *1–3*, respectively.

was controlled at regular intervals by taking *C–V* characteristics.

Spectral characteristics of PEC were recorded both on unannealed structures and on those annealed in hydrogen and subsequently exposed to UV radiation. In this case, a DKSSh-1000 continuous-spectrum xenon lamp was used as a radiation source. Radiation passed through an MDR-24 controllable-slit monochromator.

In taking PEC spectral curves, the differential capacitance of the MOS structure was kept constant by controlling the incident intensity according to [7]. An experimental PEC characteristic was converted to a spectral curve using the known frequency dependence of the internal photon photoelectric effect in silicon [8]. The spectral curve thus obtained implies that the UV intensity absorbed in the emitter is constant throughout the spectral range. The barrier height was determined by extrapolating the linear portion of the $\sqrt{I} - h\nu$ characteristic to the photon energy axis.

RESULTS AND DISCUSSION

Intense UV irradiation of the hydrogen-annealed MOS structures led to the accumulation of negative charge in the insulator. The irradiation time was sufficient for the effective charge to saturate, as evidenced by the shift of the *C–V* curves at the flat-band voltage V_{FB}.

The effect of negative charging under irradiation has been observed in MOS structures where the oxide was grown by wet oxidation [2]. It is known that if SiO_2 contains a large amount of hydrogen, negative charge

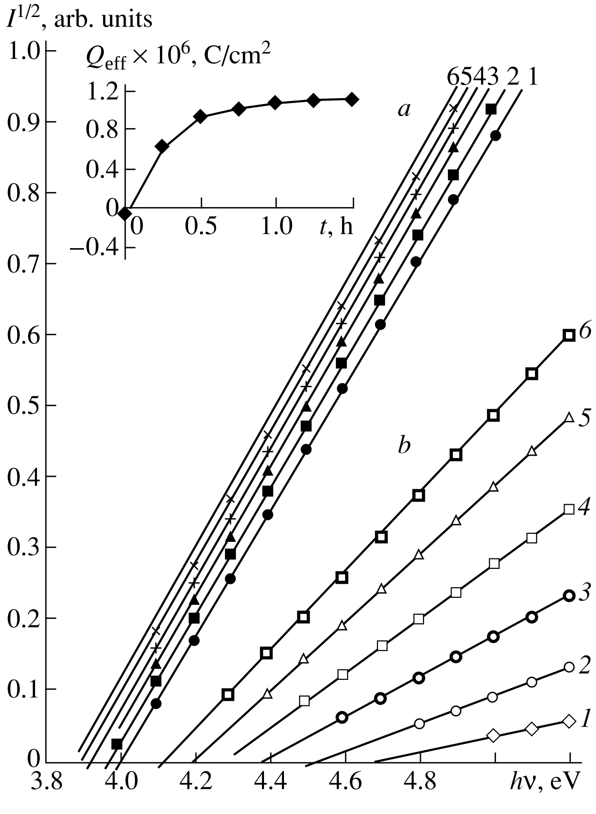

Fig. 4. Spectral curves for photoemission current in the Au–SiO_2–Si structures (a) unannealed and (b) annealed in hydrogen and exposed to intense UV radiation. Gate voltages are (*1*) 12, (*2*) 16, (*3*) 20, (*4*) 24, (*5*) 28, and (*6*) 32 V. In the insert: effective charge in the insulator of the hydrogen-annealed MOS structure vs. irradiation time.

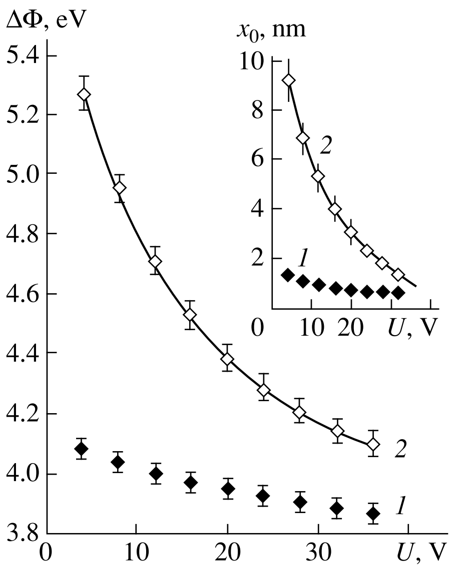

Fig. 5. Experimental field dependences of the potential barrier height at the Si/SiO_2 interface of the $Au–SiO_2–Si$ MOS structures (*1*) unannealed and (*2*) annealed in hydrogen and exposed to UV radiation. In the insert: field dependences of the barrier peak position that were calculated from corresponding field dependences of the barrier height (*1* and *2*, respectively).

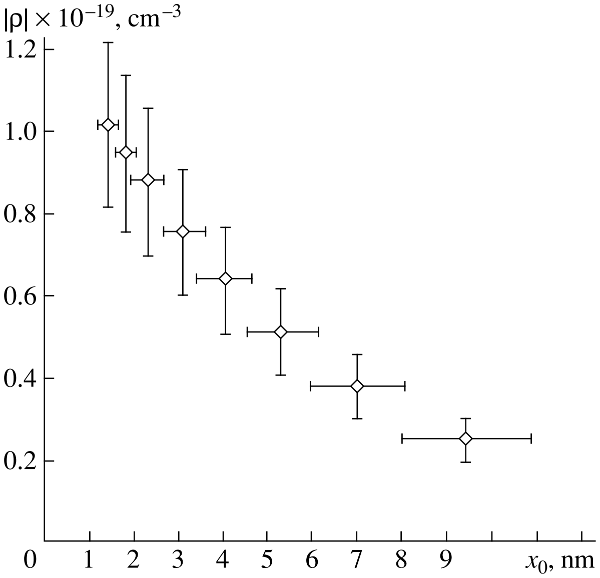

Fig. 6. Negative charge density distribution at the Si/SiO_2 interface of the hydrogen annealed and UV-processed $Au–SiO_2–Si$ MOS structure. Points were found from the spectral dependences of PEC that were constructed with our method.

may be the charge of injected electrons captured at the Si/SiO_2 interface [9]:

$$Si_3{\equiv}Si–OH + \bar{e} \longrightarrow Si_3{\equiv}Si–O^- + H^0.$$

$$Si_3{\equiv}Si–H + \bar{e} \longrightarrow Si_3{\equiv}Si^- + H^0.$$

Electrochemical reactions that involve injected electron capture and atomic hydrogen evolution may also take place in glassy SiO_2:

$$O_3{\equiv}Si–OH + \bar{e} \longrightarrow O_3{\equiv}Si–O^- + H^0,$$

$$O_3{\equiv}Si–H + \bar{e} \longrightarrow O_3{\equiv}Si^- + H^0.$$

Spectral dependences of PEC for the absorbed UV intensity constant throughout the spectral range are depicted in Fig. 4 for both types of the MOS structures.

Figure 5 demonstrates field dependences of the barrier height that were obtained from the spectral curves. Corresponding dependences for the barrier peak position that were obtained from the field dependences of the height are shown in the insert. As was expected, in the presence of negative charge in the oxide, the barrier depends on the field much more strongly and the oxide area at the interface where the position of the barrier peak is shifted by an external field considerably extends.

The charge distribution found in the area where the peak position varies is given in Fig. 6. For this distribution, the effective charge was calculated to be $Q_{eff} \approx 2 \times 10^{12}$ cm^{-2}. This value is in good agreement with $Q_{eff} \approx 4 \times 10^{12}$ cm^{-2}, obtained from the *C–V* curve.

Relationship (10) was used to find the phenomenological constant l, which characterizes the scattering of photoemitted electrons up to the barrier peak. The value of $l = 3.5 \pm 0.2$ nm, found from the spectral dependences of PEC for the MOS structures without negative charge, is very close to the value of $l = 3.4$ nm found by Powell from field dependences of PEC for an electroneutral insulator. However, for the structures with negatively charged oxide, $l = 1.2 \pm 0.5$ nm. Hence, the charge distributed in the insulator changes the l value. This means that space charge profiling using the field dependences of PEC according to the method in [3] may be in error.

CONCLUSION

It was established analytically that the position of the potential barrier for electrons photoemitted from the gate to the insulator is defined by the derivative of the barrier height with respect to the external field when the space charge density is randomly distributed in the insulator. A procedure for finding the charge profile in a MIS insulator is suggested. The profile is derived from a family of spectral characteristics of PEC that are recorded at various gate voltages. The method is suitable for profiling the negative charge in MIS insulators. Negative charge is produced in the SiO_2 layer of MOS structures annealed in hydrogen and then exposed to UV radiation.

REFERENCES

1. J. Kadlec and K. H. Gundlach, Phys. Status Solidi A **37** (9), 9 (1976).
2. E. H. Nicollian and J. R. Brews, *MOS (Metal-Oxide-Semiconductor) Physics and Technology* (Wiley, New York, 1984).
3. R. J. Powell and C. N. Berglund, J. Appl. Phys. **42**, 4390 (1971).
4. C. N. Berglund and R. J. Powell, J. Appl. Phys. **42**, 573 (1971).
5. M. N. Levin, B. N. Sakharov, and V. A. Gol'dfarb, Mikroélektronika **3**, 47 (1984).
6. R. J. Powell, J. Appl. Phys. **40**, 5093 (1969).
7. B. N. Sakharov, M. N. Levin, V. A. Gol'dfarb, and V. F. Synorov, USSR Inventor's Certificate No. 1200769 (June 15, 1984).
8. O. Christensen, J. Appl. Phys. **47**, 689 (1976).
9. E. H. Nicollian, C. N. Bergland, P. E. Schmidt, and J. M. Andrews, J. Appl. Phys. **42**, 5654 (1971).

Translated by V. Isaakyan

Technical Physics, Vol. 46, No. 3, 2001, pp. 322–325. Translated from Zhurnal Tekhnicheskoĭ Fiziki, Vol. 71, No. 3, 2001, pp. 52–56.
Original Russian Text Copyright © 2001 by Ezhov, Smirnova, Tikhonov.

Characteristics of Photopolymer Holographic Matched Filters in a van der Lugt Correlator

P. V. Ezhov, T. N. Smirnova, and E. O. Tikhonov
Institute of Physics, National Academy of Sciences of Ukraine, pr. Nauki 144, Kiev, 252650 Ukraine
e-mail: ezhov@iop.kiev.ua

Received October 19, 1999; in final form, June 14, 2000

Abstract—Parameters of van der Lugt holographic matched filters for phase and amplitude transparencies, including random phase masks, are studied. Conditions for recording such filters in a phase self-developing photopolymer are determined. A significant difference in the recording conditions for the holographic filters for amplitude transparencies and phase masks is demonstrated. The holographic filters for phase masks with a signal-to-noise ratio of 20–40 dB and η from 6 to 70% that are recorded in the photopolymerizable composition seem to be promising for optical pattern recognition. *© 2001 MAIK "Nauka/Interperiodica".*

INTRODUCTION

Van der Lugt and joint Fourier transform correlators (JFTCs) are widely used today for optical pattern recognition. These devices allow one to optically select certain image features or to pick up identical images from a set of images [1, 2]. The obvious advantages of JFTCs, such as the simplicity of tuning from one feature to another and mathematical processing (in parallel with computation) of 2D intensity distributions in the correlation plane, specify their predominant use in solving the above problems. In particular, JFTCs have been successfully applied to determining image identity by a certain distinctive feature [3–6].

The distinctive feature was formed by imposing a special phase mask (PM) as a coding element on an image. An advantage of this approach is that the PM makes it possible to introduce additional hardly reproducible complex distributions of the amplitudes into the complex amplitudes of object light fields [6]. Note that a conventional van der Lugt correlator also can effectively solve the problem of recognizing certain features of an image or entire images if the search is pursued over a large data array. When recording the Fourier holograms of phase masks on self-developing photopolymers [7], we revealed promising ways for obtaining the ultimate diffraction efficiency and signal-to-noise ratio (SNR). This has been a stimulus for looking into the application of these media as holographic matched filters.

We conducted extensive studies of the parameters of correlation signals for both phase and amplitude transparencies in a van der Lugt correlator. A photopolymer was used as a medium to *in situ* record matched holographic filters in real time.

The main purpose of this work was to study the correlation signals and conditions of recording holographic matched filters (HMFs) for a PM with a predetermined distribution of phase elements in the form of π-high steps (at a given wavelength). First, with PMs, replacing one mask by another that differs from the former in the arrangement of the phase elements (with their total number ranging up to 10^5 or more) does not cause cross-correlation signals in the case of matched spatial filtering. Therefore, the results can be used for image protection and identification in a van der Lugt correlator. In addition, PMs provide high uniformity of the spatial intensity distribution in the Fourier spectrum; hence, high-quality HMFs can be recorded.

To extend the class of objects under study, we investigated the conditions for obtaining HMFs and correlation functions for transparencies with nonuniform distributions of the Fourier intensities and with spatial frequencies ξ of 0–20 mm^{-1}.

CORRELATOR DESIGN AND EXPERIMENT

Spatial holographic matched filters were recorded by radiation from an argon ion laser (λ = 476 nm) with the conventional van der Lugt scheme (Fig. 1). The diameters of the collimated reference and object beams were $D_r = D_{obj}$ = 15 mm. The Fourier spectrum was formed by an objective F_1 with a resolution no worse than 100 mm^{-1} and a focal length L_1 = 220 mm. FPK-488 photopolymer was used as a holographic recording medium [8–10]. For this polymer, the spectral range of photosensitivity was λ = 400–515 nm and the characteristic recording time was 1–2 min at the radiation power density I = 8 mW/cm^2. A layer of the initially liquid photopolymer, whose thickness was defined by calibrated Teflon spacers, was placed between glass plates. To reduce noise, we prepolymerized the layer by using incoherent uniform UV illumination (for 1 min).

The angle between the reference and object beams was $\alpha = 18°$ for the mean spatial frequency of the object. The thickness of the photopolymer layer was $d = 25$ μm. Under such conditions (the Kock–Klein parameter $Q_2 > 10$), we recorded mostly volume holographic filters, exhibiting a high diffraction efficiency. The efficiency η was defined as the ratio $P_d/(P_d + P_t)$, where P_d and P_t are the respective powers of the diffracted and transmitted parts of a probing beam from a He–Ne laser. To monitor the efficiency in the course of recording the holographic filters, we employed a detection system consisting of photodiodes P_1 and P_2, an ADC, and a PC.

The advantage of self-developing photopolymers over standard Du Pont polymers [11] is that there is no need for postexposure processing, which simplifies the filter production process.

Once an HMF has been formed, the reference beam is shut off, the photodiodes of the detection system are removed from the correlator, and matched spatial filtering of a transparency in the object plane P_{obj} of the correlator takes place. The signal in the correlation plane P_{corr} (Fig. 1) is detected by a CCD camera operating in linear mode and recorded after digitization as a standard graphic file.

To quantify the efficiency of pattern recognition by a holographic matched filter, we used the standard measure, namely, the SNR defined as

$$\mu = 10\ln(I_{\mathrm{autocorr}}/I_n), \tag{1}$$

where I_{autocorr} and I_n are the maximum autocorrelation and noise intensities, respectively. Here, by noise, we mean the total intensity of signal components other than autocorrelation and cross-correlation ones.

The maximum value of SNR for the PM autocorrelation function was 40 dB (with the relative error less than 5%).

RESULTS

Regarding the increasing interest in the use of phase masks for image protection [4–6], we studied HMF recording for random PMs using FPK-488. Recording conditions were based on earlier data for Fourier hologram recording with this photopolymer [7], where the noise level in images reconstructed from such holograms was less than 1%. Figure 2 shows a typical result (the Fourier spectrum of the phase mask, the PM recognition signal, and the central cross section of the 2D distribution of the recognition signal). The related parameters are as follows: SNR $\mu = 30$ dB, efficiency $\eta = 21\%$, and the reference-to-object beam intensity ratio $(I_{\mathrm{ref}}/I_{\mathrm{obj}})$ 20 : 1. It was found that the recording conditions optimized for SNR were different in the case of Fourier holograms and HMFs for PMs.

If $I_{\mathrm{ref}} : I_{\mathrm{obj}} = 1 : 1$, the HMF efficiency in the frequency plane is $\eta = 70\%$ at $\alpha = 18°$ and the SNR in the correlation plane is $\mu \geq 40$ dB, although in the reconstructed image, $\mu = -4.77$ dB in the pulsed response regime. A further decrease in the ratio $I_{\mathrm{ref}}/I_{\mathrm{obj}}$ leads to increasing noise intensity in the correlation signal. We tried to measure the SNR at the minimal and maximal HMF efficiencies ($\eta = 1$ and 70%). In the former case, the noise was too low to be detected by our system, although the correlation signal was detected reliably. In the latter case, the SNR exceeded 40 dB and could not be measured accurately, since the relative error was larger than 5%. Therefore, an SNR of 30–40 dB is typical of HMFs with efficiencies between 20 and 50%.

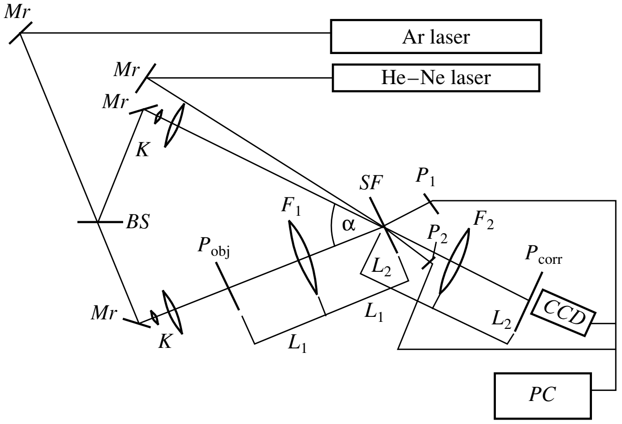

Fig. 1. Van der Lugt correlator with the detection system: *Mr*, mirrors; *Bs*, beamsplitter; *K*, collimators with spatial filtering; α, angle of beam convergence; P_{obj} and P_{corr}, object and correlation planes; F_1 and F_2, the first and the second Fourier objectives; L_1 and L_2, their focal lengths; *SF*, matched spatial filter; P_1 and P_2, photodiodes of the detection system; *CCD*, CCD camera.

Note that, for volume filters recorded in FPK-488, the effect of layer shrinkage and a corresponding change in the Bragg angle on the intensity of correlation signals was not observed.

To estimate the SNR for van der Lugt HMFs, we used the method [6] proposed for holographic filters of joint Fourier transforms, proceeding from the fact that the central cross section of the 2D intensity distributions in the correlation plane for two identical masks in a JFTC has the same shape as the autocorrelation curve in a van der Lugt correlator. In [6], the noise level was estimated as the entire curve except for its central peak (Fig. 2c). Hence, the SNR depends on the distance from the central peak. Using the formula from [6], we esti-

Table 1. Characteristics of the correlation signals of the holographic matched filters for the phase masks

Objects	Type of the object	$\xi_{\max}$ of an object, mm^{-1}	$I_{\mathrm{ref}}/I_{\mathrm{obj}}$ during filter recording	η, %	μ, dB	μ_0, dB
PM 1	Phase	50	20 : 1	21	30	–
			1 : 1	50	40	–
			1 : 1	70	≥40	–
PM 2	Phase	50	1 : 1	20	–	20

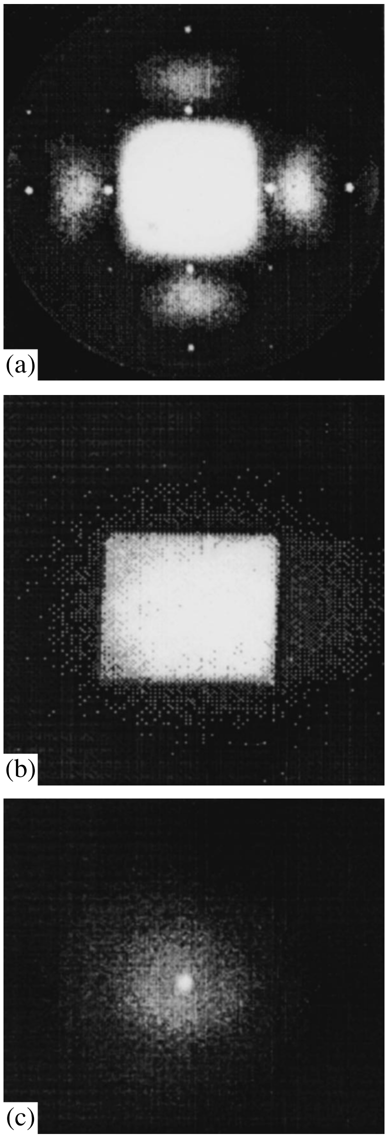

Fig. 2. Intensity distribution in the Fourier and correlation planes for PM 1: (a) Fourier spectrum, (b) autocorrelation signal, and (c) coordinate distribution of the intensity in the central cross section of the 2D distribution of the autocorrelation signal.

mated the minimum and maximum SNRs for the correlation signal of a PM:

$$\mu = (2N+1)^2/(2N+1-|n|), \qquad (2)$$

where N is the total number of phase steps and n is the distance (in terms of phase cells) from the central maximum in the central cross section.

For the number of phase cells in our mask $N = 256$ (one-dimensional case), we get $\mu_{\min} = 5.14 \times 10^2$ and $\mu_{\max} = 2.63 \times 10^5$. In the case of a van der Lugt correlator, the reliable maximum and minimum values of SNR were measured to be 10^4 and 2×10^2 dB, respectively. For the lower estimate, the entire correlation curve (except for the central peak) was taken as the noise intensity. Hence, with similar PMs in a van der Lugt correlator, one can apply the above estimation of SNR values for less accurate experimental data.

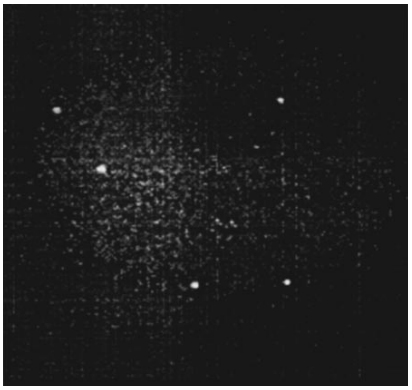

Fig. 3. Cross correlation for PM 2.

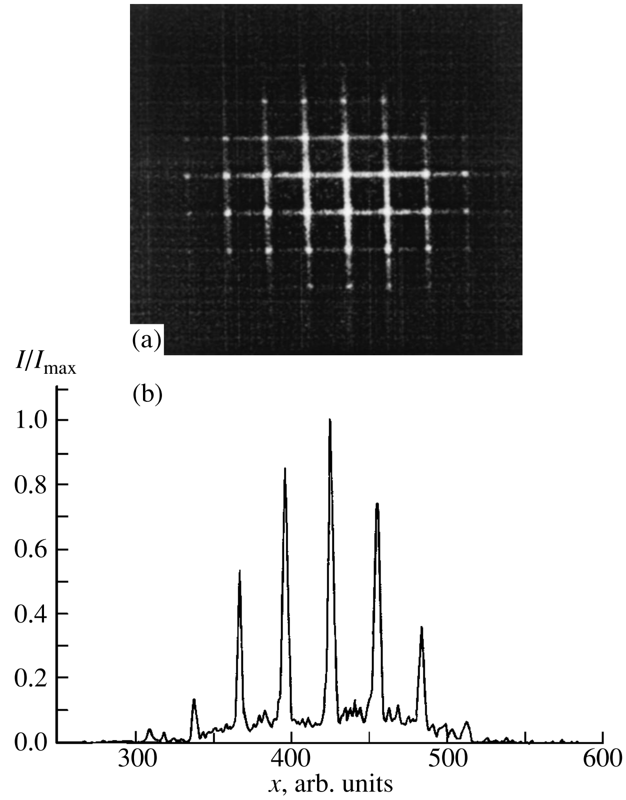

Fig. 4. Recognition signal for transparency 3: (a) intensity distribution in the correlation plane and (b) intensity versus coordinate in the central cross section of the 2D distribution of the autocorrelation signal.

We also measured cross-correlation signals for PMs. For this purpose, we recorded the HMF for PM 1 and performed matched filtering for PM 2, which consists of nine transposed fragments of the initial mask. Figure 3 demonstrates the cross-correlation signals of PM 2. Here, the SNR is 20 dB, and $I_{\text{ref}} : I_{\text{obj}} = 1 : 1$. Table 1 gives the SNR (μ_0) for such signals.

Table 2. Characteristics of the correlation signals of the holographic matched filters for the amplitude transparencies and phase masks

Objects	Type of the object	ξ_{max} of an object, mm^{-1}	I_{ref}/I_{obj} during filter recording	η, %	μ, dB	$I_{autocorr}/I_{crosscorr}$
PM 1	Phase	50	20 : 1	21	30.00	–
Transparency 2	Amplitude, a set of gratings with various periods	25	20 : 1	19	35.32	5.5×10^2
Transparency 3	Amplitude, a set of rectangular elements	12	20 : 1	17	27.48	2.15
Transparency 4	Amplitude, landscape	20	20 : 1	17	24.77	–
Transparency 5	Amplitude, an ordered set of pinholes	10	20 : 1	6	23.62	1.4×10^2

The experiments indicate that HMFs can be used as encoding elements for PMs and transposed PMs in a van der Lugt correlator. The number, intensity, or location of the correlation peaks may serve as a code. Muravsky *et al*. [12] implemented such an approach for JFTCs.

Generalizing the results for HMFs for PMs and transposed PMs (Table 1), we conclude that a van der Lugt correlator with HMFs recorded in FPK-488 processes large data arrays with the same rate and accuracy as a JFTC.

Recall that a PM represents an ideal object for HMF recording because of the uniform intensity distribution in the frequency plane.

To clarify whether or not the results on matched spatial filtering are applicable to a wider class of objects, namely, arbitrary amplitude transparencies, we recorded HMFs for transparencies characterized by narrower bands of spatial frequencies and exhibiting a nonuniform intensity distribution in the frequency plane, which is typical of Fourier holograms (Table 2). For transparency 2, Fig. 4 shows the 2D intensity distribution of the correlation signal and the coordinate dependence of the intensity in the central cross section of the 2D intensity distribution. Narrowing the spatial frequency band of the transparencies leads to a decrease in the efficiency and SNR of the HMFs. Moreover, narrow spatial frequency bands impose limitations on the ratio $I_{ref} : I_{obj} = 20 : 1$, one can measure only the SNRs that exceed 20 dB for all the transparencies. As an illustration, Table 2 lists the ratio of the maximum intensities of the autocorrelation ($I_{autocorr}$) and the first cross-correlation ($I_{crosscorr}$) signals for various amplitude transparencies. Evidently, the shape of the Fourier spectra of objects calls for further analysis in order to explain both the sharp differences in the recording conditions for PMs and arbitrary transparencies and the ratio $I_{autocorr}/I_{crosscorr}$.

CONCLUSION

We studied the conditions of recording van der Lugt holographic filters in a photopolymer film. When the conditions are optimized for noise level, the HMFs exhibit the reference-to-object beam intensity ratios of 1 : 1 and 20 : 1 for PMs and amplitude transparencies, respectively. The parameters of the correlation functions for HMFs in a van der Lugt correlator were examined. As the spatial frequency band narrows (in using amplitude transparencies instead of PM 1), the SNR of the autocorrelation function decreases from 40 to 20 dB and the diffraction efficiency decreases from 70 to 6%. The SNR is 20 dB for the cross-correlation signal of PM 2. Thus, photopolymers can be used for encoding arbitrary images by phase masks.

REFERENCES

1. R. J. Collier, C. B. Burckhardt, and L. H. Lin, *Optical Holography* (Academic, New York, 1971; Mir, Moscow, 1973).
2. *Applications of Optical Fourier Transforms*, Ed. by H. Stark (Academic, New York, 1982; Radio i Svyaz’, Moscow, 1988).
3. T. J. Grycewicz, Opt. Eng. **38**, 114 (1999).
4. Bahram Javidi and J. L. Horher, Opt. Eng. **33**, 1752 (1994).
5. Bahram Javidi, Guanshen Zhang, and Jian Li, Opt. Eng. **35**, 2506 (1996).
6. V. M. Fitio, L. I. Muravsky, and A. Stefansky, Proc. SPIE **2647**, 224 (1995).
7. P. V. Ezhov, T. N. Smirnova, and E. A. Tikhonov, Zh. Tekh. Fiz. **70** (6), 74 (2000) [Tech. Phys. **45**, 743 (2000)].
8. E. A. Tikhonov, T. N. Smirnova, and É. S. Gyul’nazarov, Opt. Spektrosk. **67**, 175 (1989) [Opt. Spectrosc. **67**, 99 (1989)].
9. E. A. Tikhonov, T. N. Smirnova, and É. S. Gyul’nazarov, Kvantovaya Élektron. (Kiev), No. 40, 1 (1991).
10. É. S. Gyul’nazarov, T. N. Smirnova, and E. A. Tikhonov, Zh. Tekh. Fiz. **58**, 2405 (1988) [Sov. Phys. Tech. Phys. **33**, 1469 (1988)].
11. R. W. Branstetter and N. J. Fonneland, Proc. SPIE **1559**, 308 (1991).
12. L. I. Muravsky, T. I. Voronyak, V. M. Fitio, and M. V. Shovgenjuk, Opt. Eng. **38**, 25 (1999).

Translated by A. Chikishev

Technical Physics, Vol. 46, No. 3, 2001, pp. 326–338. Translated from Zhurnal Tekhnicheskoĭ Fiziki, Vol. 71, No. 3, 2001, pp. 57–68.
Original Russian Text Copyright © 2001 by Bukharov, Vlasov, Demidov, Zhdanov, Ivanovskiĭ, Kornilov, Selemir, Tsareva, Chelpanov.

EXPERIMENTAL INSTRUMENTS AND TECHNIQUES

Concerning Microsecond Megaampere-Current Plasma Opening Switches

V. F. Bukharov, Yu. V. Vlasov, V. A. Demidov, V. S. Zhdanov, A. V. Ivanovskiĭ, V. G. Kornilov, V. D. Selemir, E. A. Tsareva, and V. I. Chelpanov

All-Russia Research Institute of Experimental Physics, Russian Federal Nuclear Center,
Sarov, Nizhni Novgorod oblast, 607190 Russia

Received November 10, 1999; in final form, April 24, 2000

Abstract—The operation mechanism of a microsecond megaampere-current plasma opening switch is considered. The magnetic field penetrates into the plasma via near-electrode diffusion. The increase in the degree of plasma magnetization due to electron heating results in an increase in plasma resistivity and current break. The problem of calculating a plasma opening switch is mathematically formulated. The problem reduces to simultaneously solving one-fluid two-temperature MHD equations with allowance for the Hall current and two-dimensional electric circuit equations. To analyze the solution obtained, one-dimensional equations are derived based on the assumption that the size of the electrode region in which the plasma is strongly magnetized is much smaller that the plasma column length. In this approximation, the operating modes of a plasma opening switch are studied numerically. On long time scales (≥2–3 μs), the operation is limited by plasma ejection from the interelectrode gap. On short time scales (≤1 μs), the dominant process is the penetration of the magnetic field with the current velocity. The results of the calculations are compared with the available experimental data. The developed concept and numerical procedure are used to optimize the scheme for an explosion experiment on breaking megaampere currents under conditions similar to those in the EMIR complex. *© 2001 MAIK “Nauka/Interperiodica”.*

INTRODUCTION

Microsecond plasma opening switches (POSs) have been studied since the middle of the 1980s. Due to the progress achieved in shortening current pulses by more than one order of magnitude [1–6] with increasing voltage applied to the load, these studies attract much attention in connection with possible applications to inertial confinement fusion problems. In particular, a POS is proposed as a key element of the forming system of the EMIR explosion complex [7]. Studies reported in this paper were initiated by the work on creating the base module of the EMIR complex.

In spite of the success achieved in sharpening current pulses, a complete theory and especially models and numerical procedures for calculating the POS parameters are still lacking. In order to develop the theory, it is necessary to clarify the questions of the mechanisms responsible for the penetration of the magnetic field into a plasma and the subsequent current break. The commonly accepted and best developed concept is that in the conduction phase, the POS operation is governed by electron magnetohydrodynamics (EMHD) and the magnetic field penetrates into a plasma in the form of a shock wave—the so-called Kingsep–Mokhov–Chukbar (KMC) wave [8]. This problem is examined in many papers [9–14]. The EMHD regime is realized under the following conditions [8]: $u \gg c_s$, v_A, and $\tau \ll \omega_{H_i}^{-1}$, where $u = j_0/en_e$ is the current velocity, $c_s = (ZkT_e/MA)^{1/2}$ is the ion-acoustic velocity, $v_A = B_0(\mu_0 n_i MA)^{-1/2}$ is the Alfvén velocity, and $\omega_{H_i} = ZeB_0/MA$ is the ion Larmor frequency. Here, we use the following notation: j_0 is the characteristic current density, e is the electron charge, Z is the ion charge number, M is the proton mass, A is the atomic mass of an ion, T_e is the electron temperature, $B_0 = \mu_0 H_0$ is the characteristic magnetic field, and τ is the characteristic time of the problem. The ion n_i and electron n_e densities in a quasineutral plasma are related by the equality $n_i = n_e/Z$.

The mechanism responsible for the current break has been less studied. It is generally believed that the reason why the plasma resistance grows is a decrease in the plasma density. In the opinion of the authors of [15], the density decrease (erosion) is caused by the escape of ions toward the cathode under the action of the electric field, whereas the magnetic field plays a supplementary role by insulating the arising vacuum gap. According to [16–18], a decisive role is played by plasma separation from the anode by the magnetic pressure force, which arises due to shorting the Hall electric field through the highly conductive metal electrode. The authors of [19, 20] believe that the decrease in the electron density is due to explosive ejection of electrons onto the electrodes. The conditions for this process are created by plasma bulk heating (which is enhanced when the plasma resistance is anomalous and

1063-7842/01/4603-0326$21.00 © 2001 MAIK “Nauka/Interperiodica”

the plasma density is decreased) and, simultaneously, plasma cooling near the electrodes.

In [21], a unified concept is proposed for all plasma phenomena in a POS, including the conduction and current-break phases. The concept combines the EMHD description of electron motion and the MHD description of ion motion (the Hall MHD model). One parameter of the Hall MHD model is the charge carried through the POS plasma in the conduction phase J_pt_p, where J_P is the accumulation circuit current and t_p is the accumulation time. The results of comparative analysis showed that the qualitative dependences of J_pt_p on the POS circuit parameters correlate with those predicted by the Hall MHD model. Unfortunately, a mathematical model and numerical procedure for calculating the entire process in the Hall MHD model throughout both the conduction and current-break phases with account taken of the actual plasma dynamics, heating kinetics, ionization, and plasma emission are lacking. For this reason, it is impossible to perform a correct quantitative comparative analysis.

One of the reasons why the theories of POS operation are incomplete is the lack of experimental data on the relation between the current and voltage parameters and POS plasma dynamics.

In the EMIR complex, one POS should sharpen a current pulse with an amplitude of ~2 MA and a rise time of 1–3 μs. The problem is complicated because the test runs of the current source—a POS-based disc explosion magnetic generator (DEMG)—are conducted in individual explosion experiments. For this reason, it is very important to have a physical model of a POS and a numerical procedure based on this model in order to calculate the parameters of the DEMG–POS operation. Here, the situation is encouraging, because there is a basis for creating such a model, namely the experimental data on the plasma parameters for POSs operating under similar conditions [22, 23].

Let us estimate the current and Alfvén velocities, u and v_A, and the ion Larmor frequency ω_{H_i} for the conditions of [22, 23]: $H_0 \cong J_0/2\pi r_0 \cong 2.3 \times 10^6$ A/m, the current is $J_0 = 720$ kA, the radius of the central electrode (cathode) is $r_0 = 5$ cm, the line electron density is $\int n_e dz \cong 3 \times 10^{16}$ cm^{-2}, $n_e \cong \int n_e dz/L \cong 3 \times 10^{15}$ cm^{-3}, the plasma column length is $L \cong 8$ cm, $Z = 6$, and $A = 12$. Then, we obtain

$$u = \frac{J_0}{2\pi r_0 e\int n_e dz} \approx 5\times 10^6\ \frac{\text{cm}}{\text{s}},$$

$$v_A = \frac{B_0}{\sqrt{\mu_0 n_i MA}} \approx 10^8\ \frac{\text{cm}}{\text{s}}, \tag{1}$$

$$\frac{1}{\omega_{H_i}} = \frac{MA}{ZeB_0} \approx 7\times 10^{-9}\ \text{s}.$$

It is seen that for a megaampere current with a rise time of $\tau \cong 1$ μs, the parameters of the POS plasma satisfy the inequalities $u \ll v_A$ and $\tau \gg \omega_{H_i}^{-1}$, which are opposite to the EMHD regime conditions. In this case, not only are the electrons bound to ions by electric forces, ensuring plasma quasineutrality (the Debye radius is $\lambda_D = (kT_e/4\pi e^2 n_e)^{1/2} \approx 10^{-2}$ cm, and $T_e = 1$ eV), but the electron velocity is also equal to the ion velocity; i.e., we can neglect electron inertia. Note that the equality of the electron velocity to the ion velocity is provided by both collisions and the self-consistent magnetic field ($\Pi = (v_A/u)^2 = 4\pi Z n_e e^2 L^2/Mac^2 \approx 50Z \gg 1$). These conditions are those of the one-fluid MHD regime [24]. At the same time, by comparing the energy-exchange time between electrons and ions with τ, we can see that for $T_e \geq 10$ eV, electrons and ions have different temperatures: $\tau_{ei}^{\varepsilon} = MA/2m_e\tau_e \approx 2\times 10^{-8} T_e^{3/2}$, where

$$\tau_e = \frac{1}{\nu} = \frac{3(4\pi\varepsilon_0)^2\sqrt{m_e}(kT_e)^{3/2}}{4\sqrt{2\pi}\lambda e^4 Z n_e}$$

is the electron momentum relaxation time and $\lambda \approx 10$ is the Coulomb logarithm.

In the one-fluid MHD regime, the penetration of the magnetic field into a plasma occurs via skinning or diffusion. Evaluation of the diffusion length $z_d = (\tau/\mu_0\sigma)^{1/2}$ from the Spitzer conductivity

$$\sigma = \frac{3(4\pi\varepsilon_0)^2}{4\sqrt{2\pi}}\frac{(kT_e)^{3/2}}{\sqrt{m_e}e^2 Z\lambda} \cong 1.5T_e^{3/2} 1/(\Omega\ \text{cm})$$

yields $z_d \leq 2.5$ cm for $T_e \geq 10$ eV; i.e., $z_d \ll L$. However, there may be another process, namely, near-electrode diffusion with a characteristic length of $z_e \cong \beta z_d$ [18], where $\beta = \sigma B_0/en_e = \omega_{H_e}/\nu \sim T_e^{3/2}$ is the Hall parameter and $\omega_{H_e} = eB_0/m_e$ is the electron Larmor frequency. The characteristic near-electrode diffusion length is $z_e \sim T_e^{3/4}$ and is estimated as $z_e \geq 250$ cm for $T_e \geq 10$ eV ($\beta \geq 100$).

Under conditions of near-electrode magnetic field diffusion, plasma near the electrode is magnetized. The specific energy release can be estimated from the density of the current $j_\perp$ flowing into (or flowing out of) the electrode as $\beta^2 j_\perp^2/\sigma$; i.e., it is higher than that in the plasma bulk by the factor β^2. This is related to the fact that the electrons flow into (or out of) the electrode almost at a tangent to the surface (at the angle $1/\beta \ll 1$) [16]. The increase in the specific energy release is accompanied by an increase in the electron temperature, stronger magnetization of the plasma, and the growth of the plasma resistivity near the electrodes ($\sim T_e^{3/2}$), which in turn increases the energy release, and

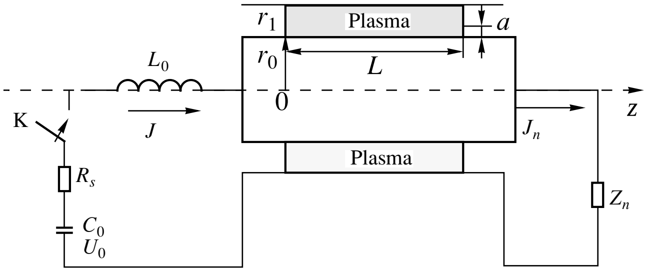

Fig. 1. Equivalent electric circuit of experiments on current break with a POS.

so on. Hence, the process of current heating may be associated with stronger plasma magnetization due to heating of the near-electrode regions. In this case, the decrease in the plasma mass density ρ perpendicular to the surface enhances the effect ($\beta \sim 1/\rho$) but does not control it. First of all, this mechanism is realized near the inner electrode, where the magnetic field and the current density are higher.

After estimating the ratio η of the near-electrode diffusion velocity $v_e \cong \beta/2(\mu_0\sigma\tau)^{-1/2}$ to the Alfvén velocity, we obtain $\eta \sim (MA/Zm_e\nu\tau)^{1/2} \sim 0.55T_e^{3/4}/Z \sim 1$ (here, $A \cong 12$, $n_e \cong 3 \times 10^{15}$ 1/cm^{-3}, and $\tau \cong 1$ μs [22, 23]); i.e., near-electrode diffusion can be accompanied by displacement of the plasma by the magnetic field (the snowplow effect).

Hence, at a reduced plasma density, between the Marshall gun and EMHD regimes, the plasma magnetization regime in the near-electrode region can be realized. Estimates made for the operating conditions of [22, 23] show that the parameters necessary for realizing this regime are close to those existing in microsecond POSs. Therefore, the operation of a microsecond POS can be explained by plasma magnetization in the near-electrode regions, the corresponding rapid penetration of the magnetic field, and the increase in the resistivity due to plasma heating. This statement can be verified by direct numerical simulations of the processes with the actual plasma parameters.

Below, we formulate the problem of calculating a POS. The problem reduces to simultaneously solving both two-dimensional MHD equations with allowance for the Hall current and the electric circuit equations. Assuming the size a of the near-electrode region where the plasma is magnetized to be small ($a/L \ll 1$), approximate 1.5-dimensional equations are derived. These equations are used to numerically study the POS operation regimes. The results of calculations are compared with the experimental data [22, 23]. In our opinion, the comparison shows that the processes occurring in a POS are described adequately based on the proposed concept. The scheme of the explosion experiment on the breaking of megaampere currents in EMGs is optimized using numerical methods.

Note that the previous comparative analysis of the currents and voltages measured in experiments with POSs in the Kovcheg device and results from simulations using the model under consideration showed that they are in good agreement [25]. The results were compared for the optimum experimental and calculated values of the plasma density. Since there was none of the necessary diagnostic equipment when these experiments were conducted, we could not directly compare the calculated value of the plasma density with that measured in experiments.

FORMULATION OF THE PROBLEM

Figure 1 shows the electric circuit diagram for the current-break experiments. At the initial instant, the capacitor bank C_0 is charged to the potential U_0. The space between two coaxial, perfectly conducting cylinders is filled with a plasma with the mass density $\rho = \rho_0(r, z)$ and temperature $T_e = T_i = T_0(r, z)$. The plasma is produced by two injectors positioned on the side of the outer cylinder of radius r_1. After closing switch K, the current starts flowing in the circuit. If both the source resistance R_s and the plasma column resistance are low (i.e., the temperature T_0 is sufficiently high), then the current is determined by the expression $J(t) = U_0/R_W\sin[t/(C_0L_0)^{1/2}]$, where $R_W = (L_0/C_0)^{1/2}$ is the circuit wave impedance. The current produces an azimuthal magnetic field B_φ. As a result of the interaction between the field and the current and also due to the gradient of the hydrodynamic pressure p, which arises because of Joule heating and is equal to the sum of the electron p_e and ion p_i pressures, the plasma starts moving. The plasma motion (by virtue of the cylindrical symmetry, the longitudinal v_z and radial v_r components of the mass velocity differ from zero) results in the redistribution of the plasma mass density ρ. The process is described by the equations

$$\frac{\partial\rho}{\partial t} + \frac{1}{r}\frac{\partial}{\partial r}(\rho v_r) + \frac{\partial}{\partial z}(\rho v_z) = 0,$$

$$\begin{aligned} \frac{\partial v_r}{\partial t} + v_r\frac{\partial v_r}{\partial r} + v_z\frac{\partial v_r}{\partial z} &= -\frac{1}{\rho}\frac{\partial p}{\partial r} - \frac{i_z B_\varphi}{\rho}, \\ \frac{\partial v_z}{\partial t} + v_r\frac{\partial v_z}{\partial r} + v_z\frac{\partial v_z}{\partial z} &= -\frac{1}{\rho}\frac{\partial p}{\partial z} - \frac{i_r B_\varphi}{\rho}, \end{aligned} \tag{2}$$

$$p = p_e + p_i, \quad p_e = \frac{\rho}{MA}ZkT_e, \quad p_i = \frac{\rho}{MA}kT_i.$$

The evolution of the longitudinal and transverse current-density components i_z and i_r and the magnetic field in the plasma is governed by the Maxwell equations

$$\frac{\partial E_r}{\partial z} - \frac{\partial E_z}{\partial r} = -\frac{\partial B_\varphi}{\partial t},$$

$$E'_r = \frac{i_r}{\sigma(T_e)} - \frac{MA}{e\rho Z} i_z B_\varphi, \quad E'_z = \frac{i_z}{\sigma(T_e)} + \frac{MA}{e\rho Z} i_r B_\varphi, \quad (3)$$

$$i_z = \frac{1}{\mu_0 r}\frac{\partial}{\partial r}(rB_\varphi), \quad i_r = -\frac{1}{\mu_0}\frac{\partial B_\varphi}{\partial z}.$$

In Ohm’s law (the second and third equations) allowance is made for the Hall current: the longitudinal and transverse electric field components in the frame of reference moving with the plasma are $E'_z = E_z + v_r B_\varphi$ and $E'_r = E_r - v_z B_\varphi$, respectively.

The electron and ion temperatures are determined from the energy balance equations. In the two-temperature MHD approximation, these equations take the form

$$\frac{\partial \varepsilon_e}{\partial t} + v_r\frac{\partial \varepsilon_e}{\partial r} + v_z\frac{\partial \varepsilon_e}{\partial z} + \frac{p_e}{\rho}\left(\frac{1}{r}\frac{\partial}{\partial}(rv_r) + \frac{\partial v_z}{\partial z}\right)$$

$$= \frac{\mathbf{iE}}{\rho} - 3\frac{m_e Z}{M^2A^2}k(T_e - T_i)\nu - q,$$

$$\frac{\partial \varepsilon_i}{\partial t} + v_r\frac{\partial \varepsilon_i}{\partial r} + v_z\frac{\partial \varepsilon_i}{\partial z} + \frac{p_i}{\rho}\left(\frac{1}{r}\frac{\partial}{\partial}(rv_r) + \frac{\partial v_z}{\partial z}\right) \quad (4)$$

$$= 3\frac{m_e Z}{M^2A^2}k(T_e - T_i)\nu,$$

$$\varepsilon_e = \frac{3}{2}Z\frac{kT_e}{m_i}, \quad \varepsilon_i = \frac{3}{2}\frac{kT_i}{m_i}, \quad \mathbf{iE}' = i_r E'_r + i_z E'_z.$$

The ionization loss q in the first equation of set (4) can be taken into account in the average-ion approximation [26]

$$q = -\frac{I(Z)}{MA}\frac{\partial Z}{\partial t}, \quad (5)$$

where the ionization energy $I(Z)$, considered as a continuous function of the ion charge number Z, is determined by the expression

$$I(Z + 1/2) = kT_e \ln\left[\frac{2MA}{Z\rho}\left(\frac{2\pi m_e k T_e}{h^2}\right)^{3/2}\right].$$

Writing Eqs. (4), we assumed that the electron and ion heat conductivities are frozen in the magnetized plasma near the electrodes.

When solving Eqs. (2)–(5), the initial conditions are chosen in the form $\rho|_{t=0} = \rho_0(r, z)$, $T_e|_{t=0} = T_i|_{t=0} = T_0(r, z)$, $v_z|_{t=0} = v_r|_{t=0} = 0$, and $B_\varphi|_{t=0} = 0$.

On the surface of the rigid perfectly conducting cylinders, we impose the conditions $E_z|_{r = r_0, r_1} = 0$ and $v_r|_{r = r_0, r_1} = 0$.

On the source side, the boundary conditions are determined from the circuit equations [27]:

$$U_s = R_s J + \frac{d}{dt}(L_0 J) + V, \quad \frac{dU_s}{dt} = -\frac{J}{C_0}. \quad (6)$$

The potential V is determined by integrating the field $\mathbf{E}_R$ along the left plasma surface, $V = \int \mathbf{E}_R\, d\mathbf{s}$ from $r = r_0$ to $r = r_1$. The magnetic field on the plasma surface B_R is related to the current J by the expression $B_R(r_1 > r > r_0) = \mu_0 J/2\pi r_0(r_0/r)$. The initial conditions for Eqs. (6) are taken as $U_s|_{t=0} = U_0$ and $J|_{t=0} = 0$.

On the load side, the boundary conditions have the form

$$Z_n J_n = V_n, \quad (7)$$

where

$$V_n = \int_{r_0}^{r_1} \mathbf{E}_L d\mathbf{s}$$

and $\mathbf{E}_L$ is the electric field along the right plasma surface. The magnetic field on the right plasma surface is written as $B_L(r_1 > r > r_0) = \mu_0 J_n/2\pi r_0(r_0/r)$.

Equations (2)–(5) with the boundary conditions determined by Eqs. (6) and (7) completely describe the POS operation. The solution of these equations in their full form goes beyond the scope of this paper. The main features of the solution will be analyzed using an approximate 1.5-dimensional model.

APPROXIMATION FOR NEAR-ELECTRODE DIFFUSION

Let us examine the character of the solution to the equations of the magnetic group (3) neglecting the mass velocity ($v_z, v_r \equiv 0 \longrightarrow E'_z = E_z$; $E'_r = E_r$) and assuming the plasma density and temperature to be constant and spatially uniform: $\rho = \rho_0$, $T_e = T_0$, and $\sigma = \sigma(T_0) = \sigma_0$. If the size of the region of near-electrode magnetic field diffusion is small, i.e., $a \ll r_0$, then the process can be described in local plane geometry: $B_\varphi \longrightarrow -B_x$, $E_r \longrightarrow E_y$; $r \longrightarrow y$, $1/r\partial(rB_\varphi)/\partial r \longrightarrow -\partial Bx/\partial y$. In this approximation, Eqs. (3) can be rewritten in the form

$$\frac{\partial E_y}{\partial z} - \frac{\partial E_z}{\partial y} = \frac{\partial B_x}{\partial t},$$

$$E_y = \frac{1}{\mu_0\sigma_0}\frac{\partial B_x}{\partial z} - \frac{MA}{e\rho_0 Z}\frac{1}{\mu_0}B_x\frac{\partial B_x}{\partial y}, \quad (8)$$

$$E_z = -\frac{1}{\mu_0\sigma_0}\frac{\partial B_x}{\partial y} - \frac{MA}{e\rho_0 Z}\frac{1}{\mu_0}B_x\frac{\partial B_x}{\partial z}.$$

When solving Eqs. (8), the longitudinal electric field component must vanish on the electrode surface,

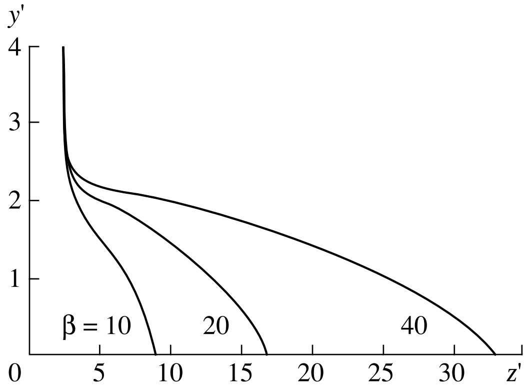

Fig. 2. Isolines of the magnetic field $B = 0.1$ at $t' = 1$ and different values of the Hall parameter.

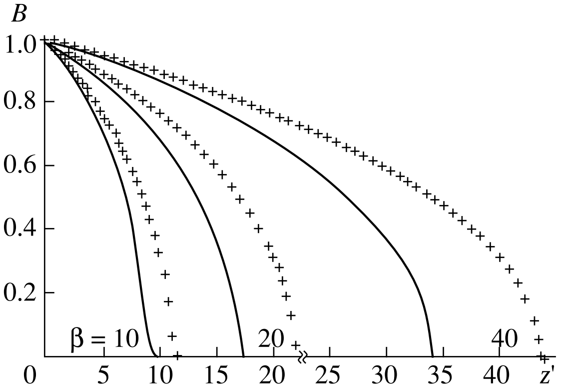

Fig. 3. Magnetic field on the electrode surface ($y' = 0$) at $t' = 1$ as a function of z' for different values of the Hall parameter. Solid curves correspond to the exact solution of Eq. (9), crosses correspond to the near-electrode diffusion approximation (13).

$E_z|_{y=0} = 0$. For $y \gg a$, the usual volume diffusion dominates; i.e., $\partial B_x/\partial y|_{y \to \infty} = 0$. The solution to Eqs. (8) is sought in a half-plane $0 \le z < \infty$ with a given magnetic field B_0 on the right end $B_x|_{z=0} = B_0$. Substituting the expression for the electric field components from the second and third equations of set (8) into the first equation, we obtain

$$\frac{\partial B}{\partial t'} = \frac{\partial^2 B}{\partial y'^2} + \frac{\partial^2 B}{\partial z'^2}, \qquad (9)$$

where the dimensionless variables $B = -B_x/B_0$, $t' = t/t_0$, $y' = y/x_0$, and $z' = z/x_0$ are introduced. Here, t_0 is the characteristic time of the problem and $x_0 = (t_0/\mu_0\sigma)^{1/2}$ is the characteristic scale length of volume diffusion.

Equation (9) is solved with the initial condition $B|_{t'=0} = 0$ and the boundary conditions

$$\left(\frac{\partial B}{\partial y'} - \beta B\frac{\partial B}{\partial z'}\right)\Bigg|_{y'=0} = 0, \quad \frac{\partial B}{\partial y'}\Bigg|_{y' \to \infty} = 0, \qquad (10)$$
$$B|_{z'=0} = 1, \quad B|_{z' \to \infty} = 0.$$

The solution to Eq. (9) with boundary conditions (10) only depends on the Hall parameter $\beta = \omega_{H_e}/\nu$.

Figure 2 shows the isolines of the magnetic field $B = 0.1$ at $t' = 1$ obtained by solving Eq. (9) with boundary conditions (10) for $\beta = 10$, 20, and 40. The penetration of the field into the plasma follows the electrode geometry: at $y' \longrightarrow 0$, the contours are extended along the z'-axis. The region near the electrode where the magnetic field is localized is determined by the characteristic scale length of volume diffusion, $\sim t'^{1/2}$. At $y' \longrightarrow \infty$, the contours of the constant magnetic field are parallel to the y'-axis, the diffusion is volumetric in character, and the magnetic field is determined by solving Eq. (9) with $\partial^2 B/\partial y'^2 \equiv 0$:

$$B = \operatorname{erfc}\left(\frac{z'}{2\sqrt{t'}}\right) = \frac{2}{\sqrt{\pi}}\int\limits_{\frac{z'}{1\sqrt{t'}}}^{\infty} \exp(-t^2)dt. \qquad (11)$$

For the electrode region, from Eq. (9), assuming $E_z \equiv 0$, we obtain

$$\frac{\partial B}{\partial t'} = \frac{\partial}{\partial z'}\left\{[1 + \beta^2 B^2]\frac{\partial B}{\partial z'}\right\}. \qquad (12)$$

The solution is sought in the form $B(\xi = z'/2t'^{-1/2})$. In this case, Eq. (12) transforms into

$$\frac{d}{d\xi}\left\{[1 + \beta^2 B^2]\frac{dB}{d\xi}\right\} + 2\xi\frac{dB}{d\xi} = 0. \qquad (13)$$

The solution satisfying the conditions $B(\xi)|_{\xi=0} = 1$ and $B(\xi)|_{\xi \to \infty} = 0$ is constructed by shooting from $\xi = 0$. Figure 3 compares the dependences of the magnetic field B on z' at $t' = 1$ obtained by solving Eq. (9) for $y' = 0$ and Eq. (13) for $\beta = 10$, 20, and 40. It is seen that the near-electrode approximation, which reduces to setting the longitudinal electric field component E_z to zero in the equations of the magnetic group [(9) or (3)], describes the penetration of the field into the plasma with an accuracy of ~25%.

QUASI-ONE-DIMENSIONAL APPROXIMATION

On the whole, the penetration of the magnetic field into the plasma is two-dimensional in character. However, the one-dimensional approximation may be used for a number of reasons. First, for the conditions of [22, 23], we have that, during the current rise time $\tau \sim 1\ \mu s$, the size a of the region of near-electrode magnetic field diffusion, which is determined by the scale length of volume diffusion z_d, becomes comparable with the interelectrode distance $a \sim (r_1 - r_0)$. Second, penetration of the field into the plasma is accompanied by an increase in the total pressure $(p + B_\varphi^2/2\mu_0)$ near the electrodes; then, the pressure levels off due to discharge in the normal direction to the electrodes. The pressure levels off with the Alfvén velocity v_A in the time $t_A \sim (r_1 - r_0)/v_A \sim 0.025$ μs, which is much shorter that the current rise time $\tau \sim 1$ μs; i.e., the solution is adiabatic in character. These circumstances allow us to simplify the problem by assuming that the transverse velocity is small ($v_r \longrightarrow 0$) and the mass density ρ, pressure p, and magnetic field B_φ profiles are nearly uniform in the cross section $z = 0$. The validity of this assumption is confirmed by the measured line electron density $\int n_e\,dz$ [22], which is nearly uniform in the conduction phase, except for a narrow region near the cathode. Neglecting the radial velocity v_r, for uniform ρ, p, and B_φ, Eqs. (2) take the form

$$\frac{\partial}{\partial t}\left(\frac{1}{\rho}\right) = \frac{\partial v_z}{\partial m}; \quad \frac{\partial z}{\partial t} = v_z; \quad \frac{\partial v_z}{\partial t} = -\frac{\partial p}{\partial m} - \frac{i_r B_\varphi}{\rho},$$
$$p = p_e + p_i, \quad p_e = \frac{\rho}{MA}ZkT_e, \quad p_i = \frac{\rho}{MA}kT_i. \tag{14}$$

Here, we introduce the Lagrange coordinate $m = \int_{z_0(t)}^{z}\rho(z', t)dz'$, where $z_0(t)$ is the coordinate of the plasma surface on the source side, $\partial/\partial t = \partial/\partial t - \rho v_z \partial/\partial m$, and $\partial/\partial z = \rho\partial/\partial m$). In the near-electrode magnetic field diffusion approximation ($E_z = E'_z = 0$), from Eqs. (3) and in view of the first equation in set (14), we obtain

$$\frac{\partial}{\partial t}\left(\frac{B_\varphi}{\rho}\right) = -\frac{\partial E'_r}{\partial m},$$
$$E'_r = -\frac{\rho}{\mu_0\sigma}\left[1 + \left(\frac{\omega}{\nu}\right)^2\right]\frac{\partial B_\varphi}{\partial m}, \tag{15}$$
$$i_r = -\frac{\rho}{\mu_0}\frac{\partial B_\varphi}{\partial m}, \quad \omega = \frac{eB_\varphi}{m_e}.$$

In the adopted approximations, Eqs. (4) and (5) can be rewritten in the form

$$\frac{\partial \varepsilon_e}{\partial t} + p_e\frac{\partial v_z}{\partial m} = \frac{i_r E'_r}{\rho} - 3\frac{m_e Z}{M^2A^2}k(T_e - T_i)\nu - \frac{I(Z)}{MA}\frac{\partial Z}{\partial t},$$
$$\frac{\partial \varepsilon_i}{\partial t} + p_e\frac{\partial v_z}{\partial m} = 3\frac{m_e Z}{M^2A^2}k(T_e - T_i)\nu,$$
$$\varepsilon_e = \frac{3}{2}Z\frac{kT_e}{m_i}, \quad \varepsilon_i = \frac{3}{2}\frac{kT_i}{m_i}, \tag{16}$$
$$I(Z + 1/2) = k/T_e \ln\left[\frac{2MA}{Z\rho}\left(\frac{2\pi m_e kT_e}{h^2}\right)^{3/2}\right].$$

The boundary conditions for Eqs. (14)–(16) reduce to Eqs. (6) and (7):

$$B_\varphi(0, t) = \frac{\mu_0 J}{2\pi r_0}, \quad B_\varphi(m_0, t) = \frac{\mu_0 J_n}{2\pi r_0},$$
$$U_S = R_S J + \frac{d}{dt}(L_0 J) + E_r(0, t)a,$$
$$\frac{dU_S}{dt} = -\frac{J}{C_0}, \quad Z_n J_n = E_r(m_0, t)a, \tag{17}$$
$$J|_{t=0} = 0, \quad U_S|_{t=0} = U_0,$$

where $a \sim (r_1 - r_0)$ is the current-break gap.

Equations (14)–(16) with conditions (17) form a closed set of quasi-one-dimensional equations. Their solution for specified initial distributions of the plasma mass density $\rho(z, t = 0) = \rho_0(z)$ ($\int_0^\infty \rho_0(z)dz = m_0$) and temperature $T_e(z, t = 0) = T_i(z, t = 0) = T_0(z)$ allow us to determine the POS operating parameters.

COMPARATIVE ANALYSIS OF CALCULATED AND EXPERIMENTAL DATA

We consider the solution to Eqs. (14)–(16) for the experimental conditions of [22, 23]. From the current $J_0 = U_0 C_0^{1/2}/L_0^{1/2} \cong 720$ kA, the voltage $U_0 \cong 600$ kA, and the oscillation period $T_0/4 = \pi/2(L_0C_0)^{1/2} \cong 1.5$ μs, we determine $L_0 \cong 0.8$ μH and $C_0 \cong 1.15$ μF (Fig. 1). When the POS operates with an inductive load, we have $Z_n \longrightarrow L_n = \mu_0/2\pi \ln(r_1/r_0)l = 0.02$ μH (where $r_1 = 7.5$ cm, $r_0 = 5$ cm, and $l = 25$ cm).

We assume that at the initial instant $\rho_0(z) = \rho_0$ and, according to [22], $L = 8$ cm. The composition of the POS plasma, i.e., the proportion between the carbon and hydrogen components, is unknown. We assume that the plasma properties are governed by the heavy C component. The ionization energies $I(Z)$ of multiply charged C ions were taken from [28]. There is uncertainty in the initial temperature distribution $T_0(z)$. In the calculations, we assumed $T_0(z) = T_0$; the value of T_0 was varied.

When the interelectrode distance is small ($r_1 \sim r_0$), the plasma parameters and magnetic field near the cathode are close to those near the anode. Under these conditions, one might expect that the magnetic field diffusion velocity near the cathode would be close to that near the anode. Figure 4 shows the calculated time dependences of the source and load currents J and J_n and the line electron density $\int n_e\,dz$ obtained for near-anode magnetic field diffusion ($B_\varphi = \mu_0 J/2\pi r_1$) for $T_0 = 3$ eV and $a = 1$ cm. The current break occurs at $t_p \sim 0.9$ μs, when the line plasma mass density is equal to $m_0 = 0.26$ μg/cm^2. The time t_p varies only slightly when

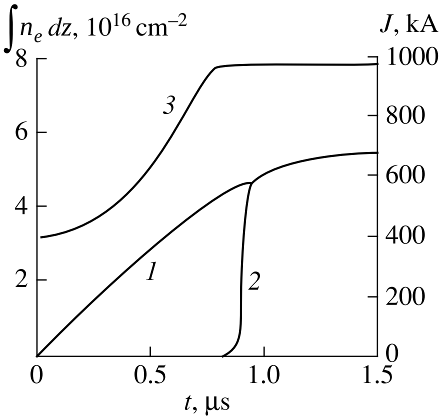

Fig. 4. Time dependences of (*1*) the source current, (*2*) load current, and (*3*) line electron density.

T_0 and a are varied ($a \le (r_1 - r_0) = 2.5$ cm). When T_0 and a are varied within the ranges $T_0 = 3$–1 eV and $a = 1$–2.5 cm, the calculated amplitudes of the source and load currents vary within 20%. Similar time dependences of the currents in near-cathode diffusion ($B_\varphi = \mu_0 J/2\pi r_0$) are obtained with $m_0 = 0.45$ μg/cm^2.

Hence, in the calculations, the current break at $t_p \sim 0.9$ μs is observed for the values of line plasma density lying in the range $\int n_e\,dz \sim 3.5$–13×10^{16} 1/cm^2, depending on the time and distance from the electrodes. The experimental value is $\int n_e\,dz \sim 2$–16×10^{16} 1/cm^2 [22, 23].

The calculated dynamics of magnetic field penetration and plasma heating are illustrated in Fig. 5, which shows the density and electron temperature profiles at various times for near-anode diffusion. In the early stage ($t = 0.6$ μs), a plasma heating wave determined by near-anode magnetic field diffusion and a compression wave (snowplow) are formed. The diffusion wave leaves behind the snowplow. The electric field E_r' at $t = 0.6$ μs does not exceed 0.6 kV/cm, and the plasma column resistance is $R_p \cong 3 \times 10^{-4}\ \Omega$. The evaluation of the plasma parameter $\gamma = 8\pi n_e k T_e / B_\varphi^2$ gives $\gamma \le 0.2$ ($n_e \le 3 \times 10^{16}$ 1/cm^3, $T_e \le 30$ eV, and $B_\varphi \sim 12$ kG); i.e., gasdynamic discharge in the transverse direction can be neglected.

Dependences of the POS characteristics on the ion density in a carbon plasma

n_i, 1/cm^3	t_p, μs	t_p^*, μs	z_{sp}, cm
1.55×10^{14}	0.21	0.20	1.47
3.1×10^{14}	0.3	0.31	2.34
6.2×10^{14}	0.45	0.47	4.1
1.55×10^{15}	0.82	0.81	7.1
3.1×10^{15}	1.27	1.23	12.2
7.8×10^{15}	2.09	2.14	27.02
1.55×10^{16}	3.16	3.24	62.5

When the diffusion wave reaches the right plasma boundary, the fraction of the current equal to R_p/R_n is switched to the load. The load resistance R_n at the instant of break is estimated from the characteristic break time $\tau_{op} \sim 30$ ns and is equal to $R_n \sim L_n/R_n \sim 1\ \Omega$. At $t = 0.8$ μs, the plasma resistance is equal to $R_p \cong 5 \times 10^{-3}\ \Omega$, the current is $J \cong 500$ kA, and the electric field strength is equal to $E_r' \cong R_p J/a \sim 2.5$ kV/cm. As the field grows, the energy release $q = i_r E_r'/\rho$ increases, which is accompanied by plasma heating. Heating is strongest near the boundary, where i_r is maximum and ρ is minimum. As the plasma magnetization increases due to an increase in the temperature T_e, the values of R_p and, consequently, E_r' also increase. At $t = 0.9$ μs, they are equal to $R_p \cong 0.8\ \Omega$ and $E_r' \sim 300$ kV/cm. The increase in the field is accompanied by an increase in the energy release q, temperature T_e, and so on. The maximum of $q(z)$ shifts inward into the plasma, where the conductivity and current density are higher because the plasma is less magnetized. At the same time, plasma magnetization is enhanced due to the density decrease caused by discharge in the longitudinal direction [16]. At $t = 0.96$ μs, the plasma resistance is equal to $R_p \cong 6\ \Omega \gg R_n$, the load current is much higher than the plasma current, and the break process is completed.

Evaluation of the plasma parameter at $t = 0.9$ μs gives the value $\gamma \sim 10$ (for $n_e \sim 2 \times 10^{16}$ 1/cm^3, $T_e \sim 3 \times 10^3$ eV, and $H_\varphi \sim 1.2 \times 10^6$ A/m). Under these conditions, one should expect a sharp decrease in the plasma density in the interelectrode gap due to gasdynamic discharge in the transverse direction, as was observed in [22]. The effect is similar to explosive ejection of the plasma onto the electrodes [19, 20] and can be described by the full set of Eqs. (2)–(5). In the concept presented here, this effect is a consequence rather than the cause of the current break.

Hence, the considered mechanism can cause the break in microsecond megaampere currents. This is evidenced by the coincidence (within a factor of 2–3) of the POS operating parameters observed in experiments [22, 23] with those calculated by averaging the plasma parameters in the POS cross section [Eqs. (14)–(16)]. A detailed analysis can only be performed after developing a numerical procedure for solving the two-dimensional equations (2)–(5).

Under the above conditions, the near-electrode diffusion velocity v_e at times t_p is on the order of the Alfvén velocity. Investigation of the process dynamics in the limiting cases $v_e \gg v_A$ and $v_A \gg v_e$ is of interest.

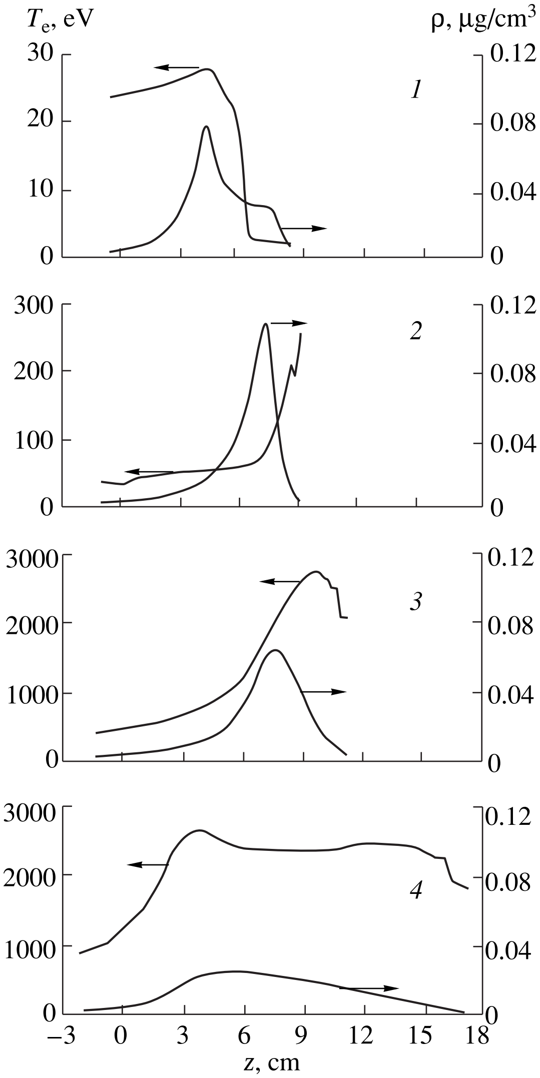

Fig. 5. Profiles of the electron temperature and plasma density at different times: (*1*) 0.6, (*2*) 0.8, (*3*) 0.9, and (*4*) 0.96 μs.

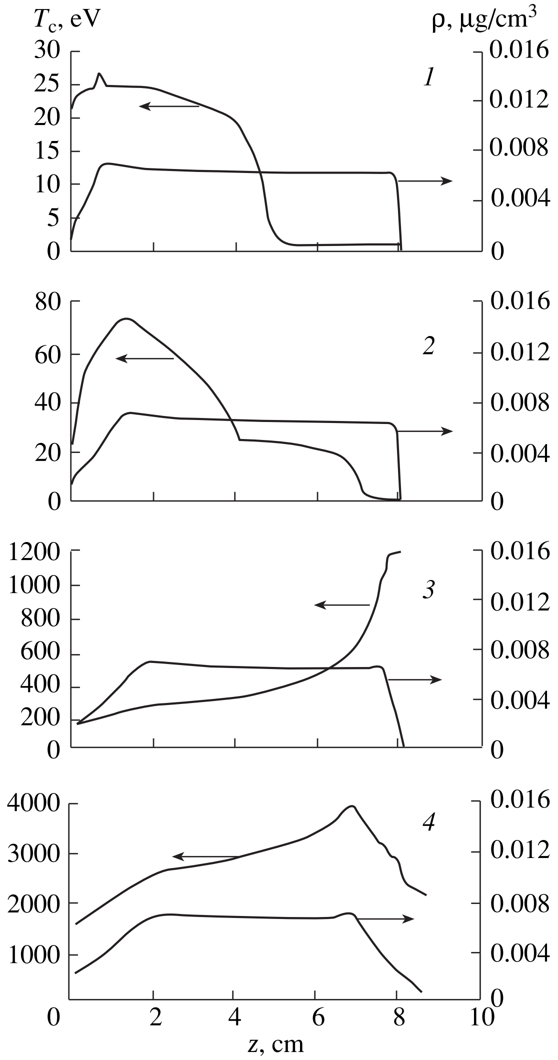

Fig. 6. Profiles of the electron temperature and plasma density for the line plasma density $m_0 = 0.05$ μg/cm² and dJ/dt = 0.75 MA/μs at different times: (*1*) 0.2, (*2*) 0.25, (*3*) 0.29, and (*4*) 0.3 μs.

MECHANISM FOR THE CURRENT BREAK

POS operation can be characterized by the value of the accumulated current and the accumulation time. Let us determine the applicability range of the current-break mechanism when the current growth rate is equal to $dJ/dt = 0.75$ MA/μs. As before, we consider a carbon plasma and assume that $L_n = 0.02$ μH, $r_0 = 7.5$ cm, $L = 8$ cm, and $T_0 = 1$ eV (operating conditions typical of microsecond POSs). The table gives the calculated dependences of the current-accumulation time t_p (the current value is $J_p \cong dJ/dtt_p$) on the density n_i (which is related to the line mass density as $m_0 \cong n_iMAL$). The table also presents the time $t_p^* = 6.25 \times 10^{-10} n_i^{0.6}$, which interpolates the calculated dependence $t_p(n_i)$, and the snowplow coordinate z_{sp} at the current-break time. The snowplow coordinate is determined from the maximum of the plasma density (see Fig. 5, $t = 0.6$ and 0.8 μs).

Although the dynamic characteristics of POS operation are different in these two cases ($z_{sp} \ll L$ for $n_i \approx 10^{14}$ 1/cm³, and the plasma motion is negligible; $z_{sp} \gg L$ for $n_i \approx 10^{16}$ 1/cm³, and the plasma motion is important), the dependences $t_p(n_i)$ in the plasma density range (current-accumulation time range) under examination are the same. This indicates that the current-break mechanisms are the same.

Figure 6 shows the time history of the process for $n_i = 3.1 \times 10^{14}$ 1/cm³. In the stage of magnetic field diffusion, the plasma is immobile. The electron-temperature peak at time $t = 0.2$ μs near $z \sim 1$ and the subsequent rapid plasma heating in the region up to $z \sim 4$ cm at $t = 0.25$ μs are related to complete ionization of the

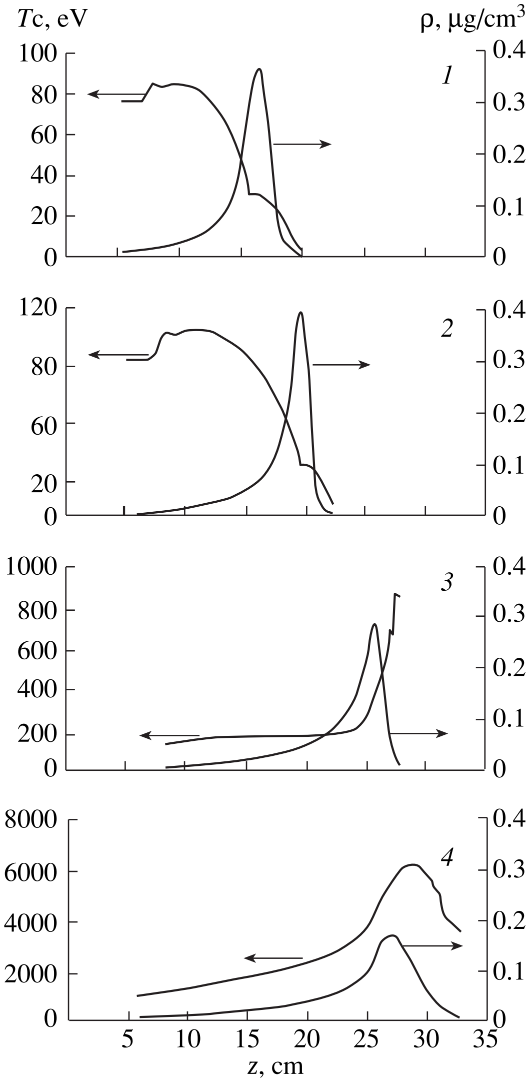

Fig. 7. Profiles of the electron temperature and plasma density for the line plasma density m_0 = 1.25 µg/cm^2 and dJ/dt = 0.75 MA/µs at different times: (*1*) 1.8, (*2*) 1.9, (*3*) 2.0, and (*4*) 2.1 µs.

plasma ($Z = 6$ for $z < 4$ cm). At $t = 0.29$ µs, the magnetic field diffusion wave arrives at the plasma boundary. In the diffusion stage (t = 0.2 and 0.25 µs), the plasma parameter is equal to $\gamma = 8\pi n_e kT_e/B_\varphi^2 \le 0.3$; i.e., as before (Fig. 5), the gasdynamic discharge in the transverse direction is unimportant. By $t = 0.3$ µs, the current break and plasma heating have finished. Later, the plasma expands at a velocity up to ~10^9 cm/s. The presented picture clearly demonstrates the current-break mechanism in an immobile plasma.

The time history of the process in the moving plasma is shown in Fig. 7 ($n_i = 7.8 \times 10^{15}$ 1/cm^3). The snowplow leaves behind the magnetic field diffusion wave (t = 1.8 and 1.9 µs). The penetration of the magnetic field into the plasma is reflected in the displacement of the kink in the T_e profile (the kink corresponds to the boundary of a fully ionized plasma). At $t = 2$ µs, the magnetic field arrives at the plasma boundary. By $t = 2.1$ µs, the current break and plasma heating have finished. In the diffusion stage ($t < 2$ µs), the plasma parameter attains the values $\gamma \sim 5$–10.

Sometimes, when processing data on microsecond POSs, the condition $z_{sp} \sim L$ is used [23]. It is seen from the table that, indeed, at times $t_p \sim 1$ µ*s*, for typical experimental conditions, we have $z_{sp} \sim L$; i.e., in view of the model under consideration, the fact that the operation of a microsecond POS is optimum at $z_{sp} \sim L$ is merely a coincidence.

If the penetration of the magnetic field into the plasma is governed by the near-electrode diffusion mechanism, we have $L \cong \omega_{H_e}/\nu(t_p/\mu_0\pi\sigma)^{1/2}$. Taking into account that $\omega_{H_e} \sim B_\varphi \sim J/r \sim t_p/r$, $\nu \sim n_i$, we obtain $t_p \sim (n_i rL)^{2/3}$ and $J_p t_p \sim (n_i rL)^{4/9}$. The Hall MHD model gives $J_p t_p \sim rL n_i^{1/2}$ [21]. For constant values of r and L, the fourfold increase in n_i leads to an increase in $J_p t_p$ by a factor of 2 in the Hall MHD model, by a factor of $4^{4/9} \cong 1.85$ in the near-electrode model, and by a factor of 1.8 in the experiment [21]. For a constant value of L and the anode radius r_1 = 105 mm, the increase in the cathode radius from r_{02} = 60 mm to r_{01} = 80 mm results in $(J_p t_p)_1/(J_p t_p)_2 \sim 1.4$ [21]. The Hall MHD model gives $(J_p t_p)_1/(J_p t_p)_2 \approx r_{01}/r_{02}\sqrt{(r_1^2 - r_{02}^2)/(r_1^2 - r_{01}^2)} \approx 1.7$ [21], and the near-electrode diffusion model gives $(J_p t_p)_1/(J_p t_p)_2 \approx [r_{01}/r_{02}(r_1^2 - r_{02}^2)/(r_1^2 - r_{01}^2)]^{4/9} \approx 1.4025$. The results of this comparison should only be considered as qualitative. In particular, calculations carried out with actual parameters of a carbon plasma give $t_p \sim n_i^{0.6}$, which is somewhat different from the estimate of $t_p \sim n_i^{2/3}$. Hence, the current-break regime under consideration is characterized by the following features. The current-accumulation time t_p is determined by the penetration of the magnetic field into the plasma via near-electrode diffusion. The plasma becomes more strongly magnetized as the electron temperature increases on the load side; when the diffusion wave arrives at the plasma boundary, the current-break occurs. The sharp increase in the plasma parameter during the current-break stage results in a decrease in the plasma density in the interelectrode gap due to explosive ejection of electrons onto the electrodes.

Since the Alfvén velocity is small at $t_p \le 1$ µs, the current break occurs against the immobile plasma background. When $t_p > 1$ µs, the Alfvén velocity is higher than the near-electrode diffusion velocity and penetration of the magnetic field into the plasma is accompanied by plasma motion in the snowplow regime. In this case, the ion-acoustic velocity may exceed the Alfvén velocity even in the magnetic field diffusion stage. Under these conditions, a premature discharge of the plasma in the transverse direction may reduce the duration and amplitude of the accumulated current; i.e., the break quality at $t_p > 1$ μs may worsen with increasing current duration. Another effect limiting this operation regime on longer time scales may be plasma ejection from the interelectrode gap (the Marshall gun regime).

For a plasma density $n_i = 3.1 \times 10^{14}$ 1/cm^3 at the time $t = 0.25$ μs (Fig. 6), the current velocity reaches the value $u_m \cong 3 \times 10^7$ cm/s for the pulse width $\Delta z_u \cong 0.4$ cm (the characteristic time is $\tau_u \cong \Delta z_u/u_m \cong 10$ ns). The value of u_m is comparable with the near-electrode diffusion velocity, $L/u_n \sim 300$ ns $\sim t_p$. However, the magnetic field cannot penetrate with the current velocity because the electrons are bound to ions through collisions ($t_e \sim 1\ ns \ll t_u$). As the plasma density and, consequently, the collision frequency decrease further, the MHD model passes to the EMHD model. Under these conditions, the magnetic field penetrates into the plasma with increasing current velocity in the KMC regime [8].

The boundaries of the time interval in which the described mechanism can be realized, 0.1 μs $\le t_p \le$ 1 μs, are rather arbitrary. For given values of the current and accumulation time, these boundaries can be shifted to one or another side by changing the plasma composition and POS geometry.

DESIGN OPTIMIZATION OF THE SCHEME OF EXPLOSION EXPERIMENTS ON BREAKING MEGAAMPERE CURRENTS IN AN EMG

When developing the forming system of the EMIR complex, it is expected that one POS will break a microsecond current with an amplitude of up to 2 MA. A peculiarity of POS operation related to the specific features of the primary energy source (EMG) is the low inductance of the accumulation circuit (~0.1 μH) and, accordingly, low supply voltages (~100 kV). Under these conditions, the planned load voltages (up to ~2 MV) can only be achieved by substantially increasing the power (up to 10 times), which is not typical of POSs (the accumulation-circuit inductance is ~1 μH, and the voltage is ~300–600 kV).

It is planned to test the POS in explosion experiments in the Potok-EMG device, which is shown schematically in Fig. 8 (the diameter of the vacuum chamber is 25 cm). The resistance and internal inductance of the EMG are assumed to be constant and equal to L_s = 0.04 μH and R_s = 0.005 Ω, respectively. At the initial instant, the EMG current is equal to $J_0(t = 0)$ = 5–50 MA and the resistance of the explosive switch is $R(t = 0) = 0$. The resistance $R(t)$ increases with time as $R(t) = kR_1(t/\tau)^{1/8}$, where R_1 = 0.23 Ω and τ = 1 μs, and the current is switched to the accumulation circuit with the inductance L_0 = 0.04 μH. The switching time can vary within the range of ~0.5–3 μs. It is planned that, in the first series of experiments, the EMG current will be $J_0(t = 0)$ = 5 MA, the switching time will be ~1 μs ($k = 1$), the length of a nitrogen plasma bridge will be $L \cong 6$ cm, and the load will be inductive ($\hat{Z}_n \longrightarrow L_n\partial/\partial t$, Fig. 1).

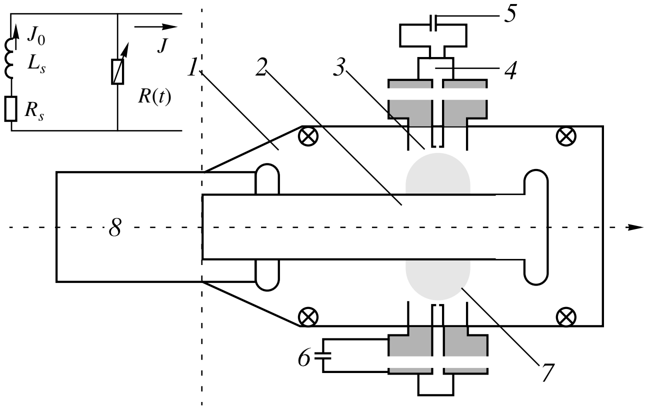

Fig. 8. Schematic of the experiment in which the POS is supplied from an EMG: (*1*) vacuum chamber, (*2*) central electrode, (*3*) coaxial plasma injector, (*4*) pulsed gas-puffing valve, (*5*) valve power supply, (*6*) discharge power supply, (*7*) plasma current channel, and (*8*) EMG.

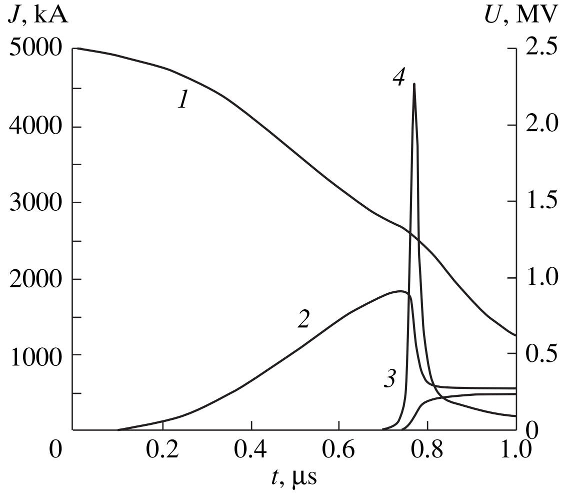

Fig. 9. Time dependences of the currents in (*1*) the EMG, (*2*) accumulation circuit, and (*3*) load and (*4*) the voltage at the load under the optimum operating conditions of the Potok-EMG device.

When numerically optimizing the current-break circuit in the Potok-EMG device, we varied the cathode radius r_0, the line density of nitrogen plasma m_0, and the load inductance L_n. The aim of the optimization was to achieve the maximum attainable potential at the load and to simultaneously retain the high efficiency of

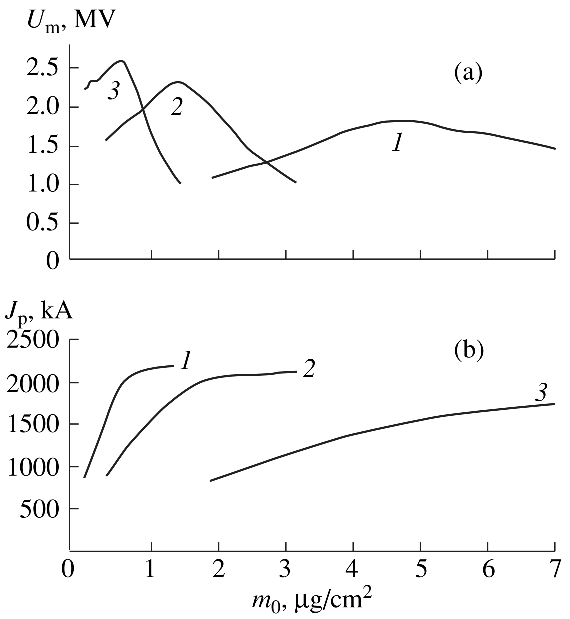

Fig. 10. (a) Voltage amplitude and (b) the corresponding current in the accumulation circuit vs. the line plasma density for different values of r_0: (*1*) 2, (*2*) 5.5, and (*3*) 10 cm.

energy transfer from the EMG circuit

$$\eta = \frac{L_n J_k^2}{L_s J_0^2(t = 0)}, \tag{18}$$

where J_k is the load current (for definiteness, we take the current value 0.1 μs after the potential reaches its maximum).

The calculated time dependences of the currents in the EMG and accumulation circuits and in the load and the load voltage under the optimum POS operating conditions are presented in Fig. 9. The accumulation-circuit current is equal to $J_p \approx 1.9$ MA, the accumulation time is $t_p \approx 0.75$ μs, and the voltage amplitude across the load is $U_m \sim 2.3$ MV.

The results of calculations optimizing the POS operation are illustrated in Figs. 10–12. Figure 10 shows the voltage amplitude at the load U_m and the corresponding value of the accumulated current J_p as functions of the line plasma density m_0 for different values of the cathode radius r_0 at $L_n = 0.16$ μH. It is seen that for every r_0, there is a corresponding optimum value of m_0 for which U_m is maximum. As the cathode radius decreases, both the voltage amplitude U_m and the accumulated current J_p decrease. This is related to the increase in the plasma bridge resistance in the conduction phase for small cathode radii. In Fig. 11, the calculated maximum voltage amplitude U_m, the corresponding value of the accumulated current J_p, and the efficiency η of energy transfer from the EMG are plotted versus the cathode radius r_0. For $r_0 \geq 5$ cm, the voltage amplitude and the effi-

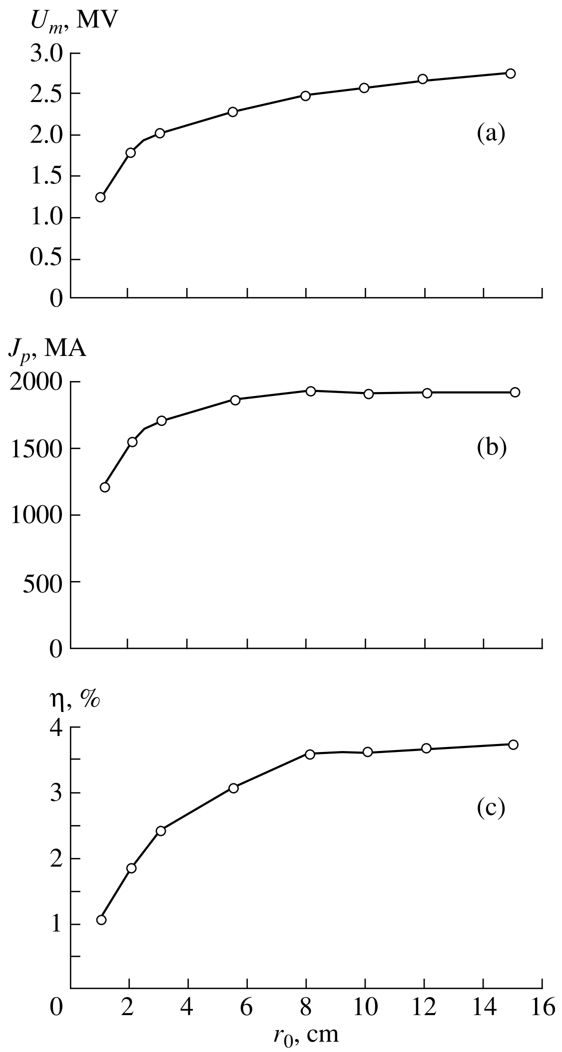

Fig. 11. (a) Voltage amplitude, (b) the corresponding current in the accumulation circuit, and (c) the efficiency of energy transfer to the load vs. the cathode radius for m_0 = 1.5 μg/cm^2 and L_n = 0.16 μH.

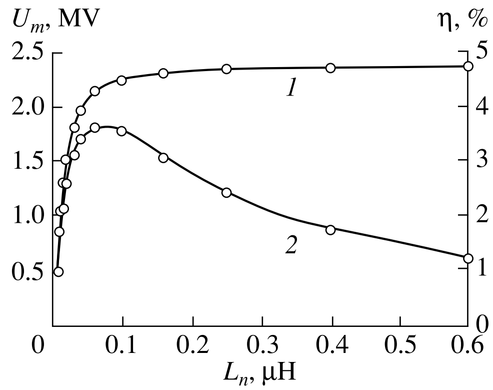

Fig. 12. (*1*) Voltage amplitude and (*2*) the corresponding efficiency of energy transfer to the load vs. the load inductance under the optimum POS operating conditions.

ciency increase more slowly and, for $r_0 \geq 10$ cm, their values and the value of the accumulated current reach their limiting values of $U_m \approx 2.5$ MV, $J_m \approx 2000$ kA, and $\eta \approx 3.5\%$. Using the data in Figs. 10 and 11, the optimum value of r_0 was chosen to be $r_0 = 5.5$ cm. In this case, the maximum line plasma density was $m_0 \approx 1.5$ mg/cm^2 and the plasma mass density was $p_0 = m_0/L \approx 0.25$ mg/cm^3.[1] It should be noted that the efficiency of energy transfer from the EMG to the load was relatively low ($\eta \sim 3.5\%$), because a two-cascade system was used to form the load current: the explosive current switch $\longrightarrow$ POS. In this case, under optimum operation conditions of the system as a whole, the efficiency of energy transfer from the EMG to the POS accumulation-current circuit is ~15% (Fig. 8). Disc EMGs (DEMG-240), which will to be used in the EMIR project [7], ensure an effective time of the current rise in the load of ≤3 μs. This will make it possible to supply the POS accumulation circuit directly, without energy loss in the stage of current sharpening by the explosive switch.

To determine the optimum load for the scheme of experiments in the Potok-EMG device, we performed a series of calculations in which, for the chosen values of $r_0 = 5.5$ cm and $m_0 = 1.5$ mg/cm^2, we varied the load inductance. The calculated dependences of the voltage amplitude U_m and the efficiency η of energy transfer from the EMG circuit to the load on the inductance L_n are shown in Fig. 12. For $L_n \geq 0.1$ μH, the voltage amplitude reaches its limiting value of $U_m \approx 2.36$ MV, corresponding to POS operation with an infinite load resistance. In the range $0.04\ \mu\text{H} \leq L_n \leq 0.16\ \mu\text{H}$, voltage amplitudes of $U_m \geq 2$ MV are attained at an efficiency of $\eta \geq 3\%$. The curves presented in Fig. 9 correspond to $L_n = 0.16$ μH.

CONCLUSION

The operation mechanism of microsecond megaampere-current plasma opening switches has been considered. The penetration of the magnetic field into the plasma occurs via near-electrode diffusion, which determines the current-accumulation time t_p. When the diffusion wave arrives at the plasma boundary, electron heating on the load side enhances the plasma magnetization. The corresponding increase in the resistance is followed by the current break. As a result, the plasma parameter increases sharply, which leads to explosive ejection of the plasma onto the electrodes.

At $t_p \leq 1$ μs, the current break occurs against an immobile plasma background. At $t_p > 1$ μs, the near-electrode diffusion velocity is less than the Alfvén velocity and the process is accompanied by plasma motion in the snowplow regime. On long time scales, this operating regime is limited by plasma ejection from the interelectrode gap (the Marshall gun regime). On short time scales ($t_p \leq 0.1$ μs), the dominant process is the penetration of the magnetic field with the current velocity in the KMC regime [8].

The problem of calculating the POS is formulated on the basis of the adopted concept. The problem reduces to simultaneously solving one-fluid two-temperature MHD equations with allowance for the Hall current and two-dimensional electric-circuit equations. To analyze the solution, one-dimensional equations are derived on the assumption that the size of the near-electrode region where the plasma is strongly magnetized is much smaller that the plasma column length. In this approximation, the POS operating conditions are studied numerically. In our opinion, a comparative analysis of the results of calculations with the experimental data of [22, 23] shows that the processes occurring in the POS can be adequately described using the model presented in this paper.

Using the concept of the POS operation mechanism and the developed numerical procedure, the scheme of the proposed explosion experiment on breaking megaampere currents in the Potok-EMG device under conditions similar to those in the EMIR complex has been optimized.

ACKNOWLEDGMENTS

This work was supported by the Russian Foundation for Basic Research, project no. 99-02-18162.

REFERENCES

1. B. M. Koval'chuk and G. A. Mesyats, Dokl. Akad. Nauk SSSR **284**, 857 (1985) [Sov. Phys. Dokl. **30**, 879 (1985)].
2. D. D. Hinshelwood, J. R. Boller, R. J. Commisso, *et al.*, Appl. Phys. Lett. **49**, 1635 (1986).
3. G. Cooperstein and P. F. Ottinger, IEEE Trans. Plasma Sci. **15**, 629 (1987).
4. B. M. Koval'chuk and G. A. Mesyats, in *Proceedings of the VIII International Conference on High-Power Particle Beams, New York, 1991*, Vol. 1, p. 92.
5. W. Rix, D. Parks, J. Shannon, *et al.*, IEEE Trans. Plasma Sci. **19**, 400 (1991).
6. B. V. Weber, R. J. Commisco, P. J. Goodrich, *et al.*, IEEE Trans. Plasma Sci. **19**, 757 (1991).
7. V. D. Selemir, V. A. Demidov, A. V. Ivanovskiĭ, *et al.*, Fiz. Plazmy **25**, 1085 (1999) [Plasma Phys. Rep. **25**, 1000 (1999)].
8. A. S. Kingsep, Yu. V. Mokhov, and K. V. Chukbar, Fiz. Plazmy **10**, 854 (1984) [Sov. J. Plasma Phys. **10**, 495 (1984)].
9. A. S. Kingsep, K. V. Chukbar, and V. V. Yan'kov, in *Reviews of Plasma Physics*, Ed. by B. B. Kadomtsev (Énergoizdat, Moscow, 1987; Consultants Bureau, New York, 1990), Vol. 16.

---

[1] Laser interferometry measurements of the plasma parameters in the Potok-EMG device show that a density of ≥1 mg/cm^3 in a nitrogen plasma can be attained with one injector.

10. A. S. Kingsep and A. A. Sevast'yanov, Fiz. Plazmy **17**, 205 (1991) [Sov. J. Plasma Phys. **17**, 119 (1991)].
11. A. V. Gordeev, A. V. Grechikha, and A. V. Gulin, Fiz. Plazmy **17**, 650 (1991) [Sov. J. Plasma Phys. **17**, 381 (1991)].
12. L. I. Rudakov, Fiz. Plazmy **19**, 835 (1993) [Plasma Phys. Rep. **19**, 433 (1993)].
13. A. Fruchtman, Phys. Fluids B **3**, 1908 (1991).
14. R. J. Mason, P. L. Auer, R. N. Sudan, *et al.*, Phys. Fluids B **5**, 1115 (1993).
15. P. F. Ottinger, S. A. Goldstein, and R. A. Meger, J. Appl. Phys. **56**, 774 (1984).
16. K. V. Chukbar and V. V. Yankov, Zh. Tekh. Fiz. **58**, 2130 (1988) [Sov. Phys. Tech. Phys. **33**, 1293 (1988)].
17. A. S. Kingsep and A. A. Sevast'yanov, Fiz. Plazmy **17**, 1183 (1991) [Sov. J. Plasma Phys. **17**, 685 (1991)].
18. A. V. Gordeev, A. V. Grechikha, and Ya. L. Kalda, Fiz. Plazmy **16**, 95 (1990) [Sov. J. Plasma Phys. **16**, 55 (1990)].
19. P. V. Sasorov, Pis'ma Zh. Éksp. Teor. Fiz. **56**, 614 (1992) [JETP Lett. **56**, 599 (1992)].
20. A. A. Esaulov and P. V. Sasorov, Fiz. Plazmy **23**, 624 (1997) [Plasma Phys. Rep. **23**, 576 (1997)].
21. A. S. Chuvatin, A. A. Kim, V. A. Kokshenev, *et al.*, Izv. Vyssh. Uchebn. Zaved., Fiz. **40** (12), 56 (1997).
22. D. Hinshelwood, B. Weber, J. M. Grossmann, *et al.*, Phys. Rev. Lett. **68**, 3567 (1992).
23. W. Rix, P. Coleman, J. R. Thompson, *et al.*, IEEE Trans. Plasma Sci. **25**, 169 (1997).
24. S. I. Braginskii, in *Reviews of Plasma Physics*, Ed. by M. A. Leontovich (Gosatomizdat, Moscow, 1963; Consultants Bureau, New York, 1963), Vol. 1.
25. V. F. Bukharov, V. I. Chelpanov, V. A. Demodov, *et al.*, in *Proceedings of the XI International Conference on Pulsed Power, Monterey, 1997*, Vol. 2, p. 1029.
26. Yu. P. Raĭzer, Zh. Éksp. Teor. Fiz. **36**, 1583 (1959) [Sov. Phys. JETP **9**, 1124 (1959)].
27. A. A. Samarskiĭ and Yu. P. Popov, *Difference Schemes in Gas Dynamics* (Nauka, Moscow, 1975).
28. A. A. Radtsig and B. M. Smirnov, *Reference Data on Atoms, Molecules, and Ions* (Énergoatomizdat, Moscow, 1986, Springer-Verlag, Berlin, 1985).

Translated by N. Larionova

Technical Physics, Vol. 46, No. 3, 2001, pp. 339–341. Translated from Zhurnal Tekhnicheskoĭ Fiziki, Vol. 71, No. 3, 2001, pp. 69–71.
Original Russian Text Copyright © 2001 by Rezinkina, Rezinkin, Nosenko.

BRIEF COMMUNICATIONS

A Correlation between Partial Discharge Characteristics and Dendrite Growth Stages in Polyethylene Insulation

M. M. Rezinkina, O. L. Rezinkin, and M. I. Nosenko
Kharkov Polytechnical Institute, Kharkov, Ukraine
e-mail: marinaR@kpi.kharkov.ua

Received May 15, 2000

Polyethylene is widely used as an insulating material (especially as cable insulation); therefore, of interest are ionization aging processes that cause its breakdown. For cable diagnostics, the partial discharge (PD) technique is used. In particular, PD characteristics may help in identifying the type of a defect [1]. Theoretical and experimental studies where the stage of dendrite growth in polyethylene was judged from the sequence of PD occurrence phases according to an applied voltage were summarized in [2]. It was concluded that this sequence is strictly determinate for either half-wave of the voltage when dendrites start to grow. Practical experience shows, however, that these processes are of stochastic nature and PD phases can hardly be reproduced regularly, as exemplified by our measurements.

Having detected PDs in a cable, one should assess how much dangerous dendrites responsible for their appearance are, i.e., how quickly they propagate. In our experiments, we tried to trace a correlation between dendrite growth stages and the characteristics of attendant PDs.

As was noted [3], the level of apparent PD charges during dendrite growth remains nearly the same, within 10^{-11}–10^{-12} C. The phases of PD occurrence rather than the PD charge level change significantly during treeing [12]. Technically, the detection of the PD initial stage without measuring the amount of apparent charge and sweeping PD current (relative to an applied voltage) seems to be the simplest and cheapest practical way of diagnostics. In our work, the initial phase of PDs vs. applied voltage was detected with an ADC and a PC.

In most laboratory studies of these processes, a needle–plane electrode system is applied (see, e.g., [3–6]). Such experimental geometry allows the location of a dendrite; moreover, it eliminates the latent time of its initiation, so that dendrite evolution can be observed from the very beginning.

Experiments were performed with braid-free pieces of an RK-100-7-13 cable. They were hot-deformed to measure 15 × 15 × 5 mm. A needle with a tip radius of 2 μm that served as a high-voltage electrode was arranged normally to the cable core at a distance of 1.5 mm. The core was grounded, and the mains-frequency voltage applied to the needle was $U = 7$ and 9 kV. To avoid a corona and gap bridging over the surface, as well as to provide optical detection of a dendrite, the specimens were immersed in a transparent cell filled with transformer oil.

Tentative experiments showed that for this electrode system, the value $U = 7$ kV was close to that of PD initiation. At this voltage, a dendrite stops propagating lengthwise 25–30 min after initiation; then, its branches thicken and simultaneously widen. The value $U = 9$ kV is close to the breakdown voltage of the system, and the primary branch of a dendrite rapidly grew in all specimens. At this voltage, one can trace changes in the statistical distributions over PD initiation phases for dendrites growing lengthwise.

Usually, statistical characteristics of PDs are compared using the third and fourth central moments [1]: skewness, S^+ and S^-, and kurtosis, K^+ and K^-, which are measured for the positive and negative half-waves of an applied voltage, respectively. Statistical phase distributions of PDs that have been obtained thus far are, as a rule, multimodular; therefore, skewness and kurtosis derived directly from experimental data do not reflect the average distribution, which smooths out statistical spikes. Statistical phase distributions of PD that are constructed relative to the applied voltage are complex functions varying in accordance with the dendrite evolution stage. Hence, the most general approach to smooth them is the use of polynomials. In order to describe the phase distributions in terms of skewness and kurtosis, we approximated them by polynomials of the tenth to twentieth degree. Along with PD detection, we optically observed dendrites causing them. Typical

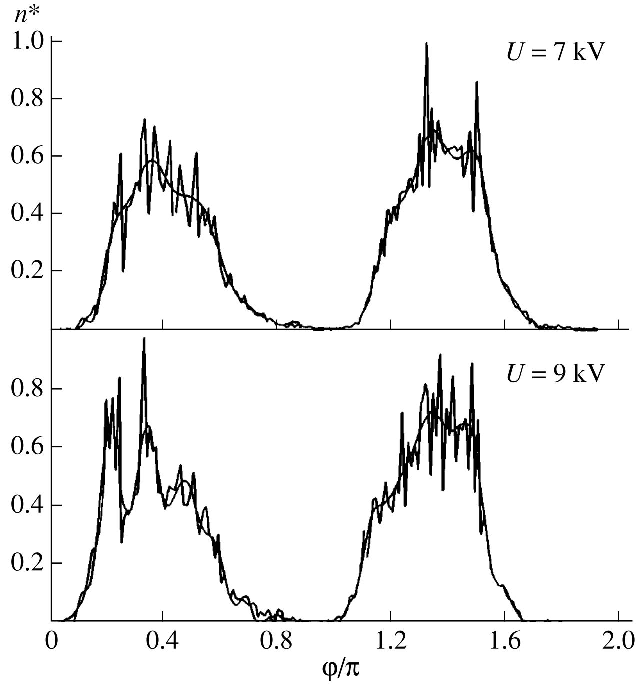

Fig. 1. Relative number of PDs in the polyethylene insulation $n^* = n/n_{\max}$ vs. phase φ of their occurrence at the early stage of dendrite growth (n and $n_{\max}$ are the number of PDs and the maximum number of PDs, respectively).

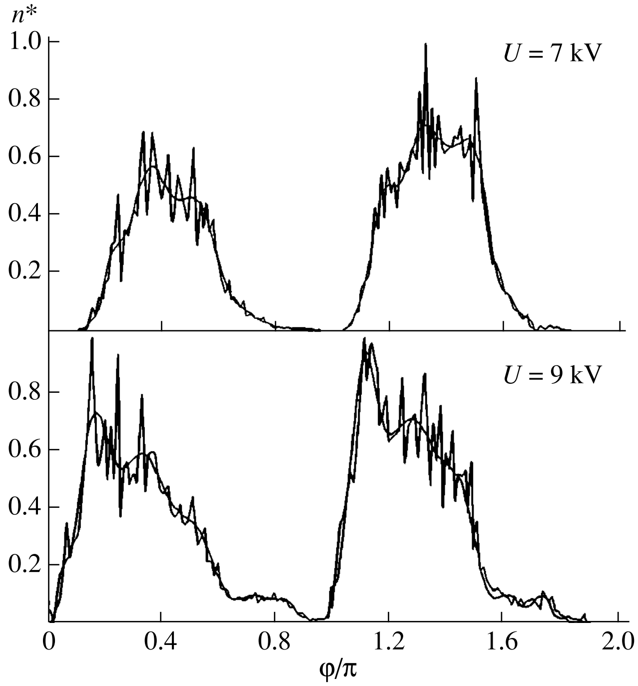

Fig. 2. n^* vs. φ 12 min after the initiation of a dendrite, when it still does not bridge the gap (U = 9 kV), and 1.5 h after the initiation of a dendrite, when it stops to grow lengthwise (U = 7 kV).

statistical curves that describe the relative number of PDs vs. phase of their occurrence at U = 7 and 9 kV are shown in Figs. 1 (initial stage of dendrite growth) and 2 (later stage of dendrite growth). In Fig. 2, the curve taken for U = 9 kV reflects the situation immediately before the breakdown of the gap, while that for 7 kV reflects the situation 1.5 h after the initiation of a dendrite, when it stopped growing lengthwise. Both figures represent the distributions approximated (smoothed) by the twentieth-degree polynomial.

The phase distribution of PD initiation significantly varies in time and may characterize a dendrite evolution stage and the rate of propagation of its primary branch. At the initial stage, these statistical distributions have a similar shape, irrespective of the applied voltage: they are skewed both in the positive and in the negative half-waves of the voltage. In the positive half-wave, they are positively skewed, their averages having $S^+ = 0.278$ for 9 kV and 0.372 for 7 kV. In the negative half-wave, the distributions are skewed weakly negatively, having $S^- = -0.09$ and -0.145 for 9 and 7 kV, respectively. Their average kurtosis is negative both in the positive and in the negative half-waves: $K^+ = -0.607$, $K^- = -0.753$ for 9 kV and $K^+ = -0.409$, $K^- = -0.628$ for 7 kV. At the later stage of dendrite evolution, the distributions, as well as the associated skewness and kurtosis, change in a different way, depending on whether the dendrite continues to propagate or not. If the primary branch of the dendrite grows, the characteristics after the breakdown of the gap (U = 9 kV) change: they remain similar in both half-waves, namely, negatively skewed ($S^+ = -0.558$ and $S^- = -0.371$), but become sharper ($K^+ = -0.19$ and $K^- = -0.388$). If the dendrite does not grow and only thickens (U = 7 kV), the distributions in both half-waves become strongly skewed: $S^+ = -0.225$, $S^- = -0.029$, $K^+ = -0.407$, and $K^- = -0.739$.

CONCLUSIONS

(1) At the initial stage of dendrite evolution and also when it stops growing lengthwise, the phase statistic distributions have the following features. They are smooth and skewed in both the positive and the negative half-waves of the applied voltage. In the former half-wave, they are positively skewed, while in the latter, they are nearly symmetric or negatively skewed (Figs. 1, 2; U = 7 kV).

(2) When the dendrite rapidly grows lengthwise and becomes dangerous (that is, can bridge the interelectrode gap), the phase distributions of PDs become similar in both half-waves: they are positively skewed and smoothed (Fig. 2, U = 9 kV).

REFERENCES

1. F. H. Kreuger, E. Gulski, and A. Krivda, IEEE Trans. Electr. Insul. **28**, 917 (1993).
2. M. Hoof and R. Patch, in *Proceedings of the 9th International Symposium on High Voltage Engineering, 1995,* Vol. 5, p. 5606.
3. G. S. Kuchinskiĭ, *Partial Discharges in High-Voltage Constructions* (Énergiya, Leningrad, 1979).
4. G. Krause, in *Proceedings of the 7th International Symposium on High Voltage Engineering, Dresden, 1991,* Vol. 7, p. 107.
5. H. Kawamura and M. Nawata, in *Proceedings of the 10th International Symposium on High Voltage Engineering, Montreal, 1997.*
6. G. Sagle, in *Proceedings of the 10th International Symposium on High Voltage Engineering, Montreal, 1997.*

Translated by V. Isaakyan

Technical Physics, Vol. 46, No. 3, 2001, pp. 342–345. Translated from Zhurnal Tekhnicheskoĭ Fiziki, Vol. 71, No. 3, 2001, pp. 72–75.
Original Russian Text Copyright © 2001 by Gurin, Shlyapin, Sabitov.

BRIEF COMMUNICATIONS

Negative Differential Resistance in Thin-Film Electroluminescent Emitters Based on Zinc Sulfide

N. T. Gurin, A. V. Shlyapin, and O. Yu. Sabitov
Ulyanovsk State University, Ulyanovsk, 432700 Russia
e-mail: soy@sv.uven.ru

Received May 15, 2000.

Abstract—*S*- and *N*-type negative differential resistance (NDR) has been observed in thin-film electroluminescent emitters based on zinc sulfide doped with manganese, and conditions for its emergence have been identified. It has been found that when a negative half-wave of voltage is applied to the nontransparent top electrode, an *S*-type NDR with a region of decreasing current is observed, and when it is applied to the transparent bottom electrode, the NDR will be *N*-type. The emergence of NDR is due to space charges which form in the near-cathode and near-anode layers of the phosphor. © *2001 MAIK "Nauka/Interperiodica".*

One of the main problems in studies on the prebreakdown electroluminescence in thin-film electroluminescent emitters (TFEE) having a metal/insulator/semiconductor (phosphor)/insulator/metal (MISIM) structure is that the phosphor layer is separated from the alternating voltage source of excitation by insulator layers, which poses problems in following the kinetics of the processes of charge carrier generation and transport and their interaction with radiation centers and defects of the phosphor crystal lattice in a strong electric field. A number of experimental studies give evidence of a considerable influence exerted by a space charge in the phosphor layer on the kinetics of electroluminescence [1–5], which, in particular, can give rise to a region of *S*-type negative differential resistance (NDR) in the dependence of the current flowing through the phosphor layer in the radiation regime of TFEE on the average field in this layer [5]. At the same time, the data reported in [1] indicate the possibility, under certain phosphor excitation conditions, of an *N*-type NDR in this dependence, the origin of which is still not clear.

In view of the above, the purpose of this work is to study the conditions for the emergence of *S*- and *N*-type NDR in TFEEs and their overall characteristics. For this purpose, experimental studies were carried out on TFEEs with a MISIM structure in which one M is a transparent bottom electrode of SnO_2 0.2 μm thick deposited on a glass substrate and the other M is a nontransparent Al thin-film top electrode 0.15 μm thick; S is an electroluminescent layer of ZnS : Mn (0.5 wt %) 0.54 μm thick; and I is an insulating layer of $ZrO_2 \cdot Y_2O_3$ (13 wt %) 0.15 μm thick. The phosphor layer was deposited by vacuum evaporation in a quasi-closed chamber and then annealed at 250°C for one hour; the nontransparent layer was deposited by vacuum evaporation; and the thin-film insulating layers, by electron beam evaporation.

Variations with time of the current and the instantaneous emission intensity of TFEEs under excitation by triangular voltage pulses of alternating polarity from a G6-34 generator with an additional amplifier-shaper and a G5-89 external driving generator were studied experimentally. Amplitude of the pulses was 160–170 V with nonlinearity not exceeding 2%. In the single starting mode the excitation voltage was a packet of two excitation periods of triangular pulses following with a frequency of 2, 10, 50, 200, 500, or 1000 Hz. The time between single starts varied from 0.1 to 100 s. In the continuous excitation mode the frequency varied from 10 to 1000 Hz. The current through the TFEEs was measured using a 100 Ω–10 kΩ resistor connected in series with the TFEE; the voltage drop across the resistor did not exceed 1 V. The instantaneous value of emission intensity was measured with an FEU-84-3 photomultiplier tube. Variations with time of the excitation intensity, the current through the TFEE, and the instantaneous value of emission intensity were registered with a C9-16 two-channel memory oscilloscope connected through an interface with a computer; this setup was capable of registering and storing 2048 points in a chosen sampling period with an error not exceeding 2%. The software used for mathematical and graphical processing was Maple V Release4. Version 4.00b and GRAPHER Version 1.06. 2-D Graphing System.

It is known [5, 6] that for excitation voltages not exceeding a threshold value for the start of emission a TFEE can be represented as a series connection of capacitors formed by the two insulating layers C_i and

1063-7842/01/4603-0342$21.00 © 2001 MAIK "Nauka/Interperiodica"

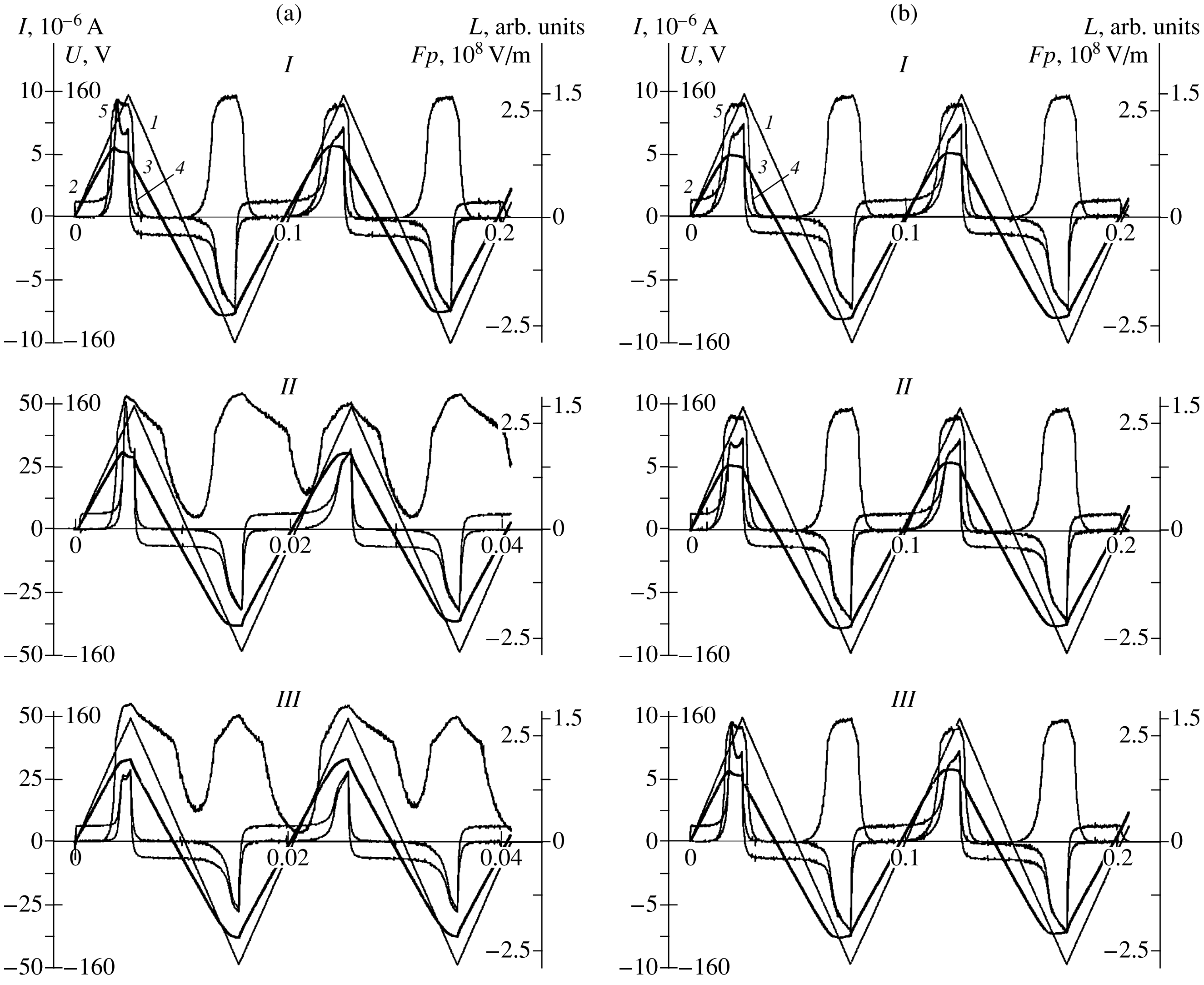

Fig. 1. $V(t)$ (*1*), $I_e(t)$ (*2*), $F_p(t)$ (*3*), $I_p(t)$ (*4*), and $L(t)$ (*5*) dependences for two periods of the excitation voltage: a—negative half-wave of the voltage in the first half-period applied to the top electrode at T_s = 100 s and the excitation voltage frequency *I*—10, *II*—50 Hz, *III*—positive half-wave of the voltage in the first half-period applied to the top electrode at T_s = 50 s and the excitation voltage frequency 50 Hz; b—negative half-wave of the voltage in the first half-period applied to the top electrode at the excitation voltage frequency 50 Hz and the starting period T_s: *I*—0.5, *II*—5, and *III*—100 s.

by the layer of phosphor C_p. When the threshold voltage is exceeded, the strong electric field causes the tunneling of electrons from states at the phosphor/insulator interface; these electrons are accelerated in the electric field and excite Mn^{2+} emission centers and produce the impact ionization of crystal lattice defects. As a result, above the threshold voltage through the phosphor layer of thickness d_p, a current $I_p(t)$ will flow consisting of the bias and conduction components, which determine the kinetics of charge carrier transport, excitation of emission centers, formation of space charges, and field redistribution in the layer.

Given a formula for variation with time of the excitation voltage $V(t)$ applied to the TFEE and the current in the external circuit $I_e(t)$, the average field $F_p(t)$ in the phosphor layer will have the form

$$F_p(t) = \frac{1}{d_p}\left[V(t) - \frac{1}{C_i}\int_0^t I_e(t)dt\right]. \qquad (1)$$

The conduction current in the phosphor layer at voltages higher than the threshold voltage and in the absence in the layer of a space charge is given by [1]

$$I_p(t) = I_e(t)\frac{C_i + C_p}{C_i} - C_p\frac{dV(t)}{dt}. \qquad (2)$$

However, because of the accumulation of space charge in the phosphor layer, the capacitance C_p also varies with time (and, accordingly, voltage) and the current $I_p(t)$ determined by (2) has a reactive compo-

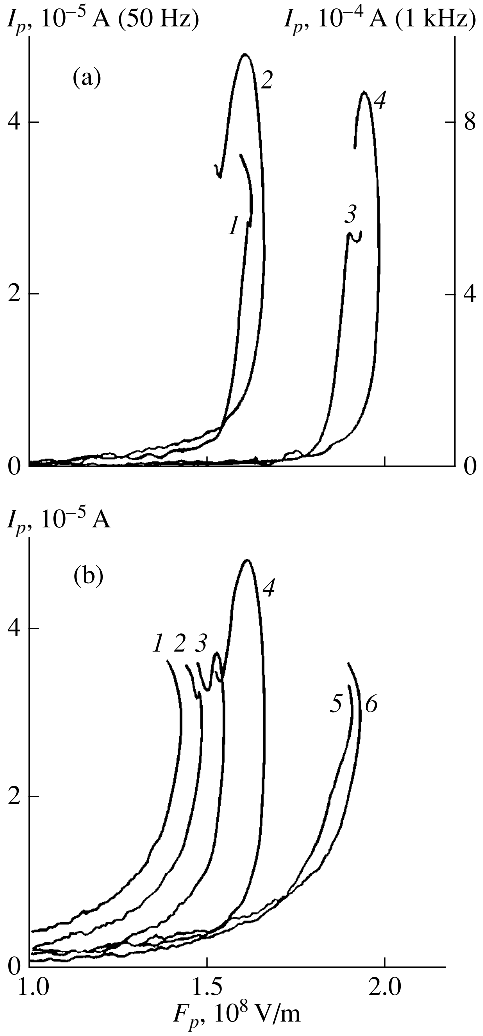

Fig. 2. $I_p(F_p)$ dependences: a—negative half-wave of the excitation voltage applied in the first half-period with the starting period T_s = 100 s to the bottom electrode (*1*, *3*) and the same applied to the top electrode (*2*, *4*); the excitation voltage frequency is 50 Hz (*1*, *2*) and 1 kHz (*3*, *4*); b—negative half-wave of the excitation voltage of frequency 50 Hz applied in the first half-period to the top electrode, single starting with T_s = 0.1 s (*1*), 0.5 s (*2*), 5 s (*3*), and 100 s (*4*); continuous excitation mode at 50 Hz with the negative half-wave of the voltage applied to the lower (*5*) and top electrodes (*6*).

nent and consequently carries information on the accumulation of space charge in the phosphor layer. Therefore, a function $I_p(F_p)$ derived from formulas (1) and (2) describes some semiconductor device containing a phosphor layer with phosphor/insulator interfaces that have an initial geometric capacitance C_p and a thickness d_p to which a voltage of $V_p(t) = F_p(t)d_p$ is applied.

Shown in Fig. 1 are typical variations with time of V, I_e, and the instantaneous emission intensity L for the single starting mode and the curves $F_p(t)$ and $I_p(t)$ calculated by formulas (1) and (2) taking into account the voltage drop across the resistor for current measurements at C_i = 986 pF and C_p = 250 pF. C_e and C_p values were determined from the measured total capacitance of TFEE C_e = 200 pF and its geometric dimensions.

The dependences obtained at all excitation voltage frequencies have the following characteristic features (Fig. 1): functions $L(t)$, $I_e(t)$, $I_p(t)$, and $F_p(t)$ are asymmetric with respect to the excitation voltage polarity because of the TFEE technology used, which produced different surface state densities at the upper and lower phosphor/insulator interfaces [4, 5], and structural defects in the phosphor layer. The field F_p changes after the onset of emission, giving evidence of an accumulation of space charge in the phosphor layer [1, 6, 7]. An additional peak of the current I_e is seen and a weaker peak of the current I_p in the first half-period of the excitation voltage, their amplitudes increasing with the starting period T_s and for the current I_p described approximately by an expression of the form $[1 - \exp(-t/\tau)]$, where $\tau = (37 \pm 3)$ s throughout the frequency range of excitation voltage. The additional peak of the current I_e (and I_p) is accompanied by an analogous peak in the curve $L(t)$, which can be explained by an increase in the excitation probability of emission centers in proportion to the current density in the phosphor layer [8]. In some ranges, the current $I_p(t)$ decreases simultaneously with the drop in $F_p(t)$ when the negative half-wave of the excitation voltage in the first period is applied to the top electrode, which is evidence of an *S*-type NDR region in the $I_p(F_p)$ curve, and there appears a region of decreasing current $I_p(t)$ coinciding with growth of the field $F_p(t)$ when the positive half-wave of the excitation voltage in the first period is applied to the top, which is characteristic of *N*-type NDR.

$I_p(F_p)$ curves corresponding to values of the voltage $V(t)$ below its amplitude value V_m (Fig. 2) fully confirm the conclusion of the existence of the *S*- and *N*-types of NDR. A feature of the $I_p(F_p)$ dependence in the negative half-wave of the first period of the excitation voltage (Fig. 2) applied to the top electrode is the emergence at $T_s \geq 0.1$–0.5 s, apart from the region of smooth *S*-type NDR, of a region where the current I_p decreases with decreasing field F_p and increases with T_s (Fig. 2b). At low excitation voltage frequencies (2, 10, 50 Hz), after decreasing, the current again rises (Fig. 2b), and at higher frequencies and the same voltage amplitude of V_m = 170 V, this region of rising current first shrinks and then disappears altogether (Fig. 2a, curve *4*). When a positive half-wave of the first period of excitation voltage is applied to the top electrode, the $I_p(F_p)$ curve shows an *N*-type NDR region (Fig. 2a), which also expands with increasing T_s and the excitation voltage frequency. This region then transforms into an *S*-type NDR, which disappears at higher frequencies. The rise of F_p with T_s results from neglecting the residual polarization field in the calculations. In the continuous excitation mode (Fig. 2b) at the excitation voltage frequencies 10 and 50 Hz, the $I_p(F_p)$ curves contain only the smooth S-region, which disappears when the frequency is raised to ~ 200 Hz. The large F_p values compared with the single starting mode are due to the initial condition used in the calculation of F_p: after the quasi-stationary excitation regime is established, the charges passing the TFEE in different half-periods of the voltage are considered equal.

The obtained results can be explained in the following way. The technology used in phosphor preparation results in a deficit of zinc atoms and an excess of sulfur atoms at the lower phosphor/insulator interface and, conversely, excess zinc atoms and a deficit of sulfur atoms at the upper interface, creating structural defects (zinc and sulfur vacancies, interstitial zinc), and various complexes with associated shallow and deep donor and acceptor levels [3–5, 7]. In a strong electric field, ionization and recharging of these centers occurs and space-charge regions form near the anode and cathode, whose fields interact differently with the external field for different polarities of the first half-period of the excitation voltage. In particular, the appearance of the smooth S-region in the $I_p(F_p)$ dependence is probably related to the ionization and recharging of deep donor centers introduced by zinc vacancies near the lower interface [3, 4]. The region of current drop in the dependence with S-type NDR and the region of N-type NDR might be due to the space charge near the top electrode whose lifetime in the excited state is ~37 s. In order to clarify the nature of these centers and their parameters, further studies are necessary.

REFERENCES

1. V. P. Singh and S. Krishna, J. Appl. Phys. **70**, 1811 (1991).
2. A. Abu-Dayah, S. Kobayashi, and J. F. Wager, Appl. Phys. Lett. **62**, 744 (1993).
3. A. Abu-Dayah, J. F. Wager, and S. Kobayashi, J. Appl. Phys. **74**, 5575 (1993).
4. A. Abu-Dayah and J. F. Wager, J. Appl. Phys. **75**, 3593 (1994).
5. K. A. Neyts, D. Corlatan, P. de Visschere, *et al.*, J. Appl. Phys. **75**, 5339 (1994).
6. E. Bringuier, J. Appl. Phys. **66**, 1314 (1989).
7. E. Bringuier, Philos. Mag. B **75**, 209 (1997).
8. N. T. Gurin and O. Yu. Sabitov, Zh. Tekh. Fiz. **69** (5), 65 (1999) [Tech. Phys. **44**, 537 (1999)].

Translated by B. Kalinin

Technical Physics, Vol. 46, No. 3, 2001, pp. 346–347. Translated from Zhurnal Tekhnicheskoĭ Fiziki, Vol. 71, No. 3, 2001, pp. 76–77.
Original Russian Text Copyright © 2001 by Dvoesherstov, Petrov, Cherednik, Chirimanov.

BRIEF COMMUNICATIONS

The Temperature Coefficients of Delay of Surface Acoustic Waves in LGS and LGN Crystals in a Wide Temperature Range

M. Yu. Dvoesherstov, S. G. Petrov, V. I. Cherednik, and A. P. Chirimanov
Lobachevsky State University, pr. Gagarina 23, Nizhni Novgorod, 603600 Russia

Received February 28, 2000; in final form, June 28, 2000

Abstract—Numerical analysis of the first- and second-order temperature coefficients of the delay of surface acoustic waves (SAWs) in LGS and LGN crystals was carried out. The calculations were performed along thermostable directions in a wide temperature range. The effect of an aluminium layer having a finite thickness on the SAW temperature characteristics is shown. © *2001 MAIK “Nauka/Interperiodica”.*

The propagation of SAWs in new LGS and LGN crystals is of considerable interest. These crystals offer good thermal stability and a high value of the electromechanical coupling coefficient K^2 [1]. To date, in LGS and LGN, cuts and directions having the zeroth first-order temperature coefficient of delay at room temperature ($t_0 = 25$°C) have been found by numerical simulation [2]. Note that low sensitivity of thermostable directions to the environmental temperature is among the basic demands in SAW technology.

In this study, we performed numerical evaluation of the first- and second-order temperature coefficients of SAW delay ($\mathrm{TCD}^{(1)}$ and $\mathrm{TCD}^{(2)}$, respectively) for thermostable orientations in the crystals under consideration at temperatures from –100 to +120°C. The calculations were carried out both for the free crystal surface and for the surface coated by an aluminium layer of a finite thickness. The temperature dependence of material constants for these crystals was found to be strongly nonlinear in contrast to ST,X-cut quartz.

It is known that the temperature (t) dependence of all the components of material constants for a crystal can be written as follows [3]:

$$\begin{aligned} &C_{ij}(t) \\ &= C_{ij}(t_0)(1 + TC_{ij}^{(1)}(t - t_0) + TC_{ij}^{(2)}(t - t_0)^{(2)} + \ldots), \\ &e_{ij}(t) = e_{ij}(t_0)(1 + Te_{ij}^{(1)}(t - t_0) + Te_{ij}^{(2)}(t - t_0)^{(2)} + \ldots), \\ &\varepsilon_{ij}(t) = \varepsilon_{ij}(t_0)(1 + T\varepsilon_{ij}^{(1)}(t - t_0) + T\varepsilon_{ij}^{(2)}(t - t_0)^{(2)} + \ldots), \\ &\rho(t) \\ &= \rho(t_0)(1 + T\rho^{(1)}(t - t_0) + T\rho^{(2)}(t - t_0)^{(2)} + \ldots), \end{aligned} \tag{1}$$

Here, $TC_{ij}^{(1)}$, $Te_{ij}^{(1)}$, $T\varepsilon_{ij}^{(1)}$, $TC_{ij}^{(2)}$, $Te_{ij}^{(2)}$, $T\varepsilon_{ij}^{(2)}$, $T\rho^{(1)}$, and $T\rho^{(2)}$ are the first- and second-order temperature coefficients of the elastic constants, piezoelectric constants, dielectric constants, and the density of the crystal, respectively; $i, j = 1, \ldots, 6$. In calculating the $\mathrm{TCD}^{(1)}$ and $\mathrm{TCD}^{(2)}$, as well as the relative change of the SAW delay time (frequency) $(\tau - \tau(t_0))/\tau(t_0) = -\Delta f/f_0$, we used the expressions [3, 4]

$$\mathrm{TCD}^{(1)} = \frac{1}{\tau(t_0)}\frac{d\tau}{dt},$$

$$\mathrm{TCD}^{(2)} = \frac{1}{2}\frac{1}{\tau(t_0)}\frac{d^2\tau}{dt^2} = \frac{1}{2}\frac{d\mathrm{TCD}^{(1)}}{dt},$$

$$\frac{\tau - \tau(t_0)}{\tau(t_0)} = -\frac{f - f(t_0)}{f(t_0)}$$

$$= \mathrm{TCD}^{(1)}(t - t_0) + \mathrm{TCD}^{(2)}(t - t_0)^2,$$

where $\tau(t)$, $\tau(t_0)$, f, and $f(t_0)$ are the SAW delay time and the frequency at t and t_0, respectively. Recent numeric

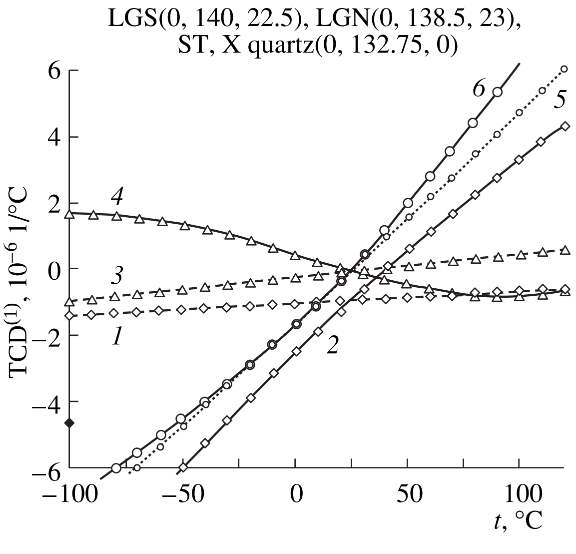

Fig. 1. Temperature dependences of the $\mathrm{TCD}^{(1)}$ for SAWs with the allowance for the first order (curves *1*, *3*, and *5*) and the first + second orders (curves *2*, *4*, and *6*) of the material constants for the LGS, LGN, and ST,X-cut quartz crystals.

1063-7842/01/4603-0346$21.00 © 2001 MAIK “Nauka/Interperiodica”

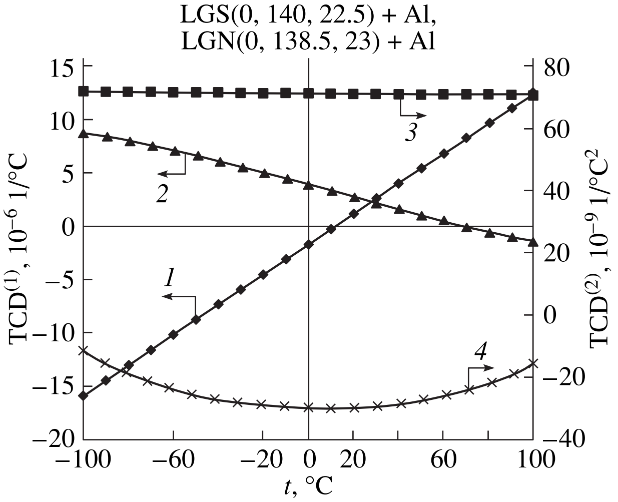

Fig. 2. Temperature dependences of the TCD$^{(1)}$ and TCD$^{(2)}$ of SAWs for the (*1*, *2*) LGS (0, 140, 22.5°) and (*3*, *4*) LGN (0, 138.5, 23°) Al-coated crystals ($h/\lambda = 0.005$).

studies [5–9] on the temperature properties of SAWs in LGS and LGN crystals have given TCD$^{(1)}$ and TCD$^{(2)}$ values that significantly differ from available experimental data [7, 8]. This is due to the fact that the values of the temperature material constants of both orders used in those calculations were different. The refined values of the temperature constants are given in [7], where the values of $\Delta f/f(t_0)$ in LGS (0, 140, 24°) crystals were calculated and measured in a wide temperature interval. When the material constants from [7] were used in the calculations, the theoretical and experimental temperature dependences of $\Delta f/f(t_0)$ completely coincide.

As an example, Fig. 1 shows the calculated temperature dependences of the TCD$^{(1)}$ for SAWs in LGS (0, 140, 22.5°), LGN (0, 138.5, 23°), and ST,X-cut quartz (0, 132.75, 0°) crystals. Both the first and the first + second orders of the temperature constants of the materials are taken into account. In our calculations, we used the method described in [3, 4]. Unlike the ST,X-cut quartz [5] (Fig. 1, curves *5* and *6*), the inclusion of the second-order term [see (1)] greatly modifies the temperature dependence of the TCD$^{(1)}$ in the LGS (curve *2*) and LGN (curve *4*) crystals. Thus, we can conclude that this dependence for the new crystals is essentially nonlinear in contrast to piezoelectric quartz. Figure 2 shows the temperature dependences of the TCD$^{(1)}$ and TCD$^{(2)}$ for the Al-coated crystals (h/λ = 0.005). Two pairs of curves (*1* and *2*) and (*3* and *4*) correspond to the LGS (0, 140, 22.5°) and LGN (0, 138.5, 23°), respectively. For the coated LGS crystal, the TCD$^{(1)}$ (curve *1*) is equal to zero at 10°C, while the TCD$^{(2)}$ (curve *3*) changes insignificantly and equals $+7 \times 10^{-8}$ 1/°C^2. For the LGN crystal, the TCD$^{(1)}$ (curve *2*) varies between $+8 \times 10^{-6}$ and -2×10^{-6} 1/°C and vanishes at 50°C. The TCD$^{(2)}$ (curve *4*) varies from -3×10^{-8} to -1×10^{-8} 1/°C^2.

REFERENCES

1. I. B. Yakovkin, R. M. Taziev, and A. S. Kozlov, Proc. IEEE Ultrason. Symp. 389 (1995).
2. M. P. Cunha and S. A. Fagundes, Proc. IEEE Ultrason. Symp. 1.6 (1998).
3. *Acoustic Surface Waves*, Ed. by A. A. Oliner (Springer-Verlag, New York, 1978; Mir, Moscow, 1981).
4. M. Yu. Dvoesherstov, V. I. Cherednick, A. P. Chirimanov, and S. G. Petrov, Proc. SPIE **3900**, 283 (1999).
5. S. Sarharov, P. Senushencov, A. Medvedev, and Yu. Pisarevsky, Proc. IEEE Freq. Control Symp. 647 (1995).
6. K. Inoue and K. Sato, Jpn. J. Appl. Phys., Part 1 **37**, 2909 (1998).
7. A. Bungo, C. Jian, K. Yamaguchi, *et al.*, Proc. IEEE Ultrason. Symp. 1 (1999).
8. Yu. Pisarevsky, P. Senushencov, P. Popov, and B. Mill, Proc. IEEE Freq. Control Symp. 653 (1995).
9. Y. Shimizu, A. Terazaki, and T. Sakaue, Proc. IEEE Ultrason. Symp. 519 (1976).

Translated by Yu. Vishnyakov

Technical Physics, Vol. 46, No. 3, 2001, pp. 348–350. Translated from Zhurnal Tekhnicheskoĭ Fiziki, Vol. 71, No. 3, 2001, pp. 78–80.
Original Russian Text Copyright © 2001 by Zakutin, Dovbnya, Reshetnyak, Volkolupov, Krasnogolovets.

BRIEF COMMUNICATIONS

Generation of High-Power Electron Beams by Magnetron Injection Guns with Secondary-Emission Cathodes

V. V. Zakutin, A. N. Dovbnya, N. G. Reshetnyak,
Yu. Ya. Volkolupov, and M. A. Krasnogolovets
Kharkov Institute of Physics and Uskoritel' Research Complex Technology, National Scientific Center,
Akademicheskaya ul. 1, Kharkov, 61108 Ukraine

Received March 13, 2000

Abstract—The generation of high-power electron beams by magnetron injection guns using a secondary-emission cold cathode is studied experimentally. Stable operation at an output power of up to 8 MW is achieved. *© 2001 MAIK "Nauka/Interperiodica".*

INTRODUCTION

Recent years have seen extensive research into cold-cathode magnetron injection guns of ordinary [1–6] and inverted [6, 7] type. Such sources employ secondary emission in crossed electric and magnetic fields. Among their merits are long operating life, high current density, relatively simple configuration, the capability of producing hollow beams, etc. Therefore, they could make emitters for long-lived high-power microwave generators [3] or fast high-voltage devices [8]. Offering intense electron beams, these guns enable one to achieve high levels of pulse power when used in klystrons or other microwave tubes.

EXPERIMENTAL SETUP

Experiments to generate high-power electron beams with magnetron injection guns using secondary-emission cathodes (SECs) were conducted in the apparatus schematically shown in Fig. 1. A magnetron injection gun is driven by modulator *1*, which produces 4- to 100-kV negative voltage pulses of width 2–10 μs and repetition rate 10–50 Hz. The pulses are applied to copper cathode *5*, whereas anode *6* is grounded via resistor R_3. The anode is made of stainless steel or copper. Two alternative techniques to initiate secondary emission were employed. They respectively use a pulse from external generator *2* or a specially generated overshoot in a cathode voltage pulse. Secondary emission takes place in the trailing edge of the initiating pulse or overshoot. A magnetic field to produce and transport a beam is created by solenoid *4*. The beam current is measured with Faraday cup *7* and resistor R_4; cathode voltage, via divider R_1–R_2; and beam size, with the help of a print on an X-ray film or a molybdenum foil. The gun is situated in stainless-steel vacuum chamber *3* kept at a pressure of about 10^{-6} torr.

The magnetic field was created by two methods. One of them generates a pulsed field when a capacitor is discharged through the solenoid [9]. The other provides a static field: a constant current is passed through the solenoid, which then requires water cooling [10]. Curves *1* and *2* in Fig. 2 depict the distributions of the magnetic field on the solenoid axis for the two cases, with *A*, *C*, and *FC* standing for the anode, cathode, and Faraday cup, respectively.

The pulsed approach (Fig. 2, curve *1*) provides magnetic fields of considerable strength (up to 5000–6000 Oe) and longitudinal uniformity (within ±5%). It is also useful for transporting a beam through the resonators of a microwave tube. On the other hand, the pulse rate here is limited by the actual designs of the storage capacitor and the switch. Furthermore, the longitudinal pulsed field distribution may alter due to the attenuation of the field as it diffuses through the walls of the resonators and the vacuum chamber (see, e.g., [9, 11]). Finally, note that contaminants enter the cathode–anode gap owing to electron bombardment and deposition on the cathode surface during time intervals between the high-voltage pulses, so that vacuum breakdown of the gap may occur if the pulse rate is too low [12].

With the static approach, the solenoid consumes more power and needs water cooling. The concomitant heating of the solenoid limits the available strength of

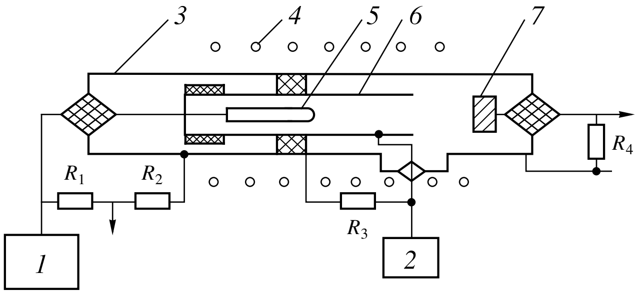

Fig. 1.

1063-7842/01/4603-0348$21.00 © 2001 MAIK "Nauka/Interperiodica"

the magnetic field. It is seen that the field is uniform in a shorter interval (curve *2* in Fig. 2). Finally, the instability of the coil current has to be taken into account, so that the rate of drive pulses from the modulator must be adjusted to the mains frequency.

RESULTS AND DISCUSSION

First, we tested a gun with a copper cathode of diameter 40 mm and a stainless-steel anode of diameter 78 mm and length about 100 mm. Secondary emission was initiated by overshoots (up to 160 kV) in cathode pulses. Figure 3 shows the beam current at the Faraday cup versus the cathode pulse height. It is seen that the current obeys the Child–Langmuir law. For each value of the cathode voltage, the magnetic field was adjusted so as to maximize the beam current. We achieved stable generation of an electron beam with a current close to 50 A at a voltage of 100 kV and a magnetic field of about 1600 Oe. Accordingly, the microperveance and the beam power approximated to 1.6 and 5 MW, respectively. The measurements revealed that the gun endures 120 kV, which allows one to produce up to 8 MW of beam power.

Then, we tested a gun with a copper cathode of diameter 40 mm and a stainless-steel anode of diameter 50 mm and length about 100 mm. It generated a beam current of 50 A at 30 kV and 2200 Oe, with the microperveance and the beam power being close to 10 and 1.5 MW, respectively.

These results are similar to those reported in [6], where experiments were performed on a gun made of BeCu and stainless steel with (1) the cathode diameter 50 mm and anode diameter 60 mm (ordinary type) and (2) cathode diameter 54 mm and anode diameter 43 mm (inverted type). A beam current of about 100 A was obtained at 40 kV and about 1800 Oe. The beam power and the microperveance were close to 4 MW and 12, respectively.

Thus, SEC magnetron injection guns provide high beam powers. However, their use in microwave electronics is hindered by large values of microperveance and the outer beam diameter. (The latter was reported to vary between 45 and 55 mm, depending on the experimental setup.)

Another way to increase the beam power is the use of several (six or more) guns connected in parallel. This may yield a high total current and power even if each gun has moderate beam current, power, microperveance, and beam size.

Admittedly, such an approach may give rise to the same difficulties as the parallel connection of switches. Once one of the guns has started generating, the cathode pulse heights of other guns may fall to impermissibly small values (the guns do not generate). Also, a multigun configuration may, in principle, have a decreased breakdown voltage, since it varies inversely as $S^{0.1}$, where S is the total area of the electrodes. Nevertheless, with a fairly large number of guns (six and even more), the decrease in breakdown voltage is insignificant (about 10–20%). So may be that in the cathode pulse height if the modulator has a small output resistance. In our experiments, the pulse height decreased by less than 30% for a modulator resistance of 2000 Ω. Note that a beam is generated if the height of the cathode pulses varies to within 40%, as was reported in [13]. Furthermore, it was shown that the cathode voltage decreases appreciably after a few nanoseconds. On

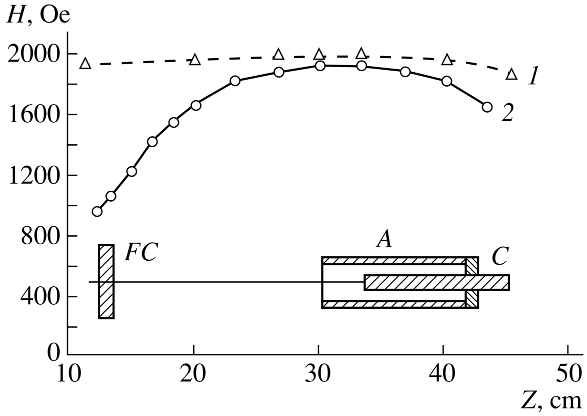

Fig. 2.

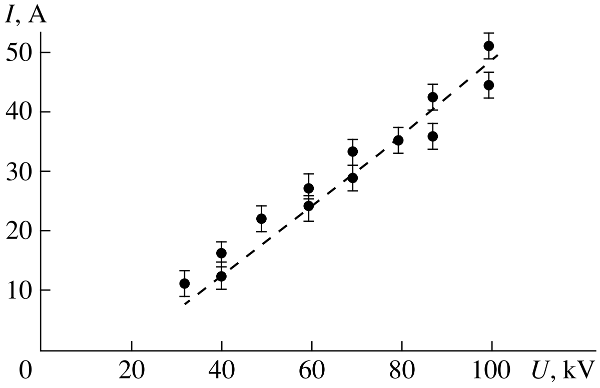

Fig. 3.

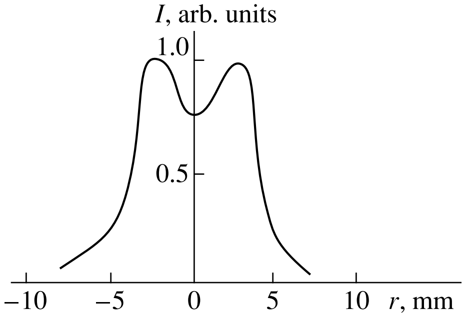

Fig. 4.

the other hand, the time to create an electron layer in an SEC magnetron injection gun, and hence the rise time of the pulsed beam current, can be reduced to 2 ns [14]. Thus, it is possible to meet the challenge of generating electron beams in multigun systems.

We tested systems with six and eight guns. In the former case, the guns were arranged in a circle of diameter about 60 mm, with the cathode and the anode diameter being 5 and 26 mm, respectively. Six beams were produced, each having an outer diameter of about 9 mm. At a cathode voltage of 40 kV and a magnetic field close to 2000 Oe, each gun delivered 18 A of beam current with a microperveance of about 2.5. The total beam current and power approximated to 100 A and 4 MW, respectively.

In the latter case, the guns were arranged in a circle of diameter about 70 mm. The cathode and the anode diameter were 5 and 22 mm, respectively. Eight beams were produced, each having an outer diameter and a microperveance of about 9 mm and 2, respectively. The total beam current and power approximated to 60 A and 2 MW for the cathode voltage and the magnetic field close to 30 kV and 2000 Oe. Research is under way to obtain a beam power up to 10 MW.

With a pulsed magnetic field (curve *1* in Fig. 2), a beam was transported for a distance of 50–100 mm from the anode. With a static field (curve *2* in Fig. 2), the distance was 50 and 180 mm. For both cases, the beam cross section at the collector was an annulus whose inner diameter is approximately equal to the cathode diameter and whose width is 1–1.3 mm. The azimuthal intensity distribution was uniform over the annulus. Figure 4 shows the radial intensity distribution at a distance of 50 mm from the anode when the cathode and anode diameters are 5 and 26 mm, respectively. It is seen that the outer beam diameter is less than 10 mm. The magnetic field near the X-ray film is found to be lower by a factor of about 1.8 compared with that at the gun, as suggested by curve *2* in Fig. 2. Nevertheless, the beam size remains almost the same. The above results indicate that the magnetic field holds the beam together and that its attenuation does not cause beam spreading. These findings are relevant to transporting and injecting electron beams.

CONCLUSIONS

The experiments have demonstrated that single SEC magnetron injection guns and their combinations can produce electron beams of considerable power. Thus, the guns could serve as electron sources in high-power microwave tubes.

REFERENCES

1. J. F. Skowron, Proc. IEEE **61** (3), 330 (1973).
2. S. A. Cherenshchikov, Élektron. Tekh., Ser. 1, No. 6, 20 (1973).
3. A. N. Dovbnya, V. V. Zakutin, V. F. Zhiglo, *et al.*, in *Proceedings of the 5th European Particle Accelerators Conference, Sitges, 1996*, Ed. by S. Myers, A. Pacheco, R. Pascual, *et al.* (Inst. of Physics Publ., Bristol, 1996), Vol. 2, p. 1508.
4. A. N. Dovbnya, V. V. Mitrochenko, *et al.*, in *Proceedings of the 1997 Particle Accelerators Conference, Vancouver, 1997*, Ed. by M. Comyn, M. K. Craddok, M. Reiser, and J. Thomson, Vol. 3, p. 2820.
5. A. V. Agafonov, V. P. Tarakanov, and V. M. Fedorov, Vopr. At. Nauki Tekh., Ser.: Yad.-Fiz. Issled. **1**, 134 (1997).
6. Y. M. Saveliev, W. Sibbett, and D. M. Parkes, Phys. Plasmas **4**, 2319 (1997).
7. G. I. Churyumov, Izv. Vyssh. Uchebn. Zaved., Radioélektron., No. 7, 77 (1997).
8. A. I. Vishnevskiĭ, A. I. Soldatenko, and A. I. Shendakov, Izv. Vyssh. Uchebn. Zaved., Radioélektron. **11**, 555 (1968).
9. H. Knoepfel, *Pulsed High Magnetic Fields* (North-Holland, Amsterdam, 1970; Mir, Moscow, 1972).
10. I. I. Kifer, *Ferromagnetic Material Tests* (Gosénergoizdat, Moscow, 1962).
11. V. V. Zakutin and A. M. Shenderovich, Prib. Tekh. Éksp., No. 5, 238 (1976).
12. A. N. Dovbnya, V. V. Zakutin, N. G. Reshetnyak, *et al.*, Vopr. At. Nauki Tekh., Ser.: Yad.-Fiz. Issled. **1**, 53 (1997).
13. Yu. Ya. Volkolupov, A. N. Dovbnya, V. V. Zakutin, *et al.*, Zh. Tekh. Fiz. **71** (2), 98 (2001) [Tech. Phys. **46**, 227 (2001) (in press)].
14. N. I. Aĭzatskiĭ, A. N. Dovbnya, V. V. Mitrochenko, *et al.*, Vopr. At. Nauki Tekh., Ser.: Yad.-Fiz. Issled. **3**, 38 (1999).

Translated by A. Sharshakov

Technical Physics, Vol. 46, No. 3, 2001, pp. 351–353. Translated from Zhurnal Tekhnicheskoĭ Fiziki, Vol. 71, No. 3, 2001, pp. 81–83.
Original Russian Text Copyright © 2001 by Petrova.

BRIEF COMMUNICATIONS

Light-Induced Anisotropy and Gyrotropy in Polarization-Sensitive Media

S. S. Petrova
Institute of Cybernetics, Academy of Sciences of Georgia, Tbilisi, 380086 Georgia

Received April 13, 2000; in final form, July 28, 2000

Abstract—Photoinduced anisotropy and photoinduced gyrotropy were studied in polarization-sensitive photochromic glass and mordant purely yellow dye introduced into gelatin. These media, memorizing the polarization state of acting actinic light, show great promise primarily for polarization holography. It is the aim of this work to draw researchers' attention to new findings in the field of light-induced anisotropy and holography so as to stimulate experimental and theoretical study of these phenomena and search for new polarization-sensitive media. *© 2001 MAIK "Nauka/Interperiodica".*

Photoanisotropy, i.e., anisotropy that arises when linearly polarized actinic light interacts with an initially isotropic medium, was discovered as early as 1919 by Weigert [1]. Photogyrotropy, a similar effect that takes place when actinic light is circularly polarized, was discovered later, in 1928, in studying silver halogenides and gelatin [2].

Both phenomena reflect the fundamental (intrinsic) properties of the interacting objects. Indeed, on the one hand, a quantum of polarized radiation is anisotropic and has the spin; on the other hand, the interacting material is anisotropic and gyroscopic. Eventually, such a set of properties results in reaction products that macroscopically are also anisotropic and gyroscopic. Basically, photoinduced gyrotropy and photoinduced anisotropy must show up, to one extent or another, in any absorbing medium and may persist infinitely long at sufficiently low temperatures [3–6].

Sensitometry of photoanisotropic and photogyrotropic media does not essentially differ from photographic sensitometry. Just as the characteristic curve is constructed in the latter case, so curves that relate the complex anisotropy and complex gyrotropy on the energy and polarization state of incident light can be obtained. Such an approach has been considered in [7], where the properties of many photoanisotropic and photogyrotropic media are described.

Figure 1 is a plot of the light-induced anisotropy and birefringence against the energy of an argon laser (λ = 4880 Å) at different reading wavelengths for mordant purely yellow dye [8].

If an initially isotropic and nongyrotropic three-dimensional medium is subjected to actinic linearly polarized light, it becomes akin to a uniaxial crystal with maximum (and equal) anisotropies in two mutually perpendicular sections. In the third section, which is orthogonal to the oscillation direction of the electric vector of the actinic radiation, the medium changes the transmission coefficient, remaining isotropic (Fig. 2).

In detecting photogyrotropy, the illumination scheme was as follows. Linearly polarized laser radiation became circularly polarized when passing through a phase quarter-wave plate, was expanded by a lens, and came to a sample whose back side was turned to a black matte color to protect the light-sensitive layer from Fresnel reflection (Fig. 3). The sample was placed into a holder that was slowly rotated about the optical axis during illumination by actinic light. This eliminates the influence of remanent ellipticity of actinic radiation, which, as a rule, interferes with the purely gyrotropic effect. After illumination, the back side was

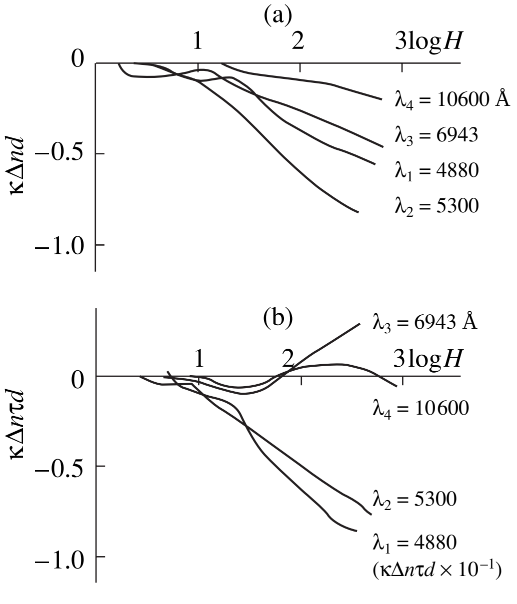

Fig. 1. Energy dependences of (a) $\kappa\Delta nd$ and (b) $\kappa\Delta n\tau d$ for mordant purely yellow dye at the actinic wavelength λ = 4880 Å and various reading wavelength.

1063-7842/01/4603-0351$21.00 © 2001 MAIK "Nauka/Interperiodica"

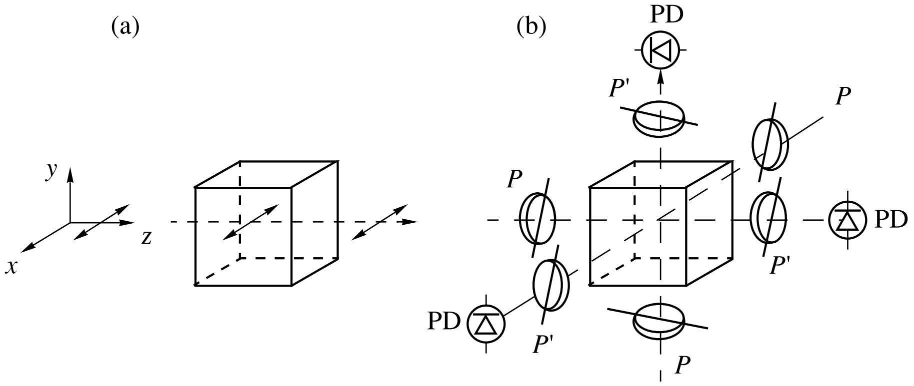

Fig. 2. (a) Illumination and (b) measuring scheme for three-dimensional photoanisotropic glass.

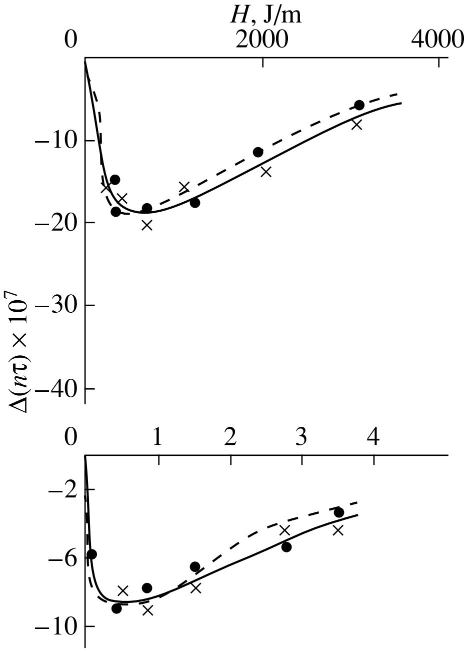

Fig. 3. Light-induced absorption anisotropy vs. light exposure for *T* centers in photochromic glass. Dots, data points for $\Delta(n\tau)^{(z)}$; crosses, data points for $[\Delta(n\tau)^{(y)}]_{CP}$; solid lines, experiment; and dashed lines, theory [9].

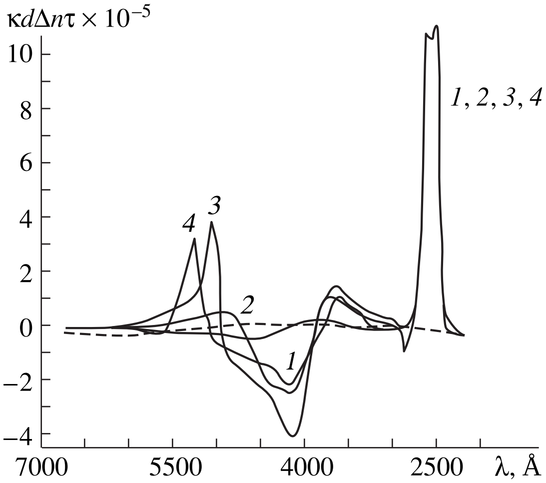

Fig. 4. Circular dichroism $\kappa d[(n\tau) = (n\tau)_+]$ ($\kappa = 2\pi/\lambda$, d is the thickness, n is the refractive index, and τ is the extinction ratio) against reading wavelength for right-hand circularly polarized actinic light. (*1*) See the text; (*2*) λ = 4416 Å, 13 J/m; (*3*) λ = 4880 Å, 31 J/m; and (*4*) λ = 5145 Å, 15 J/m. The sample is the same as in Fig. 3.

cleaned and the light-induced circular dichroism vs. reading wavelength was measured with a DKhP-02 dichrograph.

Figure 4 demonstrates the spectral dependences of the circular dichroism (the zero line is dashed). Without illumination, the dichroism is described by curve *1*, which exhibits an intense peak at λ = 2330 Å. This peak is readily identified with the circular dichroism of the protein entering into the composition of the gelatin matrix. From curve *2*, it follows that the dichroism is nearly absent at the wavelength of actinic radiation. However, the peaks at λ = 4827 and 3383 Å are positive, while at 3933 Å, an intense negative peak is observed. Curve *3* exhibits a sharp positive peak at wavelength λ = 4917 Å, which is close to that of the actinic radiation, and an additional peak at λ = 3383 Å. Finally, curve *4* has a sharp positive peak at λ = 5145 Å, also close to the wavelength of actinic radiation, and a positive peak at λ = 3933 Å. When the sample was illuminated by left-hand circularly polarized light of the same wavelength, the dichroism curves turn out to be mirror-symmetric about the abscissa axis; however, at the same illumination energies, the effect was somewhat weaker because of the presence of the initially gyrotropic matrix.

The results obtained are of interest in molecular optics and optical chemistry. Also, they may extend the range of recording media and the applicability of polarization holography [10, 12].

The purpose of this work is to concentrate researchers' attention on the field of light-induced anisotropy and holography so as to stimulate their experimental and theoretical study and search for new polarization-sensitive media. These phenomena, especially their applications, have been in disfavor for the past years. In our opinion, they are extremely promising for developing radically new concepts of computer memory, which may become dominant in the 21st century.

ACKNOWLEDGMENTS

The author thanks Sh.D. Kakichashvili for the statement of the problem and valuable discussions.

REFERENCES

1. F. Weigert, Verh. Dtsch. Phys. Ges. **21**, 479 (1991).
2. H. Zocher and K. Coper, Z. Phys. Chem., Stoechiom. Verwandtschaftsl. **132**, 313 (1928).
3. F. Weigert, Z. Phys. Chem., Abt. B **3**, 389 (1929).
4. T. Kondo, Z. Wiss. Photogr., Potophys. Potochem. **31**, 153 (1932).
5. Sh. D. Kakichashvili, Opt. Spektrosk. **63**, 911 (1987) [Opt. Spectrosc. **63**, 538 (1987)].
6. L. A. Ageev, V. B. Blokha, and V. K. Miloslavskiĭ, Opt. Spektrosk. **59**, 1247 (1985) [Opt. Spectrosc. **59**, 764 (1985)].
7. Sh. D. Kakichashvili, in *Polarization Holography* (Nauka, Leningrad, 1989), pp. 29–30.
8. Sh. D. Kakichashvili, in *Polarization Holography* (Nauka, Leningrad, 1989), p. 47.
9. Sh. D. Kakichashvili, V. I. Tarasashvili, and Ya. A. Shvaĭtser, Opt. Spektrosk. **68**, 1106 (1990) [Opt. Spectrosc. **68**, 646 (1990)].
10. V. I. Tarasashvili and Sh. D. Kakichashvili, Pis'ma Zh. Tekh. Fiz. **16** (19), 13 (1990) [Sov. Tech. Phys. Lett. **16**, 729 (1990)].
11. Sh. D. Kakichashvili, Pis'ma Zh. Tekh. Fiz. **16** (19), 30 (1990) [Sov. Tech. Phys. Lett. **16**, 736 (1990)].
12. Sh. D. Kakichashvili and S. S. Petrova, Pis'ma Zh. Tekh. Fiz. **18** (22), 31 (1992) [Sov. Tech. Phys. Lett. **18**, 736 (1992)].

Translated by V. Isaakyan

Technical Physics, Vol. 46, No. 3, 2001, pp. 354–356. Translated from Zhurnal Tekhnicheskoĭ Fiziki, Vol. 71, No. 3, 2001, pp. 84–87.
Original Russian Text Copyright © 2001 by Azamatov, Karaev, Sokolov, Fedorov.

BRIEF COMMUNICATIONS

The Modulated Magnetic Structure of α-Fe_2O_3 : Ga Weak Ferromagnet

Z. T. Azamatov*, A. A. Karaev*, B. Yu. Sokolov*, and Yu. M. Fedorov†**

**Tashkent State University, Universitetskaya ul. 95, Vuzgorodok, Tashkent, 700095 Uzbekistan*
***Kirenskiĭ Institute of Physics, Siberian Division, Russian Academy of Sciences,*
Akademgorodok, Krasnoyarsk, 660036 Russia

Received April 17, 2000

Abstract—The domain structure of a diluted weak α-Fe_2O_3 : Ga ferromagnet is considered. Magnetic fields of specific amplitudes and orientations applied in the basal plane of the crystal are found to produce nonuniform magnetic states due to a periodic deviation of the antiferromagnetic vector from the easy axis of crystallographic anisotropy. A phase diagram of the modulated magnetic state with the triad axis is constructed, and a dependence of the spatial period of modulation on an external magnetic field is studied. A phenomenological model and the nature of the magnetic superstructure discovered are discussed. *© 2001 MAIK "Nauka/Interperiodica".*

Instability of the uniform magnetic state of magnetically ordered dielectrics is commonly attributed to exchange interactions of different sign between the closest neighboring atoms and those next to them. The arising magnetic structures have been adequately studied both experimentally and theoretically (see, for example, [1]). Under specific conditions, however, the ordered uniform state may become unstable in a weak random field [2]. Among other reasons, the random magnetic field can be produced by local spatial variations in competing anisotropic interactions of a magnetoactive ion with its surroundings. For example, as theoretically shown in [3], in easy-plane antiferromagnets, the uniform antiferromagnetic state can become energy-unfavorable because of 3D or point defects present in the crystal lattice. Nonuniform magnetic states arisen in this case are less understood.

In the recent experimental study [4] of hematite, α-Fe_2O_3, and iron borate, $FeBO_3$, which are easy-plane antiferromagnets (in the weak ferromagnetic phase), a magnetic superstructure was discovered. It appears in a particular range of magnetic fields when a small amount of diamagnetic Ga and Mg ions are incorporated. In order to obtain the parameters of the modulated magnetic states in diluted weak ferromagnets, we pursued the study of the influence of a magnetic field on the magnetic structure of α-Fe_2O_3 : Ga. One reason is that hematite is a promising material for many high-frequency devices. Therefore, mechanisms behind the nonuniformity of the macroscopic magnetic parameters of the material must be carefully investigated.

EXPERIMENTAL

Hematite was synthesized with an addition of ≈0.1 wt % of gallium oxide. About 50-μm-thick plates ~3 × 3 mm in cross section were cut from the synthesized α-Fe_2O_3 : Ga single crystals so that the principle crystallographic axis C_3 was perpendicular to the sample surface. To relieve the mechanical stress and homogenize the impurity distribution, the plates were annealed in air at $T = 500°C$ for 10 h. Magnetic measurements indicated that in the presence of the Ga impurity, the Neel temperature of the samples (T_N = 950 K) was nearly the same as that of pure α-Fe_2O_3, while the Morin temperature decreased below the boiling temperature of nitrogen.

The domain structure of the α-Fe_2O_3 : Ga samples was visualized by a magnetooptic technique. A large body of experimental data for the domain structure of hematite that were obtained by this method [5] enables us to compare in detail the responses to an external magnetic field from pure (impurity-free) crystals and those diluted by a diamagnetic impurity. Moreover, the typical size of magnetic inhomogeneities discovered in [4] is about 50 μm, suggesting that studying the modulated magnetic states requires a considerably high spatial resolution, which is readily provided by the magnetooptic technique.

The domain structure was examined at room temperature in the transmission band of hematite (0.8–1.1 μm) using a crossed analyzer and a polarizing microscope. A light beam was aligned with the C_3 axis. A uniform magnetic field was produced by two pairs of Helmholtz coils. The field lay in the basal plane of the samples and was varied in magnitude and in direction about the magnetic anisotropy axes. The sample was oriented according to the technique described in [5]. The image of the domain structure was read out by a video camera, digitized, and visualized on a computer.

---

† Deceased.

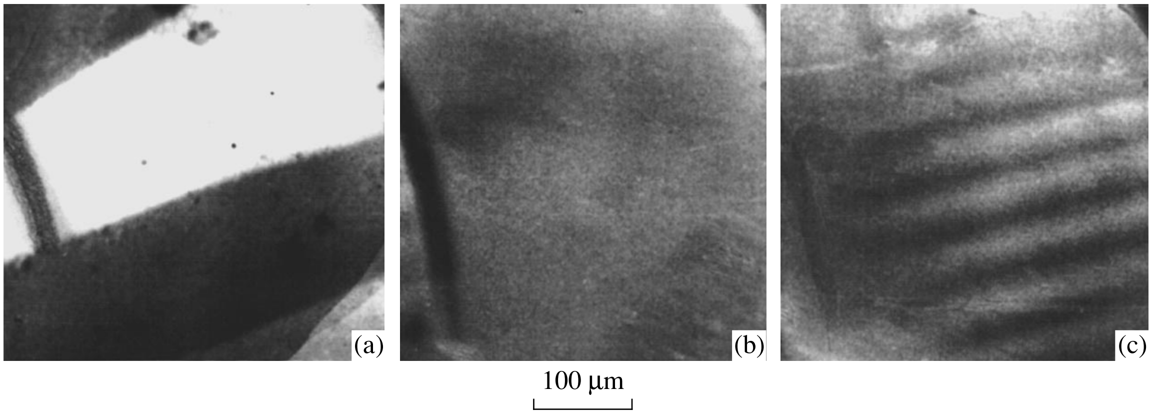

Fig. 1. Magnetooptic images of the domain structure for **H** = (a) 0, (b) 5, and (c) 7 Oe.

EXPERIMENTAL RESULTS

Figure 1 shows the evolution of the domain structure in different magnetic fields H applied perpendicular to the domain walls in the demagnetized state of the crystal. Under the applied field, the crystal first becomes single-domain; then, at $H \gtrsim 5$ Oe, there appears the quasi-periodic structure of blurred fringes with a various magnetooptic contrast. The magnetooptic contrast of the image evened up at $H \gtrsim 20$ Oe.

The fringes appeared when the direction of the applied field was close to any of the three hard magnetic axes in the basal plane (according to [5], the hard magnetic axes are perpendicular to the U_2 axes). The average period λ of the fringe pattern was H-dependent. A typical dependence of λ on the magnetic field applied perpendicular to the wave front of the arising fringes is plotted in Fig. 2. The period λ, i.e., the number of fringes per unit length, varies stepwise. Along with the pinning effect, hysteresis of λ is observed: as H decreases, the average period of the fringe pattern changes less than it does when the field increases.

The experimental magnetic state diagram in Fig. 3 depicts areas where the quasi-periodic structure of the fringes is observed according to the applied field magnitude and direction in the basal plane. In the hatched regions, the magnetooptic contrast of the image is modulated. The direction of the hatches indicates the direction of fringes with a different magnetooptic contrast.

DISCUSSION

The diffuse boundaries of the fringes suggest that the magnetization in the system is not merely alternating, which is typical of a usual domain system, but smoothly changes its direction. Such a fringe pattern was not observed in pure hematite crystals under similar magnetization conditions; therefore, one can conclude that the nonmagnetic impurity states directly affect the rotation of sublattice magnetic moments in α-Fe_2O_3 : Ga. This gives rise to the spatial-modulated ferro- and antiferromagnetic vectors in a particular range of magnetic fields. In other words, in the weak ferromagnet considered, higher-than-saturation magnetic fields cause the orientational uniform-to-modulated magnetic state transition.

To characterize the arising magnetic superstructure, let us invoke the theory of phase transitions from uniform to nonuniform magnetic states in magnetoordered structures [6, 7]. In rhombohedral antiferromagnets, including hematite, a consideration of magnetic anisotropy in the easy plane is known [6] to result in stable uniform sublattice moments in six directions, which differ from each other by an azimuth angle of $\pi/3$. Therefore, without loss in generality, the antiferromagnetic vector $\mathbf{l}$ can be assumed to be oriented close to one of these directions. In this approximation, the thermodynamic potential of the crystal can include only uniaxial anisotropy. Then, as an order parameter, we choose a small deviation β of the vector $\mathbf{l}$ from a given direction in an external magnetic field and take this direction as the X axis ($H \parallel X$). Now, following [6, 7], the thermodynamic potential of the crystal can be represented as an

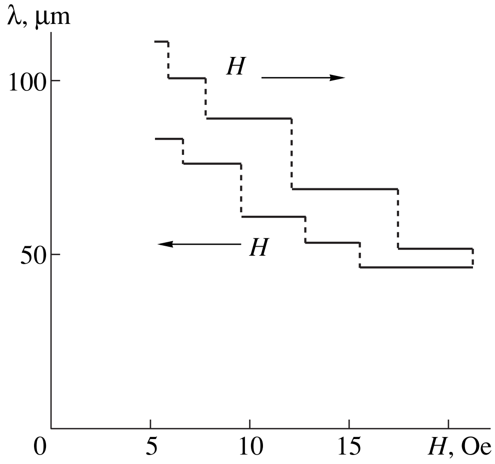

Fig. 2. Field dependence of the spatial period of the quasi-periodical fringes with different magnetooptic contrast.

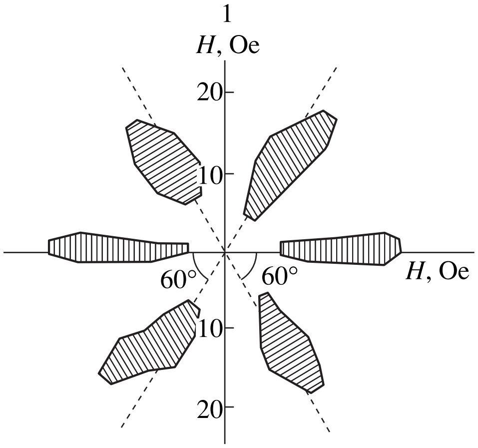

Fig. 3. Magnetic state diagram according to the external magnetic field strength **H** and azimuth for the system of fringes with different magnetooptic contrast. Hatched areas correspond to the parameters for which the modulated magnetic structure is observed. *1*, the easy magnetic axis.

expansion in the order parameter:

$$\Phi(\beta) = \int[-1/2A\beta^2 + 1/4B\beta^4 + 1/2\alpha(\beta')^2 + 1/4\gamma(\beta'')^2 + mh\beta + 1/2\mu lh(\beta')^2 + \ldots]dx, \quad (1)$$

where primes mean differentiation with respect to the corresponding argument. The external magnetic field H is taken into account through two symmetry-allowed terms: one of them, $mh\beta$ (m is the ferromagnetic vector, and $h = MH$, where M is a sublattice moment), is the Zeeman contribution into the crystal energy, and the other, $1/2\mu lh(\beta')^2$, is invariant to space–time inversion.

The functional thus constructed differs from that used in [7] only by the addition of the latter term, which accounts for the presence of the random field and renormalizes the coefficient at the first derivative, making it H-dependent.

The phase transition from the uniform to the modulated magnetic state occurs when the coefficient at the first derivative in (1) is negative; i.e., at $\mu < 0$, a field $h > \alpha/\mu l$ induces the modulated magnetic state of the crystal. In this case, functional (1) is minimized by a function like [7]

$$\beta(x) = \beta_0 + \xi\sum[C_j\exp(ik_jx) + \text{c.c.}]$$

(c.c. is the complex conjugate). Neglecting the relatively weak temperature dependence of the modulated state parameters, we can approximate the spatial distribution of the order parameter by a single harmonic:

$$\beta(x) \approx \beta_0 + \eta\cos k_0x.$$

Thus, within our model, an external magnetic field of critical value $\alpha/\mu l$ lying in the basal plane of a weak ferromagnet along the anisotropy axis initiates the orientational phase transition from the uniform to the modulated magnetic state. Modulation appears in the direction of the magnetic field, and the magnetic superstructure can be represented as a phase where the azimuth of the local antiferromagnetic (ferromagnetic) vector oscillates with a period $\lambda = 2\pi/k_0$, the vector being constantly deflected from the anisotropy axis. In accordance with the previous assumptions, there should be three directions of **l** azimuth modulation. This is consistent with the diagram of modulated magnetic states (Fig. 3).

It can be shown that under near-critical magnetic fields, the parameters of the nonuniform magnetic state are given by

$$k_0^2 = |\alpha + \mu lh|/2\gamma, \quad \beta_0 = 4\gamma h/M(\alpha + \mu lh)^2,$$

$$\eta^2 = 1/3B[A + (\alpha + \mu lh)/4\gamma - 48\gamma^2h^2B/M^2(\alpha + \mu lh)^4].$$

The above expression for the wave vector k_0 of the modulated structure gives at least a qualitative (disregarding pinning and hysteresis effects) explanation for the experimental decrease in the period of the fringes with growing H (Fig. 2).

In conclusion, let us comment on the physical interpretation of the results. Being introduced into the hematite lattice, diamagnetic Ga ions induce distortions due to a difference in the ion radii of impurity and host atoms and, possibly, due to their different charge states. This results in random anisotropy, which causes a local deviation of the ferromagnetic vector from the directions defined by crystallographic anisotropy. For **H** perpendicular to the crystallographic anisotropy axis (as in our experiment), the resulting equilibrium magnetic structure is defined by the interplay between random anisotropy, crystallographic anisotropy, and the constant magnetic field.

ACKNOWLEDGMENTS

This work was supported by INTAS, grant no. 97-0894.

REFERENCES

1. Yu. A. Izyumov, Usp. Fiz. Nauk **144**, 439 (1984) [Sov. Phys. Usp. **27**, 845 (1984)].
2. Y. Imry and S. Ma, Phys. Rev. Lett. **35**, 1399 (1975).
3. E. B. Sonin, J. Phys. C **13**, 3293 (1980).
4. A. A. Karaev, A. A. Leksikov, Yu. M. Fedorov, and V. V. Rudenko, in *Proceedings of the XV All-Russia Workshop “Novel Magnetic Materials in Microelectronics”, Moscow, 1996*, p. 455.
5. V. L. Preobrazhenskiĭ, A. A. Shishkov, and N. A. Ékonomov, Fiz. Tverd. Tela (Leningrad) **29**, 3549 (1987) [Sov. Phys. Solid State **29**, 2034 (1987)].
6. A. Michelson, Phys. Rev. B **16**, 585 (1977).
7. I. E. Dikshteĭn, F. V. Lisovskiĭ, E. G. Mansvetova, and V. V. Tarasenko, Fiz. Tverd. Tela (Leningrad) **25**, 2545 (1983) [Sov. Phys. Solid State **25**, 1465 (1983)].

Translated by A. Sidorova

Technical Physics, Vol. 46, No. 3, 2001, pp. 357–360. Translated from Zhurnal Tekhnicheskoĭ Fiziki, Vol. 71, No. 3, 2001, pp. 88–91.
Original Russian Text Copyright © 2001 by Filonenko.

BRIEF COMMUNICATIONS

Radio-Frequency Component of Transient Radiation of an Extensive Air Shower

A. D. Filonenko
East Ukrainian State University, Lugansk, 91034 Ukraine
e-mail: uni@vugu.lugansk.ua

Received June 1, 2000

Abstract—The mechanism of radio emission induced by the transient radiation of oppositely charged particles from an extensive air shower in the geomagnetic field was studied for the first time. For showers with an energy of $\sim 10^{22}$ eV, the electric field strength at a distance of 500 km from the shower axis was found to be 60 μV/mMHz. Such showers attain their maximum at sea level. The spectral intensity of emission is maximum at frequencies of about 1 MHz (at these frequencies, the intensity of atmospheric disturbances is minimum). These specific features of radio emission can be used in experiments for radio detection of high-energy cosmic rays. An experimental setup of such detection is suggested. *© 2001 MAIK “Nauka/Interperiodica”.*

The method of radio detection of extensive air showers holds much promise. One of the advantages of this method is its simplicity. Besides, conventional methods for detecting extensive air showers lack many possibilities of the radio detection method. In the 1980s, attempts to detect cosmic rays by measuring the high-frequency component of radio emission failed. Since then, studies of radio emission in the medium- and long-wave ranges have attracted particular interest, because the spectral intensity of radio emission was found to increase within these frequency ranges. Several explanations of this increase were suggested. In particular, it was shown that the shower δ-electron bremsstrahlung was a possible mechanism for radio emission within the frequency range from 50 to 100 kHz [1–3].

The role of transient radiation in inducing the low-frequency radio emission was extensively discussed in the literature [4]. The goal of this work was to theoretically study the possibilities of extensive air shower detection using transient radiation (the primary particle energy is taken to be more than 10^{21} eV). It was found that the light charged-particle separation in the geomagnetic field causes an increase in the radio emission intensity. The radio emission intensity in the geomagnetic field is almost an order of magnitude higher than the intensity of emission induced by transient radiation of excess electrons [5].

The following model of extensive air shower (EAS) was used to assess the intensity of an electromagnetic field induced by the secondary radiation of a cosmic-ray particle with energy $W_0 \geq 10^{21}$ eV [6, 7].

(1) An extensive air shower is considered as a disk of negligible thickness with a mean-square radius $r_0 = 100$ m. Electrons and positrons are distributed uniformly over the disk surface so that the disk as a whole is neutral.

(2) The dependence of the number of particles in the shower on the height z is described by a cascade function $f(z)$. In the case under consideration, the cascade function can be approximated with sufficient accuracy by the function $f(z) = N_0\exp(-\alpha^2 z^2)$, where $\alpha = 1/3 \times 10^{-3}$ m^{-1}. The α factor was calculated taking into account that the number of particles in the shower is decreased by a factor e over a distance of 6 km.

(3) The shower disk moves uniformly with a velocity $c \sim 3 \times 10^8$ m/s along a trajectory with a variable curvature radius. This departure from rectilinearity is caused by a slight deviation of the shower motion in the geomagnetic field and a loss of energy through ionization. If these factors can be neglected, the shower trajectory is considered as vertical. The majority of electrons (positrons) have an initial energy W_1 characterized by the factor $\gamma_0 = 200$. In a normal atmosphere, the ionization losses W are equal to 0.25 MeV/m and do not depend on the shower disk velocity, provided that $\gamma \geq 2$. A particle is considered as belonging to the shower disk if its energy factor γ is no less than two.

(4) The radiation field is studied at distances $R_0 \gg \lambda$. For the frequency range under consideration ($0 < \nu < 1$ MHz), the wavelength λ exceeds the radiation source size $2r_0$. Thus, in many cases, the current density can be expressed by the formula $j = \pm cf(z)q\delta(\mathbf{r}' \cdot \mathbf{r})$, where $c = 3 \times 10^8$ m/s, $\mathbf{r}'$ is the radius vector of an arbitrary point, $z = z(t) = ct$ is the shower disk motion equation, and $q = 1.6 \times 10^{-19}$ C.

(5) A neutral disk is split by the horizontal component of the geomagnetic field in the direction perpendicular to the disk motion so that a dipole is formed. The dipole moment is $0.5N_0qf(z)d$, where d is the dis-

tance between the centers of the oppositely charged disks and $0.5N_0qf(z)$ is the number of particles in each disk.

The energy W_1(~10^8 eV) of moving electrons (positrons) is lost through ionization. Thus, the electron range is $W_1/W = 400$ m. As an electron (positron) travels the distance dz, it is displaced by $dy = dz\sin\psi$ in the direction perpendicular to its motion and to the horizontal component of the magnetic field ($\psi = \psi(z)$ is the angle between the instantaneous radius of curvature $R(z)$ of the trajectory and the horizon line). The angle ψ is determined by summing $d(\psi) = dz/R(z)$ over all elements of the trajectory from zero to the current coordinate z. Thus, the total displacement $d/2$ is expressed by the following formula:

$$d/2 = \int_0^{396} \sin\left(\int_0^z \frac{dz'}{R(z')}\right) dz'. \qquad (1)$$

The limit of integration $z = 396$ m was selected taking into account that the shower velocity before colliding with the Earth would still be close to the velocity of light ($\gamma \geq 2$).

The instantaneous radius of curvature $R = mc\gamma/qB$ of a relativistic particle trajectory can be conveniently expressed in terms of the traversed path z. By definition, $\gamma = (W_1 - W_z)/mc^2$ or $\gamma = \gamma_0 - Az$, where $A = 0.5\ \mathrm{m}^{-1}$. It can be calculated from Eq. (1) that $d/2 = 25$ m. Thus, at the instant of colliding with the Earth, the shower consists of two oppositely charged disks with centers separated by a distance $d = 50$ m. The mean-square radius r_0 of each disk is 100 m. Therefore, the disks overlap significantly with one another, thereby causing a decrease in the radiation intensity. In the model under consideration, this decrease is described in terms of a phase $\exp[ik(R_0 \pm d\cos\varphi)]$, where φ is the angle between the direction of observation **n** and the dipole axis.

Soil conductance within the medium-frequency range (~1 MHz) is rather high. Therefore, in the model under consideration, the Earth's surface can be represented as a semi-infinite metal medium. The radiation field induced by the shower collision with the Earth should be determined using the expression for $E(\omega)$ in the case of an instantaneous stop of moving charge and its image [8] rather than general formulas for transient radiation. The current density (for both positive and negative charges) is expressed using the δ-function. Thus, the following equation can be written [9]:

$$E(\omega) = \frac{2i\omega qN_0 e^{ikR_0}}{4\pi\varepsilon_0 c^2 R_0} \times \int e^{i\omega z/c} f(z)[e^{ikd\cos\varphi} - e^{-ikd\cos\varphi}]dz. \qquad (2)$$

This equation was obtained on the assumption that $\mathbf{kz} \approx 0$ and $|[\mathbf{n}d\mathbf{z}]| = dz$. This assumption was made taking into account that the shower axis is almost vertical, while the observer is positioned in the wave zone on the Earth's surface, so that $(\mathbf{kz}) \approx \pi/2$. In addition, the integral over x and y is equal to one (only the delta-function depends on these variables).

If the shower subsides before reaching the Earth's surface, the limits of integration fall within the range $-\infty < z < \infty$. Thus, we obtain from Eq. (2) that

$$E(\omega) = \frac{\omega qN_0}{\sqrt{\pi}\varepsilon_0 c^2 R_0 \alpha} e^{-\frac{\omega^2}{4\alpha^2c^2}} \sin(kd\cos\varphi). \qquad (3)$$

Obviously, the amplitude of $E(\omega)$ given by Eq. (3) decreases exponentially with an increasing frequency. This allows the limiting value of ω to be determined: $\omega = 2 \times 10^5$. To obtain the absolute value of $E(\omega)$, the following values should be substituted into Eq. (3): the number of electrons in the shower maximum $N_0 = 10^{12}$ [7] (the primary particle energy is taken to be $W_0 = 10^{21}$ eV); the distance to the observer $R_0 = 10^4$ m; $d = 50$ m; $\varphi = 0$; $\alpha = 1/3 \times 10^{-3}$ m; $c = 3 \times 10^8$ m/s; $k = \omega/c$; $\omega = 2 \times 10^5\ \mathrm{s}^{-1}$; $q = 1.6 \times 10^{-19}$ C; and $(4\pi\varepsilon_0)^{-1} = 0.9 \times 10^{10}$ m/F. On substitution, we obtain that $|E(\omega)| = 10\ \mu$V/mMHz.

Taking into account the primary particle energy, the shower maximum is found to fall within the immediate vicinity of the Earth's surface. Therefore, the limits of integration in Eq. (2) should fall within the range $-\infty < z = 0$. Integration can be effectively performed by expanding the integral in terms of even powers $1/x$ [10], where $x = i\omega/\alpha c\sqrt{2}$:

$$E(\omega) = \frac{2i\omega qN_0\sqrt{\pi}}{8\varepsilon_0 c^2 R_0 \alpha} e^{-\frac{\omega^2}{4\alpha^2c^2}} \times \left[1 - \frac{e^{-\frac{x^2}{2}}}{x\sqrt{2\pi}}\left(1 - \frac{1}{x^2} + \frac{3}{x^4}\ldots\right)\right] \sin(kd\cos\varphi). \qquad (4)$$

To determine the dominant term in Eq. (4), it should be taken into account that the electron (positron) current can be described using the δ-function only within a limited range of wavelengths. The disk size is $2r_0 = 200$ m. Therefore, for $\lambda \leq 400$ m ($\omega_0 \leq 4 \times 10^6\ \mathrm{s}^{-1}$), the amplitudes of harmonics in Eq. (2) can be summed up regardless of phase. At $\omega_0 = 4 \times 10^6\ \mathrm{s}^{-1}$, the value $1/x^2$ is of the order of 10^{-3}. Therefore, the expression in round brackets in Eq. (4) can be reduced to the zeroth term. In addition, at $\omega_0 \leq 4 \times 10^6\ \mathrm{s}^{-1}$, the exponential factor $\exp(-\omega^2/4\alpha^2c^2)$ is rather small. Thus, the absolute value of $|E(\omega)|$ in the vicinity of frequency ω_0 is

$$|E(\omega)| = \frac{N_0 q}{2\pi\varepsilon_0 c R_0}\sin(kd\cos\varphi). \qquad (5)$$

Usually, semiconductor-dipole antennas have a frequency band $\Delta\omega/\omega \approx 0.1$. Therefore, it makes no sense to specify the upper and lower limits in Eq. (5). Even if $\cos\varphi = 1$, the argument of the sine function in Eq. (5) is equal to 0.66. Therefore, within the frequency range $0 < \omega < \omega_0$, the directional radiation diagram is similar to that of an elementary dipole. Using the values substituted in Eq. (3) for calculating $E(\omega)$, we obtain that the maximum (at $\varphi = 0$) spectral intensity $E(\omega)$ of the field is about 630 μV/mMHz (R_0 is taken to be 10^4 m). This value is approximately two orders of magnitude greater than that obtained from Eq. (3).

Let us compare the obtained value of the field intensity with the available experimental data and assess the possibility of the radio detection of cosmic rays with an energy exceeding 10^{21} eV. The results of long-term studies of the geomagnetic and Cherenkov mechanisms of extensive air shower radiation are reviewed in [11]. These studies were thought to hold much promise for developing methods of cosmic ray detection. It was found that the intensity of the field induced by an extensive air shower with the primary particle energy $W_0 = 10^{17}$ eV at a distance of 100 m from the shower axis is about 10 μV/mMHz. The value of $E(\omega)$ is proportional to the ratio W_0/R_0. Therefore, if $W_0 = 10^{21}$ eV and $R_0 = 10^4$ m, we obtain that $E(\omega) = 10^3$ μV/mMHz. This is close to the value obtained in this work. However, the geomagnetic mechanism of radiation provides a pencil-beam directional pattern of radiation, so that the actual signal amplitude in [11] is several orders of magnitude smaller than the obtained value. For this reason, the mechanism providing the pencil-beam directional pattern of radiation (radiation is directed almost straight downward) cannot be used for the independent detection of cosmic rays.

In my opinion, the radio emission mechanism first described in this work can be used for detecting particles with an energy exceeding 10^{21} eV without using a master signal. Two specific features of this mechanism of radio emission possibly make it valid. First, the intensity of the radio-frequency pulse field is rather high even at a large distance from the source. Second, the intensity of atmospheric disturbances is minimum at frequencies of about 1 MHz [12]. For example, in the middle latitudes of the European part of the former Soviet Union, the intensity of atmospheric disturbances is less than 10^{-3} μV/mMHz. In the circumpolar regions, this value is 20–30 dB smaller than in the Central European regions.

As an example, let us consider four vertical-polarization antennas placed at the vertices of an imaginary square 1000 km apart located on the ocean surface. A shower with energy $W_0 \geq 10^{22}$ eV within the limits of a circle 1000 km in radius would almost always fall within a distance of about 500 km from one or several antennas. Thus, the field intensity at the antenna location would be no less than 120 μV/mMHz. Taking into account the field attenuation in the diffraction region on the spherical surface of the Earth (this can be done using, for example, the tables given in [12]), we obtain the actual value of the spectral intensity: $E(\omega) \approx$ 60 μV/mMHz (R_0 is taken to be 500 km). There is evidence that the energy spectrum of cosmic rays has a second bend at $W_0 = 10^{19}$ eV, so that the coefficient of the spectrum γ is reduced to $\gamma = 2.7$ [13, 7]. In this case, the particle flux intensity is

$$J(>W_0) \approx 0.2 \times 10^4 W_0^{-1.7} (m^2 ssr)^{-1},$$

where W_0 is expressed in GeV. For $W_0 > 10^{22}$ eV, the incidence of showers over a circle of radius 1000 km was found to be approximately 20 showers per year. Such an incidence of events is quite appropriate for observations. However, the use of the system described above for the independent detection of cosmic rays by the conventional method based on scintillation counters is made difficult by the lack of a master signal. To solve the problem of the absence of such a synchronizing pulse, the following factors should be taken into account. First, local lightning discharges are the only source of signals that can be mistaken for the desired signal. If the antennas used in the experiment are implemented as crossed frames, the measurement of the amplitude ratio of currents induced by the radio-frequency pulse allows the direction to the pulse source to be determined [14]. Therefore, the four antennas can be regarded as a direction-finding system. Analysis of the directions, amplitudes, and durations of the received signals allows the problem of identification of the desired signal to be significantly facilitated. Second, it is well known that a lightning discharge is a discontinuous current pulse with an overall duration of tens or even hundreds of milliseconds. On the other hand, the signal induced by an extensive air shower consists of a single pulse with a simple shape and duration of about 1 μs. Therefore, these signals can easily be distinguished.

Thus, in addition to the method described in [15–18], there is another possibility for assessing the ultrahigh-energy particle flux intensity. The outline of this possibility given in this work should be regarded as a preliminary discussion of an actual experiment rather than the final version of the experimental scheme.

REFERENCES

1. P. I. Golubnichiĭ and A. D. Filonenko, Pis'ma Zh. Tekh. Fiz. **20** (12), 57 (1994) [Tech. Phys. Lett. **20**, 499 (1994)].
2. P. I. Golubnichiĭ and A. D. Filonenko, Pis'ma Zh. Tekh. Fiz. **20** (23), 59 (1994) [Tech. Phys. Lett. **20**, 960 (1994)].
3. P. I. Golubnichiĭ, A. D. Filonenko, and V. I. Yakovlev, Izv. Akad. Nauk, Ser. Fiz. **58** (12), 115 (1994).
4. A. D. Filonenko, Izv. Akad. Nauk, Ser. Fiz. **63** (3), 565 (1999).

5. P. Datta and K. M. Pathak, in *Proceedings of the 21th International Cosmic Ray Conference, 1990*, Vol. 9, p. 218.
6. G. B. Khristiansen, G. V. Kulikov, and Yu. A. Fomin, *Cosmic Radiation of Ultrahigh Energy* (Atomizdat, Moscow, 1975).
7. V. S. Murzin, *Introduction to the Cosmic Ray Physics* (Mosk. Gos. Univ., Moscow, 1988).
8. V. L. Ginzburg, *Theoretical Physics and Astrophysics* (Nauka, Moscow, 1981, 2nd ed.; Pergamon, Oxford, 1979).
9. L. D. Landau and E. M. Lifshitz, *The Classical Theory of Fields* (Nauka, Moscow, 1967; Pergamon, Oxford, 1975).
10. *Handbook on Special Functions*, Ed. by M. Abramowitz and I. A. Stegun (Dover, New York, 1971; Nauka, Moscow, 1979).
11. V. B. Atrashkevich, O. V. Vedeneev, H. R. Allan, *et al.*, Yad. Fiz. **28** (3), 712 (1978) [Sov. J. Nucl. Phys. **28**, 366 (1978)].
12. *Handbook on Theoretical Foundations of Radio Electronics*, Ed. by A. A. Kulikovskiĭ (Énergiya, Moscow, 1977), Vol. 1.
13. V. L. Ginzburg, Usp. Fiz. Nauk **166** (2), 169 (1996) [Phys. Usp. **39**, 155 (1996)].
14. A. A. Pistol’kors, *Antennas* (Svyaz’izdat, Moscow, 1947).
15. A. D. Filonenko, Pis’ma Zh. Tekh. Fiz. **24** (24), 65 (1998) [Tech. Phys. Lett. **24**, 975 (1998)].
16. A. D. Filonenko, Izv. Akad. Nauk, Ser. Fiz. **61** (3), 543 (1997).
17. A. D. Filonenko, Pis’ma Zh. Éksp. Teor. Fiz. **70** (10), 639 (1999) [JETP Lett. **70**, 649 (1999)].
18. A. D. Filonenko, Pis’ma Zh. Tekh. Fiz. **23** (10), 57 (1997) [Tech. Phys. Lett. **23**, 399 (1997)].

Translated by K. Chamorovskiĭ

Technical Physics, Vol. 46, No. 3, 2001, p. 361.

ERRATA

Erratum: “Silicon Dual-Drain Strain-Sensitive FETs” [*Tech. Phys*. 45, 1276 (2000)]

G. G. Babichev, S. I. Kozlovskiĭ, and N. N. Sharan

The third author’s name has been missed. The correct list should read

G. G. Babichev, S. I. Kozlovskiĭ, V. A. Romanov, and N. N. Sharan